

Transient Mixed Convection Validation for NGNP

Reactor Concepts

Barton Smith

Utah State University

In collaboration with:

Idaho National Laboratory

Steven Reeves, Federal POC
Gradon Yoder, Technical POC

Nuclear Energy University Programs U.S. Department of Energy



(Project 11-3081) Transient Mixed Convection Validation For NGNP

Final Report

Principal Investigator: Barton Smith
In collaboration with:
Richard Schultz, Idaho National Laboratory

Award Identification Number: 00118627-

Period of Performance: 9/7/2011 to 9/30/2015

Submitted 10/19/2015

Final Report: Transient Mixed Convection Validation

The results of this project are best described by the papers and dissertations that resulted from the work. They are attached in their entirety to this document. They are:

- 1) Jeff Harris PhD dissertation (focused mainly on forced convection)
- 2) Blake Lance PhD dissertation (focused mainly on mixed and transient convection)
This dissertation is in multi-paper format and includes the article currently submitted and one to be submitted shortly.
- 3) JFE paper on CFD Validation Benchmark for Forced Convection.

A COMPUTATIONAL FLUID DYNAMICS VALIDATION EXPERIMENT FOR
FORCED AND MIXED CONVECTION ON A VERTICAL HEATED PLATE

by

Jeff Robert Harris

A dissertation submitted in partial fulfillment
of the requirements for the degree

of

DOCTOR OF PHILOSOPHY

in

Mechanical Engineering

Approved:

Dr. Barton L. Smith
Major Professor

Dr. Robert Spall
Committee Member

Dr. Heng Ban
Committee Member

Dr. Aaron Katz
Committee Member

Dr. Blake Tullis
Committee Member

Dr. Mark R. McLellen
Vice President for Research and
Dean of the School of Graduate Studies

UTAH STATE UNIVERSITY
Logan, Utah

2014

Copyright © Jeff Robert Harris 2014

All Rights Reserved

Abstract

A Computational Fluid Dynamics Validation Experiment for Forced and Mixed
Convection on a Vertical Heated Plate

by

Jeff Robert Harris, Doctor of Philosophy

Utah State University, 2014

Major Professor: Dr. Barton L. Smith

Department: Mechanical and Aerospace Engineering

A computational fluid dynamics (CFD) validation experiment is conducted for convection flow from a heated plate in buoyancy aided and opposed orientations. The design of the experiment to meet CFD validation completeness standards is described. Previous experiments and simulations have been completed, but none measure or present the necessary boundary conditions to define the simulation boundary conditions. Experimental measurements of forced and mixed convection are presented, along with measured boundary conditions sufficient to compute simulations for validation purposes. Some simulation results are described, but a complete validation study is not included. Simulations are conducted to ensure all necessary boundary conditions are being measured. This document and the corresponding website will provide sufficient explanation and data to repeat the experiment and speed the setup of future validation experiments. The data and boundary conditions are available for download on a website dedicated to validation data dissemination. Along with the validation data, the response quantities provide some insight into the flow characteristics of the boundary layer for convective flow from a vertical flat plate.

(191 pages)

Public Abstract

A Computational Fluid Dynamics Validation Experiment for Forced and Mixed
Convection on a Vertical Heated Plate

by

Jeff Robert Harris, Doctor of Philosophy

Utah State University, 2014

Major Professor: Dr. Barton L. Smith
Department: Mechanical and Aerospace Engineering

A computational fluid dynamics (CFD) validation experiment is conducted for flow over a heated vertical plate. The design of the experiment to meet CFD validation standards is described. Many experiments and simulations have been completed in past studies, but none measure or present the necessary boundary conditions to define the simulation. Experimental measurements of heated flow are presented, along with corresponding boundary conditions sufficient to define the simulation's boundary conditions. Some simulation results are described, but a complete validation study is not included. The simulations are conducted by the experimentalist to ensure all necessary boundary conditions are being measured. This document will provide sufficient explanation and data to repeat the experiments and speed the setup of future validation experiments.

Acknowledgments

The author gratefully recognizes Dr. Barton Smith, Blake Lance, and Brandon Wilson for their guidance, mentoring, and continual support. My colleagues in the Experimental Fluid Dynamics Laboratory for their assistance, advice, and patience, including Scott Warner, Kyle Jones, David Reynolds, Tucker Smith, Shaun Harris, Andrew Ostler. My family for being patient with me, in spite of my impatience, thank you.

Thanks also to Utah State University for allowing me to work on the beautiful campus and in their facilities. To the Department of Mechanical and Aerospace Engineering faculty and staff, thanks for your support.

This research is being performed using funding received from the DOE Office of Nuclear Energy's Nuclear Energy University Programs and a fellowship from the Nuclear Regulatory Commission.

Contents

	Page
Abstract	iii
Public Abstract	iv
Acknowledgments	v
List of Tables	viii
List of Figures	x
Notation	xv
Acronyms	xviii
1 Introduction	1
1.1 Motivation	1
1.2 Validation	3
1.3 Convection	9
1.3.1 Forced Convection	9
1.3.2 Mixed Convection	11
2 Objectives	13
3 Equipment	15
3.1 Wind Tunnel	15
3.1.1 Structure	15
3.1.2 Test Section	18
3.2 Instrumentation	19
3.2.1 Atmospheric Conditions	21
3.2.2 Inlet Temperature	22
3.2.3 Wall Temperatures	22
3.2.4 Plate Heat Flux	25
3.2.5 Particle Image Velocimetry	25
3.3 RoBuT Test Section Assembly	30
4 Approach	31
4.1 Apparatus Design	31
4.2 Wind Tunnel Characterization	35
4.2.1 Pressure Drop	35
4.2.2 Geometry	37
4.2.3 Temperatures	39
4.2.4 Inlet Treatment	40

4.2.5	Boundary Layer	45
4.3	Measurement of System Response Quantities	46
4.3.1	Experimental Procedure	46
4.3.2	Boundary Layer Velocity	47
4.3.3	Heat Flux	48
4.3.4	Friction Velocity	48
4.4	CFD Simulation Procedure	51
4.4.1	Geometry and Mesh	51
4.4.2	Boundary Conditions and Physics	53
4.4.3	Models	54
4.5	Quality Assurance	55
4.6	Data Recording, Storage, and Backup	56
5	Results	57
5.1	Boundary Conditions	57
5.2	System Response Quantities	59
5.2.1	Isothermal Buoyancy Aided Forced Convection	60
5.2.2	Isothermal Buoyancy Aided Mixed Convection	67
5.2.3	Isothermal Buoyancy Opposed Forced Convection	73
5.2.4	Isothermal Buoyancy Opposed Mixed Convection	78
5.2.5	Constant Heat Flux Buoyancy Aided Forced Convection	80
5.2.6	Constant Heat Flux Buoyancy Aided Mixed Convection	87
5.3	Discussion of SRQ's	91
5.3.1	Gravity and Temperature Effects	91
5.3.2	Comparison of Classical Boundary Layer Shape Factors	97
5.3.3	Buoyancy Influence on Heat Flux	99
5.3.4	Shear Velocity and Shear Profile	101
5.4	Uncertainty and Repeatability	108
6	Conclusions	111
	References	114
	Appendices	118
Appendix A	Small Calibration Target	119
Appendix B	Rotatable Buoyancy Tunnel Schematic	120
Appendix C	Test Section Schematics	123
Appendix D	Custom Silicon Heater	130
Appendix E	Inlet Thermocouple Positions	132
Appendix F	Boundary Conditions Statistics	133
Appendix G	Inlet Analysis Code	143
Appendix H	Interpolator Code for StarCCM+	151
Appendix I	Code to Compute Correlations and Momentum Thickness	161
Appendix J	Shear Velocity Code to Compute u_τ	166
Appendix K	Copyright Permissions	170

List of Tables

Table	Page
2.1 Convection cases for data acquisition. The bottom row shows the plate conditions as isothermal or constant heat flux.	14
3.1 The heat flux sensor properties provided by the manufacturer. The x position of the heat flux sensors will be used in later analysis.	25
4.1 Parameters for computing the plate emissivity using an energy balance in a state of natural convection.	32
4.2 The measured as-built dimensions for the test section in inches.	38
4.3 The measured as-built dimensions uncertainty for the test section in inches.	39
4.4 The mesh properties for the three meshes used in the GCI analysis. The mesh cell count, average volume of cells, near wall cell height, and several GCI parameters and heat flux results are tabulated.	52
4.5 The GCI results using the methods described above for heat flux at the first sensor position.	53
5.1 The several cases considered in the study.	60
5.2 The von Kármán constant, intercept, shear velocity from the Spalding fit, and the shear velocity from a linear fit near the wall at the heat flux sensor positions for the buoyancy aided isothermal forced convection case. The computed friction velocity from the CFD simulation is also tabulated. . . .	65
5.3 The buoyancy aided isothermal forced convection heat flux results along with the Grashof to Reynolds number ratio (showing the cases are forced convection) and the momentum thickness Reynolds number.	67
5.4 The buoyancy aided isothermal mixed convection heat flux results along with the Grashof to Reynolds number ratio, several boundary layer thicknesses, and the momentum thickness Reynolds number.	73
5.5 The von Kármán constant, intercept, shear velocity from the Spalding fit, and the shear velocity from a linear fit near the wall at the heat flux sensor positions for the buoyancy opposed isothermal forced convection case. The resultant u_τ from the CFD simulation is also tabulated. Note that $\kappa = 0.41$ and $B = 5.0$ are classical values not included in the fit.	75

5.6	The buoyancy opposed isothermal forced convection heat flux results along with the Grashof to Reynolds number ratio and the momentum thickness Reynolds number.	78
5.7	The buoyancy opposed isothermal mixed convection heat flux results along with the Grashof to Reynolds number ratio and the momentum thickness Reynolds number.	80
5.8	The von Kármán constant, intercept, shear velocity from the Spalding fit, and the shear velocity from a linear fit near the wall at the heat flux sensor positions for the buoyancy aided constant heat flux forced convection case. .	85
5.9	The buoyancy aided constant heat flux forced convection heat flux results along with the Grashof to Reynolds number ratio and the momentum thickness Reynolds number.	87
5.10	The buoyancy aided constant heat flux mixed convection heat flux results along with the Grashof to Reynolds number ratio and the momentum thickness Reynolds number.	91
5.11	Shear velocity from the Spalding fit, and the shear velocity from a linear fit near the wall at the heat flux sensor positions for the buoyancy aided isothermal forced convection case. The computed friction velocity from the CFD simulation is also tabulated, along with the friction velocity from the total shear velocity. The two Spalding fit shear velocities correspond to the two cases with different fit parameters described previously (see Table 5.2).	104
5.12	Shear velocity from the Spalding fit, and the shear velocity from a linear fit near the wall at the heat flux sensor positions for the buoyancy aided constant heat flux forced convection case. The two Spalding fit shear velocities correspond to the two cases with different fit parameters described previously (see Table 5.8).	105

List of Figures

Figure	Page
1.1 A diagram of a HTGR showing the flow directions for convection over a vertical surface and the relative size of the core design [1].	2
1.2 Graphical description of the validation hierarchy, after [2].	5
1.3 The difficulty spectrum of SRQ's, after [3]	7
1.4 A velocity profile for the inlet of the test section is shown, along with a top hat profile and a parabolic profile. The Reynolds Stress is also plotted along with a line of 10% of the free stream.	8
3.1 The RoBuT showing the structure, wheel frame on the left. The right image shows the inlet and the coordinate system for the measurements.	16
3.2 A schematic of the wind tunnel, with nomenclature and coordinate system.	17
3.3 A photograph of the traverse mounting equipment allowing for synchronized movement of the camera and laser in the y and z directions.	18
3.4 The test section, heated plate and its several layers are shown. The plate is separated from the plastic sidewalls by a layer of Teflon [®]	19
3.5 The heated plate and its several layers are shown to relative scale with instrumentation wire leads going out of the test section to the right.	20
3.6 The wind tunnel and control system showing the heaters and power supplies.	21
3.7 The inlet honeycomb flow straightener viewed from the downstream side and showing the inlet thermocouples.	23
3.8 The installation of the plate thermocouples using a syringe to place the epoxy to hold the thermocouples in place.	24
3.9 The heat flux for a constant power forced convection case along with the $z = 0$ heated wall temperatures.	26
3.10 A photograph of a seeding canister, similar to a Laskin nozzle.	29
4.1 Pressure drop in the contraction and test section with the wind tunnel horizontally oriented. The measured pressure drop is compared with calculations using Bernoulli's equation and frictional losses.	37

4.2	Photograph of as-built geometry measurement procedure.	38
4.3	The wall temperatures and inlet temperature viewed in StarCCM+.	40
4.4	The inlet velocity magnitudes using the 9 PIV planes.	41
4.5	The orientation of the camera and laser for PIV inflow data acquisition. The laser and camera are traversed across the test section to obtain several planes of velocity data. The flow direction is out of the page. (a) shows the nominal setup that is also used to obtain the velocity over the heat flux sensors. (b) shows the inlet profile specific orientation to obtain the w component of velocity.	42
4.6	Center profiles for two orientations showing justification for several assumptions at the inlet of the test section.	43
4.7	An image of the wall, with the image width being 2.25 mm.	50
4.8	The error of the wall location computed using three methods with the image estimate being the basis for the error and a scale factor of around 84 pixels/mm.	51
5.1	The centerline ($z = 0$) temperature profiles for the buoyancy aided cases. .	58
5.2	The temperature contour for the aided isothermal forced convection case, showing the hot spot at the second heater. The segments show the heaters.	59
5.3	The boundary layer velocity profiles for buoyancy aided forced convection with isothermal heating. (a) shows the streamwise component of velocity and Reynolds Stress. (b) shows the cross-stream component of velocity and the two other measured components of the Reynolds Stress. Recall that P1 is $x = 5.87$ in., P2 is $x = 30.12$ in., and P3 is $x = 54.87$ in.	61
5.4	The boundary layer velocity profiles for buoyancy aided forced convection with isothermal heating compared with CFD results using the same boundary conditions. (a) shows the streamwise component of velocity. (b) shows the turbulence kinetic energy profiles.	63
5.5	The wall coordinate boundary layers for the three heat flux sensor positions for buoyancy aided isothermal forced convection flow and the Spalding fit profiles for comparison.	64
5.6	The heat flux compared with a CFD simulation and two correlations for the buoyancy aided isothermal forced convection case. The shear velocity from the several methods is also plotted.	66
5.7	The boundary layer velocity profiles for buoyancy aided mixed convection with isothermal heating. (a) shows the streamwise component of velocity and Reynolds Stress. (b) shows the cross-stream component of velocity and the two other components of the Reynolds Stress.	69

5.8	The boundary layer velocity profiles for buoyancy aided mixed convection with isothermal heating compared with CFD results using the same boundary conditions. (a) shows the streamwise component of velocity. (b) shows the turbulence kinetic energy.	70
5.9	The heat flux for the buoyancy aided isothermal mixed convection case. . .	72
5.10	The boundary layer velocity profiles for buoyancy opposed forced convection with isothermal heating. (a) shows the streamwise component of velocity and Reynolds normal stress. (b) shows the cross-stream component of velocity and two other measured components of the Reynolds Stress. Recall that P1 is $x = 5.87$ in., P2 is $x = 30.12$ in., and P3 is $x = 54.87$ in.	74
5.11	The boundary layer velocity profiles for buoyancy opposed forced convection with isothermal heating compared with CFD results using the same boundary conditions. (a) shows the streamwise component of velocity. (b) shows the turbulence kinetic energy.	76
5.12	The measured heat flux for the buoyancy opposed isothermal forced convection case is compared with the two correlations previously presented and the corresponding CFD simulation for this case.	77
5.13	The boundary layer velocity profiles for buoyancy opposed mixed convection with isothermal heating. (a) shows the streamwise component of velocity and Reynolds normal stress. (b) shows the cross-stream component of velocity and two other measured components of the Reynolds Stress.	79
5.14	The boundary layer velocity profiles for buoyancy opposed mixed convection with isothermal heating compared with CFD results using the same boundary conditions. (a) shows the streamwise component of velocity. (b) shows the turbulence kinetic energy profiles.	81
5.15	The heat flux for the buoyancy opposed isothermal mixed convection case compared with several CFD models with the $k-\epsilon$ Low Re being the standard model for the mixed cases in this study.	82
5.16	The boundary layer velocity profiles for buoyancy aided forced convection with constant heat flux from the plate. (a) shows the streamwise component of velocity and Reynolds normal stress. (b) shows the cross-stream component of velocity and two other measured components of the Reynolds stress.	83
5.17	The boundary layer velocity profiles for buoyancy aided forced convection with constant heat flux compared with CFD results using the same boundary conditions. (a) shows the streamwise component of velocity. (b) shows the turbulence kinetic energy profiles.	84

5.18	The wall coordinate boundary layers for the three heat flux sensor positions for buoyancy aided constant flux forced convection flow and the Spalding fit profiles for comparison.	86
5.19	The heat flux for the buoyancy aided constant heat flux forced convection case compared with the CFD results for the same boundary conditions. . .	86
5.20	The boundary layer velocity profiles for buoyancy aided mixed convection with constant flux heating. (a) shows the streamwise component of velocity and Reynolds Stress. (b) shows the cross-stream component of velocity and two other measured components of the Reynolds Stress.	88
5.21	The boundary layer velocity profiles for buoyancy aided mixed convection with constant heat flux heating compared with CFD results using the same boundary conditions. (a) shows the streamwise component of velocity. (b) shows the turbulence kinetic energy.	89
5.22	The heat flux for the buoyancy aided constant heat flux mixed convection case.	90
5.23	The boundary layer velocity comparison for the isothermal forced convection buoyancy aided and opposed cases. The relative difference between the cases is also plotted as $\Delta\bar{u}_{F,G}$	92
5.24	The heat flux comparison for isothermal forced and mixed convection comparing the buoyancy aided and buoyancy opposed conditions.	93
5.25	The convection ratio comparison for isothermal forced and mixed convection comparing the buoyancy aided and buoyancy opposed conditions.	93
5.26	The momentum thickness comparison for isothermal forced and mixed convection comparing the buoyancy aided and buoyancy opposed conditions. .	94
5.27	The boundary layer velocity profile comparison for the isothermal mixed convection buoyancy aided and opposed cases. The relative difference due to gravity effects for isothermal mixed convection is denoted $\Delta\bar{u}_{M,G}$	95
5.28	The boundary layer velocity comparison for the forced convection buoyancy aided cases, comparing the isothermal and constant flux heating conditions. The relative difference between the cases is denoted $\Delta\bar{u}_{F,T}$	96
5.29	The boundary layer velocity comparison for the mixed convection buoyancy aided cases comparing the isothermal and constant heat flux conditions. The relative difference between the cases is denoted $\Delta\bar{u}_{M,T}$	96
5.30	A comparison of the classic shape factor with the expected trend as a function of the second shape factor η (see Eqn. 5.8).	98

5.31	The boundary layer velocity profiles for an unheated and heated low Reynolds number flow.	99
5.32	A plot of the Nusselt number ratio versus the special buoyancy parameter for the data in this study and the data presented in [4].	100
5.33	The total shear stress profile with a linear fit for the buoyancy aided isothermal forced convection case.	102
5.34	The total shear stress profile with a linear fit for the buoyancy aided isothermal mixed convection case.	102
5.35	The total shear stress profile with a linear fit for the buoyancy aided constant flux forced convection case.	103
5.36	The total shear stress profile with a linear fit for the buoyancy aided constant flux mixed convection case.	104
5.37	The total shear stress profile with a linear fit for the buoyancy aided isothermal forced convection case at the first position. The $y+ = 10$ value is at $y = 0.73$ mm.	106
5.38	The total shear stress profile with a linear fit for the buoyancy aided isothermal forced convection case at the second position. The $y+ = 10$ value is at $y = 0.87$ mm.	107
5.39	The total shear stress profile with a linear fit for the buoyancy aided isothermal forced convection case at the third position. The $y+ = 10$ value is at $y = 1.13$ mm.	107
5.40	The boundary layer streamwise velocity profiles for the flow over the three positions for three repeats of the isothermal forced aided flow measurement.	108
5.41	The boundary layer streamwise velocity residuals for the flow over the three positions for three repeats of the isothermal forced aided flow measurement.	109
5.42	The boundary layer streamwise velocity Reynolds normal stress residuals for the flow over the three positions for three repeats of the isothermal forced aided flow measurement.	110
A.1	An image of the calibration target built to dewarp the SRQ data images.	119
E.1	A sketch showing the positions of the inlet thermocouples. With the test section in the buoyancy aided orientation (inlet down), up in the image is north.	132

Notation

Lower-case Roman

c_f	The coefficient of friction.
dy	The height of the near wall cell in a CFD mesh.
e_a^{21}	The absolute relative error between the second and first refined grid.
g	The standard gravity constant, 9.81 m/s ² .
k	The turbulence kinetic energy.
p^+	The nondimensional pressure.
r_{21}^p	The ratio of the characteristic length for the first and second grid refinements.
r_{32}^p	The ratio of the characteristic length for the second and first grid refinements.
u	The velocity component in the x direction.
\bar{u}_∞	The free-stream velocity.
u^+	The nondimensional streamwise velocity.
v	The velocity component in the y direction.
w	The velocity component in the z direction.
x	The stream-wise position in the test section.
y	The position measured perpendicular from the surface of the heated plate.
y_0	The wall position.
y^+	The nondimensional distance from the plate.
z	The span-wise position normal to x and y .

Upper-case Roman

B	The intercept in the wall coordinate profiles.
C	A constant to compute Nu_f .
D_h	The hydraulic diameter of the test section.

Gr_x	The Grashof number based on the local position x , $g\beta(T_s - T_\infty)x^3/\nu^2$.
H	The shape factor and ratio of δ_1/δ_2
K	The acceleration parameter in accelerating flow.
L	The length of the heated plate.
Nu_f	The forced convection Nusselt number for developing flow with variable properties used to understand buoyancy effects on heat transfer.
Nu_F	The forced convection Nusselt number.
Nu_{mix}	The mixed convection Nusselt number.
Nu_n	The natural convection Nusselt number.
Nu_x	The Nusselt number as a function of x position.
\bar{P}	The average pressure.
Pr	The Prandtl number based of air.
Ra_x	The Rayleigh number as a function of x position.
Re_x	The Reynolds number based on the local position x , $U_\infty x/\nu$.
St	The Stanton number based on the local position x .
T	A generic reference to temperature.
T_s	The temperature of the surface of the heated plate.
T_∞	The free-stream temperature of the air in the test section.

Lower-case Greek

α_{21}	The error between the second and first refined grid solutions.
α_{32}	The error between the third and second refined grid solutions.
β	The volumetric thermal expansion coefficient of a fluid (air).
δ	The boundary layer thickness.
δ_1	The displacement thickness of the boundary layer.
δ_2	The momentum thickness of the boundary layer.
δy	The wall position error
ϵ	The turbulence dissipation rate.

ϵ_M	The eddy diffusivity for the CFD turbulence models.
ϵ_{21}	The difference of a quantity (such as heat flux) between the second and first grid refinements.
ϵ_{32}	The difference of a quantity (such as heat flux) between the third and second grid refinements.
η	The second shape factor of a boundary layer.
κ	The von Kármán constant for wall coordinate transformation.
λ	The wavelength of the laser light sheet.
μ	The dynamic viscosity of the fluid.
μ_t	The turbulent viscosity for the CFD models.
ν	The kinematic viscosity of the fluid.
ρ	The density of the fluid.

Upper-case Greek

$\Delta \bar{u}_{F,G}$	The relative difference of velocity for forced convection due to a change in gravity direction.
$\Delta \bar{u}_{F,T}$	The relative difference of velocity for forced convection due to a change in heated plate temperature.
$\Delta \bar{u}_{M,G}$	The relative difference of velocity for mixed convection due to a change in gravity direction.
$\Delta \bar{u}_{M,T}$	The relative difference of velocity for mixed convection due to a change in heated plate temperature.
Δp	A pressure drop.
Δt	The time interval between images for PIV measurements.
$\Delta \bar{u}$	Streamwise velocity residual.
$\Delta \overline{u'u'}$	Normal Reynolds stress residual.
Δx	The particle image displacement in PIV measurements.

Acronyms

ASME	American Society of Mechanical Engineers
CFD	Computational Fluid Dynamics
GCI	Grid Convergence Index
LDA	Laser Doppler Anemometry
M&S	Modeling and Simulation
NGNP	Next Generation Nuclear Plant
PIV	Particle Image Velocimetry
RMS	Root Mean Square; in PIV data, the standard deviation
SRQ	System response quantity
TKE	Turbulence kinetic energy
VEC	Validation Experiment Completeness
VHTR	Very High Temperature Reactor
V&V	Verification and Validation

Chapter 1

Introduction

This project is to provide high fidelity experimental validation data for use in computational fluid dynamics simulation validation. Computer simulations are often used to predict the flow of coolant and heat transfer characteristics in nuclear reactors. Most cost effective simulations require models to predict the flow characteristics. These models will yield erroneous predictions if used in scenarios where they are not wholly valid because the assumptions and approximations inherent in the model are not applicable. Validating the model with experimental results is necessary for simulation accuracy [5]. This chapter will describe the motivation for the project, validation of computational fluid dynamics simulations, and convection. The objectives of the project are discussed in Chapter 2. The design of the experimental apparatus and the instrumentation are described in Chapter 3. The procedures used to conduct the tests and the methods of data analysis are included in Chapter 4. The results from the experiments and discussion of the results are contained in Chapter 5. Lastly, the conclusions are presented in Chapter 6.

1.1 Motivation

As the next generation of nuclear reactors are designed, numerical analysis of the reactor and its new features must be performed for operating and accident conditions. However, without experimental validation, a simulation of fluid flow should not be considered as a reliable prediction of real-world behavior [5].

The Next Generation Nuclear Plant (NGNP) uses a High Temperature Gas-cooled Reactor (HTGR) to generate the heat. The core and containment buildings have many surfaces that are cooled by forced/mixed/free convection, depending on the situation. As a specific example, consider the core and reactor vessel shown in Fig. 1.1. The convection on

the several vertical surfaces can be simplified to vertical planes for validation purposes. The core is cooled using buoyancy-opposed forced convection under normal operating conditions. In the up-comer leading into the core, the flow is buoyancy-aided forced convection. In an accident situation such as a loss of flow accident (a loss of power to the pumps forcing the coolant through the reactor), the downward forced flow may stop and the coolant would transition to natural convection (flowing opposite of the arrows in Fig. 1.1).

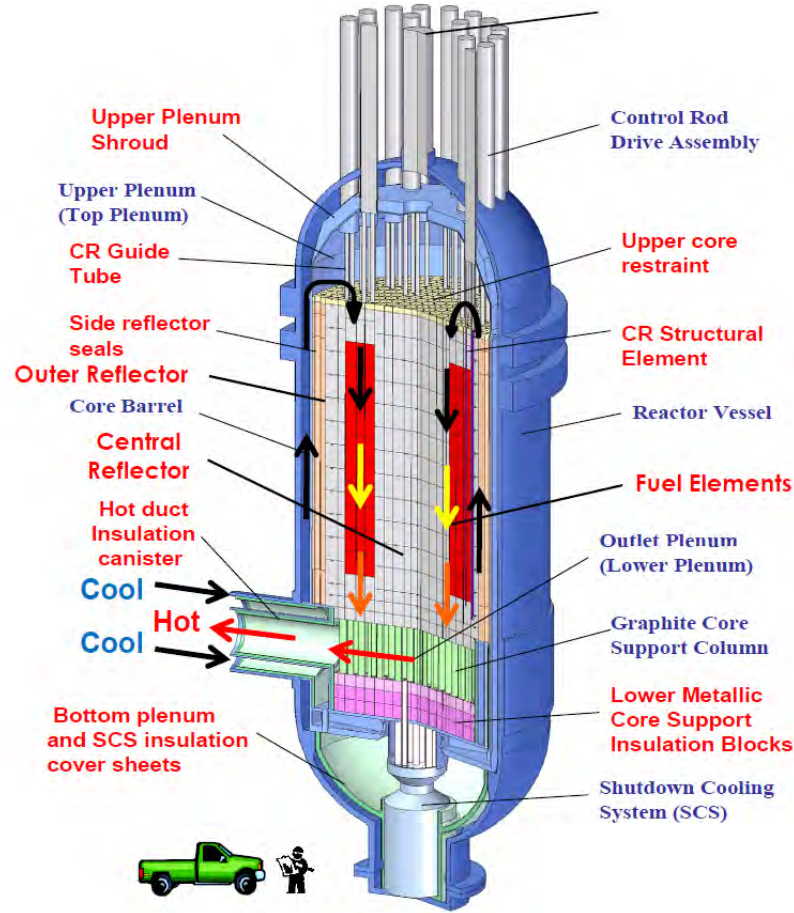


Fig. 1.1: A diagram of a HTGR showing the flow directions for convection over a vertical surface and the relative size of the core design [1].

The Rotatable Buoyancy Tunnel (RoBuT) was constructed to allow for measurement of all the convection regimes that exist in the core in Fig. 1.1. Both buoyancy aided and opposed, with the blower speed adjusting to make the convection forced, mixed, natural, or transitioning between the three. The blower can be programmed to create a transient case

where the convection transitions from forced to natural. The design of the test section and experiments are described in Chapter 3 and Chapter 4.

Simulations are used to predict the flow, heat transfer, and the transition of flow in an accident scenario, but transient simulations often have high uncertainty. Experimental data is necessary to validate the models used in the simulations, but it is not feasible to build a reactor or scale model. The simplified geometry used in the RoBuT is sufficient for modeling and simulation (M&S) validation purposes. Some basic theory of validation is presented in the following section. Relevant studies of convection are also presented in the following sections.

1.2 Validation

The word validation is often used interchangeably with verification. The two terms mean very different processes in ensuring simulation reliability. The ASME Standard is useful in providing a background of validation, and additional detail is available in literature from the AIAA Guide for the Verification and Validation of Computational Fluid Dynamics Simulations [2] and Oberkampf, *et al.* [3,6]. Validation experiments often compare computer simulations to benchmark data or experimental data. The simulation and experimental system response quantities are compared using a validation metric, which is an objective mathematical operator [3, pg. 473]. It is important to know the difference between verification and validation and the AIAA definitions are included below [2,3,6].

Verification: the process of determining that a model implementation accurately represents the developers conceptual description of the model and the solution to the model.

Validation: the process of determining the degree to which a model is an accurate representation of the real world from the perspective of the intended uses of the model.

The present work is focused on validation, so validation is discussed in more detail. A major component of validation includes quantification and identification of errors and

uncertainties in the experiment and simulations [6]. When comparing the simulation and the experimental results, it is assumed that the experiment is “our best measure of reality” [6]. For a comparison of experimental data and computational results to be useful, the errors and uncertainties of both must be quantified [6]. In very basic terms, a validation study would include measuring a physical phenomena and at the same time measuring all of the relevant boundary conditions. A simulation is then conducted based on the measured boundary conditions. Several different mathematical models would be used in the simulations. Finally, the simulation response quantities are compared with the experimental response quantities using validation metrics. The models can be selected based on the quantification of model error when compared with the experiment.

Because of the complex nature of systems that would benefit from predictive models, a complete system is separated into several tiers of detail for validation experiments, as described by Oberkampf and Roy [3]. These tiers are shown in Fig. 1.2 with a summarized description of each tier. This dissertation describes an apparatus made for Benchmark Tier validation experiments. All model inputs are measured, most model outputs are measured, and experimental uncertainty is computed for all measured quantities [3]. Since the heat transfer and the fluid flow are coupled, this problem cannot be considered as a unit problem. The unit problem is often referred to as a separate effects test. To meet the requirements of the benchmark tier in the validation hierarchy, the hardware used in this wind tunnel is specially fabricated to validate specific aspects of flow over a heated flat plate. The complete system of interest is the passively cooled high temperature gas-cooled nuclear reactor discussed above (the accurate simulation of which, in addition to its validation, is extremely costly). The heated flat plate is meant to represent a component in the reactor and/or containment building. The wind tunnel and plate then become the simplified hardware meant to improve understanding of flow physics and the simulation accuracy in predicting real-world scenarios [3].

The inputs required to define the simulation (boundary conditions) are measured in the test section walls (tunnel geometry and wall temperature) and flow at the wind tunnel

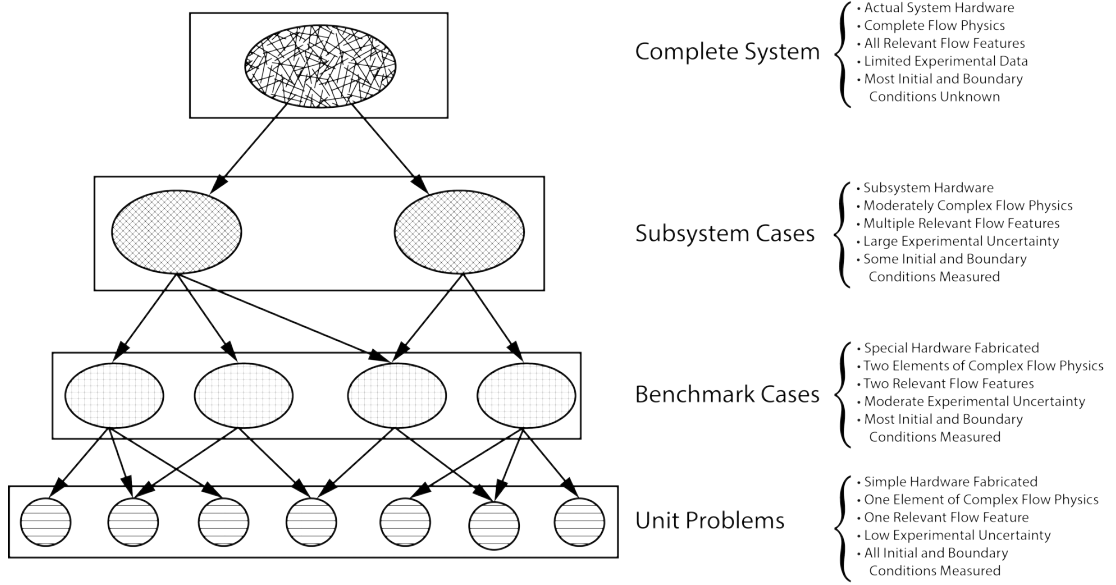


Fig. 1.2: Graphical description of the validation hierarchy, after [2].

inlet (inlet temperature, inlet velocity). These measurements include uncertainty estimates and the turbulence quantities at the inlet which can be computed from the inlet velocity data. The experimental data to be documented to meet the requirements for this tier of validation include [3]:

1. Detailed inspection of all hardware
2. Characterization of the variability of materials used in the experiment
3. Detailed information concerning assembly of the hardware
4. Detailed measurement of boundary conditions and excitation that were produced by the experimental apparatus or testing equipment

The hardware inspection and materials variability is included in the measurement of the boundary conditions. The hardware inspection is done whenever the geometrical boundary conditions are changed. The atmospheric variability is measured, and the conditions are recorded for each data set, including the data constituting the boundary conditions. The test section assembly procedures are recorded for repeatability. The last point is the

measurements themselves, which include the boundary conditions and the system response to excitation.

The boundary conditions are measured in the experiment at the same time as the measurement of the system response quantities. The system response quantity (SRQ) is the quantity used in the validation metric to compare the simulation to the experiment. Measured and computed SRQ's are compared to validate the simulation with experimental measurements where both the simulation and the experiment are based on the same boundary conditions. For the purposes of this project, convection from a vertical heated plate with several convection regimes (forced, mixed, etc.) is considered. The SRQ's include the boundary layer velocity over the heated plate, the heat flux from the plate, and the shear velocity.

Another aspect of the validation study is determining the SRQ's to be used in the validation study. The procedures described by Oberkampf and Roy [3], and Wilson and Boyack [7] outline methods that can be used to define what aspects of the system should be used as SRQ's. Oberkampf and Roy [3] also describe the difficulty spectrum of measurements and computed quantities, as shown in Fig. 1.3. Using SRQ's from a wider range on the spectrum will ensure a more robust validation study. For instance, a model in a simulation that best predicts boundary layer velocity or temperature profile (a dependent variable) may not predict the heat flux very accurately (a first derivative). Using SRQ's from a wide range on the spectrum will aid in determining which simulation and model is the best predictor of the physical phenomena.

Often, analysts use approximate or idealized boundary conditions in simulations. To illustrate the importance of using measured boundary conditions in a simulation, we observe Fig. 1.4. In many CFD simulations, a parabolic or uniform inlet profile is used. For the wind tunnel considered herein, a uniform inlet velocity assumption is valid for most of the inlet area, but not in the boundary layer. The parabolic assumption is totally erroneous for this application.

The turbulence levels at the inlet of the simulation are often assumed to be a percentage

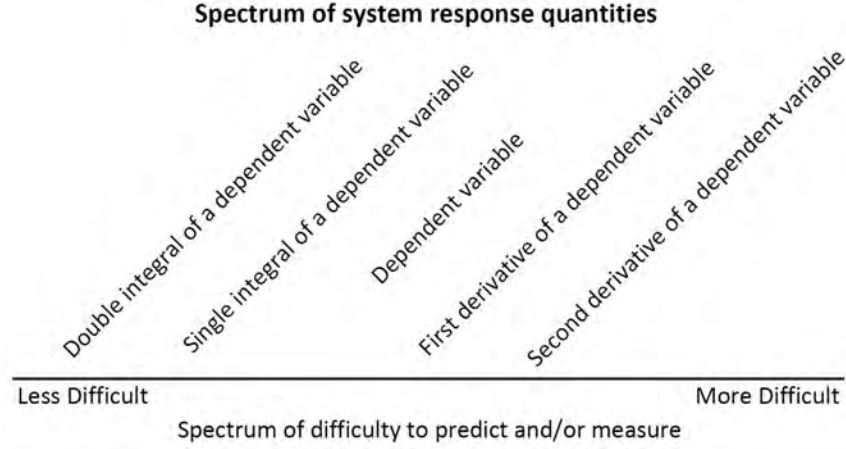


Fig. 1.3: The difficulty spectrum of SRQ's, after [3]

of the inlet velocity. The profiles in Fig. 1.4 show these assumptions to be invalid for this wind tunnel. A 10% of free stream turbulence level provides a trend that gives high turbulence in the center of the test section. However, the peak values are actually in the boundary layer with very little turbulence in the free-stream. The slight asymmetry of the inlet turbulence levels would be missed if the incorrect assumptions were made. Without measurements of the inlet, the assumptions used in simulations for the inlet are likely to be invalid. This would then make the validation study irrelevant, as the SRQ's from the experiment and the simulation are not based on the same boundary conditions.

One purpose of this work is to provide data for CFD validation, but obtaining such data from a written article is difficult, if not impossible. An online database is better suited for dissemination of data and documentation of the experiment. Though many validation datasets are available from several online databases, these normally lack the necessary detail to provide CFD simulation boundary and inflow conditions. Many such sources are listed at the CFD-Online website [8], including the National Aeronautics and Space Administration (NASA) NPARC Alliance Verification and Validation Archive [9] and the European Research Community on Flow, Turbulence and Combustion database [10]. Though valuable, these databases lack completeness for CFD validation as discussed in [11]. As part of the present effort, a database was developed to enable users to download the boundary condi-

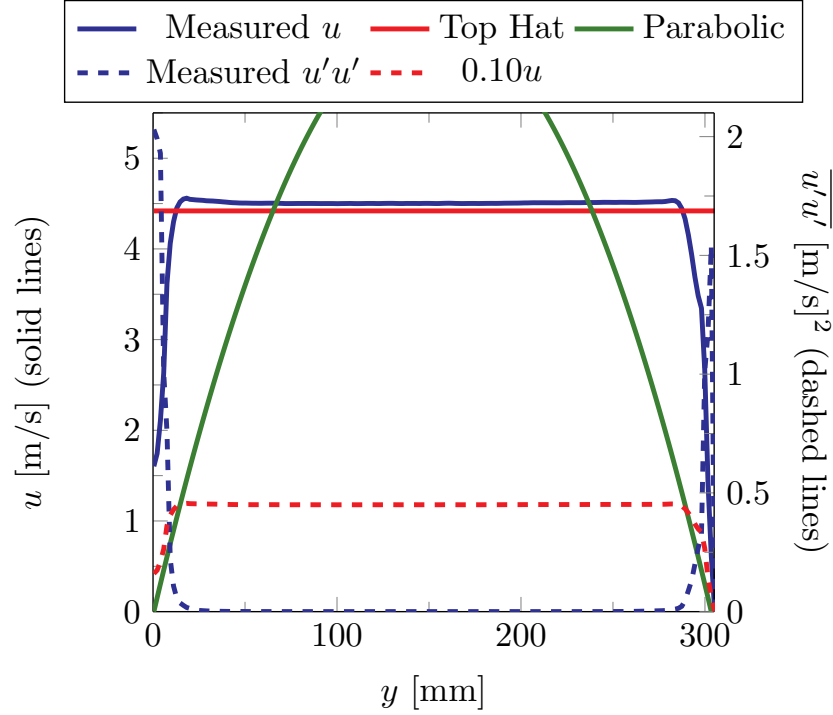


Fig. 1.4: A velocity profile for the inlet of the test section is shown, along with a top hat profile and a parabolic profile. The Reynolds Stress is also plotted along with a line of 10% of the free stream.

tions, SRQ data, and other relevant information to conduct their own validation studies, using the same boundary conditions to which the SRQ data correspond [12].

A more detailed outline of required measurements and documentation is found in the validation experiment completeness (VEC) table [11]. The detailed description of the information relating to the completeness level of the data are found on the project website, as it is too difficult to present all of the necessary data here. The information on the website is outlined following the layout of the VEC table. Most of the information is also contained in this dissertation, but the website eases the navigation of the relevant documentation.

As the uncertainty of the SRQ's is critical for computing the validation metrics, documentation of the uncertainty is included for both the SRQ's and the boundary conditions. The uncertainty of the velocity measurements is computed using the methods described by Timmins, *et al.* [13], Warner, *et al.* [14] and Wilson and Smith [15, 16]. Uncertainty of

dimensions are found using methods presented by Coleman and Steele [17]. The heat flux uncertainty was provided by the sensor manufacturer. The methods used to quantify the uncertainties of the measurements (except velocity) are discussed in Chapter 4 and Chapter 5.

1.3 Convection

Many studies have been conducted to measure convective flows over heated flat plates. Few have used modern non-intrusive measurement techniques, and none have complete measurement systems sufficient to define a simulation's boundary conditions. A collection of studies is included herein, separated into their respective convection regimes (although some sources cover several of the regimes). Though not an exhaustive treatise of convection and boundary layer flow, the cited sources are useful in showing the difference between a discovery experiment (which includes most of the cited works) and a validation experiment (the proper implementation of which is impossible to find).

1.3.1 Forced Convection

Forced convection is commonly considered as flow with a convection ratio greater than 0.3, or $Gr_x/Re_x^2 < 0.3$ [18]. The local Grashof number $Gr_x = g\beta(T_s - T_\infty)x^3/\nu^2$ and the local Reynolds number is defined as $Re_x = \bar{u}_\infty x/\nu$. Lloyd and Sparrow conducted a theoretical analysis of forced convection over an isothermal vertical surface and cite experimental data for the same flow scenario [19]. Another experimental study of convection from a vertical heated plate is presented by Gryzagoridis [20]. This study (and many experiments of that time) used hot-wire anemometry to measure the flow velocity. Temperature profiles were used to find heat transfer rates. The available measurement equipment of the time limited the measurements rendering them insufficient for CFD validation.

McEligot and Jackson [21] discuss decades of research in convection and appropriate parameters that should be used when studying turbulent convection. The laminarization of accelerating flow is discussed. They also present the parameters in a form that can be used to compare non-circular ducts to circular tubes. These parameters would make more

previous research applicable to this study. However, the caveat of turbulent flow at the inlet is required for their analysis to be valid.

Wang *et al.* present an experimental study of a vertical plane similar to the one considered in this work [4]. The velocity was measured using a two-component laser Doppler anemometry (LDA) system, which provides a point velocity rather than a velocity field. Temperature measurements were acquired using a thermocouple rake. The optical velocity measurements are beneficial and measurement of some boundary conditions were acquired, but the study was not meant for CFD validation and cannot be used for such (though it does provide much useful insight). The necessary boundary conditions were not all measured and the measurement uncertainties were not reported. The flow regimes and measurements reported are similar to those considered in this work.

Finally, a study that uses particle image velocimetry (PIV) to study the flow velocity is described by Hattori, *et al.* [22]. The measurements were also acquired using hot-wire anemometry. The studies focused on the laminarization of the flow and provide valuable information using PIV measurements and convection data. However, the measurements obtained are also not intended for CFD validation (and are thus insufficient). Wall shear stress was also measured using the velocity and temperature data [23] using what appears to be the same apparatus as the study in [22].

The studies cited (and there are many more) show the depth of knowledge about forced convection from a heated vertical plate. The studies lack presentation of the acquisition of the boundary conditions, nullifying their use for simulation validation purposes. In essence, they are discovery experiments rather than validation experiments, and should not be used solely for validation purposes.

This flow regime was studied mostly to prove the wind tunnel characteristics and that the measurements acquired are sufficient to define the simulation boundary conditions. One reason to study the buoyancy aided forced convection is for the initial characterization of the new wind tunnel. Buoyancy aided forced convection is a well understood and documented flow regime. Comparison of the experimentally measured results with previous well

understood studies is critical if the results for less understood flow regimes are to be trusted. The buoyancy opposed forced convection is studied to characterize the wind tunnel, and to provide a solid foundation for the future transient studies. The NGNP reactor normally operates in buoyancy opposed forced convection. Providing validation data for the transient from buoyancy opposed forced convection to natural convection is the end goal of the NEUP project.

1.3.2 Mixed Convection

Mixed convection is commonly considered as flow with a convection ratio greater than 0.3 and less than 16, or $0.3 < Gr_x/Re_x^2 < 16$ [18], where the Grashof and Reynolds numbers are defined in Section 1.3.1. Mixed convection is a more interesting flow regime than forced convection because the buoyancy of the fluid has a larger impact on the flow, making it more difficult to accurately match the experiment with CFD simulations. Several studies of mixed convection are referenced by Jackson, *et al.* [24], but are focused on convection in tubes. Much of the theory presented is valid for mixed convection from vertical surfaces. The turbulent characteristics of the flow changes with buoyancy effects. The studies of convection in tubes might prove more useful using the theory presented in [21]. Jackson also describes many studies of mixed convection for various flow scenarios in vertical passages [25].

Correlations are presented by Chen, *et al.* [26] for mixed convection from a vertical plate for both buoyancy aiding and buoyancy opposing flow. Those correlations are compared with experimental measurements by Ramachandran, *et al.* [27]. The measurements provided valuable data for the correlations, but could not provide detailed information for CFD validation. The study by Wang [4] is again presented, as mixed convection is studied therein. Again, this study lacks the detail necessary for CFD validation.

Hattori, *et al.* [28] present hot and cold wire measurements of convection from a vertical plate. A study of transition and heat transfer rates is presented. The authors discovered a transition from random to harmonic fluctuations with laminarization of the flow. Again, the focus of the study was for discovery, not validation, and presents valuable information

about convective flow.

The transition to turbulence was studied by Krishnamurthy and Gebhart [29] for mixed convection from a uniform heat flux vertical surface. Several key parameters are presented to quantify thermal and velocity transition. The measurements were acquired using a hot wire and thermocouples, as well as voltage and current to measure the power into the test section.

Gavara, *et al.* [30] present a theoretical study of mixed convection for laminar flow. The study did not include simulations (being laminar flow) so the validation mentioned therein is not congruent with CFD validation discussed in this paper. Yadav and Kant [31] describe a validation study of mixed convection. The experiment and analytical solutions are compared. Again, the complexities of a CFD validation effort is not included in the scope of this study.

Abedin, *et al.* [32] discuss a direct numerical simulation for convection from a vertical plate for both buoyancy aided and opposed convection. The transition point and laminarization of the flow is discussed, comparing the simulation to the experimental data of the sources previously presented. The mixed convection studies provide much helpful insight into the response of flow to heating. The studies were all meant as discovery experiments, thus the measurements acquired are insufficient for CFD validation.

The laminarization of the flow is another topic briefly considered in this study. The previously mentioned study by Hattori, *et al.* [28] present relatively recent work in laminarizing flow. An acceleration parameter K_v less than $2-3 \times 10^{-6}$ suggests that the flow would not laminarize [21, 33, 34]. The heat flux can be suppressed in buoyancy aided flow, depending on the significance of the buoyancy forces [21]. Some of the data presented in this dissertation show laminarizing characteristics and its effects on heat transfer. The observations from the measurements by Shehata and McEligot [35] are comparable to the results presented herein. The case 635 in [35] has about the same acceleration parameter as the buoyancy aided mixed convection case considered herein. However, as will be shown, this flow does show signs of laminarization, unlike the case considered in [35].

Chapter 2

Objectives

This paper will show the design process for a CFD validation experiment. The validation of the simulations is not included with the scope of this work. The objectives of this report include:

- Description and demonstration of experimental design for CFD validation experiments and developed a methodology consistent with validation theory explained by Oberkampf and Roy [3].
- Acquisition of experimental data sufficient to define simulation boundary conditions and system response quantity validation for forced and mixed convection in buoyancy aided and opposed orientations with an isothermal and constant flux heated plate (6 cases). These cases are graphically shown in Table 2.1. Data acquisition includes:
 - Inlet velocity profiles for forced, mixed, buoyancy aided, and opposed convection each with an isothermal or constant flux heated plate
 - Boundary layer velocity profiles at three streamwise locations for each case
 - Heat flux from the wall at three streamwise locations
 - Pressure drop through the test section for each case
 - Atmospheric conditions for each case
 - Experimental setup/settings for each case
 - Geometric measurements of the test section
 - Temperature of all 4 test section walls and wind tunnel inlet for each case
- Dissemination of experimental data (boundary conditions and system response quantities).

Table 2.1: Convection cases for data acquisition. The bottom row shows the plate conditions as isothermal or constant heat flux.

Forced			Mixed		
Aided		Opposed	Aided		Opposed
Isothermal	q''	Isothermal	Isothermal	q''	Isothermal

- Comparison of generic simulations to experimental data (not a complete validation study) for demonstration that the described methods are sufficient and the facility is adequate for CFD validation purposes.
- Development of procedures for data acquisition in the RoBuT to speed future validation efforts.

Chapter 3

Equipment

This chapter will describe the equipment available and what is built for this experiment. Hardware and software integration is necessary for an efficient validation experiment. The hardware is described with the relevant validation information. The experiment control software and data processing parameters were fixed for the final data acquisition and are described in this chapter. The chapter exists for this validation facility to meet the validation requirements described in Chapter 1.

3.1 Wind Tunnel

The experimental apparatus used for this project is a rotatable wind tunnel (RoBuT), built under a previous grant from the Department of Energy. The $12 \times 12 \times 78$ in. test section is fixed to a ferris-wheel like frame that allows the direction of gravity relative to the wind tunnel to be changed. Fig. 3.1 shows the RoBuT and the coordinate system for the measurements and simulations. The origin is at the center of the leading edge of the heated plate. The x coordinate runs the length of the plate, y is the coordinate away from the plate, and z is the coordinate normal to x and y . The velocity components u , v , and w

The wind tunnel is shown in Fig. 3.2, and the components are labeled for future reference. There are flow straighteners and turbulence screens at the inlet of the contraction. The contraction has trips magnetized into its outlet, 4.58 in. upstream of the heated plate leading edge. The blower is on the downstream end of the test section.

3.1.1 Structure

The framework was designed and built by Engineering Design Laboratories [36]. The ferris-wheel is 20 ft. in diameter. Four 4×4 in. steel beams were installed off of the

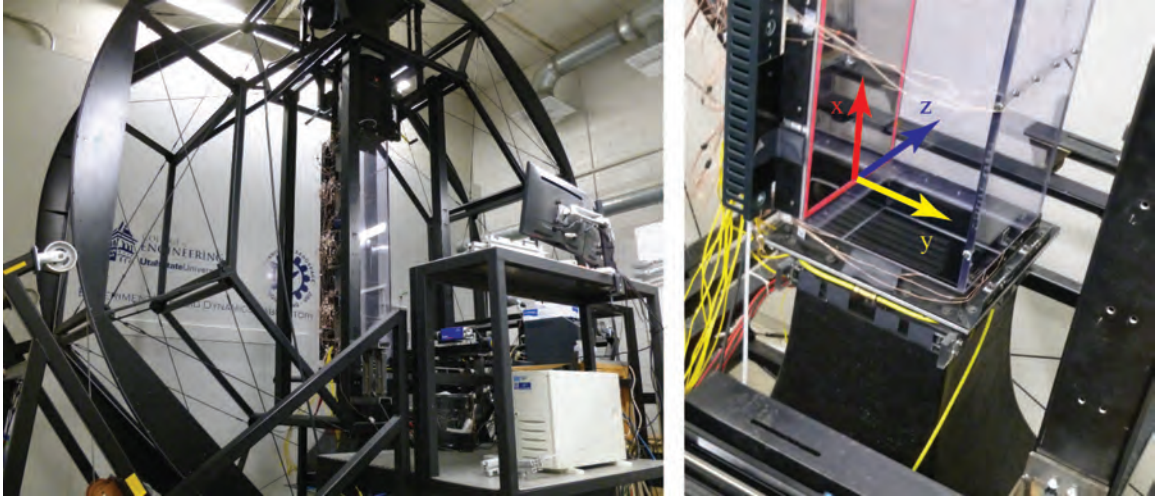


Fig. 3.1: The RoBuT showing the structure, wheel frame on the left. The right image shows the inlet and the coordinate system for the measurements.

corners of the test section and parallel to the direction of flow. These beams exist to mount the camera, laser, and other measurement equipment anywhere in along the test section. Ideally, a traverse stage would be mounted to these beams to ease x direction placement of the PIV equipment. However, the cost was too great for installation. These beams are visible in Fig. 3.1, with a close up of part of one beam on the far right of the right image. A drawing of the design is provided in Appendix B and was provided by the manufacturer.

Several mounting structures were designed to mount to those beams to hold traverse stages, camera, and laser while attenuating vibration caused by the flow inducing fan. Fig. 3.3 shows the completed traverse mounts. The mount toward the bottom of the image (the one with the blue camera and two traverse stages) is vibration dampening and easily removable to move the camera in the x direction, thus overcoming the lack of traverse stages in the x direction. The traverse stages allow the camera to be precisely moved in the y and z directions.

The laser traverse (top, center of Fig. 3.3) allows the laser to be precisely moved in the z direction. The laser traverse is fixed to a cart on rails and linked to the y direction camera traverse. Thus, when the camera is moved in the y direction, the laser moves with it. This linkage speeds data acquisition capabilities by only requiring one calibration at an

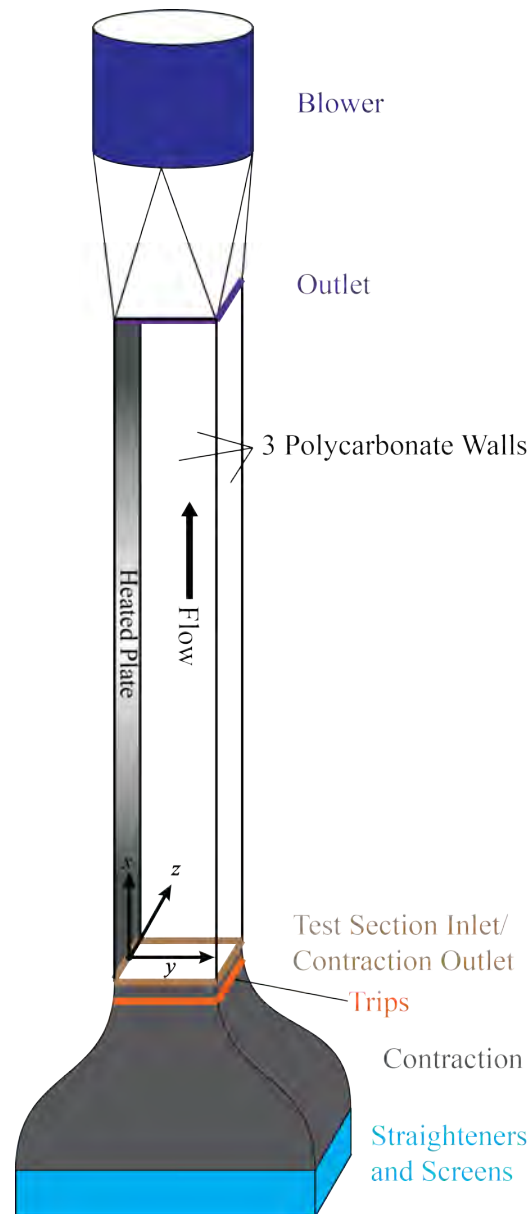


Fig. 3.2: A schematic of the wind tunnel, with nomenclature and coordinate system.

x position. This is most useful when measuring the inlet profile of the test section.

A hoist was also designed to remove the test section from the wind tunnel. Some features of the hoist include the capability to lift the test section and instrumentation from the wind tunnel to the center of the room. The test section can then be set on service stands, or moved to another location while another experiment is placed in the wind tunnel.

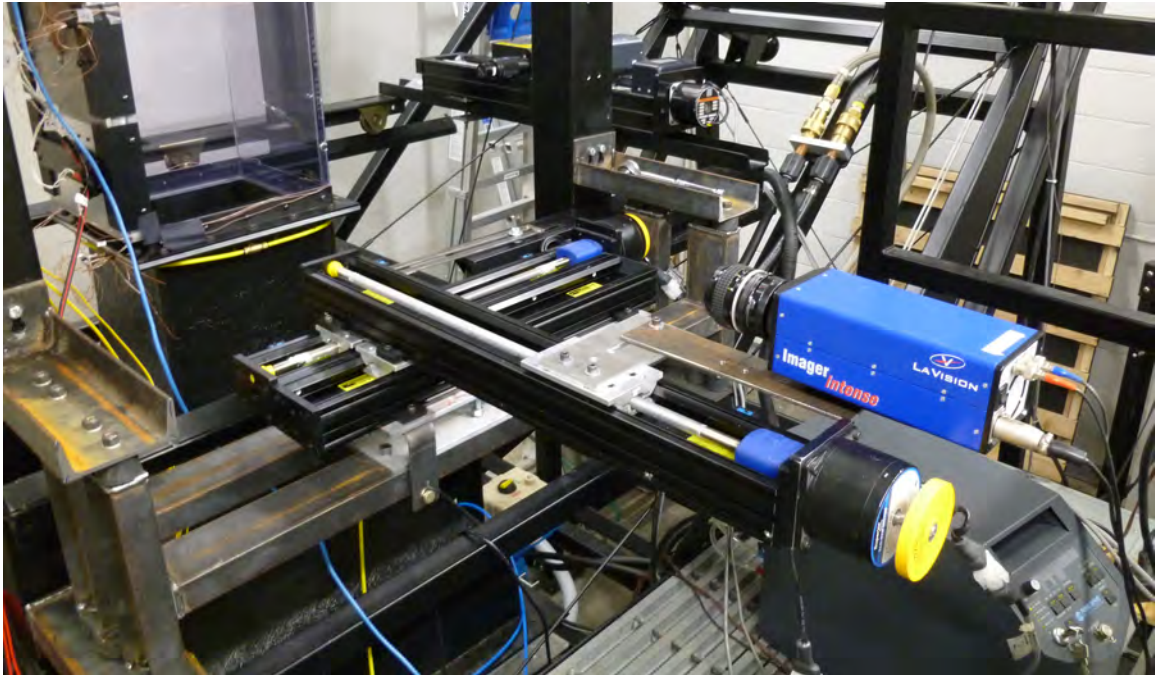


Fig. 3.3: A photograph of the traverse mounting equipment allowing for synchronized movement of the camera and laser in the y and z directions.

3.1.2 Test Section

The test section is made of three optically clear Lexan[®] polycarbonate walls, 0.5 inches thick. The walls will be referenced using the coordinate system in Fig. 3.1, where the heated plate is at $y = 0$, the left and right walls are at $z = -6$ in. and $z = 6$ in. respectively, and the top wall is at $y = 12$ in. The top wall is split into three sections, with the two ends being fixed into the mounting brackets and the center section removable for cleaning purposes (olive oil tends to build up in the test section over time, making optical measurements less reliable). The drawings for the test section components are included in Appendix C.

The fourth wall is the heated plate and its several components. The design for this plate was not completed as part of this work, and credit for its design goes to Blake Lance. However, it is necessary to understand its construction. The aluminum top plate is plated with nickel to decrease the thermal radiation heat transfer. Fig. 3.4 shows the heated plate assembly and the layout of the insulating layers surrounding the heated plate. The heated plate is surrounded with a layer of Teflon[®] to allow for thermal expansion and to increase

the thermal resistance between the heated plate and the plastic side walls. The silicone rubber gasket at the outlet of the test section is to force pressure on the plate assembly to push it toward the inlet, minimizing gaps at the inlet. Springs are also inside the Teflon[®] liners at the outlet to push the liners against the inlet. A layer of insulation is under the heaters to maximize the heat from the plate into the test section and resist the heat from being wasted out the backside of the plate. The position of the instrumentation will be discussed in Chapter 3.2 (See also Appendix C).

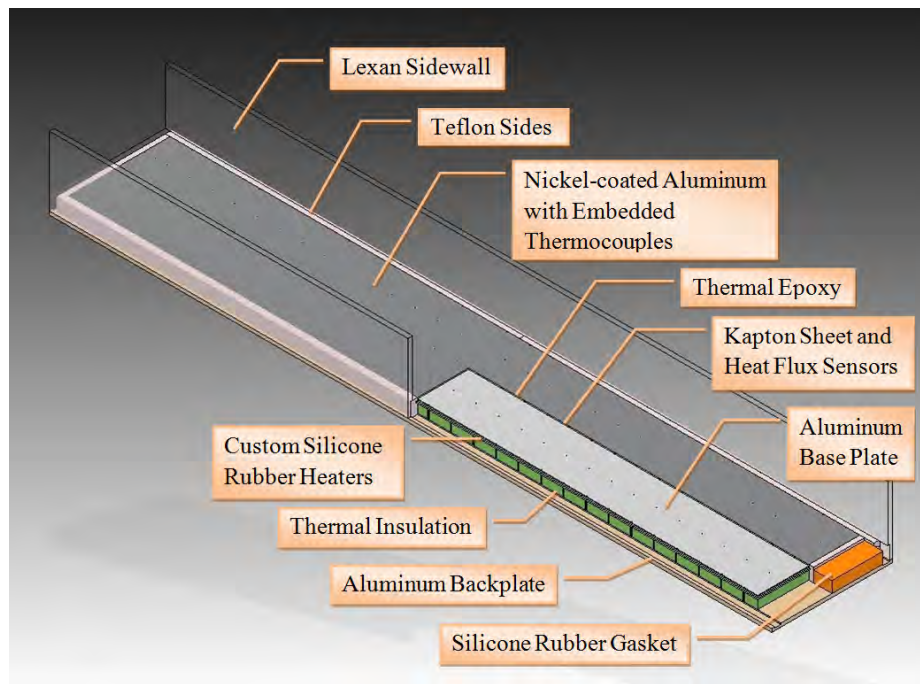


Fig. 3.4: The test section, heated plate and its several layers are shown. The plate is separated from the plastic sidewalls by a layer of Teflon[®].

A more zoomed in diagram of the heated plate is shown in Fig. 3.5. The schematic of the layers are scaled relative to each other. The wire leads for a thermocouple and heat flux sensor are shown going through the layers to the outside of the test section (which is to the right).

3.2 Instrumentation

The instrumentation and control systems are run with a .vi code in LabVIEW [37].

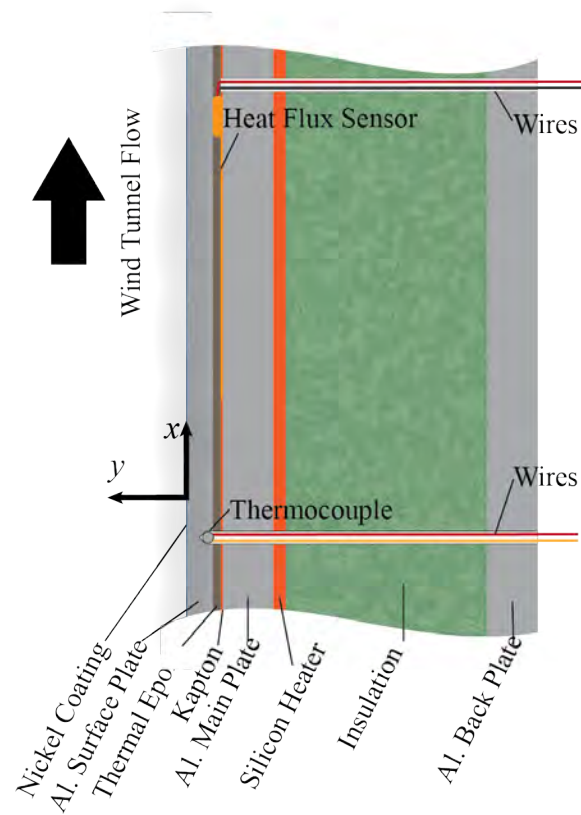


Fig. 3.5: The heated plate and its several layers are shown to relative scale with instrumentation wire leads going out of the test section to the right.

The Master VI is a Labview code that runs all of the hardware except the PIV system. It samples all of the temperatures, controls the room and plate temperatures, the seeding for the PIV, the blower speed, records the boundary conditions and the room conditions. This is a significant contribution to the success of the experiment, but there is no way to include it in this document. The National Instruments hardware includes 5 NI-cDAQ-9188 chassis that hold 20 NI-9213 16 channel thermocouple modules. All thermocouples and heat flux sensors were plugged into the modules for measurement. All thermocouples were calibrated before installation to a 0.03 degree source using a medium IsoTech Fast-Cal Temperature Calibrator. Another module and chassis control the larger voltage equipment, including the three power supplies for the six plate heaters and the room temperature control system. Fig. 3.6 shows the test section assembly and the layout of the heaters and heat flux sensors.

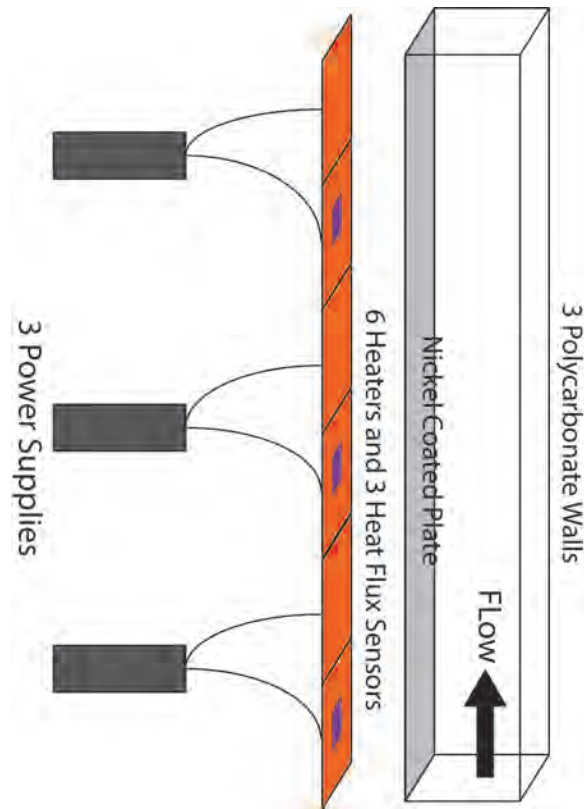


Fig. 3.6: The wind tunnel and control system showing the heaters and power supplies.

Pressure measurements are also acquired with the validation data and boundary condition acquisition. A Baratron 1-Torr pressure sensor with a MKS 270D signal conditioner. The wind tunnel manufacturer installed two pressure taps at the inlet and outlet of the contraction. These taps are used to measure the pressure drop through the contraction. Two more taps were installed at the test section inlet and outlet to measure pressure drop through the test section. These 4 taps are used to characterize the wind tunnel and to aid in measuring boundary conditions.

3.2.1 Atmospheric Conditions

The temperature of the room housing the RoBuT is kept constant using a control system in LabVIEW, a steam heater, and an air conditioning unit. The Master VI reads the ambient room temperature near the wind tunnel and adjusts the fan speed on the steam heater to compensate. The air conditioning unit holds the temperature at a comfortable

level during the summer months, but cycles such that the room temperature fluctuates several degrees. The heater and control system compensate for the fluctuations from the air conditioner.

The air properties in the room are computed using the room temperature, humidity, and atmospheric pressure. The temperature and humidity are measured using Omega's HX92A which is accurate to 0.6°C and 2.5% relative humidity. The atmospheric pressure was sampled using a Barometric Pressure Sensor SB100 from Apogee Instruments, which is accurate to 1.5% of the reading for atmospheric conditions.

A separate .vi was written that samples and records the room air properties every minute. The properties are uploaded to a website in real time for reference purposes. The air properties can be pulled for any specific data acquisition. The code writes .lvm files that can be opened with a text editor. The columns include a date/time stamp, the temperature, pressure, and relative humidity.

3.2.2 Inlet Temperature

The inlet temperature is measured in the flow straightening honeycomb (see Appendix B). Figure 3.7 shows the inlet honeycomb on the downstream side (the contraction has been removed and the wind tunnel is in the buoyancy opposed orientation). There are 3 thermocouples installed by the manufacturer to control the inlet heat exchanger. The EFDL installed 15 thermocouples spaced uniformly in the honeycomb, as shown. These thermocouples were epoxied into position, leaving the thermocouple joint exposed to the inlet air flow. The position of the thermocouples are included in Appendix E. These thermocouples were fitted with Type K extension wire and plug ends for easy test section removal. The inlet stays fixed when the test section and instrumentation are removed, necessitating the connection between the thermocouples and the extension wire.

3.2.3 Wall Temperatures

Heating the plate is an important feature of the Master VI. There were 160 type K thermocouples are embedded from the underside of the plate to within 0.06 inches from

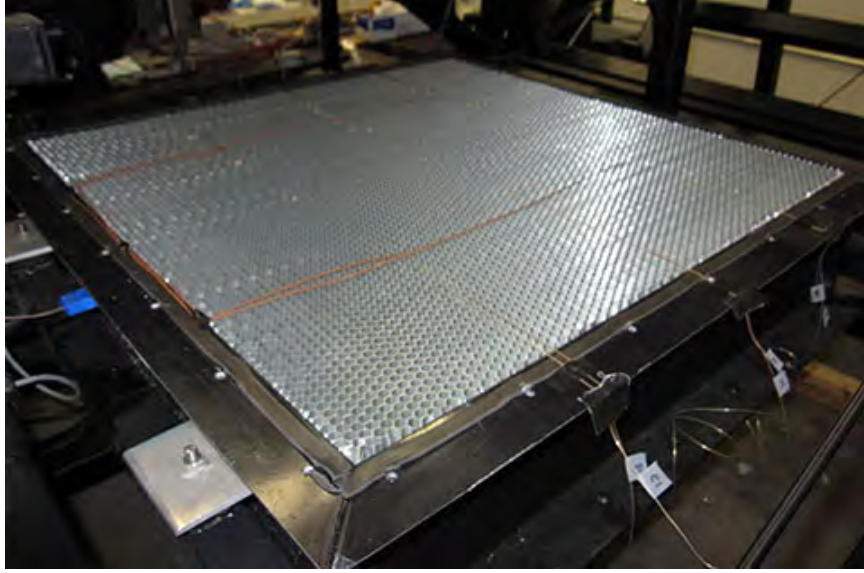


Fig. 3.7: The inlet honeycomb flow straightener viewed from the downstream side and showing the inlet thermocouples.

the surface of the plate using Dow Corning® 3-6751 Thermally Conductive Adhesive. The holes drilled into the plate are measured with a large micrometer several times to account for the uncertainty of the hole depth (and therefore, the position of the thermocouple). The thermocouples were all labeled for sorting after test section assembly, then installed. The epoxy was inserted with the thermocouple using a syringe. The plate was heated to 100°C for 30 minutes to cure the epoxy. Figure 3.8 shows the installation of the thermocouples into the heated plate.

The holes for the clear side walls are drilled in similar fashion to the ones in the heated plate. The thermocouples in the clear walls require an epoxy that would cure at room temperature. Weld On 40™ from IPS Corporation is used to fix the thermocouples into the clear side walls.

The thermocouples in the clear walls are at $x = 0.0, 33.66, 62.55, 96.84, 123.8, 166.4, 192.4$ cm. On the two side walls, at those x positions, the thermocouples are placed at $y = 19.05, 95.25, \text{ and } 247.7$ mm. On the top wall, the thermocouples are placed at $z = -76.2, 0.0, \text{ and } 76.2$ mm and $x = 0.0, 33.66, 76.2, 103.2, 137.5, 166.4, 192.4$ cm.

Six custom flexible silicone rubber heaters from Tempco are used to heat the plate.

3.2.4 Plate Heat Flux

Several heat flux sensors are embedded under the surface of the heated plate at positions 5.868, 30.118, and 54.868 inches from the heated plate leading edge. These sensors are centered in the z direction. Three RdF Corporation heat flux sensors, model 20457-3, are used, with each sensor having manufacturer specified properties and uncertainty of 5%. Table 3.1 shows the properties for each sensor.

Table 3.1: The heat flux sensor properties provided by the manufacturer. The x position of the heat flux sensors will be used in later analysis.

Heat Flux Sensor	Output $\mu\text{V}/\text{BTU}/\text{ft}^2\text{hr}$	Thermal Resistance $^{\circ}\text{F}/\text{BTU}/\text{ft}^2\text{hr}$	Heat Capacity $\text{BTU}/\text{ft}^2\text{hr}/^{\circ}\text{F}$	Response Time second
P1 = 5.87 in.	11.5	0.012	0.05	0.400
P2 = 30.12 in.	12.0	0.012	0.05	0.400
P3 = 54.87 in.	11.3	0.012	0.05	0.400

The heat flux measurements of sensor 2 show evidence of higher uncertainty than the manufacturer specifications. Figure 3.9 shows that for constant power to the heaters, the second heat flux sensor reads a lower heat flux than the other two sensors. The dip in heat flux is not driven by a drop in temperature because the temperature of the plate is smooth. The heat flux measurements in Fig. 3.9 are shown with 5% of reading uncertainty bands. As the second heat flux sensor is 10% lower than what it is expected to read, a 10% uncertainty is used in the reported heat flux SRQ for sensor 2. The first and third heat flux sensor readings are reported with the manufacturer specified uncertainty of 5%.

3.2.5 Particle Image Velocimetry

PIV is a major data acquisition component of the validation experiment. The equipment and processing parameters are included herein. For background purposes, PIV is a velocity measurement technique that uses a digital camera and a laser to take images of particles in a flow. The images are specially timed and correlated with each other to compute the velocity field. More detail on PIV can be found in Adrian and Westerweel's book [38], or in Raffel, *et. al* [39].

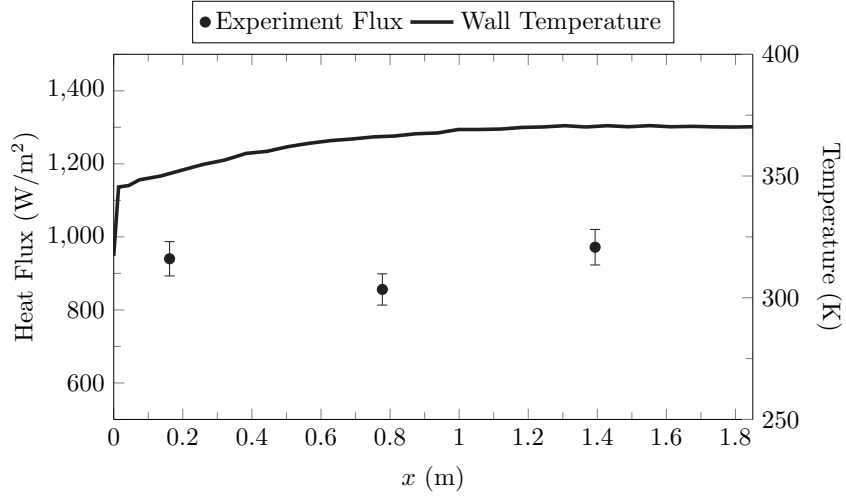


Fig. 3.9: The heat flux for a constant power forced convection case along with the $z = 0$ heated wall temperatures.

The PIV camera is an Imager Intense 12-bit digital camera from LaVision [40]. The CCD sensor is 1376×1040 pixels with a pixel size of $6.45 \mu\text{m}$ square. Two cameras can be used to acquire stereo PIV data, but the method proved infeasible for this project. The laser is a New Wave Research Solo PIV III 15. Two lasers at 50 mJ/pulse and 532 nm can fire up to 15 Hz with data acquired at 4 Hz in double-pulse mode.

Two different lenses are used on the camera, depending on what measurement is being acquired. A 105 mm. lens with an extension tube is used when acquiring images for the boundary layer flow over the heat flux sensors. A 28 mm. lens is used when acquiring images for the inlet boundary condition. In both cases, a filter is placed over the lens to decrease reflections allowing only 532 nm light is passed through the filter.

The data was acquired and processed using DaVis 8.1.6 [41]. A ruler was used to calibrate the camera for the inlet data, and a single plane calibration plate was used to calibrate and dewarp the images for the SRQ data using a pinhole model. The calibration plate uses laser etched circles on an anodized aluminum plate. The dots are 0.980 mm (0.03 in) in diameter and spaced 3.175 mm (0.125 in) apart. The particle displacements were generally around 12 pixels in the free stream, with the particle diameters of 2 pixels. This diameter is near the optimum for small RMS errors due to particle diameter [39]. The

uncertainty method accounts for the variation in particle diameter and displacements.

The images for the SRQ data used the entire imaging chip (1376×1040 pixels). The inlet data region of interest was generally 1376×256 pixels, with the focus being at the inlet of the test section. The images were processed using the following steps after the acquisition of the images:

1. The images were corrected for small vibrations and rotation using the wall as a reference (making the wall straight up and down and in the same position for every image).
2. The average image was subtracted from all of the images to decrease the background noise.
3. PIV Processing using 64×64 window with 1 pass, then decreased to a 32×32 windows with 75% overlap for 2 passes (the SRQ images were processed with image correction, per the dewarping calibration).
4. The PIV data were post-processed with an allowable vector range of 5 m/s (± 5 m/s) in v and 0 m/s (± 1 m/s) in u (w was not measured for the validation data). The vectors were deleted if the peak ratio was less than 2. A median filter was used to remove vectors for which the difference to the average was greater than $1.75 \times \text{RMS}$ of its neighbors and inserted (or reinserted) if the difference to the average was less than $2.5 \times \text{RMS}$ of its neighbors. Also, groups with less than five vectors were removed and the allowable vector range was computed again.
5. The average and standard deviation (RMS or $\overline{u'u'}$, $\overline{v'v'}$) were also computed.

The laser was mounted such that only a spherical lens and cylindrical lens were used to focus the laser into a thin sheet. The cylindrical lens was selected to provide the maximum intensity to the laser sheet. Meaning, the sheet was just wide enough to obtain the inlet profiles and SRQ data. As measuring the laser sheet thickness inside of the test section was impossible, some simple qualitative sheet thickness techniques were used just outside of the

test section ($z > 0.1651$ m.). Laser burn paper was used to aid in focusing the laser sheet. The sheet focal point was near the center ($y \approx 0.127$ m.) of the test section for the inlet profile measurements. The focal point was near the heated wall for the SRQ measurements.

PIV measurements require seed particles to be distributed in the flow. Compressed air is let into canisters using an electronically controlled pressure regulator (controlled using the Maser VI). The canisters are filled to a certain level with olive oil, covering small holes in the inlet pipe by 0.5 in. Olive oil is vaporized using the air and a Laskin nozzle style atomizer to make seed particles that are around $0.8 \mu\text{m}$ in diameter. The seeder is built similar to the description by Kähler [42], and more details can be found in the literature. Several of these seeding canisters are shown in Fig. 3.10. The particles are blown into a system of PVC pipe that is fixed to the inlet of the wind tunnel. The system is laid out in a grid pattern allowing for even dispersion of the seed particles.

The PVC grid is placed in a framework that is mounted to the wind tunnel frame. Pegboard and clear vinyl are used to disperse the seed uniformly and allow mixing before entering the contraction. The air/seed mixture then passes through a heat exchanger, flow straightener, and turbulence screens before the area contraction and finally entering the test section. The inlet temperature thermocouples are placed in the flow straightening honeycomb.

There were initially several optical problems with the PIV images. The first was high reflections from the laser light off of the Teflon[™]. Bulldog[™] Adhesion Promoter was used to treat the non-stick surface of the Teflon[™]. After the treatment, Rhodamine paint was applied to the Teflon[™] surfaces, allowing the reflections to be filtered out optically.

The second problem with the images was an optical distortion resulting from a change in air properties near the heated wall (like the familiar heat waves observable from car surfaces exposed to sunlight). This was corrected by moving the camera in the positive y direction and looking at the region of interest from an angle of several degrees (this angle changes slightly for each setup). The angle required a dewarping of the images and a small calibration target was designed for the calibration. As the calibration target is not a part



Fig. 3.10: A photograph of a seeding canister, similar to a Laskin nozzle.

of this dissertation, it's attributes are included in Appendix A.

The camera and laser were both fixed to Velmex [43] traverse stages that allow for synchronized motion in the y and z directions. The traverses were each independently controlled with LabVIEW and allow for sub-millimeter displacements. To move the equipment in the x direction, the hardware was designed to mount easily at increments of 5 in. (127 mm), with mounts for the laser and camera providing more accurate placement.

Additionally, the room conditions are monitored and logged continuously, including temperature, pressure and relative humidity. These are used to determine the air properties for each run.

3.3 RoBuT Test Section Assembly

To meet the validation requirements, the assembly of the test section is described. The plate assembly is completed first, as shown in Fig. 3.4. The top plate is set upside down (with a protective semi-adhesive layer) on a level, smooth surface. Appropriate thermocouples are then threaded through the heaters and the 6 heaters are placed in position on the bottom surface of the top plate. Then the thermocouple wire is threaded through a layer of insulation, Kapton, and the aluminum support plate holes, see Fig. 3.5. Then the leads can be inserted into the appropriate channels in the thermocouple modules. With the plate assembly completed, the assemblage can be carefully turned upside up and set on the test section service stand.

The instrumentation is to be kept from being pinched, severed, or otherwise damaged during the assembly process. The plate assembly is set on a stable support constructed for this specific purpose. The Teflon[®] side pieces are fixed into place with long furniture clamps, with care taken to not damage the smooth nickel surface of the heated plate. The clear walls (previously assembled with the mounting brackets) can then be lowered onto the plate assembly, moving the clamps as needed. Weather stripping is used between the Teflon[®] and the clear side walls to help seal the wind tunnel. All instrumentation is tested before installation into the wind tunnel. After installation, all seams are checked for leakage.

As the installation or removal of the test section is a delicate task, the hardware required to do so was carefully designed and constructed. The hardware (hoist, test section stand, etc.) is documented in manuals and videos in the Experimental Fluid Dynamics Laboratory.

Chapter 4

Approach

This chapter summarizes the calculations done for the design of the experiment, during the experiment, and after the results were obtained. Discussion of the simulations is also included in this chapter. The results and discussion from the calculations are included in Chapter 5.

4.1 Apparatus Design

The general design of the rotating framework for the wind tunnel was completed previously. The contraction inlet and the test section itself are both designed to enhance the accuracy and spacial resolution of the measurements, thus making the simulation boundary conditions more reliable and the experiments more repeatable. The specifics regarding the equipment are described in Chapter 3 and in the appendices.

The measurement of the SRQ's were also considered in the test section design. The measurement of the boundary conditions could not interfere with SRQ measurements, so thermocouples and wires are strategically placed to not interfere optically with the PIV system. Since the velocity SRQ is at the same position as the heat flux sensor, thermocouples should not be in the way of the camera and laser on the three clear walls. To ensure the thermocouple placement in the test section walls would not interfere with PIV measurements, simple geometric calculations were conducted. The possible orientations of the PIV equipment was considered to enable the system to see the boundary layer flow at the heat flux sensor positions without obstruction. Another feature of the test section is a removable section on the top ($y = 12$ in.) lid. This allowed for parallel experiments to be conducted without removing the entire test section. The removable lid also allowed for test section cleaning, rhodamine repainting, and other minor maintenance procedures.

The radiative properties of the nickel-coated aluminum plate were considered. A high emissivity of the plate would correspond to elevated levels of measured heat flux going to radiative heat transfer rather than convection. Ideally, all of the heat flux would transfer to the air through convection. However, a quantification of the radiative contribution to heat flux is necessary.

To ensure the radiative heat transfer from the plate is small, two methods are used to predict the emissivity of the nickel coated plate. First, from Howell [44], the normal emissivity is

$$\epsilon_n = \frac{4n}{(n+1)^2 + k^2} \quad (4.1)$$

where $n = 5.76$ and $k = 27.34$ are material constants for nickel plated aluminum at 413 K ($\lambda = 7.0\mu\text{m}$). Eqn. 4.1 gives a normal emissivity of 0.029. More thorough documentation of n and k can be obtained from the *Handbook of Chemistry and Physics* [45]. The uncertainty of the emissivity using this method is not obtainable from the sources in the literature.

The second method uses an energy balance on the surface of the nickel plate, written as

$$q'' = h(T_s - T_\infty) + \epsilon_n \sigma T_s^4 - \epsilon_L \sigma T_L^4 \quad (4.2)$$

where all quantities are measured (or reasonably estimated) to find the nickel plate emissivity. The emissivity of the Lexan ϵ_L is set to 0.9. Using data from a natural convection state, the emissivity of the heated plate is 0.034.

Table 4.1: Parameters for computing the plate emissivity using an energy balance in a state of natural convection.

q''	h	T_s	T_∞	T_L	ϵ
400 W/m ²	6.36 W/m ² K	410 K	294 K	296 K	0.034

The radiation heat flux is 10% of the total heat flux measured from the plate in natural convection. If the same radiation flux is assumed for forced convection, then radiation is 3% of the forced convection flux. The h for natural convection is computed from a correlation

presented by Incropera [46], and is

$$h = k/L \left[0.825 + \frac{0.387 Ra^{1/6}}{\left[1 + \left(\frac{0.492}{Pr} \right)^{9/16} \right]^{8/27}} \right]^2. \quad (4.3)$$

The energy balance in Eqn. 4.2 is solved for ϵ_n and the Taylor series expansion to find the uncertainty of the emissivity of the nickel coated plate is

$$U_{\epsilon_n}^2 = \left(U_{q''} \frac{\partial \epsilon_n}{\partial q''} \right)^2 + \left(U_h \frac{\partial \epsilon_n}{\partial h} \right)^2 + \left(U_{T_s} \frac{\partial \epsilon_n}{\partial T_s} \right)^2 + \left(U_{T_\infty} \frac{\partial \epsilon_n}{\partial T_\infty} \right)^2 + \left(U_{\epsilon_L} \frac{\partial \epsilon_n}{\partial \epsilon_L} \right)^2. \quad (4.4)$$

The uncertainty and derivative terms in Eqn. 4.4 are

$$\frac{\partial \epsilon_n}{\partial q''} = \frac{1}{\sigma T_s^4}, \quad U_{q''} = 2\%, \quad (4.5)$$

$$\frac{\partial \epsilon_n}{\partial T_s} = \frac{-4q'' \sigma T_s^3}{(\sigma T_s^4)^2} + \frac{3h \sigma T_s^2}{(\sigma T_s^3)^2} + \frac{-4h T_\infty \sigma T_s^3}{(\sigma T_s^4)^2} + \frac{-4\epsilon_L T_L^4 T_s^3}{T_s^8}, \quad (4.6)$$

$$\frac{\partial \epsilon_n}{\partial T_\infty} = \frac{h}{\sigma T_s^4}, \quad (4.7)$$

$$\frac{\partial \epsilon_n}{\partial \epsilon_L} = \frac{T_L^4}{T_s^4}, \quad (4.8)$$

$$\frac{\partial \epsilon_n}{\partial h} = \frac{T_\infty - T_s}{\sigma T_s^4}, \quad U_h = \sqrt{\left(U_k \frac{\partial h}{\partial k} \right)^2 + \left(U_L \frac{\partial h}{\partial L} \right)^2 + \left(U_{Ra} \frac{\partial h}{\partial Ra} \right)^2}. \quad (4.9)$$

U_k is the uncertainty of the thermal conductivity of air, and $U_L = U_x = 1/32$ in. is the uncertainty of the plate length. The uncertainty of temperature is $U_{T_s} = U_{T_\infty} = 1^\circ\text{C}$. Equation 4.9 has further uncertainty and sensitivity terms that are

$$U_{Ra}^2 = \left(U_\nu \frac{\partial Ra}{\partial \nu} \right)^2 + \left(U_{T_s} \frac{\partial Ra}{\partial T_s} \right)^2 + \left(U_{T_\infty} \frac{\partial Ra}{\partial T_\infty} \right)^2 + \left(U_x \frac{\partial Ra}{\partial x} \right)^2, \quad (4.10)$$

$$\frac{\partial h}{\partial k} = 1/L \left[0.825 + \frac{0.387 Ra^{1/6}}{\left[1 + \left(\frac{0.492}{Pr} \right)^{9/16} \right]^{8/27}} \right]^2, \quad (4.11)$$

$$\frac{\partial h}{\partial L} = -k/L^2 \left[0.825 + \frac{0.387 Ra^{1/6}}{\left[1 + \left(\frac{0.492}{Pr} \right)^{9/16} \right]^{8/27}} \right]^2, \quad (4.12)$$

$$\frac{\partial h}{\partial Ra} = k/L \left[\frac{0.1064 Ra^{-5/6}}{\left[1 + \left(\frac{0.492}{Pr} \right)^{9/16} \right]^{8/27}} + \frac{0.0215 Ra^{-2/3}}{\left[1 + \left(\frac{0.492}{Pr} \right)^{9/16} \right]^{8/27}} \right]. \quad (4.13)$$

Equation 4.10 requires further definition of uncertainty terms and these are presented below. The kinematic viscosity is a function of dynamic viscosity and the air density. Thus, the uncertainty of the kinematic viscosity can be expressed as

$$U_\nu = \sqrt{\left(U_\mu \frac{1}{\rho} \right)^2 + \left(U_\rho \frac{-\mu}{\rho^2} \right)^2}. \quad (4.14)$$

The dynamic viscosity μ is found from a polynomial fit to data contained in [45]. As a function of the temperature in Celsius, the viscosity is

$$\mu = 1.714 \times 10^{-5} + 4.879 \times 10^{-8} T - 4.5675 \times 10^{-11} T^2 + 7.3469 \times 10^{-14} T^3. \quad (4.15)$$

The uncertainty of the viscosity is governed by the uncertainty of the air properties in [45].

The density is found from the ideal gas law $\rho = P/(TR_{air})$ and the air density uncertainty is

$$U_\rho = \sqrt{\left(\frac{U_P}{TR_{air}} \right)^2 + \left(U_T \frac{-PR_{air}}{(TR_{air})^2} \right)^2 + \left(U_{R_{air}} \frac{-PT}{(TR_{air})^2} \right)^2} \quad (4.16)$$

where the air gas constant is found from $R_{air} = 8.31434/M_{mix}$ and

$$M_{mix} = (1 + \omega) / \left(\frac{\omega}{18.02} + \frac{1}{28.97} \right). \quad (4.17)$$

The humidity ratio ω is found as a function of the measured relative humidity, pressure, and temperature and is defined as

$$\omega = \frac{0.622}{\frac{P}{\phi P_{sat}} - 1} \quad (4.18)$$

with $P_{sat} = 0.57574 + 0.0554T + 4.1195 \times 10^{-4}T^2 + 6.0733 \times 10^{-5}T^3$. The uncertainty of the air gas constant is negligible. The uncertainty of temperature $U_T = 0.6^\circ\text{C}$ and the uncertainty of pressure $U_P = 1.5\%$ of reading. The last few sensitivities in Eqn. 4.10 are

$$\frac{\partial \text{Ra}}{\partial \nu} = \frac{-g\beta(T_s - T_\infty)x^3\alpha}{(\nu\alpha)^2}, \quad (4.19)$$

$$\frac{\partial \text{Ra}}{\partial T_s} = \frac{g\beta x^3}{\nu\alpha}, \quad (4.20)$$

$$\frac{\partial \text{Ra}}{\partial T_\infty} = \frac{-g\beta x^3}{\nu\alpha}, \quad (4.21)$$

$$\frac{\partial \text{Ra}}{\partial x} = \frac{3g\beta(T_s - T_\infty)x^2}{\nu\alpha}. \quad (4.22)$$

Using these equations and data from the experiment, the uncertainty of the emissivity is on the order of the emissivity itself. Thus, the energy balance yields $\epsilon_n = 0.03 \pm 0.03$.

4.2 Wind Tunnel Characterization

Being a brand new wind tunnel, the flow characteristics should be determined [47]. Several components that characterize the wind tunnel flow are included in this section. Further analysis of the characteristics of the flow and boundary layers are included in Chapter 5, as they are only understood after an analysis of the SRQ data.

4.2.1 Pressure Drop

The test-section flow calibration is completed using pressure taps in the contraction

and PIV for velocity measurements. The wind tunnel manufacturer did a similar procedure using a pitot probe, but the test section has been replaced and the inlet modified, requiring an updated calibration. The wind tunnel manufacturer completed a characterization that is in closer harmony to that outlined in [47].

Bernoulli's equation is used at the contraction (see Fig. 3.2) to compute the velocity at the inlet of the test section. For Bernoulli's equation to be valid, the flow in the contraction must be steady, incompressible, and with negligible frictional losses. As the flow in this experiment is steady, subsonic, and the contraction is smooth, these are reasonable assumptions and Bernoulli's equation is a reasonable energy balance along streamlines. The pressure taps are at the contraction inlet and the contraction outlet. The pressure is known at the contraction inlet and outlet as well as the area ratio. Bernoulli's equation is

$$P_1 + \frac{1}{2}\rho U_1^2 + \rho g z_1 = P_2 + \frac{1}{2}\rho U_2^2 + \rho g z_2. \quad (4.23)$$

$P_1 - P_2 = \Delta P$ is measured with a Baratron 1-Torr pressure sensor. The air density is found by using the air properties in the room. Pressure taps were also placed the the test section inlet (several inches downstream of the contraction outlet) and test section outlet. These are used to compute the test section pressure drop.

The pressure drop through the inlet contraction and the test section are measured for the wind tunnel in a horizontal configuration (this eliminates any gravitational effects). Figure 4.2.1 shows the measured and predicted pressure drop for the test section and the inlet contraction.

The test section pressure drop is calculated using the Haaland equation [48] with no surface roughness. The test section frictional losses are computed using

$$\Delta P_f = f \frac{L}{D_h} \rho \frac{\bar{u}_\infty^2}{2} \quad (4.24)$$

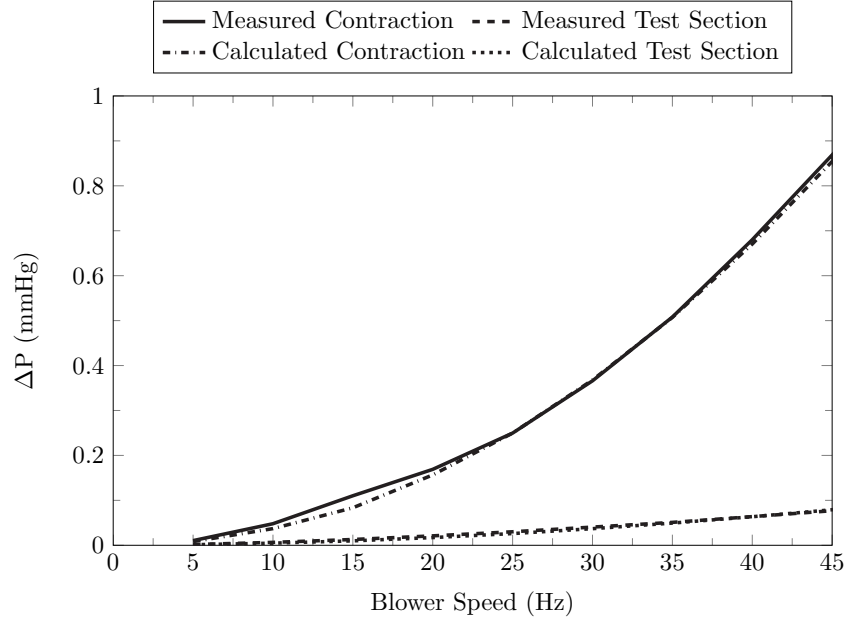


Fig. 4.1: Pressure drop in the contraction and test section with the wind tunnel horizontally oriented. The measured pressure drop is compared with calculations using Bernoulli's equation and frictional losses.

where the friction factor was found using

$$f = \left[-0.782 \ln \left(\frac{6.9}{\text{Re}} \right) \right]^{-2}. \quad (4.25)$$

The contraction pressure drop agrees with the Bernoulli prediction using PIV velocity measurements. The frictional losses agree with the predicted loss from Eqn. 4.24.

4.2.2 Geometry

The test section as-built geometry was measured using a micrometer capable of measuring 12 inches with an accuracy of 0.0005 inches. As the test section when built is too long to measure using human arms, an apparatus was built to hold the micrometer in position and a string turned the micrometer until the measurement could be taken. Figure 4.2 shows a student holding the micrometer apparatus while a measurement is taken.

The as-built dimensions were defined as the height at $z = -5.75, 0.0$, and 5.75 in. and



Fig. 4.2: Photograph of as-built geometry measurement procedure.

width of the test section at $y = 0.25, 6.0,$ and 11.75 in. At each position, the micrometer was reset and the measurement repeated 3 times, providing an estimate of the repeatability of the measurement. Table 4.2 summarizes the last test section as-built measurements and Table 4.3 shows the uncertainty of those measurements.

Table 4.2: The measured as-built dimensions for the test section in inches.

Position x	Height			Width		
	-5.75	0.00	5.75	11.75	6.00	0.25
00.000	11.982	11.995	11.991	11.996	12.001	12.005
13.285	12.020	12.019	12.020	12.023	12.007	12.003
24.635	12.029	12.017	12.023	12.018	12.027	12.013
38.135	12.003	12.023	12.028	12.035	12.035	11.996
48.775	12.040	12.041	12.034	12.036	12.042	12.018
65.525	12.044	12.046	12.025	12.014	12.038	12.001
75.810	12.002	12.018	12.019	12.005	12.025	11.992

These data are used to construct a virtual test section for the simulation geometry definition (see Section 4.4). The measurement geometry and the simulation geometry are

Table 4.3: The measured as-built dimensions uncertainty for the test section in inches.

Position x	Height			Width		
	-5.75	0.00	5.75	11.75	6.00	0.25
00.000	± 0.004	± 0.001	± 0.004	± 0.004	± 0.001	± 0.007
13.285	± 0.001	± 0.004	± 0.004	± 0.002	± 0.004	± 0.007
24.635	± 0.012	± 0.002	± 0.013	± 0.001	± 0.005	± 0.002
38.135	± 0.001	± 0.007	± 0.006	± 0.004	± 0.005	± 0.009
48.775	± 0.004	± 0.002	± 0.001	± 0.007	± 0.007	± 0.007
65.525	± 0.007	± 0.002	± 0.008	± 0.005	± 0.002	± 0.007
75.810	± 0.001	± 0.001	± 0.000	± 0.001	± 0.003	± 0.017

then in agreement, within the stated uncertainty. These measurements are taken any time the test section is taken apart and/or removed. The removable lid does not introduce significant errors in the wall dimensions. A previous study for this project showed that the difference between the as-built geometry and the as-designed geometry was insignificant in the simulation [49].

4.2.3 Temperatures

The thermocouples in the walls, inlet, and room are used to quantify the wall temperatures, inlet temperatures, and atmospheric temperature for the simulations. The air properties are defined by measuring the air temperature, humidity, and atmospheric pressure, as described in Chapter 3.2.1. Every PIV measurement has a corresponding measurement of temperatures.

For example, data for the forced, isothermal case has 12 instances of independent PIV measurements (9 inlet measurement planes and 3 SRQ planes). Each of these has recorded wall temperatures and atmospheric conditions. The average of the atmospheric conditions and the average of the wall temperatures is computed to define the corresponding simulation boundary conditions. This method also provides data to compute the precision uncertainty of those boundary conditions, where the systematic uncertainty is defined in Chapter 3.2. The code that accomplishes this is included in Appendix F.

The temperatures are recoded in .csv files that are easily imported into StarCCM+

to define the temperature of the walls and inlet. The files also contain the uncertainty of the temperatures. An example of the wall and inlet temperatures in StarCCM+ is shown in Fig. 4.3 for the buoyancy aided mixed convection constant heat flux case. The flow in Fig. 4.3 is from left to right.

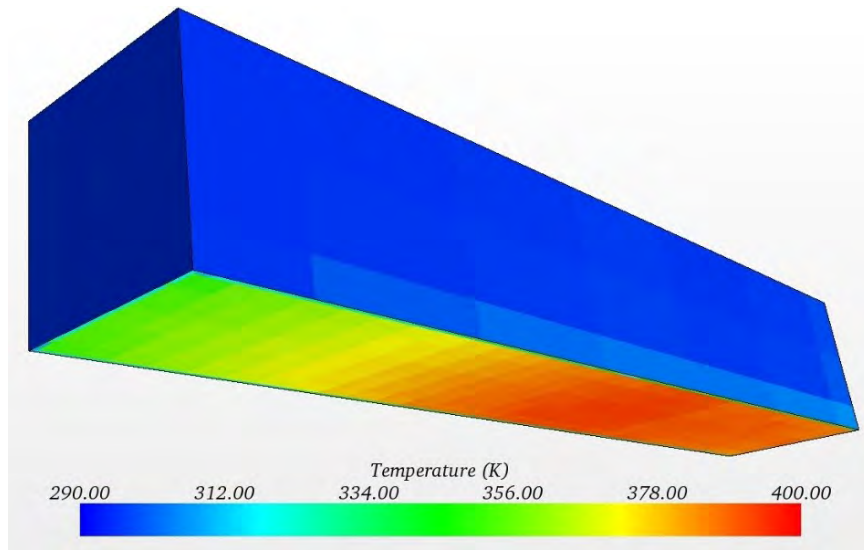


Fig. 4.3: The wall temperatures and inlet temperature viewed in StarCCM+.

4.2.4 Inlet Treatment

The PIV system is used to measure the inlet velocity on 9 planes, measuring u and v . These planes of data are used to define the simulation inflow conditions. The turbulence parameters for a specific model is derived from the measured velocities. An example of the measured inflow is shown in Fig. 4.4.

Rather than measuring the u and v velocities, then moving the PIV gear to measure u and w for every case, as shown in Fig. 4.5, a simplifying assumption can be made requiring the measurement of all three components only once. Data is acquired in Orientation A to obtain u and v at the inlet. The equipment is moved to Orientation B to obtain u and w at the inlet using the same spacial resolution. The results for the center profile of the two orientations are shown in Fig. 4.6.

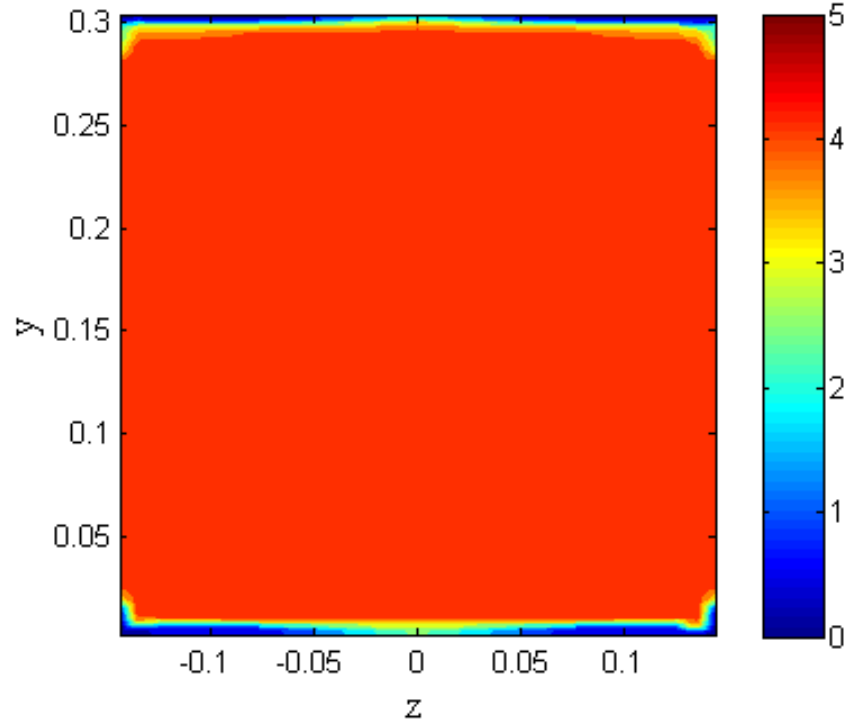


Fig. 4.4: The inlet velocity magnitudes using the 9 PIV planes.

In Fig. 4.6, several conclusions can be made. First, v and w are the same over the width of the test section and in the boundary layer. Another observation is that the streamwise fluctuations are significantly higher than the cross-flow fluctuations in the boundary layer, $\overline{u'u'} > \overline{v'v'} = \overline{w'w'}$ and $\overline{v'v'} = \overline{w'w'} < 0.2 \pm 0.017\text{m/s}$. At this location, $\overline{u'u'} = 1.8 \pm 0.17\text{m/s}$ justifying an approximation that $\overline{v'v'} = \overline{w'w'} \approx 0$. These conclusions can be used to simplify the definition of the turbulence dissipation rate [18, p. 64], shown as

$$\epsilon = \nu \overline{\frac{\partial u'_i}{\partial x_j} \frac{\partial u'_i}{\partial x_j}}. \quad (4.26)$$

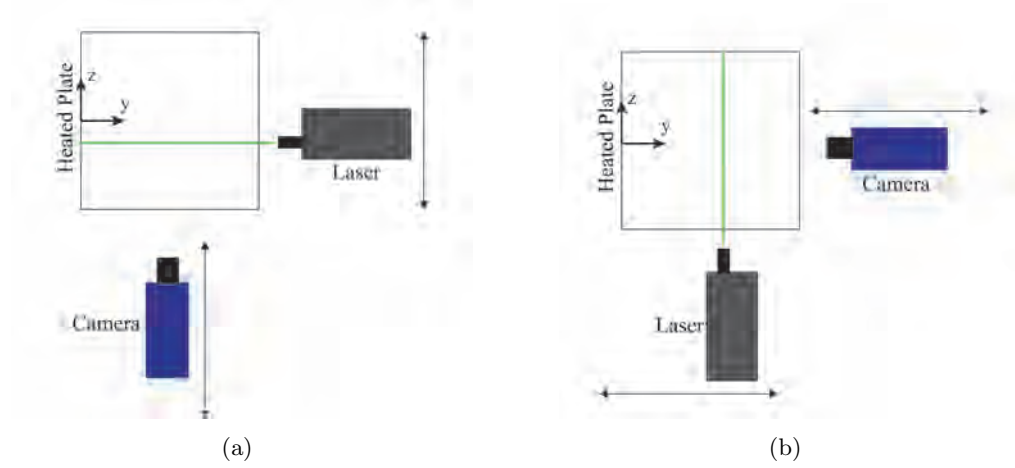


Fig. 4.5: The orientation of the camera and laser for PIV inflow data acquisition. The laser and camera are traversed across the test section to obtain several planes of velocity data. The flow direction is out of the page. (a) shows the nominal setup that is also used to obtain the velocity over the heat flux sensors. (b) shows the inlet profile specific orientation to obtain the w component of velocity.

Equation 4.26 can be written in the form

$$\epsilon = \nu \left\{ 2 \left(\frac{\partial \overline{u'}^2}{\partial x} + \frac{\partial \overline{v'}^2}{\partial y} + \frac{\partial \overline{w'}^2}{\partial z} \right) + \frac{\partial \overline{u'}^2}{\partial y} + \frac{\partial \overline{u'}^2}{\partial z} + \frac{\partial \overline{v'}^2}{\partial x} + \frac{\partial \overline{v'}^2}{\partial z} + \frac{\partial \overline{w'}^2}{\partial x} + \frac{\partial \overline{w'}^2}{\partial y} \right. \\ \left. + 2 \left(\frac{\partial \overline{u'}}{\partial y} \frac{\partial \overline{v'}}{\partial x} + \frac{\partial \overline{u'}}{\partial z} \frac{\partial \overline{w'}}{\partial x} + \frac{\partial \overline{v'}}{\partial z} \frac{\partial \overline{w'}}{\partial y} \right) \right\} \quad (4.27)$$

where $\overline{u'}$, $\overline{v'}$, $\overline{w'}$ are the fluctuating values. We can measure $\frac{\partial \overline{u'}}{\partial x}$, $\frac{\partial \overline{u'}}{\partial y}$, $\frac{\partial \overline{v'}}{\partial x}$, $\frac{\partial \overline{v'}}{\partial y}$. Also, measurements have shown that $v = w$ and $\overline{v'} = \overline{w'}$ at the inlet of the test section. Using these facts, Eqn 4.27 can be rewritten as

$$\epsilon = \nu \left\{ 2 \left(\frac{\partial \overline{u'}^2}{\partial x} + \frac{\partial \overline{v'}^2}{\partial y} + \frac{\partial \overline{v'}^2}{\partial z} \right) + \frac{\partial \overline{u'}^2}{\partial y} + \frac{\partial \overline{u'}^2}{\partial z} + 2 \frac{\partial \overline{v'}^2}{\partial x} + \frac{\partial \overline{v'}^2}{\partial z} + \frac{\partial \overline{v'}^2}{\partial y} \right. \\ \left. + 2 \left(\frac{\partial \overline{u'}}{\partial y} \frac{\partial \overline{v'}}{\partial x} + \frac{\partial \overline{u'}}{\partial z} \frac{\partial \overline{v'}}{\partial x} + \frac{\partial \overline{v'}}{\partial z} \frac{\partial \overline{v'}}{\partial y} \right) \right\}. \quad (4.28)$$

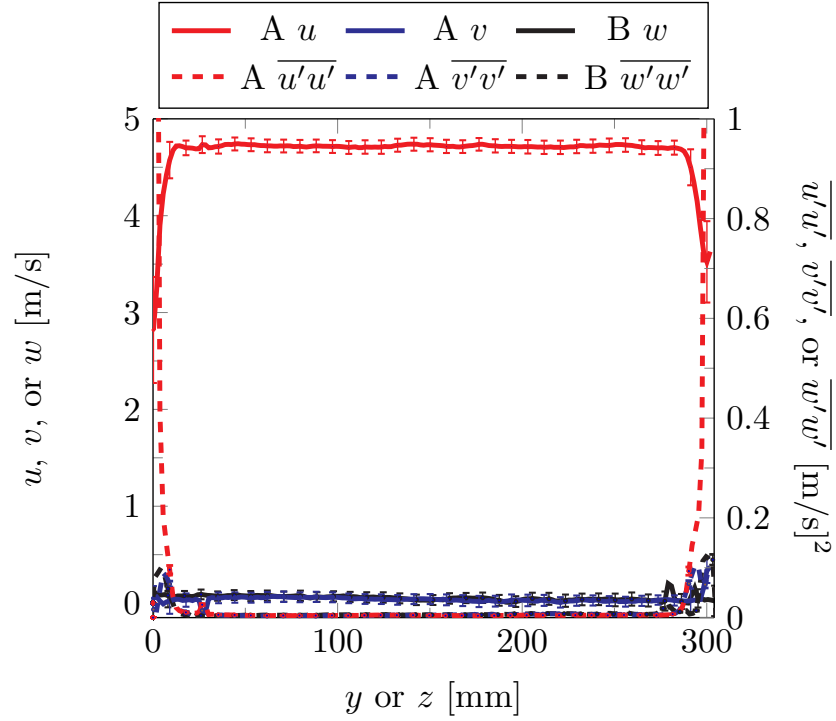


Fig. 4.6: Center profiles for two orientations showing justification for several assumptions at the inlet of the test section.

However, Since $\overline{v'v'} = \overline{w'w'} < \overline{u'u'}$ we can derive an equation for ϵ for our specific case as

$$\epsilon = \nu \left\{ 2 \left(\frac{\partial \overline{u'^2}}{\partial x} \right) + \frac{\partial \overline{u'^2}}{\partial y} + \frac{\partial \overline{u'^2}}{\partial z} \right\}. \quad (4.29)$$

The turbulence kinetic energy is also found from the measured inlet data. The definition of the turbulence kinetic energy [18, p. 64] is

$$k = \frac{1}{2} (\overline{u'u'} + \overline{v'v'} + \overline{w'w'}). \quad (4.30)$$

It is assumed that $\overline{v'v'} = \overline{w'w'}$, simplifying the equation to

$$k = \frac{1}{2} (\overline{u'u'} + 2\overline{v'v'}). \quad (4.31)$$

However, further simplification eliminates the $\overline{v'v'}$ term making the turbulence kinetic energy a function of $\overline{u'u'}$ only. To be slightly more accurate, the small values of $\overline{v'v'}$ are left in for the computation, as they are measured with $\overline{u'u'}$ at no extra cost.

The procedure for acquiring the inlet data is described in the following list. For the inlet data, 9 planes of 2-component PIV data are acquired in Orientation A. Orientation B is only acquired to prove that it is not a necessary measurement at the inlet. So, 9 planes are acquired at Orientation A. Orientations A and B are shown in Fig. 4.5.

1. Setup laser, camera, and respective traverse stages, and align with the calibration target.
2. Calibrate camera and match laser plane to calibration plane.
3. Set acquisition timing for sufficient particle displacements.
4. Set seeder flow rate.
5. Set laser intensity.
6. Set f-stop (which impacts particle image intensity and size).
7. Stabilize room, wall and flow conditions.
8. Record PIV data, temperatures, heat flux, equipment position, blower speed, heater and seeding settings, camera and laser settings, and room conditions.
9. Move to next plane and repeat.

After the inlet data are acquired, several computer codes were written to analyze the inlet data and prepare them for use in simulations. The computer code would take the mean velocity data from each inlet plane and combine them into a common .csv file with the corresponding z coordinate for each plane. The turbulence parameters discussed above are also computed in this code, but an analyst should independently compute the necessary model parameters. This code is included in Appendix G. This code defines the inlet conditions for the CFD simulations. Post-processing the results from this code is required to use this inlet velocity profile in StarCCM+.

4.2.5 Boundary Layer

In the results obtained, there are several parameters that are used to describe the flow phenomena. These are not necessary considered as SRQ in this study, but some studies might consider them as such. Such parameters include the momentum thickness δ_2 with the corresponding momentum thickness Reynolds number Re_{δ_2} , the displacement thickness, and the boundary layer thickness. These parameters are reported along with the SRQ's in Chapter 5.

The boundary layer thickness is computed as [46]

$$\delta = 0.37x\text{Re}_x^{-1/5}. \quad (4.32)$$

This equation is valid for local Reynolds number less than 10^8 . Although this is just an approximation, it is useful for the comparison of turbulent boundary layer thickness growth. Other common boundary layer thickness quantities are discussed below. The approximation in Eqn. 4.32 is used because many of the measurements of the boundary layer velocity do not measure the free-stream velocity. Thus, a simple 99% of the free-stream is not feasible in all cases.

The momentum thickness is computed using its definition [18]

$$\delta_2 = \int_0^\infty \frac{\rho \bar{u}}{\rho_\infty \bar{u}_\infty} \left(1 - \frac{\bar{u}}{\bar{u}_\infty} \right) dy, \quad (4.33)$$

with an assumption. The density of air at the inlet is the same as the density of air in the boundary layer ($\rho = \rho_\infty$). The density at the inlet of the test section is nominally 1.01 kg/m^3 and the boundary layer density for air at the heated plate temperature is 0.9 kg/m^3 . Using these two extremes, the ratio of densities is 0.9. Thus, the ratio of the densities is near unity for most of the boundary layer. For increased accuracy, the momentum thickness presented in this report should be corrected with the inlet density and boundary layer density profile. Future experiments will include measurement of the temperature profiles, providing data to compute the density ratio. A Matlab intrinsic trapezoidal integration is used and the code

is included in Appendix I.

Another boundary layer quantity of interest is the displacement thickness [18]

$$\delta_1 = \int_0^\infty \left(1 - \frac{\bar{u}\rho}{\bar{u}_\infty\rho_\infty} \right) dy. \quad (4.34)$$

The ratio of the momentum thickness and the displacement thickness defines a boundary layer shape factor [18]. This is discussed in more detail later, when the boundary layer profiles have been presented. Again, the same assumption is made regarding the density ratio for the displacement thickness as was made for the momentum thickness.

4.3 Measurement of System Response Quantities

The measurement of the system response quantities is now described in more detail. Each SRQ section addresses the measurement of the SRQ, the analysis corresponding with the measurement and the uncertainty of the SRQ. Details and discussion of the results are included in Chapter 5 after the results are presented. The PIV equipment for each of these setups was described in Chapter 3.

4.3.1 Experimental Procedure

The procedure for acquiring the SRQ boundary layer velocity data is described in the following list. The SRQ data are all acquired using Orientations A (see Fig. 4.5).

1. Setup laser, camera, and respective traverse stages, and align calibration target.
2. Calibrate camera and match laser plane to calibration plane.
3. Set acquisition timing for sufficient particle displacements.
4. Set seeder flow rate.
5. Set laser intensity.
6. Set f-stop (which impacts particle image intensity and size).
7. Stabilize room, wall and flow conditions.

8. Record PIV data, temperatures, heat flux, equipment position, blower speed, heater and seeding settings, camera and laser settings, and room conditions.
9. Change boundary conditions (i.e. change flow rate from mixed to forced, or isothermal to constant flux), wait for stabilization of conditions, and take another data set.

As the design of the experiment was under consideration, the validation system response quantities were defined. Three heat flux sensors are embedded under the surface of the plate and the heat flux at their respective positions is used for three SRQ's. The sensors are described in more detail in Section 3.2.4.

The velocity field over the plate at the three heat flux sensor positions is used for another set of SRQ's. The velocities include \bar{u} , \bar{v} , $\overline{u'u'}$, $\overline{v'v'}$, and $\overline{u'v'}$. These velocities are measured using PIV at a high resolution using the calibration and analysis described in Chapter 3.2.5.

The friction velocity u_τ , which is defined as $u_\tau = \sqrt{\nu du/dy}$ where ν is the kinematic viscosity, is also a SRQ. In summary, the SRQ's measured are:

1. Boundary layer profiles at three x locations, including \bar{u} , \bar{v} , $\overline{u'u'}$, $\overline{v'v'}$, and $\overline{u'v'}$.
2. The heat flux at the same x locations.
3. The friction velocity u_τ .

4.3.2 Boundary Layer Velocity

The first SRQ is the boundary layer velocity profile at the three heat flux sensor positions. The \bar{u} , \bar{v} , $\overline{u'u'}$, $\overline{v'v'}$, and $\overline{u'v'}$ velocities are measured and used for SRQ's. For many common turbulence models, a CFD simulation may not compute the Reynolds stresses. In such cases, the turbulence kinetic energy is used for validation purposes. The turbulence kinetic energy is easily obtained from the experimental SRQ data.

The measurements are acquired using the steps outlined above and in Chapter 3.2.5. The camera and laser are setup in Orientation A (see Fig. 4.5), with the camera at an angle about x of around 5° . The small calibration plate is used to scale and dewarp the

images. The plate is heated to 150° and the flow conditions are allowed to stabilize. Details regarding the equipment and measurement of velocity and the analysis of the PIV data was outlined in Chapter 3.2.5.

Uncertainty of all SRQ's must be reported. The repeatability of the boundary layer measurements is discussed in Chapter 5.4, as this analysis is only performed after data acquisition. The method used to determine the uncertainty of the PIV velocity measurements is outlined in the literature using an uncertainty surface method [13, 14]. The uncertainty of the position is discussed later.

4.3.3 Heat Flux

The heat flux is more difficult to both compute and measure than the velocity. It was selected to provide a wider range in the difficulty spectrum for validation [3]. The heat flux is measured using the heat flux sensors at the positions described previously. The sensors are embedded a small distance from the surface of the plate.

A possible limitation of this design is the assumption that no axial conduction takes place. The heat flux sensor has some material between it and the plate surface where conduction could move measured heat flux to another location. The measured heat flux is assumed to be the entire heat flux into the flow (convection/radiation). To mitigate this error, thermal gradients in the plate are kept small and all of the data presented herein is steady-state. Correlations are used to compare with the experimental measurements and CFD computations. These are described for each case in Chapter 5.

4.3.4 Friction Velocity

The friction velocity u_τ is obtained in one of two ways. The first is to use a linear fit of the first several data points of the velocity in the boundary layer near the wall to obtain $\partial u / \partial y$. This method has many limitations, including a high susceptibility to position error. That position error can come from error in wall position (which is normally specified by the experimentalist), or an error from non-uniform seeding in interrogation regions in the PIV processing.

The second method used to obtain the friction velocity is to use a fit to a Spalding profile, as outlined by Kendall and Koochesfahani [50]. The quantities u_τ , κ , B , and y_0 can be found by fitting the measured PIV profiles to the Spalding profile and optimizing the fit to compute the friction velocity, and other relevant parameters, including the wall position. The equation for the Spalding profile is

$$y^+ = u^+ + \exp(-\kappa B) \left[\exp(\kappa u^+) - 1 - \kappa u^+ - \frac{(\kappa u^+)^2}{2} - \frac{(\kappa u^+)^3}{6} \right] \quad (4.35)$$

where $y^+ = (y - y_0)u_\tau/\nu$ and $u^+ = \bar{u}_\infty/u_\tau$.

The Spalding fit method outlined in [50] is only valid for fully turbulent flow. In the forced convection regime where buoyancy forces are insignificant compared to inertial forces, the fit is more applicable than in situations where the buoyancy forces are more dominant. These ratios were discussed in Chapter 1.

The uncertainty of the wall shear velocity u_τ based on examination of the gradient at the wall is found using the Taylor Series Method [17] and the data reduction equation $u_\tau = \sqrt{\nu du/dy}$. The uncertainty of the shear velocity is

$$U_{u_\tau} = \sqrt{\left(U_{du/dy} \frac{\sqrt{\nu}}{2\sqrt{du/dy}} \right)^2 + \left(U_\nu \frac{\sqrt{du/dy}}{2\sqrt{\nu}} \right)^2}, \quad (4.36)$$

where U_ν is the uncertainty of the kinematic viscosity, Eqn. 4.14, and $U_{du/dy}$ is the uncertainty of the velocity gradient

$$U_{du/dy} = \sqrt{\left(\frac{U_{u1}}{dy} \right)^2 + \left(\frac{U_{u2}}{dy} \right)^2 + \left(U_{dy} \frac{u1 - u2}{dy^2} \right)^2} \quad (4.37)$$

where the velocity uncertainties are computed using the methods described in [13–16] and the velocities are data points in the velocity profile. The dy term is the vector spacing of the data and the uncertainty of dy is explained below.

The dynamic viscosity μ was defined in Eqn. 4.15 and it's uncertainty described, along with the air density computation and it's uncertainty. The uncertainty of temperature

$U_T = 0.6^\circ\text{C}$ and the uncertainty of pressure $U_P = 1.5\%$ of reading.

The uncertainty of the position of the PIV data can be a significant contributor to the uncertainty of the friction velocity (and velocity itself). The most obvious method for setting an origin is to locate a non-moving object (such as the wall) in the raw PIV images. However, the laser source commonly generates a wide flare in the camera image at the wall making it difficult to pinpoint its location. An example is shown in Fig. 4.7 which shows a small part of the image. The wall is the white band near the left side of the image.

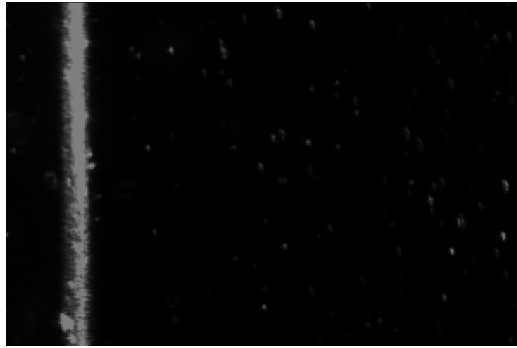


Fig. 4.7: An image of the wall, with the image width being 2.25 mm.

This estimate can be improved upon using information from the turbulent flow along a wall. The error in the wall location was found first by fitting theoretical (Spalding) velocity profiles to the hundreds of streamwise time-averaged velocity data points (some of which are located in the viscous sublayer, and most of which are in the log layer), and using the wall location as a parameter of the fit. In addition, the wall location is found by fitting a line through the three velocity values closest to the wall. These should behave linearly and go to zero at the wall. It was found that replications of this process, with the measurement system set up from scratch each time, resulted in large variations in the wall location error.

Seven replications are shown in Fig. 4.8. The error δy of each method relative to the wall location based on inspection are shown. For both methods, the variations in the wall position error were on the order of 16 pixels. The average of these samples could be viewed as the bias of each method relative to the wall location by inspection. Unfortunately, we have no evidence that any one of these methods is clearly superior to any other, but these

data are sufficient to provide a reasonable uncertainty estimate of the wall location.

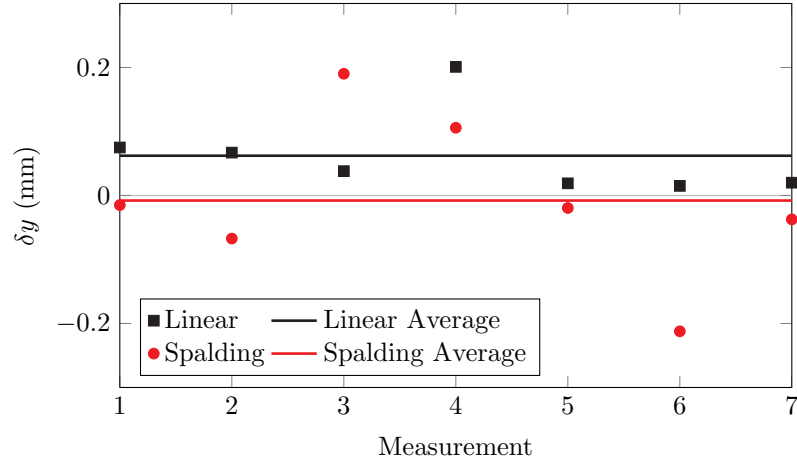


Fig. 4.8: The error of the wall location computed using three methods with the image estimate being the basis for the error and a scale factor of around 84 pixels/mm.

4.4 CFD Simulation Procedure

The CFD simulations are conducted using STAR-CCM+ from CD-adapco [51]. A best estimate for the appropriate turbulence models is used, since the validation of the models is not in the scope of this work. Use of these models is based on preliminary simulation work done by Iverson [49].

4.4.1 Geometry and Mesh

The geometry was modeled using the as-built measurements of the test section. The 7 planes of measured dimensions were used to define the air volume of the wind tunnel. This volume was exported as a parasolid. The parasolid file was imported to STAR-CCM+ and the regions defined as necessary (inlet, outlet, heated wall and 3 walls). The as-built dimensions are shown in Table 4.2. The assumptions that are used in building this geometry include: the heated plate is flat, the 7 reference cross-sections are lined up on that flat plate, the corners nearest the heat plate are right angles.

The mesh was generated using the directed mesher function in StarCCM+. The square

test section allowed for a simple mesh to be created using the directed mesher. The patch mesh (the source of the mesh that is extruded through the volume) uses a two sided hyperbolic distribution with end spacing define as in Table 4.4.

Three meshes were constructed on the geometry, and the parameters are shown in Table 4.4, where the Average Volume is the average cell volume of the cells nearest the heated plate. These meshes were constructed based on the y^+ computed using the mixed buoyancy opposed boundary conditions. The M2 mesh was defined to keep the wall y^+ below 1, then the other two meshes were defined such that the cell height ratio between the near wall cells was 2. The means that $dy_{M1} = 2dy_{M2} = 4dy_{M3}$, where dy is the cell height of the near wall cell.

Table 4.4: The mesh properties for the three meshes used in the GCI analysis. The mesh cell count, average volume of cells, near wall cell height, and several GCI parameters and heat flux results are tabulated.

Mesh	Cells	Avg. Vol.	dy	r	y^+	q''_1	q''_2	q''_3
M1	12600000	5.61E-10	0.0358 mm	$r_{21}=2.00$	0.44	1609.6	1099.6	1070.4
M2	1575000	4.52E-09	0.0716 mm	$r_{32}=2.02$	0.87	1641.1	1142.7	1103.6
M3	191660	3.73E-08	0.1432 mm		1.75	1110.2	1175.9	1128.1

These meshes are all used to compute the grid convergence index (GCI) based on the heat flux at the three heat flux sensor positions (although the measured heat flux has nothing to do with this GCI analysis). Following the procedure outlined by the Journal of Fluids Engineering [52], the GCI was computed. First, the length scale dy was defined as the height of the near wall cells which was computed from the cube root of the average near wall cell volume. The ratio between dy for the several meshes was 2. Second, the resultant heat flux at a certain position (such as the first heat flux sensor) was recorded from the simulations at each mesh refinement (M1, M2, and M3). Third, Eqns. 4.38, 4.39, 4.40, and 4.41 are used to compute the GCI in Eqn. 4.42. In Eqns. 4.38 and 4.40, ϵ_{21} and ϵ_{32} are simply the difference between the resultant heat fluxes from the respective simulations ($\epsilon_{21} = q''_{M2} - q''_{M1}$).

$$p = \frac{1}{\ln r_{21}} |\ln |\epsilon_{32}/\epsilon_{21}| + q(p)| \quad (4.38)$$

$$q(p) = \ln \left(\frac{r_{21}^p - s}{r_{32}^p - s} \right) \quad (4.39)$$

$$s = 1 \cdot \text{sgn}(\epsilon_{32}/\epsilon_{21}) \quad (4.40)$$

$$e_a^{21} = \left| \frac{q_1'' - q_2''}{q_1''} \right| \quad (4.41)$$

$$GCI_{fine}^{21} = \frac{1.25e_a^{21}}{r_{21}^p - 1} \quad (4.42)$$

Equation 4.42 represents the discretization error on the fine mesh based on the heat flux computed. It is noted that iterative convergence is achieved in these simulations as each equation's residuals decrease more than four orders of magnitude [52]. Table 4.5 shows the GCI results for this study.

Table 4.5: The GCI results using the methods described above for heat flux at the first sensor position.

Position	p	q	e_a^{21}	e_a^{32}	GCI ²¹	GCI ³²
P1	4.01	-0.03	31.6	-530.9	0.002	0.026
P2	0.39	-0.01	43.0	33.2	0.158	0.116
P3	0.46	-0.01	33.2	24.5	0.103	0.073

4.4.2 Boundary Conditions and Physics

The boundary conditions for the walls are defined from the measured boundary conditions. Each of the four walls was set to the temperatures measured in the experiment, as described in Chapter 3.2. The temperature from the experiment was recorded in a .csv file that is imported into StarCCM+. The columns of the file are x , y , z , and the temperature.

The inlet temperature was defined in a similar fashion, along with the relevant turbulence model inputs (such as k , ϵ , or ω).

All of these boundary conditions are necessarily interpolated spatially (the measurements are much too coarse to be used directly in the simulation, and STAR-CCM+ does not interpolate the boundary condition tables). The interpolation codes are included in Appendix H. One code interpolates the inlet velocity components, turbulence kinetic energy, and turbulence dissipation rate ϵ . The second code interpolates the plate temperature and the inlet temperature. The variation in the other three wall temperatures is small, so interpolation is unnecessary.

Since a few turbulence models are considered, there are several physical parameters in the simulations that are all consistent. The consistent physics settings for the simulations include:

1. Steady State - the simulations included herein do not change in time
2. Coupled energy/momentum - the heat transfer contributes to changes in momentum
3. Ideal Gas - we assume air is an ideal gas
4. Turbulent - we assume that all flow scenarios presented are turbulent
5. Gravity - the models include body forces due to gravity

4.4.3 Models

The selected models are based on the work done in [49]. For the mixed convection buoyancy aided flow, the Standard k - ϵ Low Reynolds number is used, with an all $y+$ wall treatment [53]. This model is better than the standard k - ϵ model because it utilizes damping functions which allow the solver to compute in the viscous-affected region near the heated wall [51].

The forced convection buoyancy aided flow simulations use a Standard (Wilcox) k - ω model [54]. These simulations also use an all $y+$ wall treatment. In these buoyancy aided solutions, the Courant Number was increased to decrease solution computation time.

Mostly, the default settings were used in these models. In all cases, the residuals started at unity and decreased more than 6 orders of magnitude.

4.5 Quality Assurance

To ensure the experiment design, data acquisition, and analysis are sufficient to meet project funding agency requirements, the NEUP QA Requirements are used [55]. A summary of the requirements is included below:

- Equipment Calibration and Documentation
 - Specified requirements of accuracy, precision of equipment
 - Measurement uncertainty is documented
 - All equipment is controlled
 - Equipment calibration is recorded
- Analysis/Modeling V&V
 - Documented software used in analysis
 - Modeling uses software packages that have received V&V, with referenced software version
- Records
 - Regularly used laboratory notebook to record project work activity
 - Electronic records kept and backed up
- Data Acquisition and Analysis
 - Testing of data acquisition equipment before data collection
 - Investigation of data anomalies
 - Define the assumptions stated in data analysis, methods used to identify and minimize uncertainty, and the analytical models used

4.6 Data Recording, Storage, and Backup

All data are written to removable hard drives in the PIV computer. When the drive is full, it is moved to another location for future use. As all of the data are recorded digitally, it is necessary to back up the data to another site. A system is built in a different building that houses several hard drives. The PIV data and other relevant recordings are uploaded to those hard drives as a second copy. All data are stored in a hard drive in the Experimental Fluid Dynamics Laboratory and backed up to a remote location in the main Engineering building at USU.

Chapter 5

Results

The results from the experiment are presented and discussed in this chapter. The boundary conditions acquired for the cases are presented here, and the data are available on the project website. The SRQ results are presented along with the SRQ results from the simulations. Some discussion and comparison is provided. Finally, the uncertainty of the measurements are presented. In the discussion, several cases are referred to using the heating condition “constant heat flux.” This nomenclature is used because the three heat flux sensors are used to fix the heat flux at a specified value. However, the second sensor is known to have a higher uncertainty than the other two sensors, invalidating its nomenclature as constant heat flux. The case is valid as a different heating condition than the isothermal cases, but it should be understood that constant heat flux is not exactly the heating condition on the plate.

5.1 Boundary Conditions

The boundary conditions are measured every time PIV data are acquired. For each case, there are 9 PIV inlet planes and 3 PIV SRQ measurements, making 12 boundary condition data sets for each flow scenario. For instance, the isothermal forced convection buoyancy aided case has 12 measurements of the boundary conditions. The 12 sets of boundary conditions are averaged together and used for the buoyancy aided isothermal forced convection boundary conditions. The sample size requires a Student-t distribution to quantify the precision uncertainty of the boundary conditions [18].

The spanwise centerline $z = 0$ temperature profiles are shown in Fig. 5.1 for the cases under consideration. The isothermal cases (forced and mixed) are quite similar, as the control software compensates for the change in flow rate to hold the near-uniform temper-

ature. The discrepancy of 1.7° at the first thermocouple is due to the nature of the power supplied to the heaters, as discussed in the following paragraph. The constant flux cases have an average temperature difference of 1.2%. This figure should be referred to when the difference in plate temperature is referenced in later discussions.

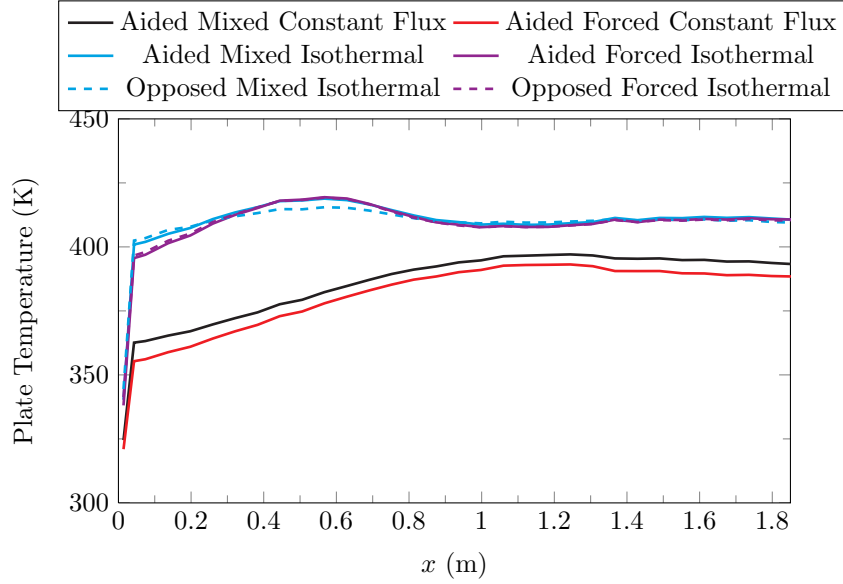


Fig. 5.1: The centerline ($z = 0$) temperature profiles for the buoyancy aided cases.

The forced convection isothermal case cools the first heated section more than the mixed convection case, therefore decreasing the temperature. This is observed in the heat flux trends discussed later. The power supplied to heaters 1 and 2 are governed by the temperature at the center of heater 1, $x = 5.87$ in. (see Fig. 3.6). The limited power allowed to the heaters kept the forced convection case cooler than the mixed convection case at the first heater. The power supplied to the first two heaters was at maximum for the forced convection case but not for the mixed convection case. The plate temperatures would be identical if the heaters could safely provide more power. This is also apparent in Fig. 5.2 where the constant power to heaters 1 and 2 create a cooler leading edge and a too warm region over heater 2.

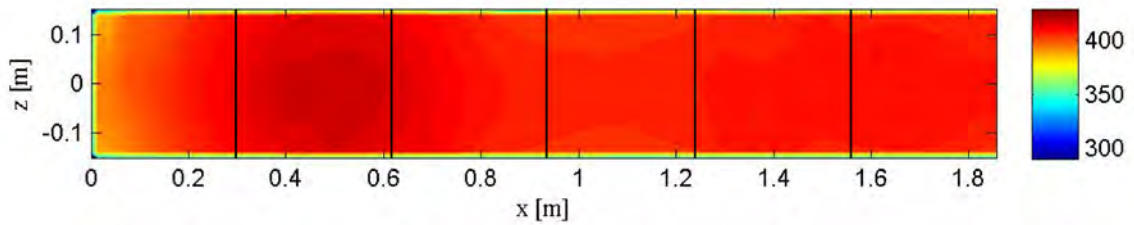


Fig. 5.2: The temperature contour for the aided isothermal forced convection case, showing the hot spot at the second heater. The segments show the heaters.

The centerline plate temperature for the buoyancy aided and buoyancy opposed isothermal cases are nearly identical when comparing the mixed aided to the mixed opposed, and similarly for the forced aided to forced opposed centerline temperatures. The buoyancy aided and opposed cases were acquired several months apart, with a rotation of the wind tunnel 180° in between. The plate temperature showing this repeatable boundary condition for forced isothermal convection is shown in Fig. 5.1.

It is noted that the cases labeled “constant heat flux” are not actually constant heat flux. The second heat flux sensor is suspected to have elevated uncertainty compared with the other two sensors. Since this is one of the control parameters for driving the heated wall boundary conditions, it cannot be considered as “constant heat flux.” However, the case is still valid as a comparison with a different temperature profile on the heated wall.

5.2 System Response Quantities

A summary of the cases is included in Table 5.1. The hydraulic diameter is 12 inches. The CFD results presented are calculated from the models outlined in Chapter 4.4.3. The system response quantities in this study include the boundary layer velocity profiles near the heated wall and the heat flux from the wall. At the same location as the heat flux sensors, the boundary layer profiles are measured with the PIV system, and the uncertainty is quantified using the uncertainty surface method described in Section 1.2. A third SRQ to consider is the friction velocity, u_τ .

Table 5.1: The several cases considered in the study.

Case	Re_{D_h}
Aided Forced Isothermal	75,900
Aided Mixed Isothermal	44,100
Aided Forced Constant Flux	75,800
Aided Mixed Constant Flux	44,400
Opposed Forced Isothermal	77,900
Opposed Mixed Isothermal	44,600

5.2.1 Isothermal Buoyancy Aided Forced Convection

The first system response quantity for the buoyancy aided isothermal forced convection case is the boundary layer velocity. The measured velocity profiles with uncertainty bands are shown in Fig. 5.3. The \bar{u} component of velocity and the Reynolds normal stress $\overline{u'u'}$ with 95% confidence are shown in Fig. 5.3(a). The y direction velocity \bar{v} is shown in Fig. 5.3(b) with the other two measured components of the Reynolds stress $\overline{v'v'}$ and $\overline{u'v'}$.

In Fig. 5.3(a), the velocity profile at the first position appears to be higher in magnitude than the other two positions. This is because the flow is developing, and the profile at the first position is not fully developed. The second and third positions show a more developed velocity profile. The Reynolds normal stress has the standard trend expected for boundary layer flow. It is noted that at the first position, the Reynolds stress decreases as the flow approaches the free stream. The free stream is not measured in the other two positions, so the Reynolds stress at P1 and P2 show a different slope. The Reynolds stresses at P2 and P3 are nearly the same. The first position again shows a different trend than the more developed second and third position's Reynolds stress.

Figure 5.3(b) shows the cross-stream velocity component and two other measurable quantities of the Reynolds stress. The velocity in the boundary layer has a slight trend toward the wall at all three positions. However, the values are very small compared to the streamwise velocity component (around 1% of the streamwise velocity). The uncertainty of \bar{v} is about the same order as the \bar{v} . This does give further justification for our treatment at the inlet of the test section for this buoyancy aided isothermal forced convection case.

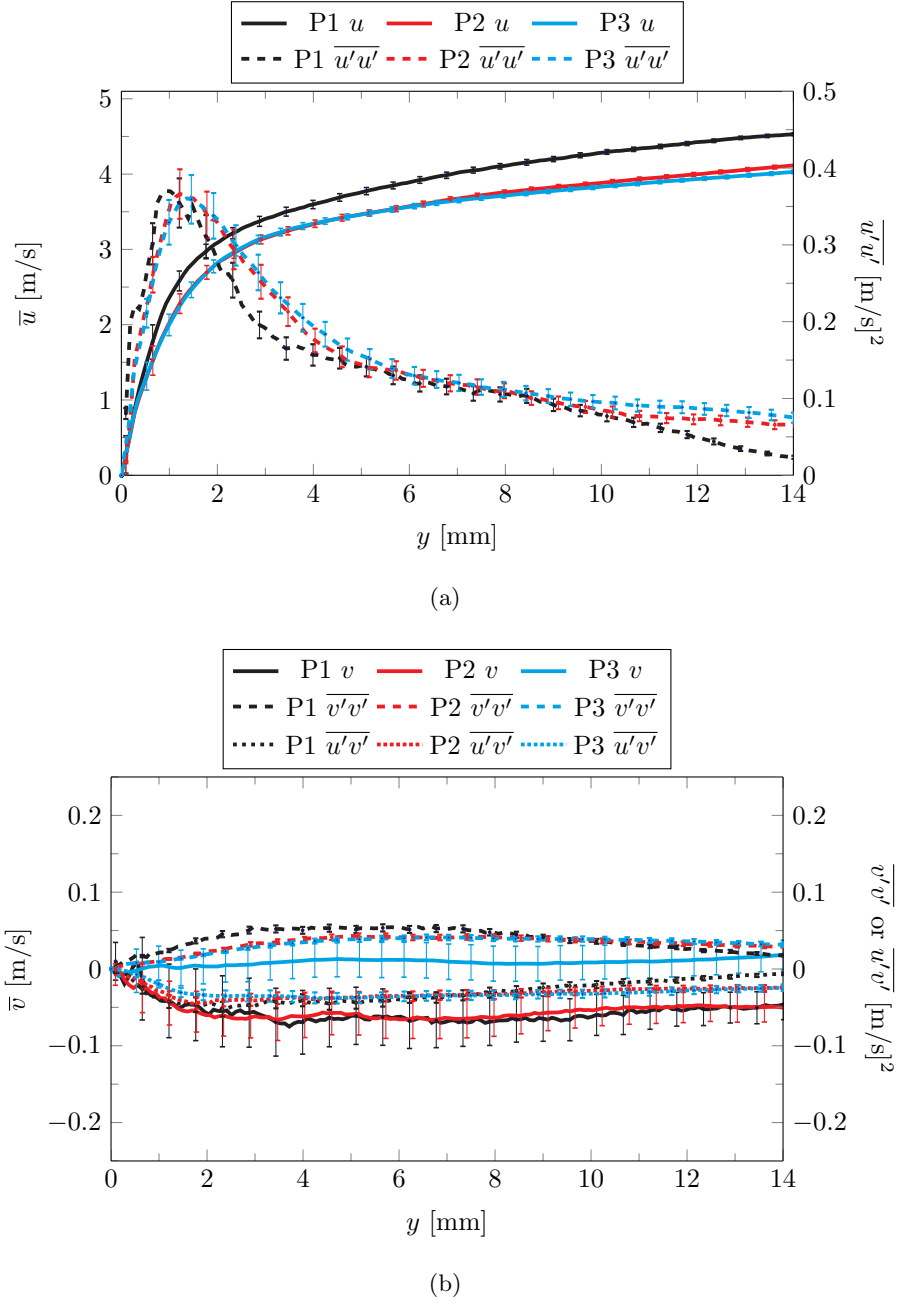


Fig. 5.3: The boundary layer velocity profiles for buoyancy aided forced convection with isothermal heating. (a) shows the streamwise component of velocity and Reynolds Stress. (b) shows the cross-stream component of velocity and the two other measured components of the Reynolds Stress. Recall that P1 is $x = 5.87$ in., P2 is $x = 30.12$ in., and P3 is $x = 54.87$ in.

Note that the third position velocity profile is calibrated using a linear scale, rather than the calibration plate that is used in the other cases.

The SRQ's presented in Fig. 5.3 are compared in Fig. 5.4 with the corresponding SRQ's from the CFD simulation that use the measured boundary conditions for this case. Figure 5.4(a) shows the boundary layer streamwise velocity component for both the experimental and CFD. The turbulence kinetic energy \bar{k} (TKE) is shown in Fig. 5.4(b). The turbulence kinetic energy is used for comparison (instead of $\overline{u'u'}$ etc.) as the CFD models employed do not compute the Reynolds stresses directly (some discussion relating to the Reynolds shear stress is included in Section 5.3.4). The \bar{k} for the experimental measurements are calculated using the definition of the turbulence kinetic energy and assuming that $\overline{v'v'} = \overline{w'w'}$. Note that these plots do not represent a validation study. They simply demonstrate that the measured boundary conditions are sufficient for the CFD simulations.

In Fig. 5.4(a), the first position CFD simulation is furthest from the measured velocity profile. The other two positions are more consistent, but still show noticeable error from the measured velocity profile. It appears that the CFD simulation free stream velocity might be more accurately predicted than the boundary layer velocity, based the converging trend of each profile with it's CFD computed profile. Figure 5.4(b) shows that the CFD simulation predicts the TKE to within the measured uncertainty near the wall for the second and third positions. The first position is poorly predicted by the CFD. However, the CFD TKE is within the experimental uncertainty for most of the boundary layer velocity profile for the third position. The first and second position CFD TKE profiles are not within the measurement uncertainty.

Non-dimensional plots of the boundary layer velocity are presented in Fig. 5.5 using the standard wall coordinates y^+ and u^+ . The quantities required to compute the wall coordinate profiles, namely u_τ , κ , y_0 , and B can be found using the method described by Kendall and Koochesfahani [50]. A curve fit to the Spalding profile yields shear velocities shown in Table 5.2, where the Spalding profile is given in Eqn 4.35. Two results are shown for each profile: one using the standard values $\kappa = 0.41$ and $B = 5.0$ and a second where κ

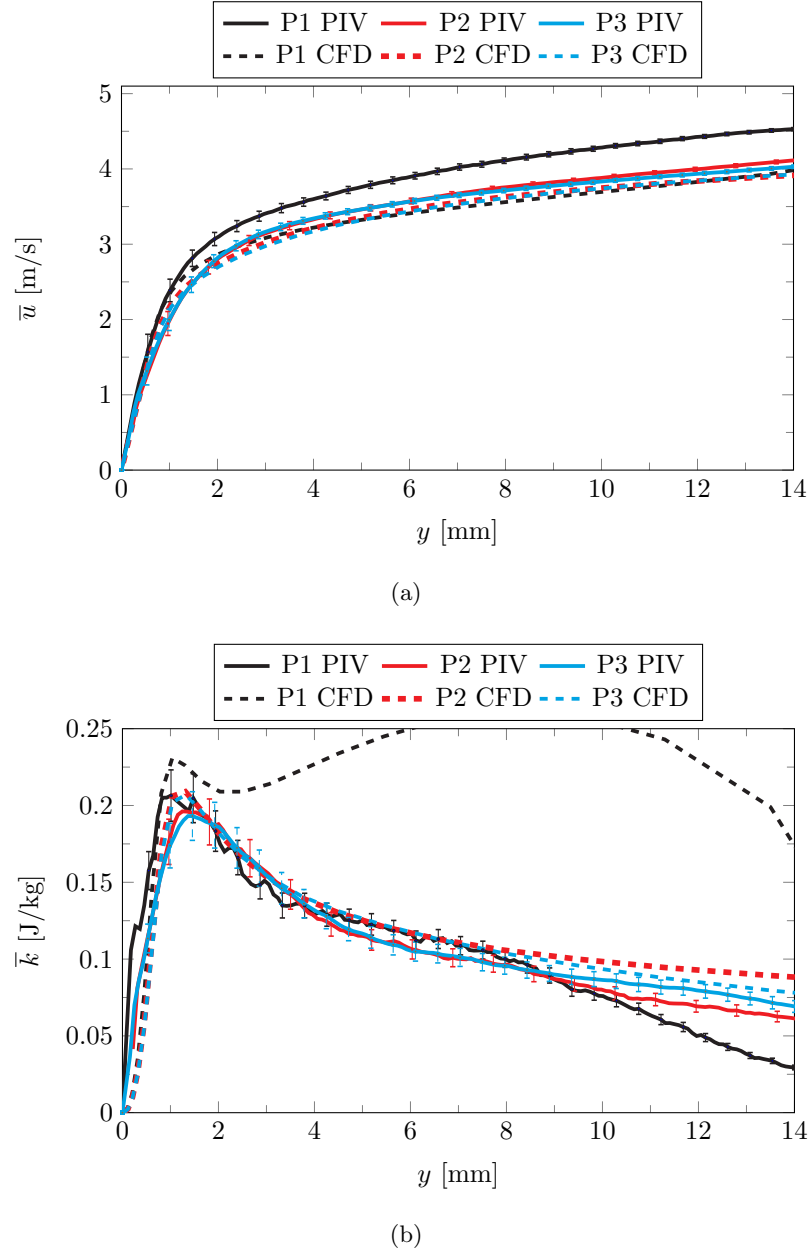


Fig. 5.4: The boundary layer velocity profiles for buoyancy aided forced convection with isothermal heating compared with CFD results using the same boundary conditions. (a) shows the streamwise component of velocity. (b) shows the turbulence kinetic energy profiles.

and B are found in the fitting process along with the wall position y_0 and friction velocity. Care was taken to exclude wake region data for the curve fit. The simulation u_τ is found by plotting the density and shear stress as a function of x on the heated wall with $z = 0$.

Then the friction velocity is computed using its definition, $u_\tau = \sqrt{\tau_s/\rho}$. A linear fit to the first three valid vectors is also used to compute the shear velocity.

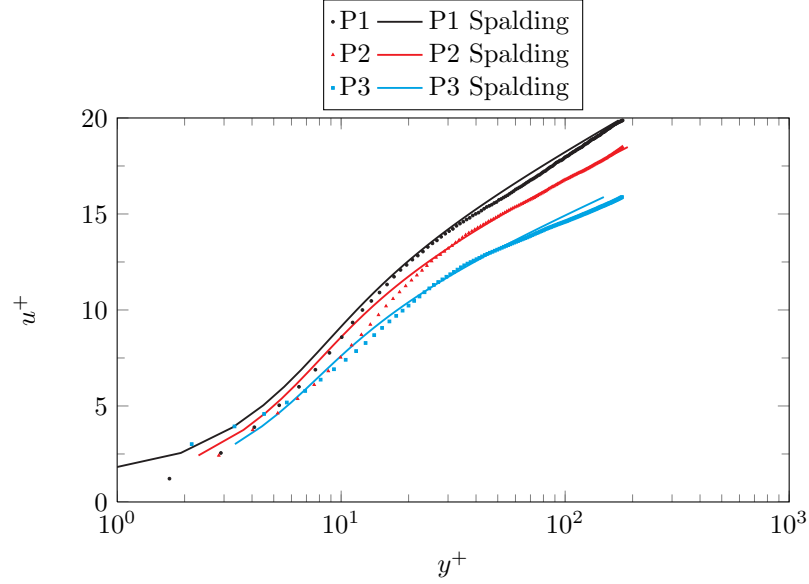


Fig. 5.5: The wall coordinate boundary layers for the three heat flux sensor positions for buoyancy aided isothermal forced convection flow and the Spalding fit profiles for comparison.

The profiles shown in Fig. 5.5 show that the curve fit does not match the data in every region of the boundary layer. The most reliable velocity data to use for the Spalding fit is inside of the wake region and outside of the viscous sublayer. Since the fit excludes the data in the linear and wake regions, the fit and the data are unmatched in the those regions. This slight discrepancy between the data and the fit has little impact on the resulting shear velocity, but does change the trend of the wall coordinate profiles.

Table 5.2 shows that there is a range of friction velocities that can be computed using the methods outlined. For this case, the CFD and the Spalding fit are in closer agreement than the linear fit friction velocity, particularly at the second and third positions. Using the shear velocities shown in Table 5.2, the wall coordinate profiles for velocity at the heat flux sensor positions are shown in Fig. 5.5. Each profile is compared with its respective Spalding profile using the 4 parameter fit. The code to fit the data to the Spalding profile

is included in Appendix J.

Table 5.2: The von Kármán constant, intercept, shear velocity from the Spalding fit, and the shear velocity from a linear fit near the wall at the heat flux sensor positions for the buoyancy aided isothermal forced convection case. The computed friction velocity from the CFD simulation is also tabulated.

Position	κ	B	u_τ Spalding	u_τ Linear	u_τ CFD
P1	0.41	5.00	0.248	0.233±0.004	0.215
P1	0.36	5.49	0.228		
P2	0.41	5.00	0.233	0.216±0.004	0.231
P2	0.405	5.61	0.223		
P3	0.41	5.00	0.235	0.216±0.004	0.233
P3	0.40	5.23	0.229		

The values of the shear velocity in Table 5.2 show a range of magnitudes. For forced convection, the Spalding fit is assumed to be more correct than a linear fit. The velocity data points nearest the wall are the most uncertain, so it seems reasonable that using more data points with the Spalding fit is more accurate. The CFD shear velocity presents the wrong trend entirely, increasing along the streamwise direction. A high value of the shear velocity at the first position is expected to correspond to the highest value of heat flux from the plate. The shear velocity is based on the velocity gradient, and a high gradient near the wall often means a thinner boundary layer. The temperature gradient in the thin boundary layer corresponds to a higher heat flux. The drop in shear velocity from P1 to P2 is expected to decrease the heat flux. The shear velocity trend from P2 to P3 does not decrease significantly for either of the Spalding or linear fits. This suggests that the heat flux should not decrease from P2 to P3. This is shown in Fig. 5.6, where the heat flux at P3 is actually greater than that at P2.

The measured heat flux at the three heat flux sensors is shown in Fig. 5.6. The measured heat flux is the reading from the sensors described in Chapter 3.2.4 and is an ensemble average of the 12 acquisition cases for the forced isothermal condition. The trend labeled Kays is the heat flux predicted by Eqn. 5.1 [18, pg. 249]. The Incropera trend is based on the correlation for convection over an isothermal flat plate, shown in Eqn. 5.2 [46, pg.

411]. The Stanton number is the Nusselt number divided by the product of the Reynolds and Prandtl numbers. Once the Nusselt number is computed, the heat flux can be found as $q'' = \text{Nu}_x k (T_x - T_\infty)/x$. It is noted that these correlations may have an error as high as 25% [46].

$$\text{St} = \frac{\text{Nu}_x}{\text{Re}_x \text{Pr}} = \frac{0.0287 \text{Re}_x^{-0.2}}{0.169 \text{Re}_x^{-0.1} (13.2 \text{Pr} - 9.25) + 0.85} \quad (5.1)$$

$$\text{Nu}_x = 0.0296 \text{Re}_x^{4/5} \text{Pr}^{1/3} \quad (5.2)$$

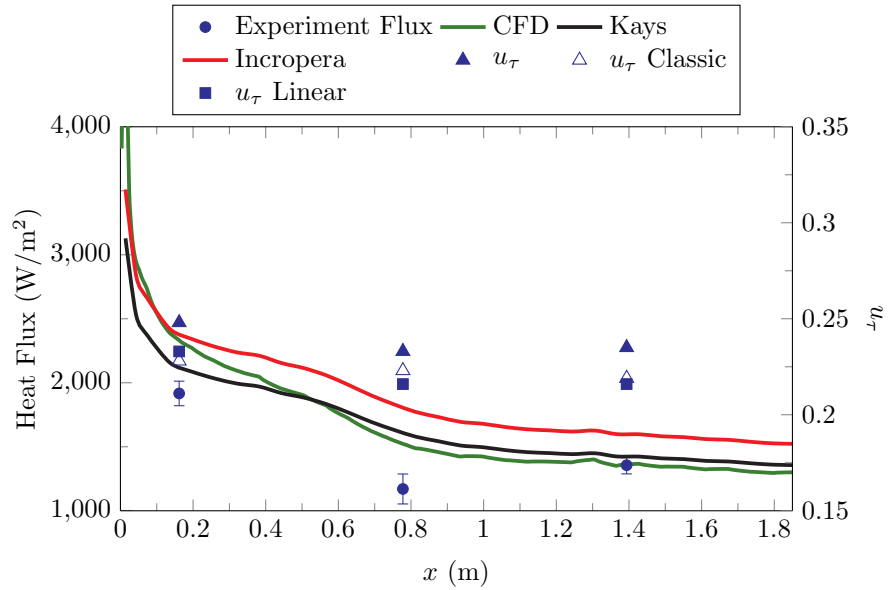


Fig. 5.6: The heat flux compared with a CFD simulation and two correlations for the buoyancy aided isothermal forced convection case. The shear velocity from the several methods is also plotted.

Figure 5.6 also shows the computed streamwise variation in heat flux from the CFD simulation along the center ($z = 0$) of the heated plate. The experimental measurements and the CFD computation have very similar heat flux responses at the first and third positions. The second position is quite different with the heat flux, being outside of the measurement uncertainty. The correlations show a similar trend to the results and simulation, but have

noticeably different magnitude.

In this case (and all of the isothermal cases) the plate is heated to a nominally isothermal condition of 150°C. The controller seeks isothermal heating, but the boundary condition thermocouples are much more resolved spatially than the PID controller (which uses only three temperature readings), limiting the ability to actually achieve isothermal heating. The corner of the leading edge is 30°C cooler than the hottest spot in the entire plate. The plate temperature contour for this case is shown in Fig. 5.2.

The heat flux, Reynolds number, surface temperature, and Grashof to Reynolds squared ratio are shown in Table 5.3, along with several of the boundary layer thicknesses and the momentum thickness Reynolds number. The flow at the location of the third heat flux sensor is nearing the boundary of forced convection based on [18]. Kays and Crawford show that the critical momentum thickness Reynolds number is 162 [18], which is exceeded at all three positions.

Table 5.3: The buoyancy aided isothermal forced convection heat flux results along with the Grashof to Reynolds number ratio (showing the cases are forced convection) and the momentum thickness Reynolds number.

x Position (in)	Flux (W/m ²)	Re_x	Temp. (K)	Gr_x/Re_x^2	δ (mm)	δ_1 (mm)	δ_2 (mm)	Re_{δ_2}
P1 = 5.87	1917	40,300	403	0.026	7.18	2.2	1.4	357
P2 = 30.12	1170	194,000	413	0.131	25.2	3.3	2.2	554
P3 = 54.87	1356	347,000	410	0.232	40.2	3.4	2.3	564

The development of the boundary layer from position 1 to 2 to 3 is shown in Fig. 5.3, where it appears that positions 2 and 3 have nearly the same boundary layer. This is confirmed by the momentum thickness Reynolds number Re_{δ_2} in Table 5.3, where the second and third positions are higher in magnitude than the first position momentum thickness Reynolds number.

5.2.2 Isothermal Buoyancy Aided Mixed Convection

The measured boundary layer velocity profiles for the buoyancy aided isothermal mixed

convection case are shown in Fig. 5.7. The streamwise velocity and Reynolds normal stress profiles are shown in Fig. 5.7(a) and the cross-stream velocity and Reynolds stress profiles are shown in Fig. 5.20(b). The effects of buoyancy on the flow is observable when comparing the trends in Fig. 5.7(a) with the forced case shown in Fig. 5.3. The trends shown in Fig. 5.7 suggest a laminarization of the flow at this flow speed and plate temperature. Figure 5.7(a) shows that the first and third positions have nearly the same boundary layer velocity profile. The trend from the first to the second suggests a thickening of the boundary layer, as was the case in Fig. 5.3. However, the trend from P2 to P3 shows that the flow has reverted to a similar boundary layer velocity profile as the one at P1. The cross-stream profile of velocity and Reynolds cross-stream normal and shear stress are shown in Fig. 5.7(b). The \bar{v} component of velocity is negative, suggesting an average flow toward the plate. However, the values are very small with particle displacements in the y direction of less than 0.3 pixels. The streamwise particle displacements are around 16 pixels. The two measured quantities of Reynolds stress are practically zero for this case suggesting a lack of turbulent mixing.

The boundary layer velocity profiles in Fig. 5.7 are compared in Fig. 5.8 with CFD simulation results for this case. The boundary conditions measured during the SRQ data acquisition were used in the CFD simulation. The CFD simulation fails to compute the boundary layer velocity profiles within the measurement uncertainty. The laminarization trend does not exist in the CFD simulation and the boundary layer velocity profiles from the CFD show a more turbulent boundary layer velocity profile than the measurements show. The CFD model fails to accurately predict the TKE at the first heat flux sensor position. The TKE at the other two positions are closer to the measured trends than the first position, but still not within the measurement uncertainty.

Flow laminarization is discussed by Kays and Crawford [18], McEligot and Jackson [21], and Perkins *et al.* [34]. In the literature, an acceleration parameter is defined as

$$K = \frac{\nu}{u_\infty^2} \frac{du_\infty}{dx}. \quad (5.3)$$

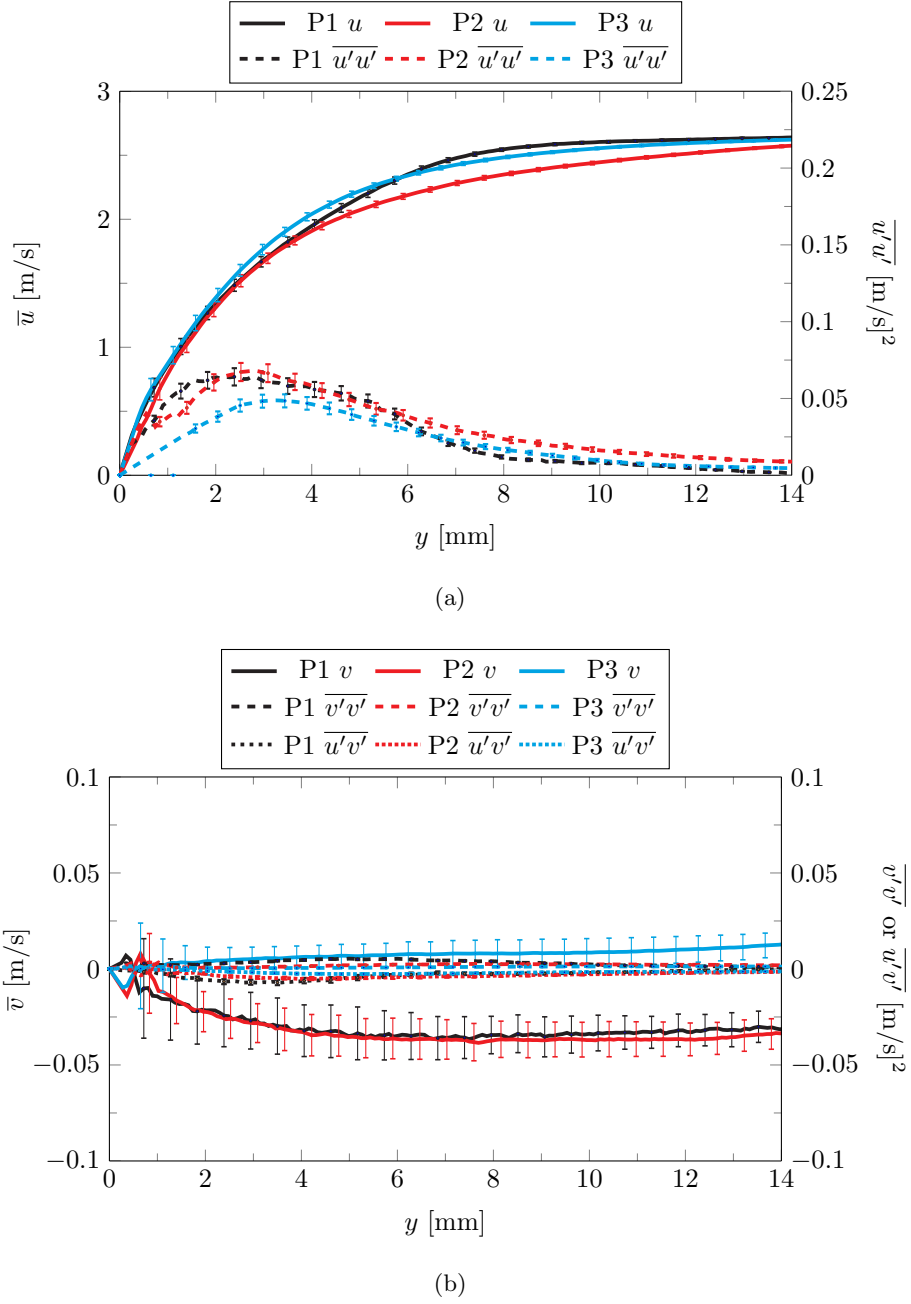


Fig. 5.7: The boundary layer velocity profiles for buoyancy aided mixed convection with isothermal heating. (a) shows the streamwise component of velocity and Reynolds Stress. (b) shows the cross-stream component of velocity and the two other components of the Reynolds Stress.

This parameter is found using the relation

$$p^+ = \frac{K}{(c_f/2)^{3/2}} = \frac{\mu d\bar{P}/dx}{\rho^{1/2}\tau_s^{3/2}} \quad (5.4)$$

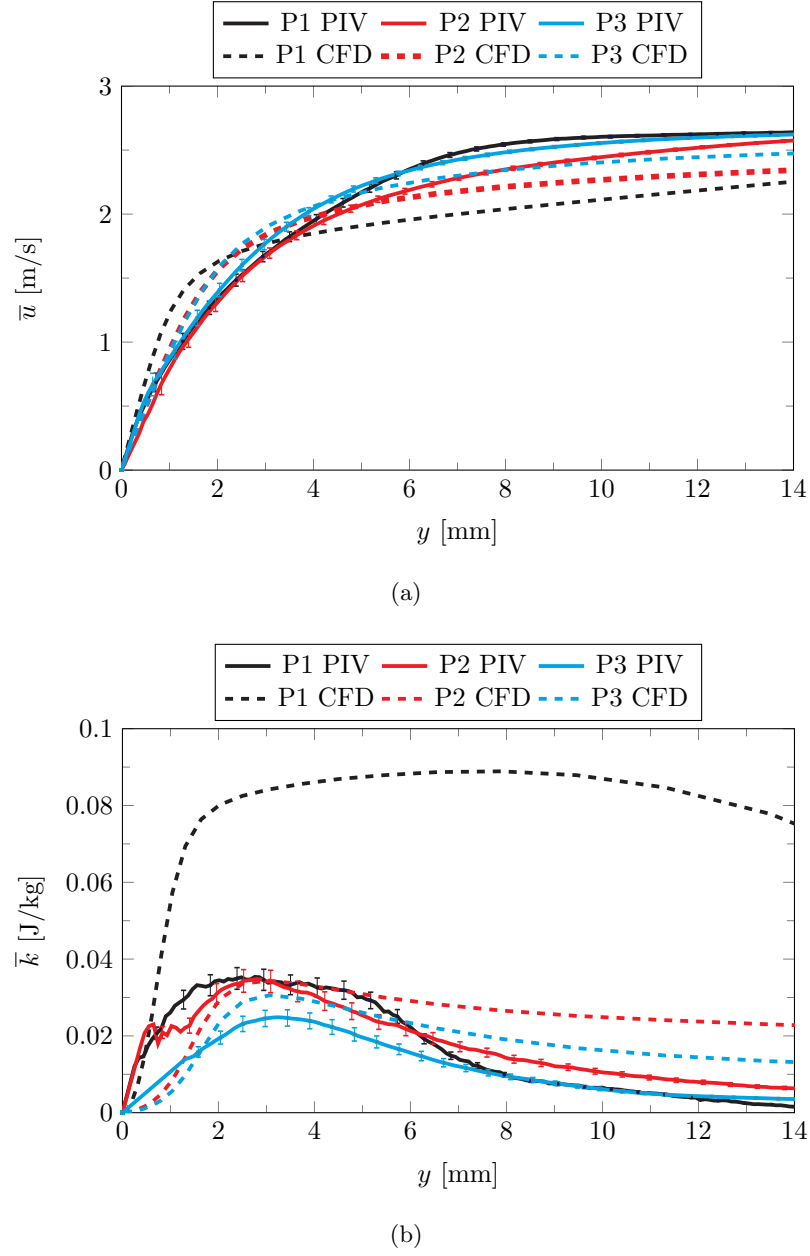


Fig. 5.8: The boundary layer velocity profiles for buoyancy aided mixed convection with isothermal heating compared with CFD results using the same boundary conditions. (a) shows the streamwise component of velocity. (b) shows the turbulence kinetic energy.

and the definition of the pressure gradient parameter p^+ .

The pressure drop through the test section ($d\bar{P}/dx$) is measured when the SRQ data are acquired using the installed pressure taps. The shear stress is found using the gradient

of the velocity data near the wall and the air properties are found using the measured atmospheric conditions. For the mixed isothermal buoyancy aided case, the acceleration factor K is computed to be 2×10^{-6} . This is near the suggested laminarization point of $K = 3 \times 10^{-6}$, so we would expect some laminar-like behavior of the flow [18, pg. 211].

The friction velocity analysis for the mixed convection cases was inconclusive. Several methods were attempted to compute the shear velocity, but none were physically sound. The velocity profiles near the wall are not linear, negating the validity of the linear approximation for computing the velocity gradient. Thus, the measured shear velocity as a SRQ is not available.

The measured heat flux for the buoyancy aided isothermal mixed convection case is shown in Fig. 5.9, compared with the CFD heat flux and two correlations. The correlations are based on the theory presented in the literature where the mixed convection Nusselt number is the sum or difference of the forced convection and natural convection Nusselt numbers [18, 46]. The natural convection Nusselt correlation was shown in Eqn. 4.3.

The mixed convection Nusselt number is shown in Eqn. 5.5, where the sum is used for buoyancy aided flow and the difference is for buoyancy opposed. The forced convection Nusselt number Nu_F is provided in Eqns. 5.1 and 5.2. In Fig. 5.9, the Kays correlation is the combination of Eqn. 5.1 and Eqn. 4.3. The Incropera correlation in Fig. 5.9 is the combination of Eqns. 5.2 and 4.3.

$$Nu_{\text{mix}}^3 = Nu_F^3 \pm Nu_n^3 \quad (5.5)$$

A laminar correlation is plotted in Fig. 5.9 as well showing the heat flux is in between the laminar regime and the fully turbulent. The laminar correlation is [18]

$$Nu_x = 0.332Pr^{1/3}Re_x^{1/2}. \quad (5.6)$$

As is shown in Fig. 5.9, the correlations are a poor representation of the heat flux as they predict nearly double the measured heat flux at the third position. The CFD simulation is

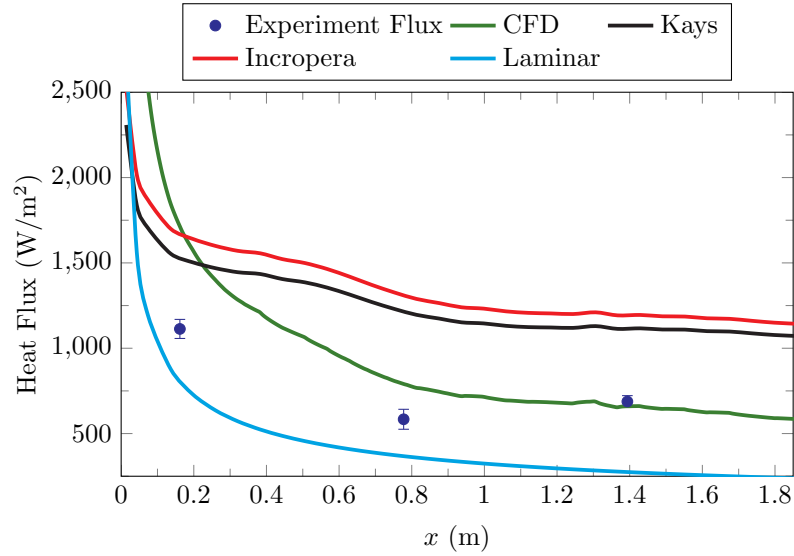


Fig. 5.9: The heat flux for the buoyancy aided isothermal mixed convection case.

closer to the measured values, but there are still large discrepancies between the experiment and the simulation. However, we reiterate that validation of the CFD model is not the scope of this dissertation. The data provide for a more robust validation study in the future. The correlations are not expected to be accurate for this flow because of the laminarization. The correlations were developed for either laminar or turbulent flow. The CFD also has difficulty predicting the heat flux for this laminarizing flow, but is more accurate than the correlations.

The heat flux results and several other relevant parameters are tabulated in Table 5.4. The local Reynolds number and the ratio of buoyant forces to viscous forces is also presented. The results in Table 5.4 show that this case is in the mixed convection regime for most of the length of the plate. The fact that the first section (at least up to the first heat flux sensor) is forced convection is shown by the low ratio at the first position. This could be a contributing factor to the error in the flux computation from the CFD simulation.

Another observation from Table 5.4 is that the momentum thickness Reynolds number at the first and third positions is very near the critical momentum thickness Reynolds number specified in [18]. That means that the flow at P1 and P3 is near the transition to

Table 5.4: The buoyancy aided isothermal mixed convection heat flux results along with the Grashof to Reynolds number ratio, several boundary layer thicknesses, and the momentum thickness Reynolds number.

x Position (in)	Flux (W/m ²)	Re_x	Temp. (K)	Gr_x/Re_x^2	δ (mm)	δ_1 (mm)	δ_2 (mm)	Re_{δ_2}
P1 = 5.87	1113	23,400	406	0.08	8.0	2.6	1.3	183
P2 = 30.12	584	113,000	414	0.39	28.1	3.2	1.7	247
P3 = 54.87	688	202,000	411	0.69	44.8	2.5	1.2	174

turbulence, with a more fully turbulent flow at P2. This further suggests that the flow is undergoing a relaminarization (although not fully laminarizing).

5.2.3 Isothermal Buoyancy Opposed Forced Convection

The boundary layer velocity SRQ's for the buoyancy opposed isothermal forced convection case are shown in Fig. 5.10. To compare the gravitational (and therefore buoyancy) effect on the boundary layer, one compares Fig. 5.10 to Fig. 5.3. As can be observed, the development of the boundary layers are different between the cases, suggesting that buoyancy forces affect the boundary layer flow for the forced convection isothermal cases. Revisiting Table 5.3, the ratio of Gr_x/Re_x^2 is near the onset of mixed convection at the third position. This means that the third position is somewhat influenced by the buoyancy forces, being nearly in the mixed convection regime. So, it is expected that the profile at the third heat flux sensor will be different depending on the orientation of gravity. Figure 5.23 shows the buoyancy aided and opposed isothermal forced convection cases plotted for comparison, and will be discussed in more detail later.

The boundary layer velocity profiles in Fig. 5.10(a) show a developing boundary layer that is not fully developed even at P3. A fully developed boundary layer profile would have a slightly lower magnitude than the P3 trend in Fig. 5.10(a), causing the boundary layer to increase in thickness. The profiles of the Reynolds normal stress in Fig. 5.10(a) also show that the boundary layer is developing. Again, the trend is due to the change in gravity direction and is discussed in Section 5.3.1. The \bar{v} component of velocity is shown in

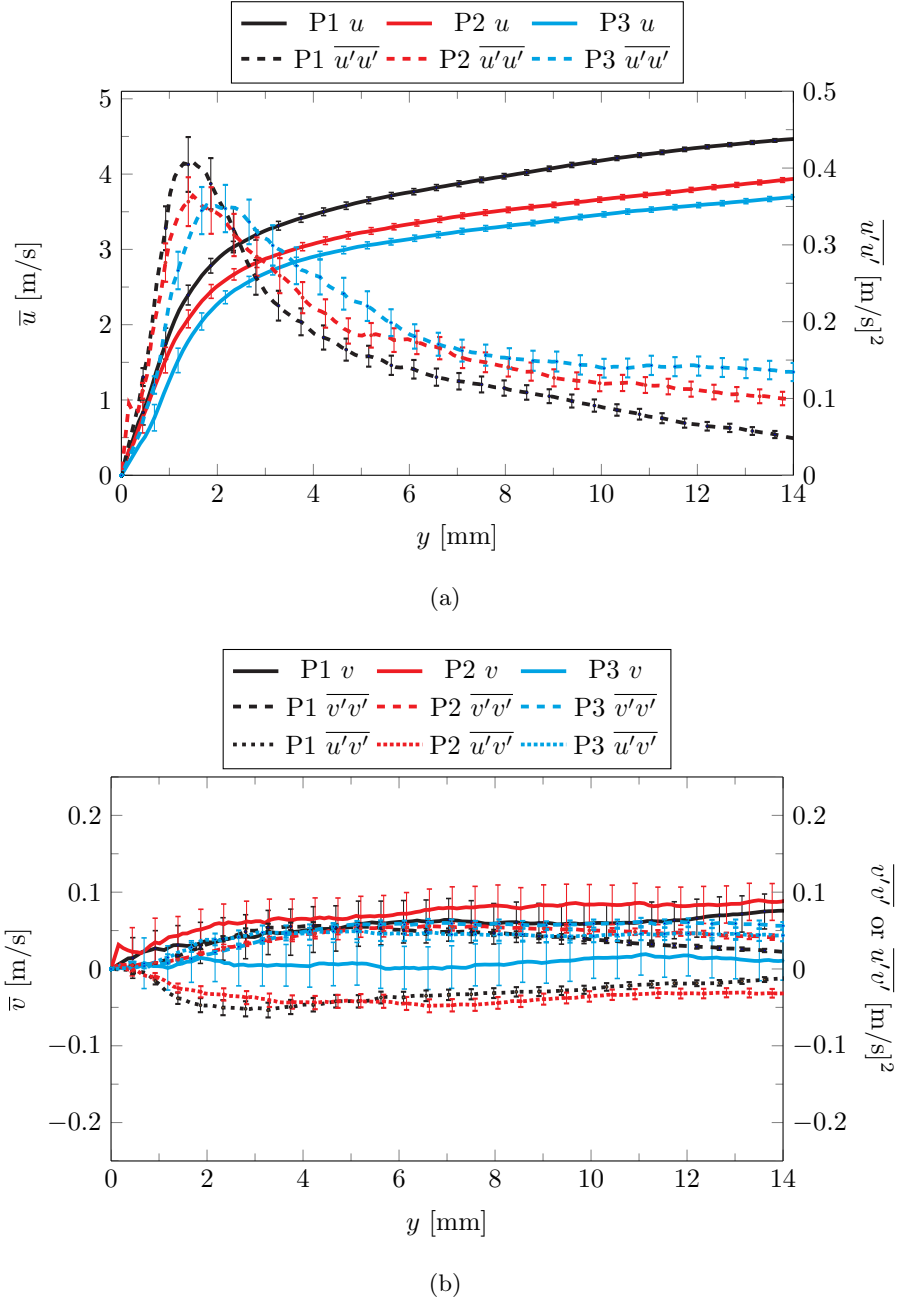


Fig. 5.10: The boundary layer velocity profiles for buoyancy opposed forced convection with isothermal heating. (a) shows the streamwise component of velocity and Reynolds normal stress. (b) shows the cross-stream component of velocity and two other measured components of the Reynolds Stress. Recall that P1 is $x = 5.87$ in., P2 is $x = 30.12$ in., and P3 is $x = 54.87$ in.

Fig. 5.10(b) and has a positive magnitude. This shows that the flow is away from the heated plate, opposite from the \bar{v} component in the buoyancy aided isothermal forced convection case. Again, the values are much smaller than the streamwise component of velocity, and the uncertainty is about the same magnitude as the measurement.

The boundary layer velocity flow field for this case is compared with CFD in Fig. 5.11. The TKE is also plotted for comparison between the simulation and the experiment. The streamwise mean velocity trends of the simulation and the experiment are similar, with the simulation at the second position being nearly within the experimental uncertainty. The TKE trends show a different behavior, with the experiment and simulations being very different at the first position. The second and third positions' simulation TKE is nearly within the experimental uncertainty for the entire profile.

The friction velocity at each heat flux sensor position for this case are tabulated in Table 5.5. A linear fit of the first three vectors is used to compute the velocity gradient term in the SRQ u_τ . This linear fit also has a corresponding uncertainty shown in the table. The method to compute the friction velocity uncertainty was described in Chapter 4.3.4. The Spalding fit is also used to find the friction velocity, as shown in the table. The von Kármán constant and intercept are shown for the two different Spalding fits, where one fit uses the classical values and the other fit includes the constants in the optimization. The CFD computation of the u_τ SRQ is also tabulated in Table 5.5.

Table 5.5: The von Kármán constant, intercept, shear velocity from the Spalding fit, and the shear velocity from a linear fit near the wall at the heat flux sensor positions for the buoyancy opposed isothermal forced convection case. The resultant u_τ from the CFD simulation is also tabulated. Note that $\kappa = 0.41$ and $B = 5.0$ are classical values not included in the fit.

Position	κ	B	u_τ Spalding	u_τ Linear	u_τ CFD
P1	0.41	5.00	0.244	0.184±0.016	0.269
P1	0.39	5.17	0.237		
P2	0.41	5.00	0.220	0.176±0.015	0.236
P2	0.448	4.40	0.240		
P3	0.41	5.00	0.210	0.137±0.017	0.233
P3	0.499	6.16	0.221		

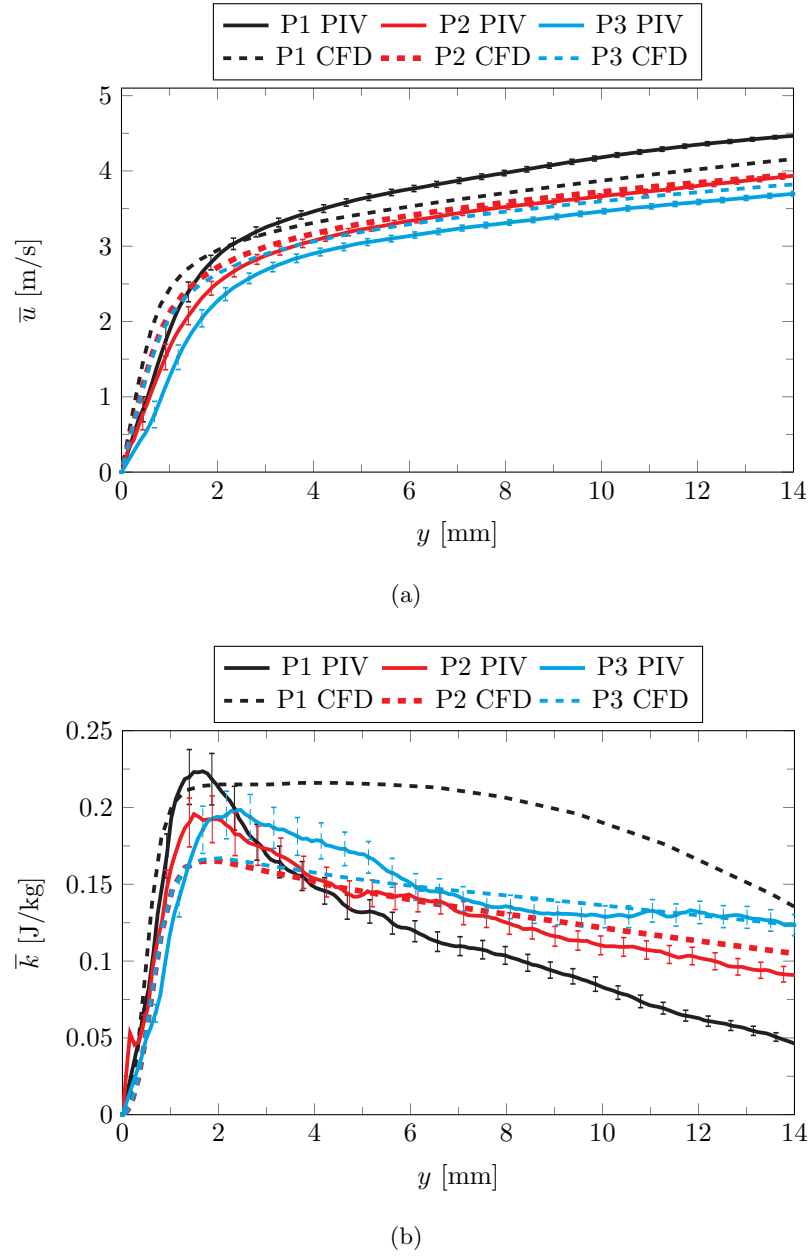


Fig. 5.11: The boundary layer velocity profiles for buoyancy opposed forced convection with isothermal heating compared with CFD results using the same boundary conditions. (a) shows the streamwise component of velocity. (b) shows the turbulence kinetic energy.

Table 5.5 shows that the friction velocity magnitude is smaller than the friction velocity for the buoyancy aided isothermal convection case, shown in Table 5.2. This is due to the smaller near wall velocity gradient in the buoyancy opposed case. This suggests that

buoyancy has a slight contribution to the boundary layer flow, even in forced convection. The difference in boundary layer development is also observed in Figs. 5.3 and 5.10. The linear method underpredicts the other methods for the computation of the shear velocity. This is likely because the data do not resolve the viscous sublayer as much as the buoyancy aided case. Only 3 to 4 velocity vectors could be considered within the viscous sublayer. As the data are so close to the transition layer, the linearity of the data must be questioned.

The heat flux SRQ is shown in Fig. 5.12. The measurements are compared with the Kays correlation from Eqn. 5.1 and the Incropera correlations from Eqn. 5.2. The similarity between this case and buoyancy aided isothermal case is obvious when comparing with Fig. 5.6. However, the simulation predicts a higher heat flux trend during the first 0.25 m. of the test section comparing Figs. 5.6 and 5.12.

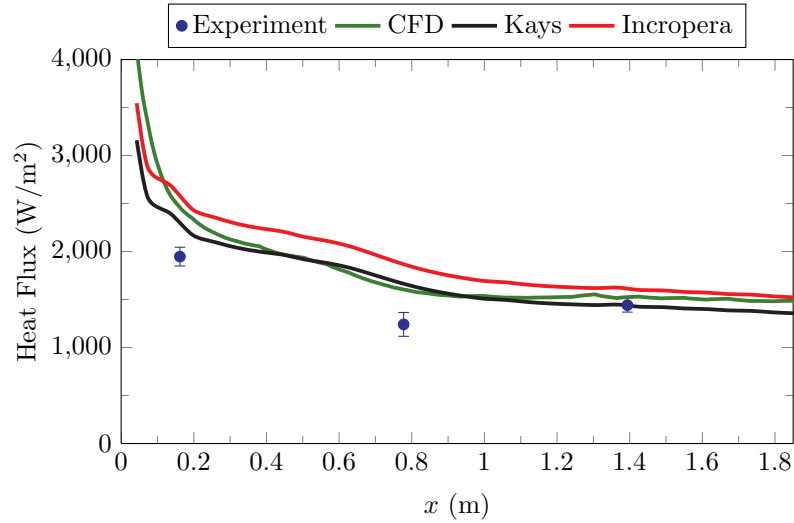


Fig. 5.12: The measured heat flux for the buoyancy opposed isothermal forced convection case is compared with the two correlations previously presented and the corresponding CFD simulation for this case.

The correlations and the CFD simulation are also closer together in the resultant heat flux SRQ than the buoyancy aided case. The difference between the correlations and the simulation is not as consistent through x as the buoyancy aided case. The simulation is further from the experimental measurements for this buoyancy opposed case.

The heat flux and several relevant boundary layer and dimensionless parameters are tabulated in Table 5.6. The convection ratio Gr_x/Re_x^2 shows that this case is in the forced convection regime at the three positions. The momentum thickness Reynolds number at all three positions is higher than the critical momentum thickness Reynolds number. This means that this case can be considered turbulent flow throughout, but it is noted that the flow is developing along the length of the plate. This is shown by (among other quantities) the momentum thickness Reynolds number increasing at each x position.

Table 5.6: The buoyancy opposed isothermal forced convection heat flux results along with the Grashof to Reynolds number ratio and the momentum thickness Reynolds number.

x Position (in)	Flux (W/m ²)	Re_x	Temp. (K)	Gr_x/Re_x^2	δ (mm)	δ_1 (mm)	δ_2 (mm)	Re_{δ_2}
P1 = 5.87	1947	41,400	360	0.02	7.1	3	1.8	466
P2 = 30.12	1241	199,000	386	0.12	25.1	5.9	2.8	713
P3 = 54.87	1442	357,000	391	0.22	40.0	7.3	3.2	813

5.2.4 Isothermal Buoyancy Opposed Mixed Convection

The velocity SRQ's for the buoyancy opposed isothermal mixed convection case are shown in Fig. 5.13. A comparison of these data with those shown in Fig. 5.7 reveals the significant difference in the boundary layers when the direction of gravity is the only change. This discussion is deferred to Section 5.3.1.

The velocity profiles presented in Fig. 5.13(a) show the streamwise component of the velocity at the three heat flux sensor positions. The flow is affected by gravity (as expected) and shows drastically different boundary layers at the first position when compared with the second and third positions. The free stream velocity can be seen at the first position, but not at P2 nor P3. The \bar{v} component of the velocity in Fig. 5.13(b) shows a positive (away from the plate) velocity, just as the buoyancy opposed forced convection case but unlike the buoyancy aided isothermal mixed convection case. The other two measured quantities of the Reynolds stress are small.

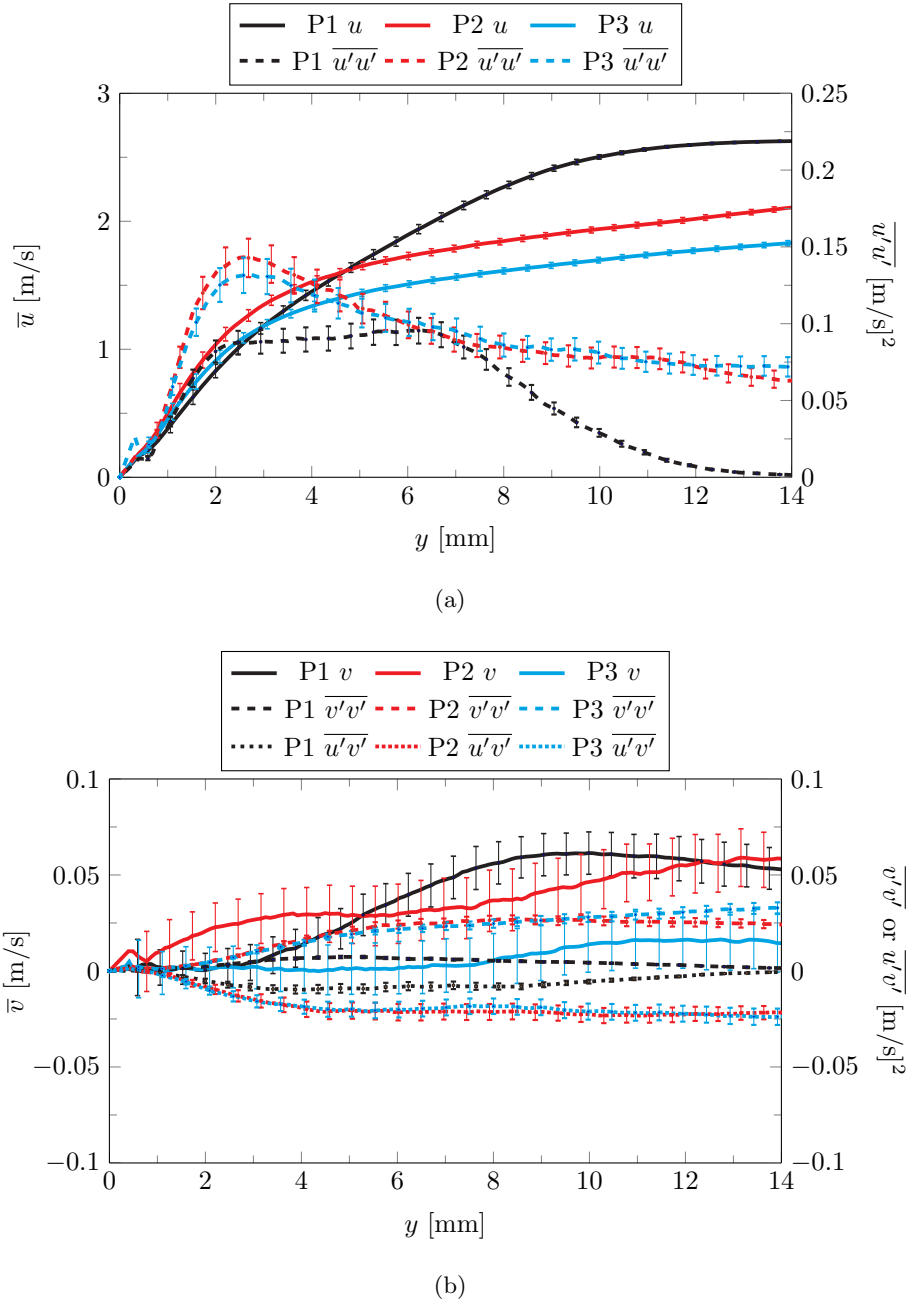


Fig. 5.13: The boundary layer velocity profiles for buoyancy opposed mixed convection with isothermal heating. (a) shows the streamwise component of velocity and Reynolds normal stress. (b) shows the cross-stream component of velocity and two other measured components of the Reynolds Stress.

Figure 5.14 shows the boundary layer velocity profiles and TKE compared with the corresponding CFD simulation for this case. The CFD simulation predicts the streamwise

component of velocity reasonably well near the free-stream. Near the wall and at the other two streamwise positions, the streamwise velocity is not as well predicted. The CFD simulation boundary layer velocity profiles are not contained within the measurement uncertainty. It is interesting that the CFD simulation for this case predicts the same viscous sublayer velocity profile for all three positions. The TKE presented in Fig. 5.14(b) shows that for the first position and near the wall, the CFD simulation under-predicts \bar{k} by nearly 50%. The simulation matches the experiment further away from the wall near the free-stream. The CFD simulation TKE is nearly within the experimental uncertainty for the other two positions.

The heat flux from the plate at the three heat flux sensor positions is plotted in Fig. 5.15. The CFD resultant heat flux and two correlations are also presented in Fig. 5.15. Comparing the heat flux presented in Fig. 5.9 and that in Fig. 5.15, we see that buoyancy effects on the heat flux, correlations, and CFD simulation are not negligible. It is interesting that the correlations are not consistently higher than the experiment for this case (as it was in the isothermal aided mixed convection case).

The heat flux, dimensionless numbers, and relevant boundary layer parameters are tabulated in Table 5.7. The convection ratio shows that most of the plate can be considered as mixed convection. The momentum thickness Reynolds numbers show that the flow is in the turbulent regime, and still developing.

Table 5.7: The buoyancy opposed isothermal mixed convection heat flux results along with the Grashof to Reynolds number ratio and the momentum thickness Reynolds number.

x Position (in)	Flux (W/m ²)	Re _{x}	Temp. (K)	Gr _{x} /Re _{x} ²	δ (mm)	δ_1 (mm)	δ_2 (mm)	Re _{δ_2}
P1 = 5.87	1180	23,700	366	0.08	7.14	4.2	1.7	248
P2 = 30.12	932	114,000	390	0.38	25.1	5.9	3.1	459
P3 = 54.87	1055	204,000	395	0.67	44.7	7.3	3.7	535

5.2.5 Constant Heat Flux Buoyancy Aided Forced Convection

The measured boundary layer velocities at the three heat flux sensor positions for the

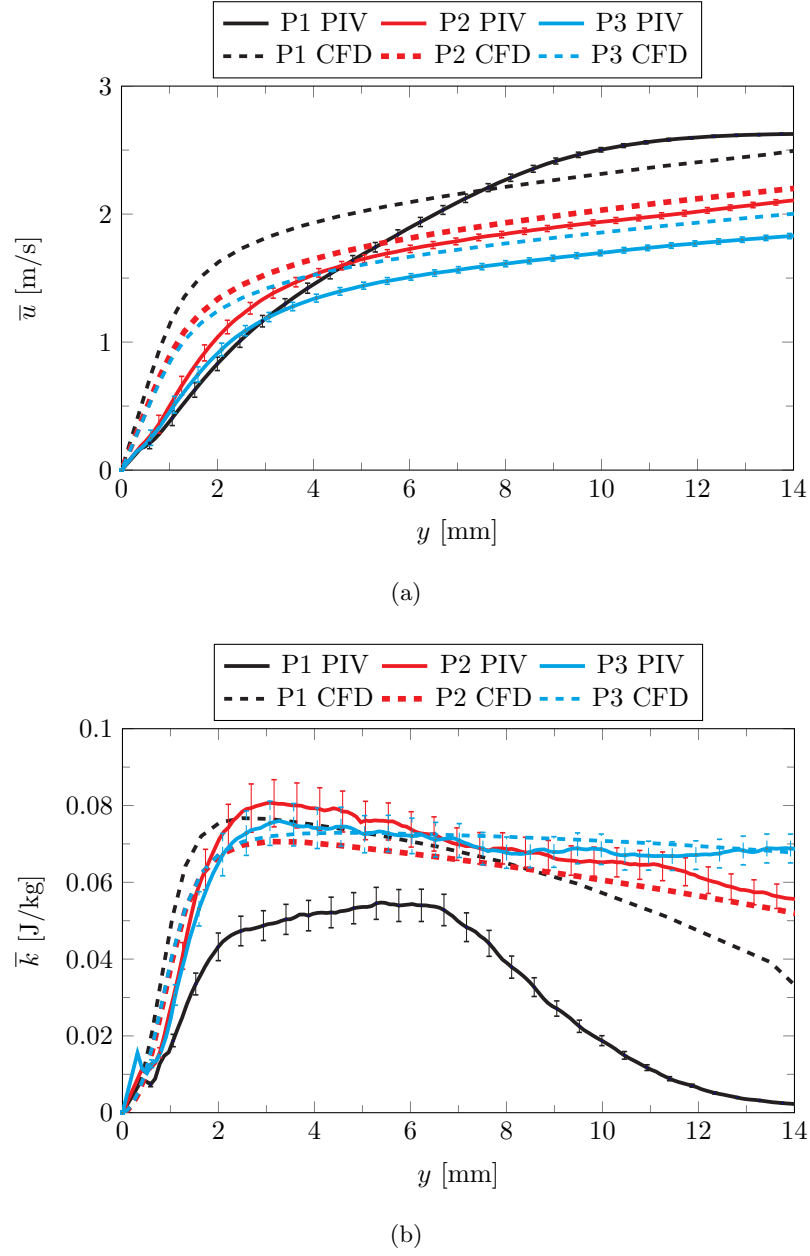


Fig. 5.14: The boundary layer velocity profiles for buoyancy opposed mixed convection with isothermal heating compared with CFD results using the same boundary conditions. (a) shows the streamwise component of velocity. (b) shows the turbulence kinetic energy profiles.

buoyancy aided constant heat flux forced convection case are shown in Fig. 5.16. These profiles are compared to those in the buoyancy aided isothermal forced convection case

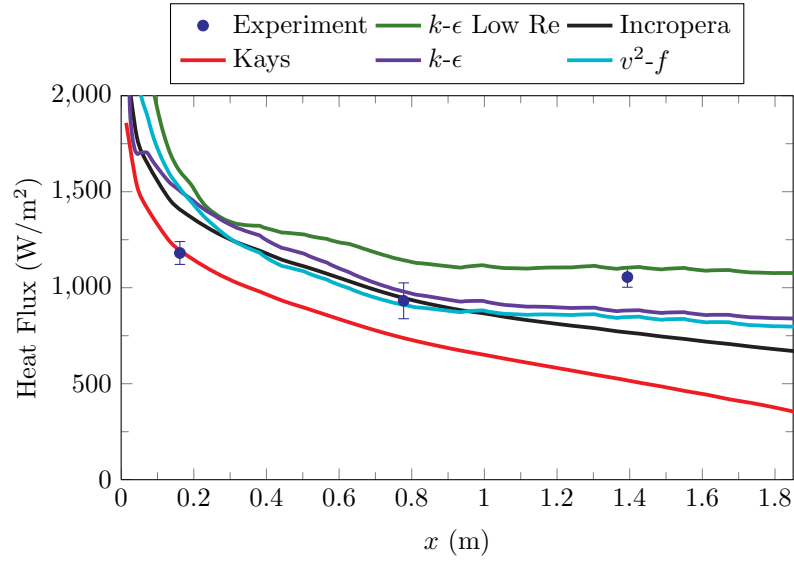


Fig. 5.15: The heat flux for the buoyancy opposed isothermal mixed convection case compared with several CFD models with the $k-\epsilon$ Low Re being the standard model for the mixed cases in this study.

shown in Fig. 5.3 and it is observed that the trends are practically the same. The change in plate temperature appears to have no influence on the profiles. A more thorough comparison is included in Fig. 5.28 and is discussed in detail in Section 5.3.1.

The streamwise boundary layer velocity profiles presented in Fig. 5.16 are plotted with the CFD results for the same boundary conditions in Fig. 5.17(a) and the TKE comparison is plotted in Fig. 5.17(b). The first position velocity and TKE are poorly predicted using this CFD model. The CFD simulation streamwise velocity boundary layer at the second and third positions are somewhat similar. The TKE near the wall is poorly predicted by the CFD at all positions. This is an example of using several SRQ's in the difficulty spectrum of Fig. 1.3. A model may predict a quantity (such as the streamwise velocity) reasonably well, but fails to predict another quantity (such as the turbulence kinetic energy and heat flux). Also, the TKE may be computed in the simulation accurately for the free-stream, but not near the wall.

The friction velocity SRQ for the buoyancy aided constant heat flux forced convection case is shown in Table 5.8. The shear velocity u_τ is comparable to the isothermal heating

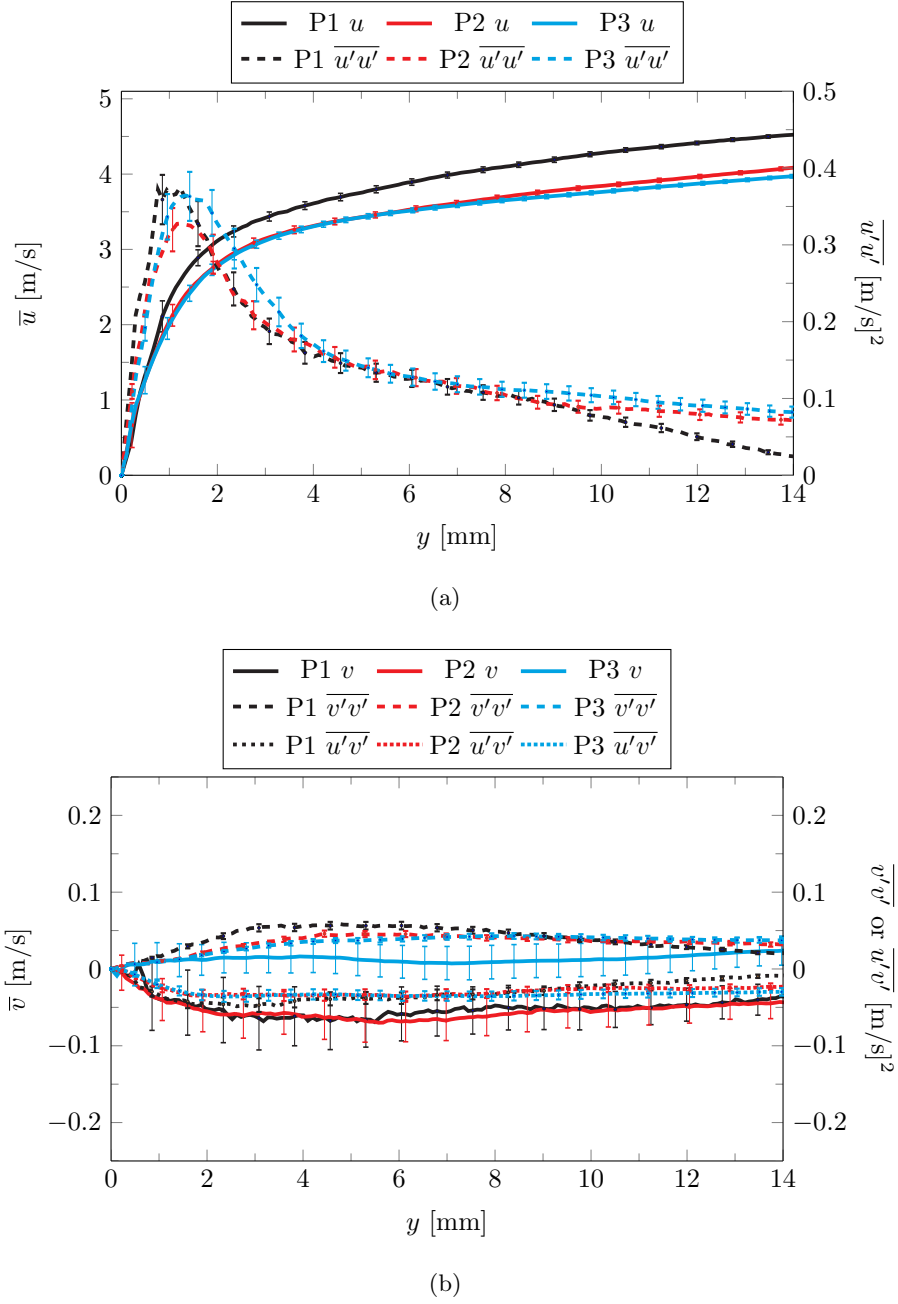


Fig. 5.16: The boundary layer velocity profiles for buoyancy aided forced convection with constant heat flux from the plate. (a) shows the streamwise component of velocity and Reynolds normal stress. (b) shows the cross-stream component of velocity and two other measured components of the Reynolds stress.

case for buoyancy aided forced convection, shown in Table 5.2. It is worth noting that the shear velocity resulting from the Spalding fit is much more consistent between these

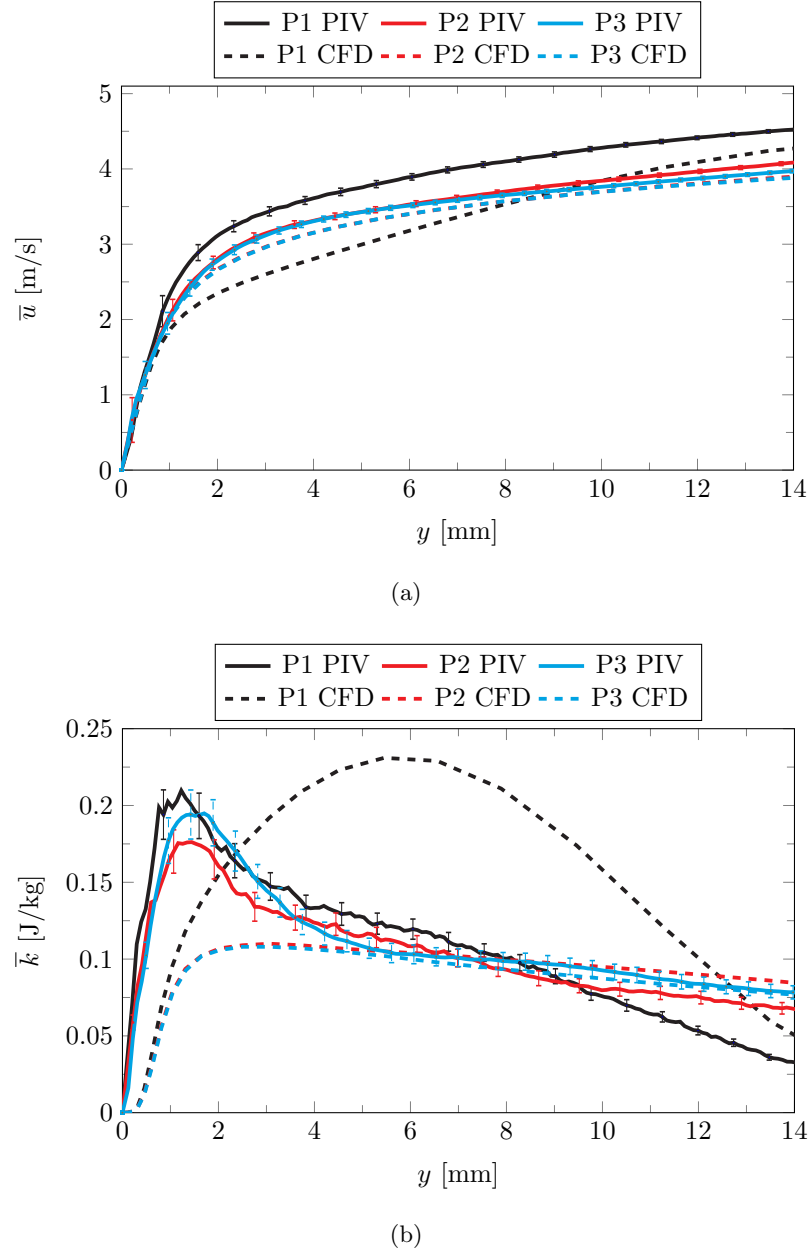


Fig. 5.17: The boundary layer velocity profiles for buoyancy aided forced convection with constant heat flux compared with CFD results using the same boundary conditions. (a) shows the streamwise component of velocity. (b) shows the turbulence kinetic energy profiles.

cases than u_τ resulting from the linear fit near the wall. Since the buoyancy aided forced convection cases have practically the same flow field (the plate temperature has little effect on the flow), the shear velocities should be nearly identical when comparing the isothermal

and constant flux cases.

Table 5.8: The von Kármán constant, intercept, shear velocity from the Spalding fit, and the shear velocity from a linear fit near the wall at the heat flux sensor positions for the buoyancy aided constant heat flux forced convection case.

Position	κ	B	u_τ Spalding	u_τ Linear	u_τ CFD
P1	0.41	5.00	0.249	0.220 ± 0.011	0.200
P1	0.39	4.50	0.251		
P2	0.41	5.00	0.228	0.227 ± 0.012	0.203
P2	0.46	5.79	0.234		
P3	0.41	5.00	0.223	0.233 ± 0.015	0.206
P3	0.41	7.37	0.207		

The wall coordinate velocity profiles using the optimized von Kármán constant and intercept are shown in Fig. 5.18. This case shows a slight acceleration at the third position. This suggests that buoyancy effects are not completely insignificant even at this Reynolds number. However, the fit at the second position and discussion in Section 5.3.1 suggests that the fit method is not reliable enough to presume that the trend shows an acceleration or deceleration of the flow.

The measured heat flux for the buoyancy aided constant heat flux forced convection case is shown in Fig. 5.19. This can be compared with Fig. 5.6 as the only difference between the two data sets is the plate temperature. The CFD resultant SRQ heat flux is also plotted with the experimental measurements, showing a drastic difference between the two. Again, the importance of using several SRQ's in the difficulty spectrum is emphasized. The computed boundary layer velocity might be within the validation error limits, but derivative or integral quantities could be far from within the allowable limits. The correlation for the Incropera trend is given in Eqn. 5.7, showing only a slight difference from the isothermal correlation given in Eqn. 5.2.

$$\text{Nu}_x = 0.0308 \text{Re}_x^{4/5} \text{Pr}^{1/3} \quad (5.7)$$

The measured heat flux is tabulated in Table 5.9, along with the local Reynolds number,

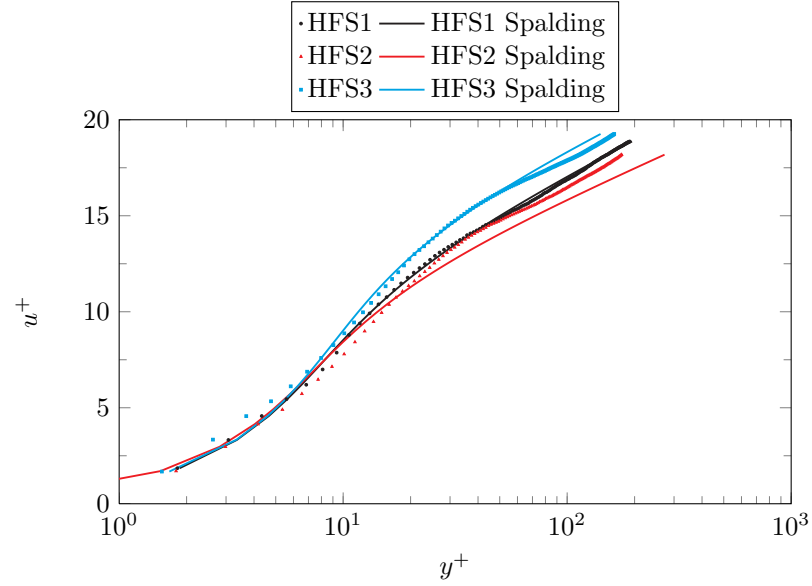


Fig. 5.18: The wall coordinate boundary layers for the three heat flux sensor positions for buoyancy aided constant flux forced convection flow and the Spalding fit profiles for comparison.

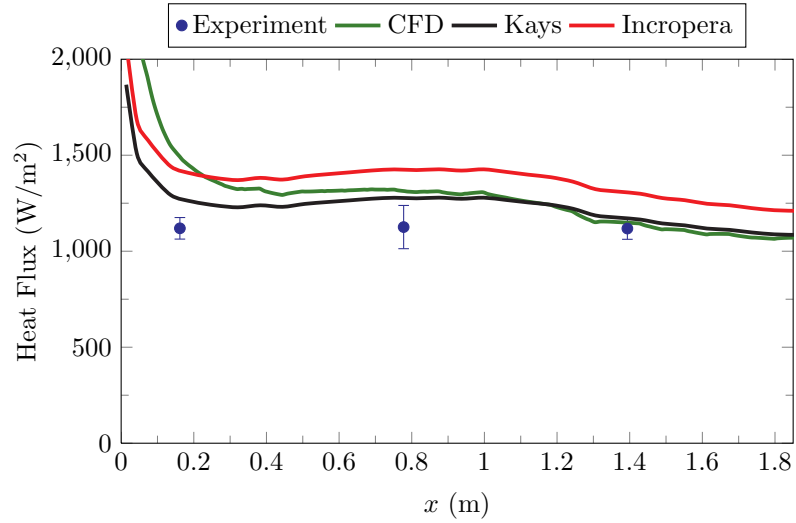


Fig. 5.19: The heat flux for the buoyancy aided constant heat flux forced convection case compared with the CFD results for the same boundary conditions.

surface temperature, the ratio of the Grashof number to the Reynolds number squared, and the momentum thickness Reynolds number. The ratio Gr_x/Re_x^2 in Table 5.9 shows that this

case is also in the forced convection regime, but that the buoyancy forces become somewhat significant at the third heat flux sensor position. Table 5.9 also shows that the flow is turbulent and developing along x .

Table 5.9: The buoyancy aided constant heat flux forced convection heat flux results along with the Grashof to Reynolds number ratio and the momentum thickness Reynolds number.

x Position (in)	Flux (W/m ²)	Re_x	Temp. (K)	Gr_x/Re_x^2	δ (mm)	δ_1 (mm)	δ_2 (mm)	Re_{δ_2}
P1 = 5.87	1119	40,200	404	0.015	7.18	2.3	1.4	357
P2 = 30.12	1126	193,000	413	0.104	25.2	3.6	2.3	574
P3 = 54.87	1118	346,000	410	0.193	40.2	3.6	2.3	582

5.2.6 Constant Heat Flux Buoyancy Aided Mixed Convection

The measured boundary layers at the three heat flux positions for the buoyancy aided constant flux mixed convection case are shown in Fig. 5.20. These profiles are compared to those in Fig. 5.7 in Section 5.3.1. The streamwise velocity profile at the first position clearly captures the free-stream velocity and near zero Reynolds normal stress. The second and third positions are nearly the same, but shows a slight relaminarization trend at the third position. The \bar{v} component of velocity is negative for this case (flow toward the plate), and the two other measured components of the Reynolds stress are nearly zero.

It is observed that the velocity profiles develop differently than the isothermal case. This is due to the different heating conditions. The isothermal case has a higher plate temperature than the constant flux case (see Fig. 5.1). This higher temperature in the isothermal case drives an elevated heat flux when compared to the constant flux case. The increased flux to the flow increases the buoyancy effects and changes the velocity profile and development. This fact also suggests that the constant flux case does not laminarize as much as the isothermal case.

The comparison with the simulations for the constant heat flux buoyancy aided mixed convection case is shown in Fig. 5.21, with the streamwise velocity profiles shown in Fig. 5.21(a) and the TKE shown in Fig. 5.21(b). The models employed fail to predict most aspects of

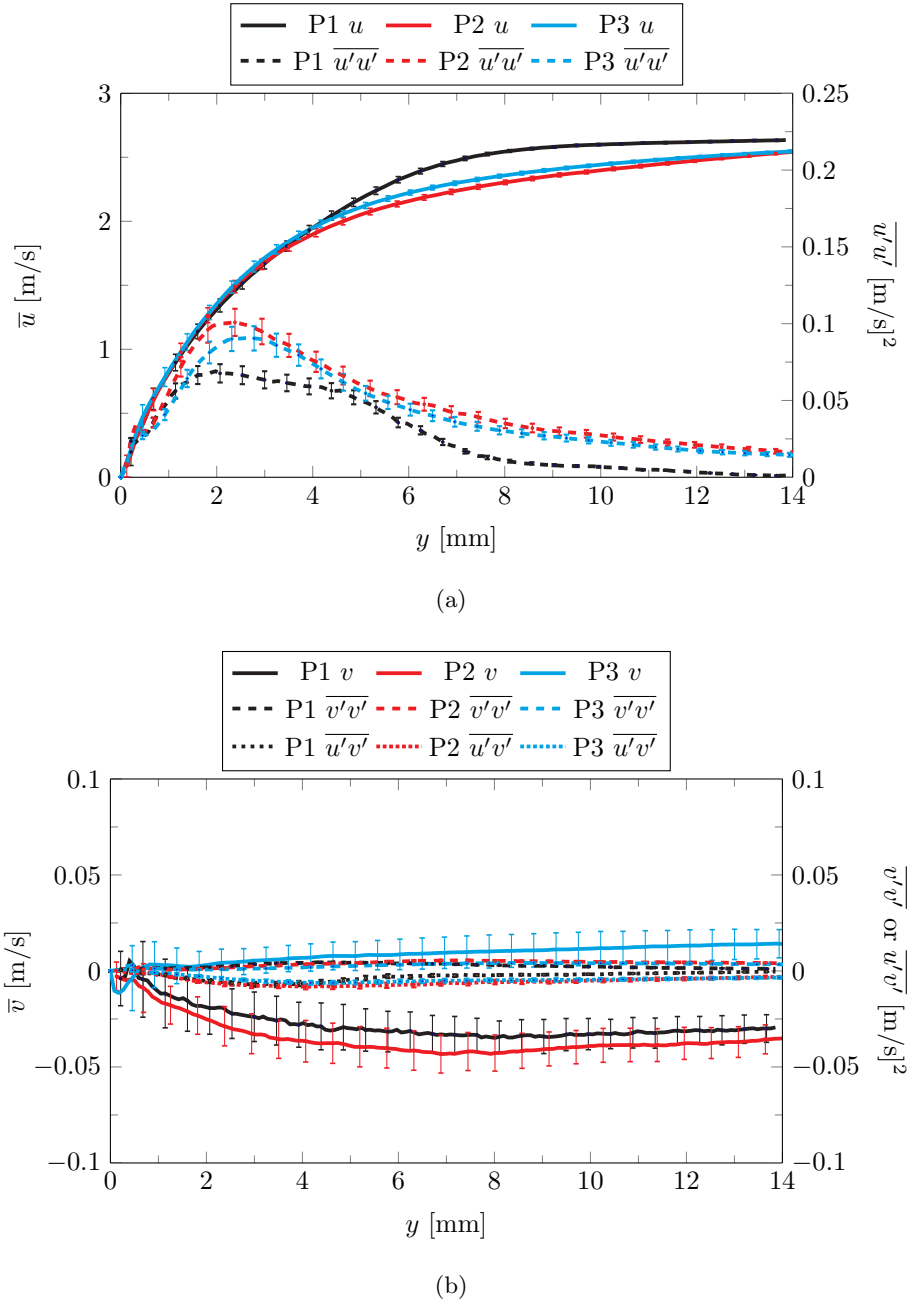
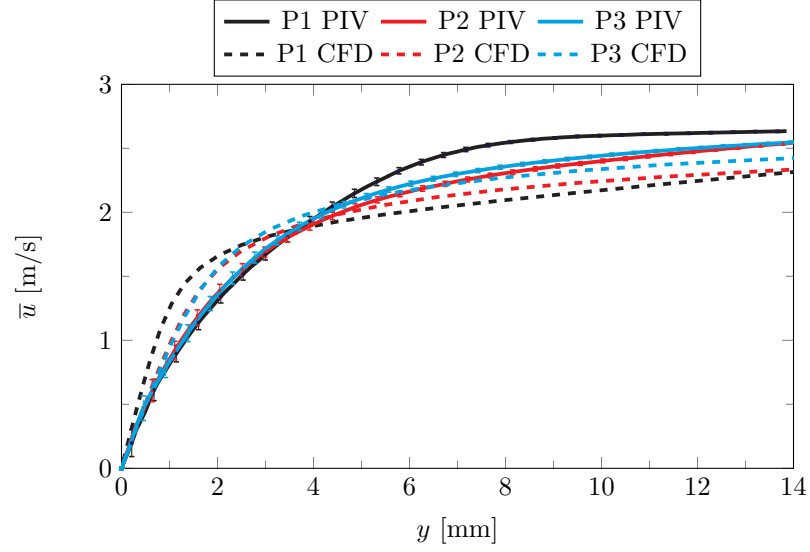


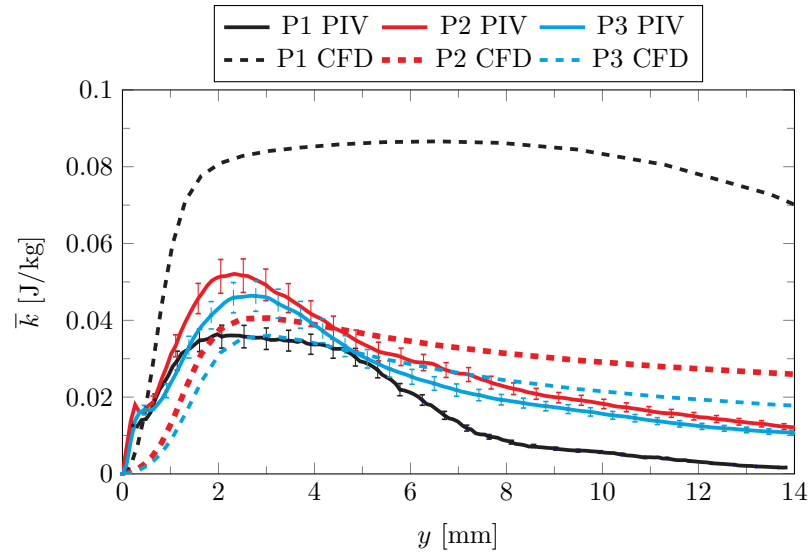
Fig. 5.20: The boundary layer velocity profiles for buoyancy aided mixed convection with constant flux heating. (a) shows the streamwise component of velocity and Reynolds Stress. (b) shows the cross-stream component of velocity and two other measured components of the Reynolds Stress.

this flow. The velocity profiles have significant differences and the TKE also has large error. The models are similar to those shown in Fig. 5.8 and have similar issues in predicting the

experimentally measured SRQ's. The first position CFD simulation is particularly different from the measured quantities.



(a)



(b)

Fig. 5.21: The boundary layer velocity profiles for buoyancy aided mixed convection with constant heat flux heating compared with CFD results using the same boundary conditions. (a) shows the streamwise component of velocity. (b) shows the turbulence kinetic energy.

The measured heat flux for the buoyancy aided constant heat flux mixed convection

case is shown in Fig. 5.22. This can be compared with the measured flux in of the isothermal buoyancy aided mixed case from Fig. 5.9, as the only difference between the measurements in the plate temperature. This temperature difference is shown in Fig. 5.1. The measured heat flux is also compared with the CFD computed SRQ of heat flux along the $z = 0$ centerline. The simulation trend is similar to the isothermal case, but the constant flux case has a steeper gradient. The experiment and the simulation are in near agreement at the third position.

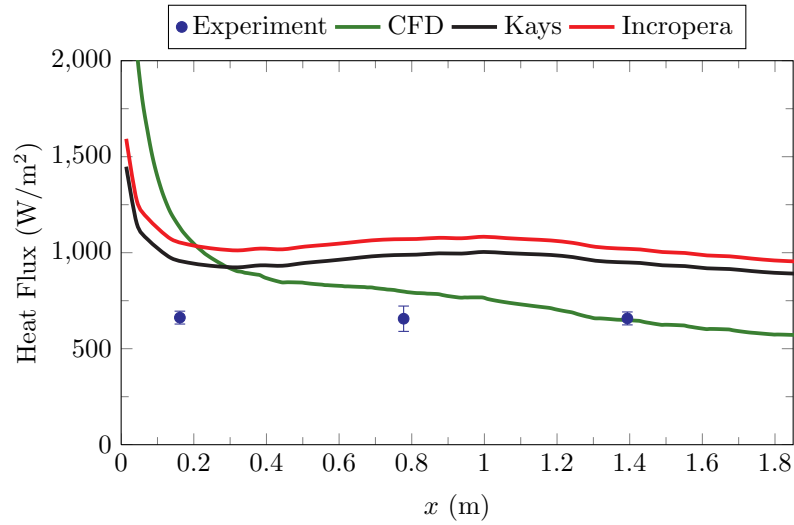


Fig. 5.22: The heat flux for the buoyancy aided constant heat flux mixed convection case.

The measured heat flux is tabulated in Table 5.10 along with the local Reynolds number, the convection ratio, the momentum thickness, and the momentum thickness Reynolds number. The ratio Gr_x/Re_x^2 shows that after the second heat flux sensor position, the flow is in the mixed convection regime. The leading section of the plate including the first heat flux sensor is considered to be in the forced convection regime. Table 5.10 also shows that the first position is near the critical momentum thickness Reynolds number, suggesting a transition near that point to turbulent flow. The third position momentum thickness Reynolds number is lower than the second position, suggesting a relaminarization of the flow.

Table 5.10: The buoyancy aided constant heat flux mixed convection heat flux results along with the Grashof to Reynolds number ratio and the momentum thickness Reynolds number.

x Position (in)	Flux (W/m ²)	Re_x	Temp. (K)	Gr_x/Re_x^2	δ (mm)	δ_1 (mm)	δ_2 (mm)	Re_{δ_2}
P1 = 5.87	662	23,600	407	0.049	8.0	2.4	1.2	181
P2 = 30.12	656	113,000	413	0.315	28.1	3.2	1.8	268
P3 = 54.87	658	203,000	410	0.560	44.8	3.1	1.6	233

5.3 Discussion of SRQ's

The system response quantities presented above are compared and discussed in more detail in this section. Several comparisons are made between the buoyancy aided and buoyancy opposed cases, and the isothermal and constant heat flux cases. Classical boundary layer theory is also presented and compared with some of the boundary layer velocity profiles previously presented.

5.3.1 Gravity and Temperature Effects

Figure 5.23 shows the boundary layer velocity profiles for the buoyancy aided and opposed isothermal forced convection. Figure 5.23 shows that not only is the flow at position 3 affected by gravity (as previously stated), but also at position 2. The difference between the aided and opposed cases at the second position is smaller than the difference between the cases at the third position, suggesting that the effects of gravity affect the development of the boundary layer in forced convection. The difference at the first position is the smallest, as shown in Fig. 5.23.

The relative difference for the isothermal forced convection is also shown in Fig. 5.23, with the difference being attributed to the effects of the change in the direction of gravity. The relative difference in this forced convection case due to a gravity change is denoted $\Delta\bar{u}_{F,G}$. The relative difference was computed by taking the difference between the buoyancy aided and opposed and dividing by the buoyancy opposed velocities.

The effects of gravity direction on measured heat flux for isothermal forced and mixed convection is presented with Fig. 5.24. The measured heat flux for the forced convection

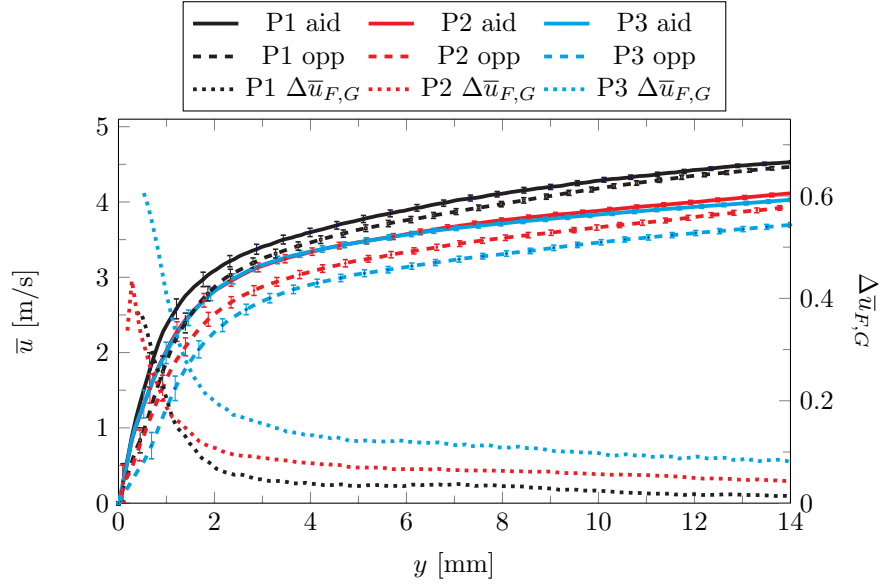


Fig. 5.23: The boundary layer velocity comparison for the isothermal forced convection buoyancy aided and opposed cases. The relative difference between the cases is also plotted as $\Delta \bar{u}_{F,G}$.

cases are similar. The buoyancy opposed forced convection case shows a slightly elevated heat flux compared to the buoyancy aided forced convection at the second and third positions. The heat flux at the first position for the forced convection is practically the same. The heat flux measured at the first position for the mixed cases is also nearly the same. The mixed convection buoyancy opposed case has much higher heat flux than the buoyancy aided case at the second two positions.

The convection ratio Gr_x/Re_x^2 for the isothermal cases is shown in Fig. 5.25. Both cases show that the convection ratio is not influenced by the change in gravity. This is not surprising because the free-stream air temperature and the wall temperature between all of the cases are the same. This makes the properties and other terms in the computation the same.

The effects of the direction of gravity on the momentum thickness is shown in Fig. 5.26. For both forced and mixed convection, the momentum thickness at the first position is not significantly affected by the direction of gravity. The buoyancy opposed cases show an

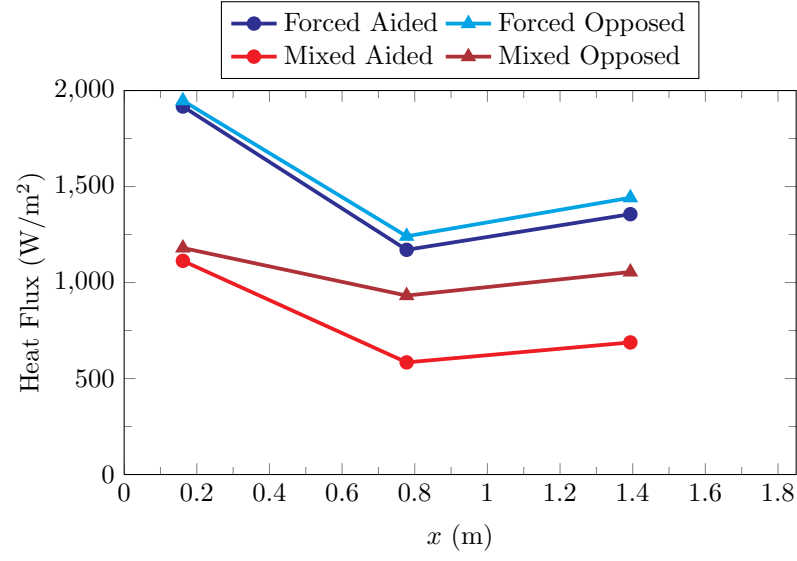


Fig. 5.24: The heat flux comparison for isothermal forced and mixed convection comparing the buoyancy aided and buoyancy opposed conditions.

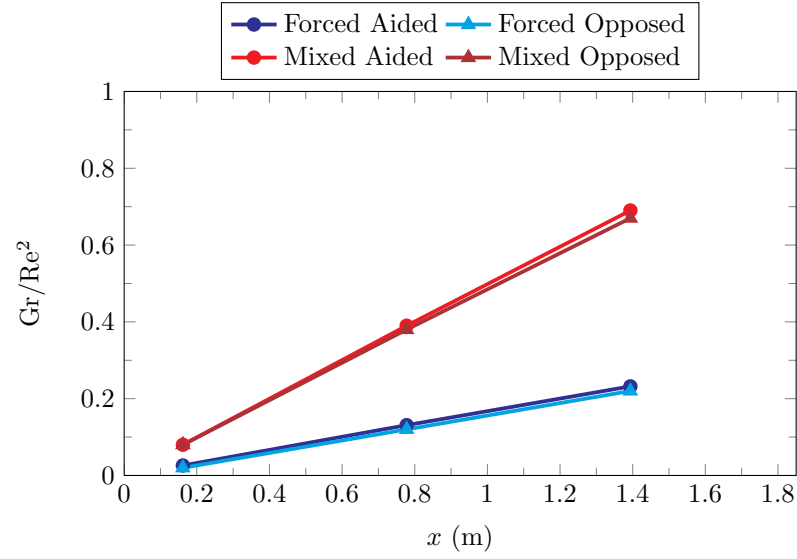


Fig. 5.25: The convection ratio comparison for isothermal forced and mixed convection comparing the buoyancy aided and buoyancy opposed conditions.

increase in the momentum thickness as a function of x . The buoyancy aided cases show a constant momentum thickness (forced) or a decrease in the momentum thickness (mixed) from the second to third positions.

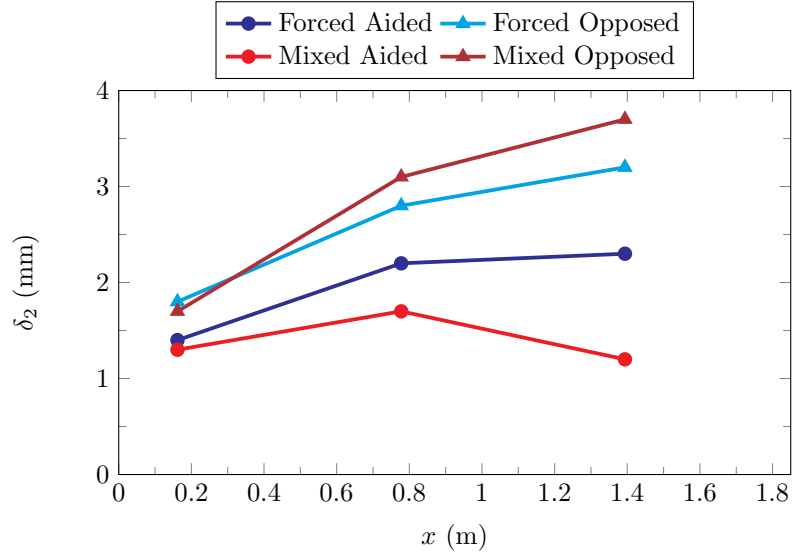


Fig. 5.26: The momentum thickness comparison for isothermal forced and mixed convection comparing the buoyancy aided and buoyancy opposed conditions.

Figure 5.27 shows the comparison of the boundary layer velocity profiles between the buoyancy aided and opposed isothermal mixed convection cases. As expected, the trends are significantly different. The aided case shows the laminarization (as discussed previously). The opposed case shows a developing boundary layer that appears to never fully develop. Even the first position boundary layers are different between the two cases. The mixed convection flow is influenced strongly by gravity. It is also interesting that the measured free stream at the first position for both cases is the same. This is shown by the near zero relative difference in Fig. 5.27.

The boundary layer velocities plotted in Figs. 5.3 and 5.16 are plotted for comparison in Fig. 5.28 to compare the effects of isothermal and constant flux heating for buoyancy aided forced convection. The slight change in heating conditions has little effect on the boundary layer velocity flow for buoyancy aided forced convection. The trends in Fig. 5.28 are nearly indistinguishable. This is shown by computing the relative difference between the data, plotted as $\Delta \bar{u}_{F,T}$. The magnitude of the difference is much smaller than that presented in Fig. 5.23. As previously stated, the forced convection flow is influenced by

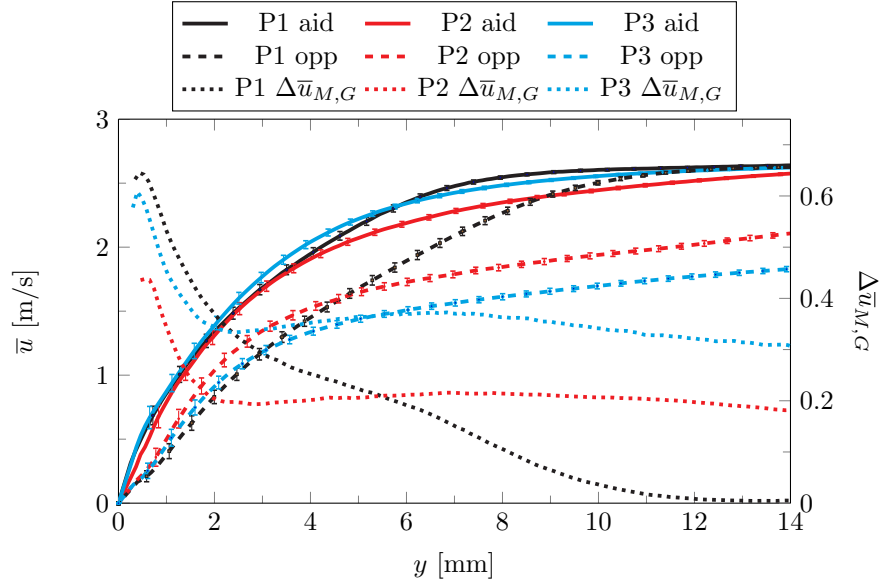


Fig. 5.27: The boundary layer velocity profile comparison for the isothermal mixed convection buoyancy aided and opposed cases. The relative difference due to gravity effects for isothermal mixed convection is denoted $\Delta \bar{u}_{M,G}$.

buoyancy, shown in Fig. 5.23. However, the change in buoyant forces due to the change in heating conditions does not significantly influence the boundary layer velocity profiles. The effects due to gravity changes are much more significant.

Figure 5.29 shows the boundary layer velocity for the buoyancy aided mixed convection cases comparing the constant heat flux and isothermal heating effects on the boundary layer velocity. The third position is influenced most heavily by the change in heating conditions. The first position is not influenced significantly. The second position shows some difference due to the different heating. As with the forced convection case mentioned above, the effects due to gravity changes are more significant than the changes resulting from the plate temperature. Although this is only for the plate temperatures outlined in Fig. 5.1.

The data presented in Figs. 5.23, 5.27, 5.28, and 5.29 show that the boundary layer velocities are more significantly effected by gravity than by the wall temperature, all other boundary conditions being practically the same. The mixed convection cases are more significantly effected by the change in buoyant forces than the forced convection cases (as

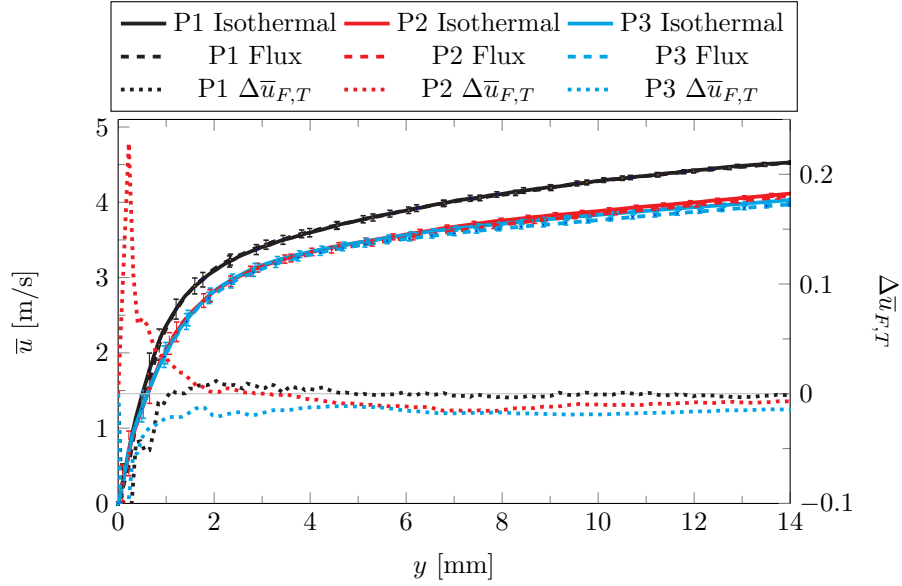


Fig. 5.28: The boundary layer velocity comparison for the forced convection buoyancy aided cases, comparing the isothermal and constant flux heating conditions. The relative difference between the cases is denoted $\Delta \bar{u}_{F,T}$.

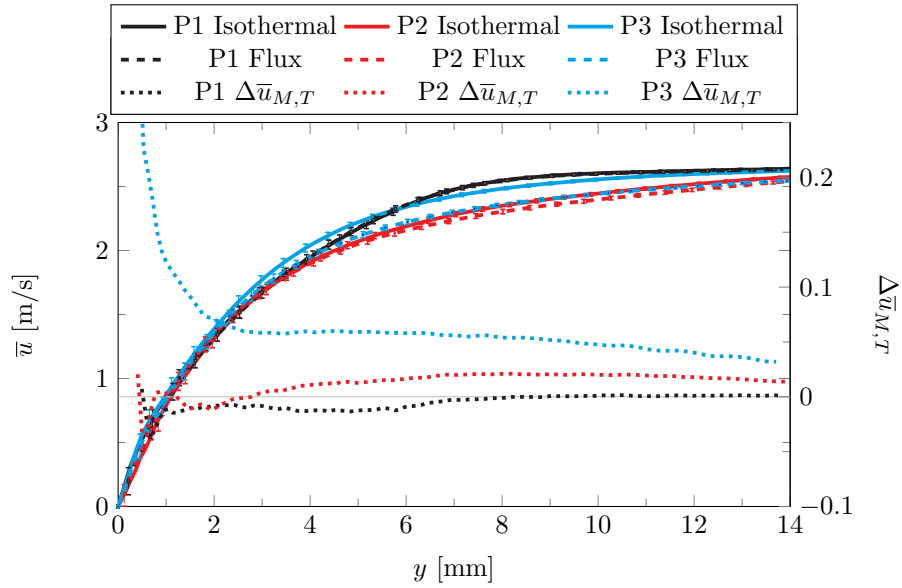


Fig. 5.29: The boundary layer velocity comparison for the mixed convection buoyancy aided cases comparing the isothermal and constant heat flux conditions. The relative difference between the cases is denoted $\Delta \bar{u}_{M,T}$.

expected). The forced convection cases do show some influence from buoyancy on the boundary layer velocity profiles.

5.3.2 Comparison of Classical Boundary Layer Shape Factors

The classic literature provides some insight into what one can expect in the measured boundary layer velocity. The shape factor H , which is the ratio of the displacement thickness and the momentum thickness, is plotted in Fig. 5.30. The displacement thickness δ_1 and the momentum thickness δ_2 were presented earlier. The shape factor is plotted as a function of a second shape factor, η , which is defined as [56]

$$\eta = 1 - \left(\frac{u(H)}{\bar{u}_\infty} \right)^2. \quad (5.8)$$

The $u(H)$ term in Eqn. 5.8 is the measured velocity at a distance H from the wall. The expected trend is for η as a function of H is [56]

$$\eta = 1 - \left[\frac{H - 1}{H(H + 1)} \right]^{H-1}. \quad (5.9)$$

It is noted that for $\eta > 0.46$ a pressure rise exists in the flow, which is also called an adverse pressure gradient [56]. From Fig. 5.30, we see that all of the buoyancy aided cases are in the adverse pressure range. The experimental measurements also match trends shown in the data presented by Schlichting and others (see Fig. 22.6 in [56]). The cases at the higher magnitudes of η are nearer the expected trend than those at lower values of η for the buoyancy aided cases. The text also states that separation occurs near $\eta \approx 0.8$. The data show no signs of separation, however.

To ensure that the flow in this wind tunnel can be considered valid for the shape factor analysis, an unheated case is desired. The unheated shape factor should fit the expected trend. Thus, an additional two data sets are now considered but are not part of the validation data presented. They include an unheated and heated flow at a Reynolds number (based on hydraulic diameter) of 13400. This flow is much slower than the cases

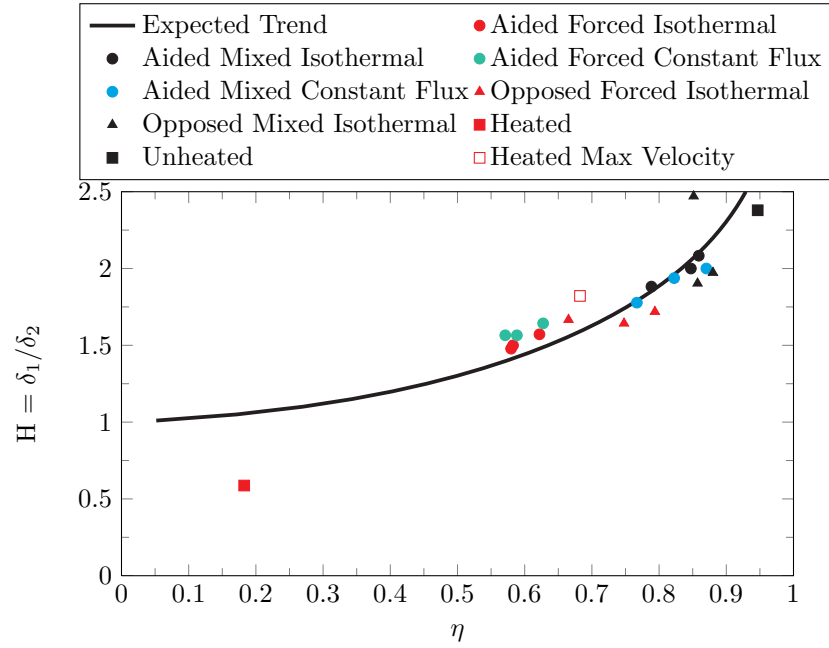


Fig. 5.30: A comparison of the classic shape factor with the expected trend as a function of the second shape factor η (see Eqn. 5.8).

considered previously, having a free stream velocity of 0.7 m/s. The buoyancy effects on the flow are significant for this flow rate. The velocity profiles for these additional cases are presented in Fig. 5.31. It is obvious that the heating accelerates the boundary layer when compared with the unheated case. In both cases, the Reynolds normal stress is small.

The corresponding shape factor correlation is included in Fig. 5.30 labeled as Heated, Unheated, and Heated Max Velocity. Notice that when the free stream velocity is used to compute η in the Heated case (filled in red square), the resultant point is far different from an expected trend. The free stream velocity is used in the literature and the other cases previously presented. However, if the maximum velocity is used (Heated Max Velocity, hollow red square), the point is closer to expected values. The unheated case is near the expected trend as well (filled in black square). This suggests that the boundary layers considered in this flow behave similarly to unheated boundary layers considered in the classical literature. Also, when discussing this shape factor trend, the maximum velocity should be used, particularly when significant accelerations are in the flow. The maximum

velocity is higher than the free stream velocity for the very slow flow case shown by Fig. 5.31.

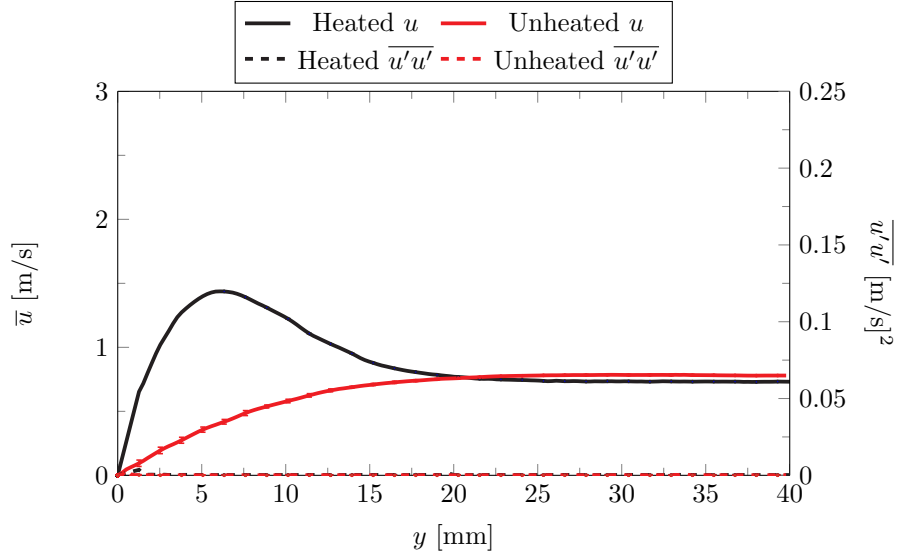


Fig. 5.31: The boundary layer velocity profiles for an unheated and heated low Reynolds number flow.

5.3.3 Buoyancy Influence on Heat Flux

Now we consider the buoyancy influence on heat flux from the plate. Wang *et al.* show data comparing the effects of buoyancy on heat transfer for buoyancy aided and opposed flow [4]. The Nusselt number is divided by a forced convection Nusselt number and plotted as a function of the special buoyancy parameter

$$Bo^* = \frac{Gr^*}{Re^{3.425} Pr^{0.8}}. \quad (5.10)$$

This is shown in Fig. 5.32 and is compared with the data presented in [4].

In this analysis, the Nusselt number Nu characteristic length is the hydraulic diameter of the test section (12 in.). The developing, variable property forced convection Nusselt number Nu_f is

$$Nu_f = C \times 0.0228 Re^{0.79} Pr^{0.4} \left(\frac{T_s}{T_\infty} \right)^{-0.34} \quad (5.11)$$

with

$$C = 1.0 + \left(\frac{x}{D_h}\right)^{-0.29} \exp\left(-0.07 \frac{x}{D_h}\right) \times \left[0.69 + \frac{5520}{Re} \left(\frac{x}{D_h}\right)^{-0.7}\right] \quad (5.12)$$

as described in [4].

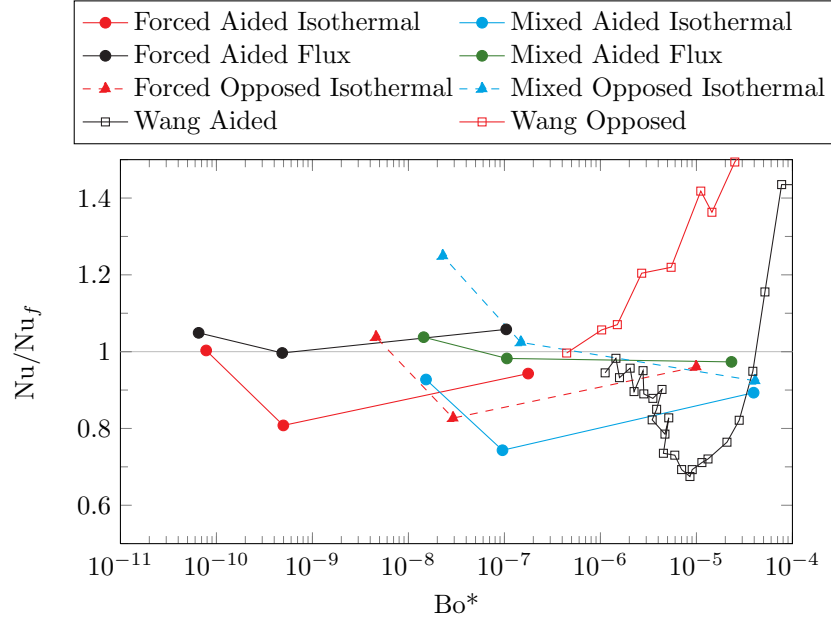


Fig. 5.32: A plot of the Nusselt number ratio versus the special buoyancy parameter for the data in this study and the data presented in [4].

It is shown in the Wang *et al.* data and study [4] that the buoyancy aided data experiences a suppression of heat transfer followed by a recovery of the heat flux for an increase in buoyancy effects. The data obtained in this study shows a similar trend. For example, the mixed buoyancy aided isothermal case shows a decrease in the Nusselt number ratio from position 1 to 2 and an increase again from 2 to 3 (right to left in Fig. 5.32). The forced aided isothermal trend shows a similar heat flux suppression, but with smaller magnitude than the mixed convection aided isothermal case. The constant heat flux cases show a flat trend, not giving any significant suppression of the heat flux due to buoyancy. The buoyancy opposed forced case shows an impairment of heat flux similar to the buoyancy aided case. However, the buoyancy opposed mixed case shows an improvement of heat flux

due to the effect of buoyancy.

5.3.4 Shear Velocity and Shear Profile

There is another method that can be used to compute the shear velocity from the data. The total shear stress is the sum of the Reynolds stress ($-\rho\overline{u'v'}$) and the viscous stress, $\tau(y) = -\rho\overline{u'v'} + \mu d\bar{u}/dy$ [57]. The total shear stress is linear in fully developed pipe and channel flow due to the absence of streamwise acceleration [57]. The intercept at $y = 0$ is the total shear stress at the wall, and is used to find the friction velocity tabulated in the previous sections. Those tables are repeated for discussion in this section.

Figure 5.33 shows the total shear stress for the buoyancy aided isothermal forced convection case. This case has negligible streamwise acceleration and the second and third positions appear to be fully developed. The trends closely match the linear fit, except nearest the wall. The shear stress is expected to be zero in the free stream. As is shown, the first position nearly reaches the free stream shear stress, but the second and third positions do not. The velocity profiles in Fig. 5.3 show that the free stream velocity is not measured except nearly at the first position. This is why the second and third positions shear stress do not go to zero within the bounds of the plot.

Figure 5.34 shows the total shear stress trends for the buoyancy aided isothermal mixed convection case. The flow is not fully developed and has significant acceleration effects from buoyant forces, causing disagreement with the theory that the shear stress profile should be linear. The first position trend is the most different from the linear fit. As the trends are all near zero at the furthest points from the wall ($y \approx 14$ mm), the free stream velocity is measured in these profiles. This is confirmed by reviewing Fig. 5.7. The non-linear nature of the shear stress profile suggests that this is a poor method for estimating the friction velocity in the mixed convection regime.

Figure 5.35 shows the total shear stress for the buoyancy aided constant flux forced convection case. This figure shows similar trends to the isothermal case in Fig. 5.33. As was previously discussed, the boundary layer velocity profiles are very similar, so the similarity in the shear stress is not unexpected. It is worth noting that the data near the wall (inwards

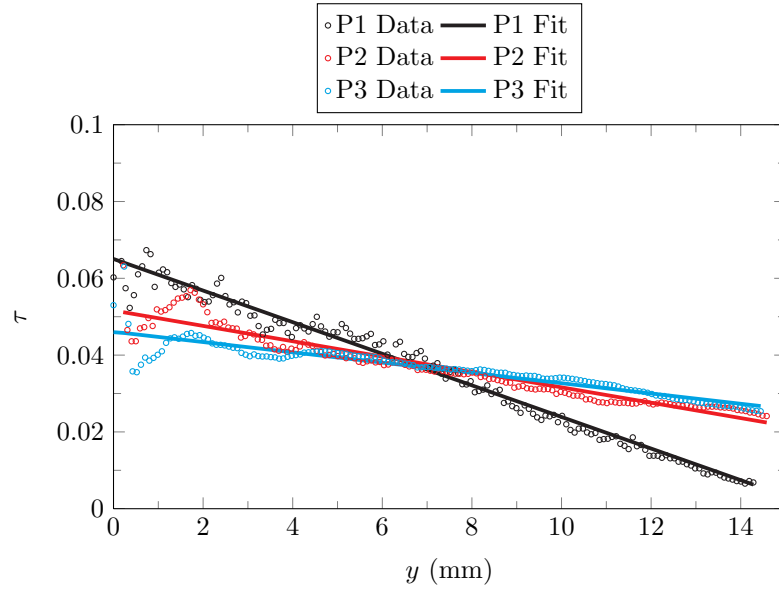


Fig. 5.33: The total shear stress profile with a linear fit for the buoyancy aided isothermal forced convection case.

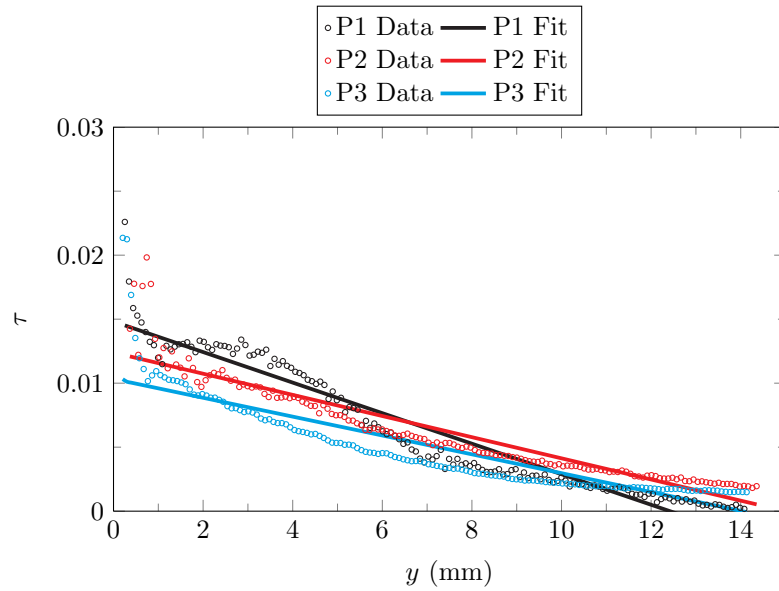


Fig. 5.34: The total shear stress profile with a linear fit for the buoyancy aided isothermal mixed convection case.

from 2 mm.) shows a slightly different trend than the isothermal forced convection case. Also, the data for position 2 and 3 do not cross in this case, as they do in the isothermal

case (Fig. 5.33).

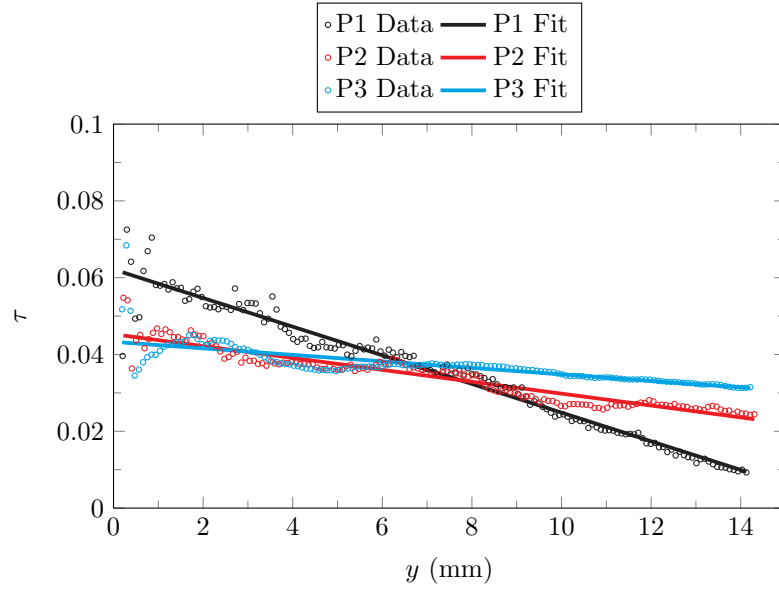


Fig. 5.35: The total shear stress profile with a linear fit for the buoyancy aided constant flux forced convection case.

The total shear stress for the buoyancy aided constant heat flux mixed convection case is shown in Fig. 5.36. The trends are not similar to the isothermal counterpart in Fig. 5.34. At each streamwise location, the constant heat flux case has similar wall shear stress, whereas the isothermal case does not. They both do exhibit a non-linear profile, particularly at the first position. Again, this is no surprise, as the linearity is only expected in fully developed turbulent flow, and the mixed cases are neither fully developed nor fully turbulent.

The shear stress at $y = 0$ is used to find the friction velocity. For the forced convection cases, the wall shear stress is used directly to compute u_τ . However, for the mixed convection cases, this value is not accurate since the trends are not linear.

Table 5.11 shows the previously presented friction velocities, with the addition of the friction velocity resulting from the total shear stress linear fit for the buoyancy aided isothermal forced convection case. With the exception of the first position, this method is near the other methods for predicting the friction velocity. The first position gives a high estimate

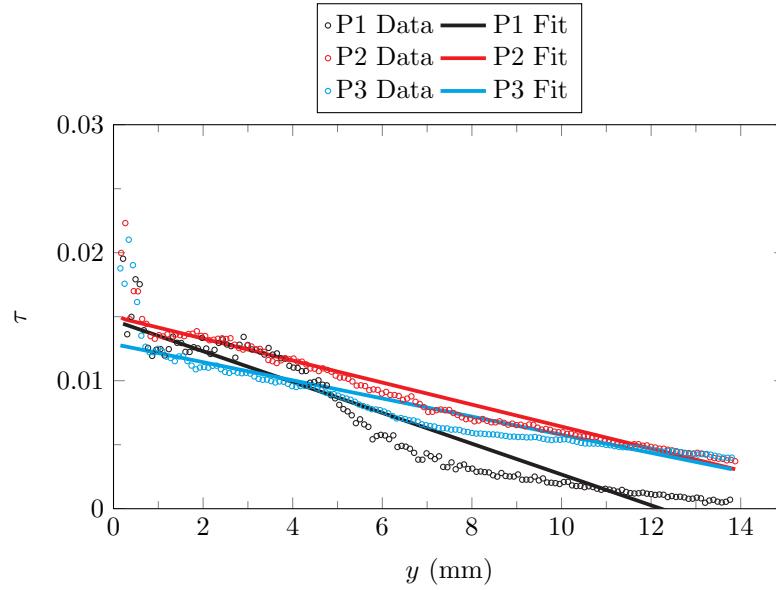


Fig. 5.36: The total shear stress profile with a linear fit for the buoyancy aided constant flux mixed convection case.

of the shear velocity using the total shear method. It is interesting that this method is most closely matched with the Spalding fit method using the classical parameters of κ and B .

Table 5.11: Shear velocity from the Spalding fit, and the shear velocity from a linear fit near the wall at the heat flux sensor positions for the buoyancy aided isothermal forced convection case. The computed friction velocity from the CFD simulation is also tabulated, along with the friction velocity from the total shear velocity. The two Spalding fit shear velocities correspond to the two cases with different fit parameters described previously (see Table 5.2).

Position	u_τ Spalding	u_τ Linear	u_τ CFD	u_τ Total Shear
P1	0.248	0.233 ± 0.004	0.215	0.252
P1	0.228			
P2	0.233	0.216 ± 0.004	0.231	0.225
P2	0.223			
P3	0.235	0.216 ± 0.004	0.233	0.220
P3	0.219			

The shear velocity is again tabulated in Table 5.12 for the buoyancy aided constant heat flux forced convection case with the addition of u_τ from the total linear shear stress

method. The linear shear stress method provides a similar shear velocity to the other methods for this case, but slightly under-predicts the value compared to the other methods for the second and third positions. The total shear method over-predicts the friction velocity at the first position compared to the three point linear fit and the CFD, but under-predicts when compared to the Spalding fit at the first position.

Table 5.12: Shear velocity from the Spalding fit, and the shear velocity from a linear fit near the wall at the heat flux sensor positions for the buoyancy aided constant heat flux forced convection case. The two Spalding fit shear velocities correspond to the two cases with different fit parameters described previously (see Table 5.8).

Position	u_τ Spalding	u_τ Linear	u_τ CFD	u_τ Total Shear
P1	0.249	0.220 \pm 0.011	0.200	0.247
P1	0.251			
P2	0.228	0.227 \pm 0.012	0.203	0.211
P2	0.234			
P3	0.223	0.233 \pm 0.015	0.206	0.217
P3	0.198			

The two components that make up the total shear inspire another question; can the components of the total shear be used for validation? The two components that are summed to compute the total shear stress previously presented are $\mu du/dy$ and $\rho \overline{u'v'}$. These components are plotted for the three positions of the buoyancy aided isothermal forced convection case and compared with the CFD computation of the same. One assumption necessary for the CFD components is that $-\overline{u'v'} = \epsilon_M \delta \bar{u} / \delta y$. The eddy diffusivity is ϵ_M and \bar{u} is the measured average streamwise velocity. The models used for the forced convection case compute a turbulence viscosity μ_t that is related to the eddy diffusivity by $\mu_t = \rho \epsilon_M$ [18].

Figure 5.37 shows the shear stress components for the buoyancy aided forced isothermal case at the first position comparing the CFD computation to the experiment. As is shown, the CFD under-predicts the Reynolds stress compared to the experiment. Also, the CFD trend for the Reynolds stress is non-linear. The assumptions that make for a linear total shear stress are not valid for this case, as the flow is not fully developed. However, the experimental data show that the total shear stress is linear, but the CFD prediction is not

linear.

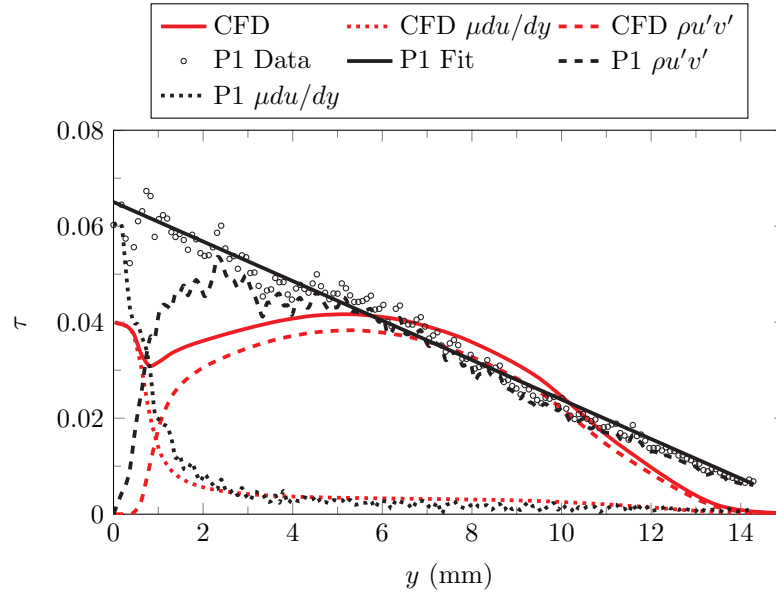


Fig. 5.37: The total shear stress profile with a linear fit for the buoyancy aided isothermal forced convection case at the first position. The $y^+ = 10$ value is at $y = 0.73$ mm.

Figure 5.38 shows the shear stress components for the second position in the buoyancy aided forced isothermal case, comparing the CFD and experiment. The total shear stress at this position is linear, but the simulation still under-predicts the experiment Reynolds stress. The viscous stress is similar when comparing the CFD and the experiment, giving further credence to the limitations of the model to predict the Reynolds shear stress. The difference between the CFD simulation and the experiment in the viscous shear stress and the Reynolds shear stress within the viscous sublayer is significant.

Figure 5.39 shows the the shear stress components for the third position in the forced isothermal case, comparing the CFD and experiment. The total shear stress at this position is linear, but the simulation still under-predicts the experiment Reynolds stress. It is interesting that the near wall trends at the second and third positions are very similar (both experimentally and in the simulation). The viscous shear stress in the viscous sublayer does not follow the trend predicted in the experiment, as was the case at the second position.

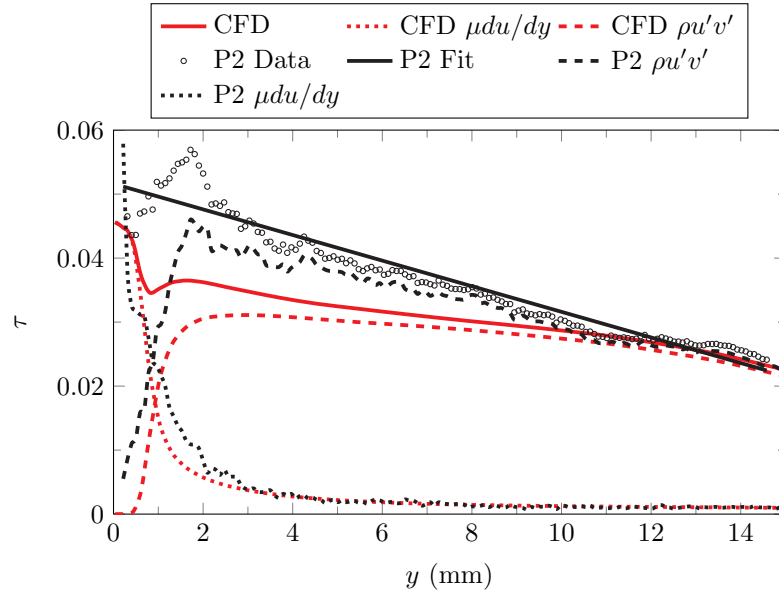


Fig. 5.38: The total shear stress profile with a linear fit for the buoyancy aided isothermal forced convection case at the second position. The $y_+ = 10$ value is at $y = 0.87$ mm.

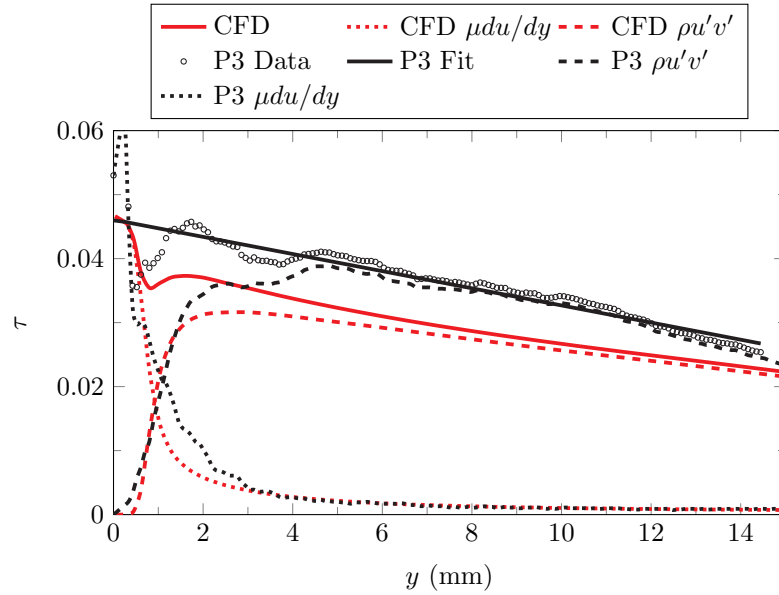


Fig. 5.39: The total shear stress profile with a linear fit for the buoyancy aided isothermal forced convection case at the third position. The $y_+ = 10$ value is at $y = 1.13$ mm.

5.4 Uncertainty and Repeatability

To quantify the uncertainty of the measurements, several methods are used. The PIV position uncertainty is found using three different methods to compute the wall position. The position of the wall is the primary source of uncertainty for the position, since all spatial dimensions in the PIV data are derived from the wall location. For a discussion of this component of uncertainty, refer to Chapter 4.3.4. The PIV data uncertainty is quantified as outlined in the literature mentioned earlier.

The repeatability of the velocity measurement is considered as suggested by Oberkamp and Trucano [6]. Figure 5.40 shows the boundary layer velocity for several repeats of the buoyancy aided forced isothermal data at each position. The velocity profile for the boundary layer over the first heat flux sensor (P1 r1-r3) is repeatable. The profiles over the second and third heat flux sensors are repeatable as well. These cases were recorded several months apart, with a disassemble and remount of the PIV equipment between r2 and r3 cases. The free stream velocity \bar{u}_∞ for these cases is 4.487 m/s.

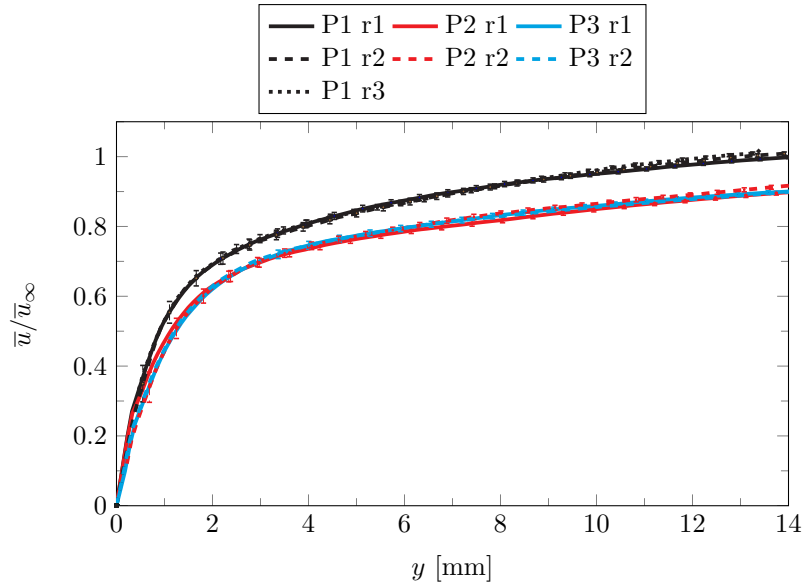


Fig. 5.40: The boundary layer streamwise velocity profiles for the flow over the three positions for three repeats of the isothermal forced aided flow measurement.

Figure 5.41 shows these profiles as a difference from the mean of the data, also called

the velocity residual $\Delta\bar{u}$. We note that between replications, the camera was removed, replaced, and recalibrated. The mean of the profiles at the first position is used to compute the residual at the first position, and similarly for the other two positions. It is shown that 3 repeats of the boundary layer velocity over the first heat flux sensor have an average residual level of 0.05 m/s with larger values near the wall. The PIV data near the wall has larger uncertainty. The large residual here could also result from an error in the y position in the presence of the large velocity gradient. The fact that the P2 and P3 trends are equal and opposite in Fig. 5.41 is because there are only two data points to compute the average. This suggests that the repeatability of the boundary layer velocity measurement is approximately 0.05 m/s, with the error as high as 0.18 m/s.

The Reynolds normal stress residual $\Delta\overline{u'u'}$ is similarly plotted in Fig. 5.42. The peak Reynolds normal stress residual is 0.04 (m/s)^2 . The average Reynolds normal stress residual magnitude is 0.015 (m/s)^2 . This suggests that the Reynolds normal stress is repeatable to within 0.04 (m/s)^2 with an average repeatability of 0.015 (m/s)^2 .

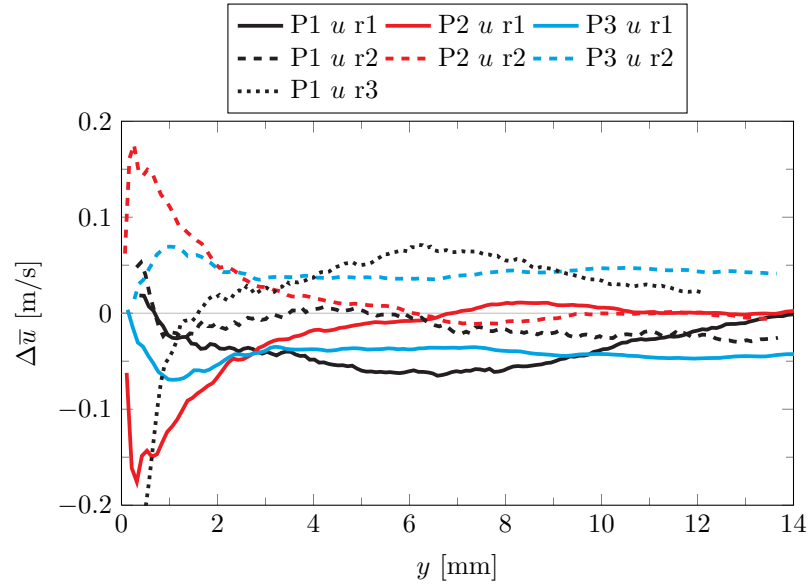


Fig. 5.41: The boundary layer streamwise velocity residuals for the flow over the three positions for three repeats of the isothermal forced aided flow measurement.

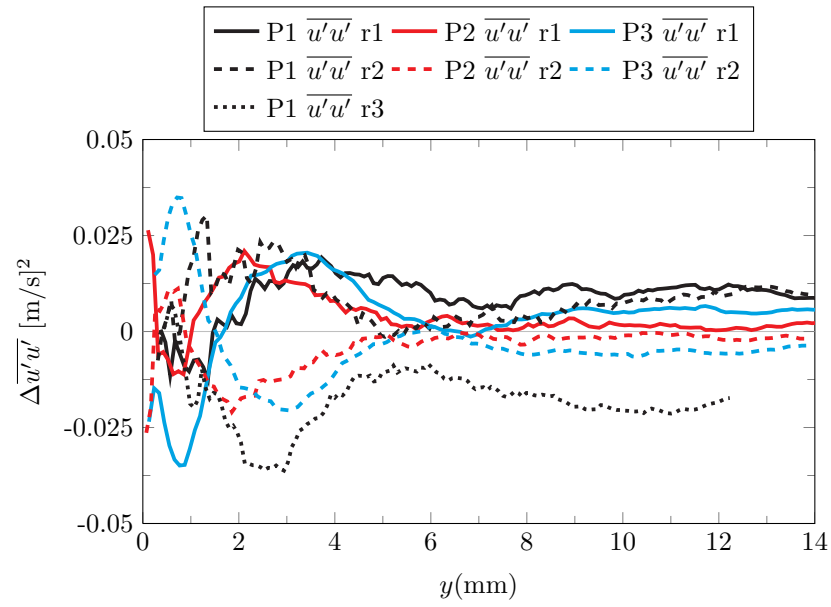


Fig. 5.42: The boundary layer streamwise velocity Reynolds normal stress residuals for the flow over the three positions for three repeats of the isothermal forced aided flow measurement.

Chapter 6

Conclusions

Validation of CFD simulations is an important aspect of pre-production analysis for many complicated systems, including nuclear reactors. The design of a validation experiment is presented. This design allows for simultaneous measurement of the boundary conditions and system response quantities. The boundary conditions measured include: the wall temperatures, flow inlet temperature, inlet velocity with statistical quantities sufficient to quantify turbulence model parameters, and atmospheric conditions. These measured boundary conditions were designed with a goal of Level 2 Completeness in the Validation Experiment Data Completion table [11].

The boundary condition treatment is outlined, with uncertainty quantification. It is not prudent to present the boundary conditions in a report such as this, so a website was created to disseminate the boundary conditions and system response quantities. This website also contains the details necessary for an external party to conduct validation studies of their own. They simply gather the necessary details from the pages describing the experimental apparatus, material properties, boundary conditions, and system responses. They can use the boundary conditions to compute their own simulations. Then they can compare their simulation system responses to those on the website (which are the ones presented in this work). A validation study is mostly useless unless the data are made available for model developers around the world to use.

The repeatability of the measurements are discussed in Chapter 5.4, where it is shown that the boundary layer measurements are repeatable. To properly quantify that repeatability, the velocity residuals were also presented. The worst case error of repeatability is shown to be 0.2 m/s, with an average repeatability error of 0.05 m/s. The repeatability error could be combined with the velocity uncertainty to provide a more accurate estimate

of the total velocity uncertainty.

Another aspect of the uncertainty of the velocity measurements is the position uncertainty. As there are several methods that can be employed to find the wall position, only a few of these methods were used to estimate the wall position and uncertainty, and therefore the overall velocity position uncertainty. It was found that the position uncertainty can be as high as 0.2 mm, with an average of our cases below 0.1 mm, depending on the method used to find the wall position.

The system responses presented also provide much insight into the behavior of convective boundary layer flow. Forced convection flow is usually considered to have no influence from buoyant forces. However, the unique capability of this experimental apparatus to change gravity without changing other boundary conditions shows that this is not always true. Even when the Gr_x/Re_x^2 ratio is in the forced convection regime, the effects of buoyancy are still present. This is even more prevalent in the mixed convection case, but this was expected. The isothermal heating and constant flux heating did not effect the boundary layer profiles as much as the effect of buoyancy from gravity changes. The heat flux SRQ was changed significantly with the change in heating conditions, however.

The mixed convection buoyancy aided case shows a laminarizing flow. The flow inlet starts with a laminar-like profile, and develops into a more turbulent profile before returning to the laminar-like flow. The heat flux trend also provides some insight into this phenomenon, where the flux at the second position is lower than expected. The impairment of the heat flux is further quantified by using a Nusselt number ratio and a special buoyancy parameter. It is shown that buoyancy tends to suppress the heat flux and then improve it, depending on the flow rate and orientation. It is noted that the Gr/Re^2 ration is nearly identical for the forced convection buoyancy aided and opposed cases, as well as for the mixed buoyancy aided and opposed cases. The momentum thickness is also compared as a function of the direction of gravity. The laminarizing flow shows a decrease in the momentum thickness during the onset of laminarization.

The classical boundary layer shape functions were also presented. It was found that

even this convective flow behaves as an unheated boundary layer, so long as similar pressure gradients are in effect. It was also found that when the flow rate is very slow (buoyancy effects are large), the shape factors agree with expected trends so long as the maximum velocity is used instead of the free stream velocity.

Several simulations were conducted using models that were expected to be reasonably accurate for these flow conditions. The simulations are presented simply to show that the measured boundary conditions are sufficient to define the boundary conditions in the models presented. The simulation response quantities show that the models may predict the flow reasonably well, but Reynolds stress or heat flux may not be as well predicted.

References

- [1] Idaho National Laboratory, *Module 05a Prismatic HTGR Core Design Description*, https://inlportal.inl.gov/portal/server.pt/community/ngnp_public_documents.
- [2] Oberkampf, W. L., Sindir, M., and Conlisk, A., “Guide for the verification and validation of computational fluid dynamics simulations,” *Am. Institute of Aeronautics and Astronautics*, 1998.
- [3] Oberkampf, W. L. and Roy, C. J., *Verification and Validation in Scientific Computing*, Cambridge University Press, 2010.
- [4] Wang, J., Li, J., and Jackson, J., “A study of the influence of buoyancy on turbulent flow in a vertical plane passage,” *International Journal of Heat and Fluid Flow*, Vol. 25, No. 3, 2004, pp. 420–430.
- [5] ASME, “ANSI Standard V&V 20. ASME guide on verification and validation in computational dynamics and heat transfer,” Tech. rep., American Society of Mechanical Engineers, 2008.
- [6] Oberkampf, W. L. and Trucano, T. G., “Verification and validation in computational fluid dynamics,” *Progress in Aerospace Sciences*, Vol. 38, No. 3, 2002, pp. 209–272.
- [7] Wilson, G. E. and Boyack, B. E., “The role of the PIRT process in experiments, code development and code applications associated with reactor safety analysis,” *Nuclear Engineering and Design*, Vol. 186, No. 1, 1998, pp. 23–37.
- [8] CFD-Online, “Validation Cases Links References,” 2013, from <http://www.cfd-online.com/Links/refs.html>.
- [9] NPARC Alliance, “Turbulent Flat Plate,” 2013, from <http://www.grc.nasa.gov/WWW/wind/valid/fpturb/fpturb.html>.
- [10] ERCoFTC, “Classic Collection Database,” 2013, from <http://cfd.mace.manchester.ac.uk/ercoftac/classif.html>.
- [11] Oberkampf, W. and Smith, B., “Assessment Criteria for Computational Fluid Dynamics Validation Benchmark Experiments,” *AIAA SciTech Conference*, 2014.
- [12] Experimental Fluid Dynamics Laboratory, “Buoyancy Aided Forced Convection Database,” 2014, <http://efdl.neng.usu.edu/ValidationPages/FC-Validation/Main.html>.
- [13] Timmins, B. H., Wilson, B. W., Smith, B. L., and Vlachos, P. P., “A method for automatic estimation of instantaneous local uncertainty in particle image velocimetry measurements,” *Experiments in Fluids*, Vol. 53, No. 4, 2012, pp. 1133–1147.

- [14] Warner, S. O., Smith, B. L., and Vlachos, P. P., "Autocorrelation based estimate of particle image density in PIV," Bulletin of the American Physical Society, DFD, San Diego, CA, 2012.
- [15] Wilson, B. M. and Smith, B. L., "Uncertainty on PIV mean and fluctuating velocity due to bias and random errors," *Measurement Science and Technology*, Vol. 24, No. 3, 2013, pp. 035302.
- [16] Wilson, B. M. and Smith, B. L., "Taylor-series and Monte-Carlo-method uncertainty estimation of the width of a probability distribution based on varying bias and random error," *Measurement Science and Technology*, Vol. 24, No. 3, 2013, pp. 035301.
- [17] Coleman, H. W. and Steele, W. G., *Experimentation, Validation, and Uncertainty Analysis for Engineers*, John Wiley and Sons, Hoboken, NJ, 3rd ed., 2009.
- [18] Kays, W. M., Crawford, M. E., and Weigand, B., *Convective Heat and Mass Transfer*, McGraw-Hill, New York, 4th ed., 2004.
- [19] Lloyd, J. and Sparrow, E., "Combined forced and free convection flow on vertical surfaces," *International Journal of Heat and Mass Transfer*, Vol. 13, No. 2, 1970, pp. 434–438.
- [20] Gryzagoridis, J., "Combined free and forced convection from an isothermal vertical plate," *International Journal of Heat and Mass Transfer*, Vol. 18, No. 7, 1975, pp. 911–916.
- [21] McEligot, D. M. and Jackson, J. D., "Deterioration criteria for convective heat transfer in gas flow through non-circular ducts," *Nuclear engineering and design*, Vol. 232, No. 3, 2004, pp. 327–333.
- [22] Hattori, Y., Tsuji, T., Nagano, Y., and Tanaka, N., "Effects of freestream on turbulent combined-convection boundary layer along a vertical heated plate," *International journal of heat and fluid flow*, Vol. 22, No. 3, 2001, pp. 315–322.
- [23] Tsuji, T. and Nagano, Y., "Characteristics of a turbulent natural convection boundary layer along a vertical flat plate," *International Journal of Heat and Mass Transfer*, Vol. 31, 1988, pp. 1723–1734.
- [24] Jackson, J. D., "Review of some experimental studies of turbulent mixed convection covering a wide range prandtl number," NURETH-14, Sept. 25-29, 2011.
- [25] Jackson, J., "Studies of buoyancy-influenced turbulent flow and heat transfer in vertical passages," *International Heat Transfer Conference 13*, Begel House Inc., 2006.
- [26] Chen, T., Armaly, B., and Ramachandran, N., "Correlations for laminar mixed convection flows on vertical, inclined, and horizontal flat plates," *ASME Transactions Journal of Heat Transfer*, Vol. 108, 1986, pp. 835–840.
- [27] Ramachandran, N., Armaly, B., and Chen, T., "Measurements and predictions of laminar mixed convection flow adjacent to a vertical surface," *Journal of Heat Transfer*, Vol. 107, No. 3, 1985, pp. 636–641.

- [28] Hattori, Y., Tsuji, T., Nagano, Y., and Tanaka, N., "Characteristics of turbulent combined-convection boundary layer along a vertical heated plate," *International journal of heat and fluid flow*, Vol. 21, No. 5, 2000, pp. 520–525.
- [29] Krishnamurthy, R. and Gebhart, B., "An experimental study of transition to turbulence in vertical mixed convection flows," *Journal of Heat Transfer (Transactions of the ASME (American Society of Mechanical Engineers), Series C);(United States)*, Vol. 111, No. 1, 1989.
- [30] Gavara, M. R., Dutta, P., and Seetharamu, K., "Mixed convection adjacent to non-isothermal vertical surfaces," *International Journal of Heat and Mass Transfer*, Vol. 55, No. 17, 2012, pp. 4580–4587.
- [31] Yadav, V. and Kant, K., "Experimental Validation of Analytical Solutions for Vertical Flat Plate of Finite Thickness Under Natural-Convection Cooling," *Journal of Heat Transfer*, Vol. 130, 2008, pp. 032503–1.
- [32] Abedin, M. Z., Tsuji, T., and Lee, J., "Turbulence characteristics and vortical structures in combined-convection boundary layers along a heated vertical flat plate," *International Journal of Heat and Mass Transfer*, 2012.
- [33] Moretti, P. and Kays, W., "Heat transfer to a turbulent boundary layer with varying free-stream velocity and varying surface temperaturean experimental study," *International Journal of Heat and Mass Transfer*, Vol. 8, No. 9, 1965, pp. 1187–1202.
- [34] Perkins, K. R., Schade, K. W., and McEligot, D. M., "Heat laminarizing gas flow in a square duct," *International Journal of Heat and Mass Transfer*, Vol. 16, 1973, pp. 897–916.
- [35] Shehata, A. M. and McEligot, D. M., "Turbulence structure in the viscous layer of strongly heated gas flows," Tech. rep., Lockheed Idaho Technologies Co., Idaho Falls, ID (United States), 1995.
- [36] "Engineering Laboratory Design," PO Box 278, 2021 S. HWY 61, Lake City, MN 55041.
- [37] National Instruments, *LabView*, <http://www.ni.com/labview/>.
- [38] Adrian, R. J. and Westerweel, J., *Particle Image Velocimetry*, Cambridge University Press, 2010.
- [39] Raffel, M., Willert, C., Wereley, S., and Kompenhans, J., "Particle Image Velocimetry—A Pratical Guide," *Particle image velocimetry: a pratical guide*, 2007.
- [40] LaVision, *DaVis[®] version 8.1*, Goettingen, Germany, <http://www.lavision.de/en/techniques/piv.php>.
- [41] LaVision, "DaVis[®] version 8.1," 2013.
- [42] Kähler, C., "General design and operating rules for seeding atomisers," *Proc. of the 5th Int. Symp. on Particle*, 2003.

- [43] Velmex, Inc., *Linear Motor-driven Bi- and UniSlide Assemblies*, <http://www.velmex.com/index.asp>.
- [44] Howell, J. R., Siegel, R., and Mengüç, M. P., *Thermal Radiation Heat Transfer*, CRC Press, 2011.
- [45] Weast, R. C., Astle, M. J., and Beyer, W. H., *CRC handbook of chemistry and physics*, Vol. 69, CRC press Boca Raton, FL, 1988.
- [46] Incropera, F. P. and DeWitt, D. P., *Introduction to Heat and Mass Transfer*, Wiley, 5th ed., 2002.
- [47] Barlow, J. B., Rae, W. H., and Pope, A., *Low-Speed Wind Tunnel Testing*, Wiley New York, 3rd ed., 1999.
- [48] Janna, W., *Design of Fluid Thermal Systems-SI Version*, Cengage learning, 2010.
- [49] Iverson, J. M., *Computational Fluid Dynamics Validation of Buoyant Turbulent Flow Heat Transfer*, Ph.D. thesis, UTAH STATE UNIVERSITY, 2013.
- [50] Kendall, A. and Koochesfahani, M., “A method for estimating wall friction in turbulent wall-bounded flows,” *Experiments in Fluids*, Vol. 44, No. 5, Nov. 2007, pp. 773–780.
- [51] CD-adapco, *STAR-CCM+*, <http://www.cd-adapco.com/products/star-ccm-plus>.
- [52] Celik, I. B., Ghia, U., Roache, P. J., et al., “Procedure for estimation and reporting of uncertainty due to discretization in CFD applications,” *Journal of fluids Engineering-Transactions of the ASME*, Vol. 130, No. 7, 2008.
- [53] Lien, F., Chen, W., and Leschziner, M., “Low-Reynolds-number eddy-viscosity modelling based on non-linear stress-strain/vorticity relations,” *Engineering turbulence modelling and experiments*, Vol. 3, 1996, pp. 91–100.
- [54] Wilcox, D. C., “Formulation of the kw Turbulence Model Revisited,” *AIAA journal*, Vol. 46, No. 11, 2008, pp. 2823–2838.
- [55] Department of Energy, NEUP, *Quality Assurance Requirements*, https://inlportal.inl.gov/portal/server.pt?open=514&objID=7362&parentname=CommunityPage&parentid=1&mode=2&in_hi_userid=2&cached=true.
- [56] Schlichting, H., *Boundary-layer theory*, McGraw-Hill, 1968.
- [57] Adrian, R. J., “Hairpin vortex organization in wall turbulence,” *Physics of Fluids*, Vol. 19, No. 4, 2007, pp. 041301.

Appendices

Appendix A

Small Calibration Target

The calibration plate uses laser etched circles on an anodized aluminum plate. The dots are 0.980 mm (0.039 in) in diameter and spaced 3.175 mm (0.125 in) apart.

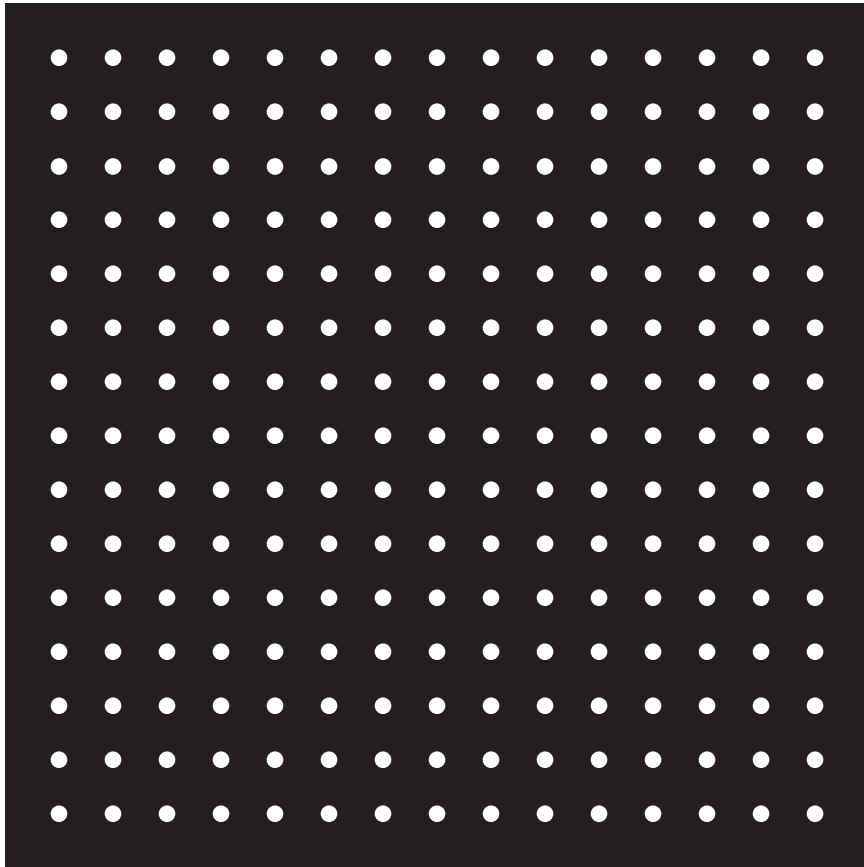
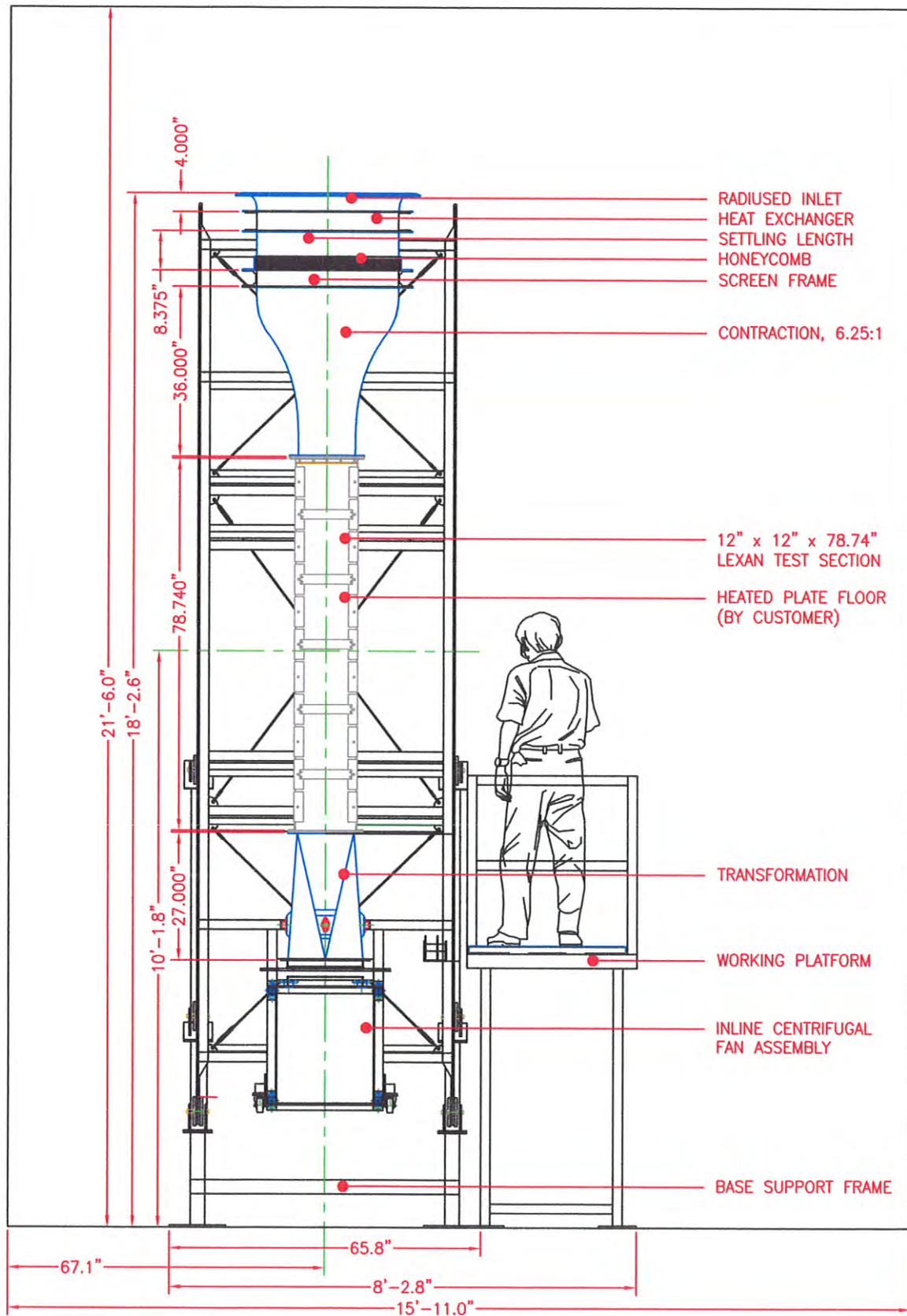


Fig. A.1: An image of the calibration target built to dewarp the SRQ data images.

Appendix B

Rotatable Buoyancy Tunnel Schematic

The schematic of the wind tunnel, provided by Engineering Laboratory Design, Inc. and used with permission.



SECTION A-A

THIS DRAWING AND THE INFORMATION THAT IT CONTAINS ARE THE PROPERTY OF ENGINEERING LABORATORY DESIGN, INC. REPRODUCTION AND/OR TRANSMISSION WITHOUT EXPRESS WRITTEN AUTHORIZATION IS PROHIBITED.

ENGINEERING LABORATORY DESIGN, INC.
P.O. Box 278
Lake City, Minnesota 55041 USA
800-795-8536 FAX 651-345-5095

PROJECT: 12" O.C. ROTATING WIND TUNNEL
END ELEVATION - SECTION A-A

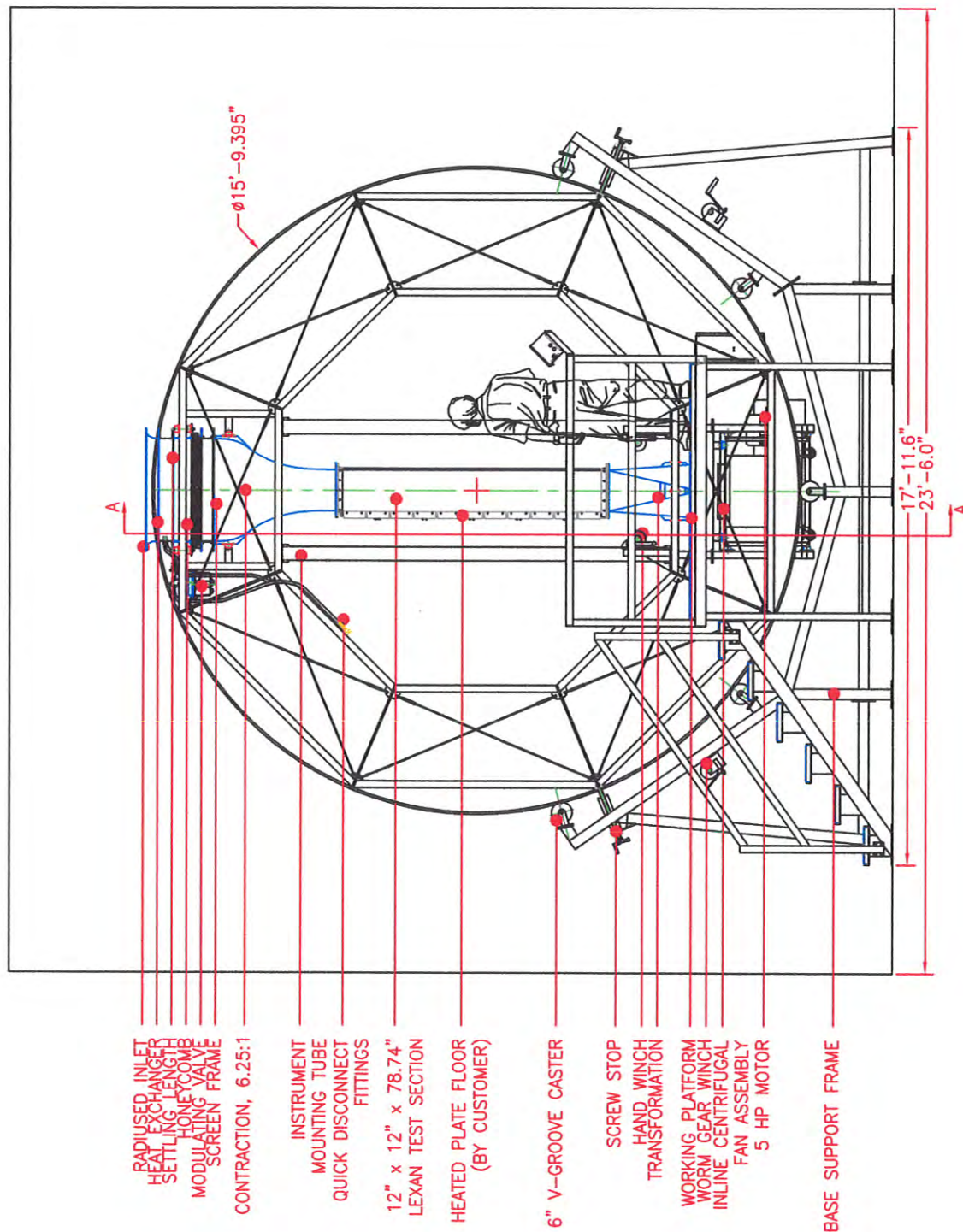
ORGANIZATION: UTAH STATE UNIVERSITY

REFERENCE: PO NO. P0103934

DATE: 9/13/10

SCALE: 3/8" = 1'-0"





THIS DRAWING AND THE INFORMATION THAT IT CONTAINS ARE THE PROPERTY OF ENGINEERING LABORATORY DESIGN, INC. REPRODUCTION AND/OR TRANSMISSION WITHOUT EXPRESS WRITTEN AUTHORIZATION IS PROHIBITED.

ENGINEERING LABORATORY DESIGN, INC.
 P.O. Box 278
 Lake City, Minnesota 55041 USA
 800-795-8536 FAX 651-345-5095

PROJECT: 12" O.C. ROTATING WIND TUNNEL
 OVERALL ELEVATION

ORGANIZATION: UTAH STATE UNIVERSITY

REFERENCE:
 PO NO. P0103934

DATE: 9/13/10

SCALE: 1/4" = 1'-0"



Appendix C

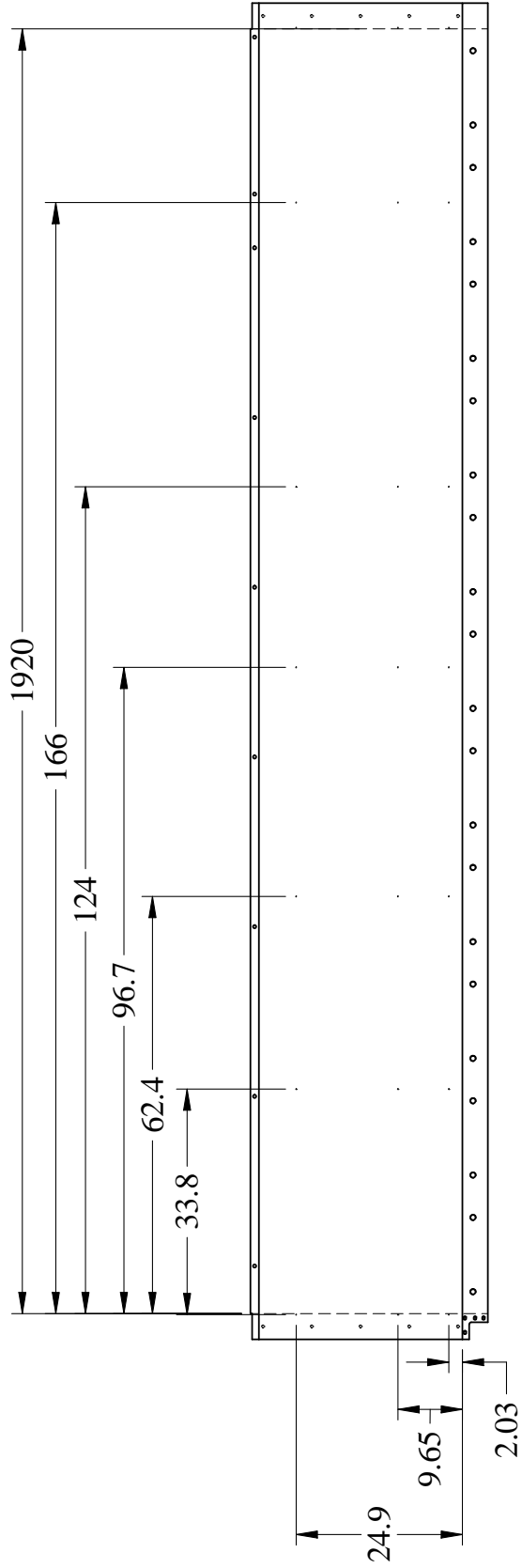
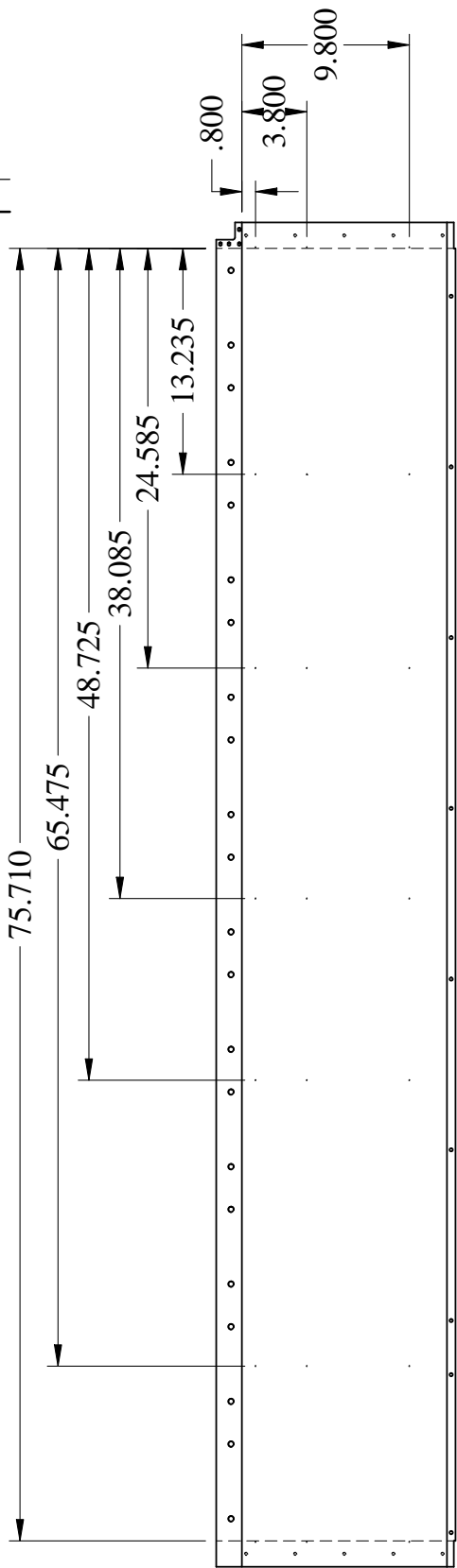
Test Section Schematics

Schematics of the test section walls. The order of the drawings is

1. Left Wall
2. Right Wall
3. Top Wall 1st Section
4. Top Wall 2nd Section
5. Top Wall 3rd Section
6. Inlet Floor

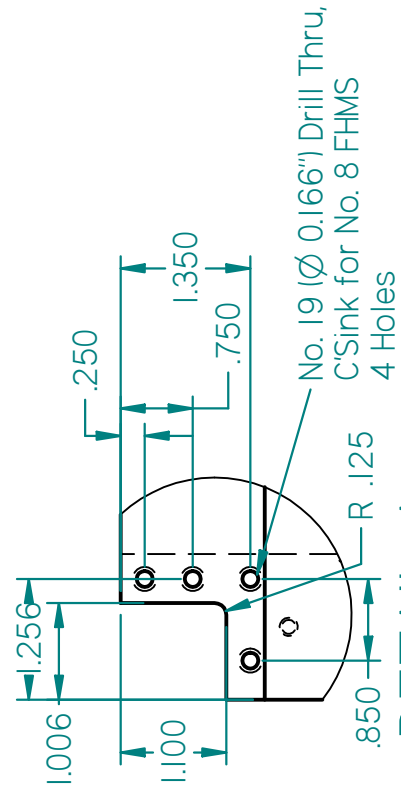
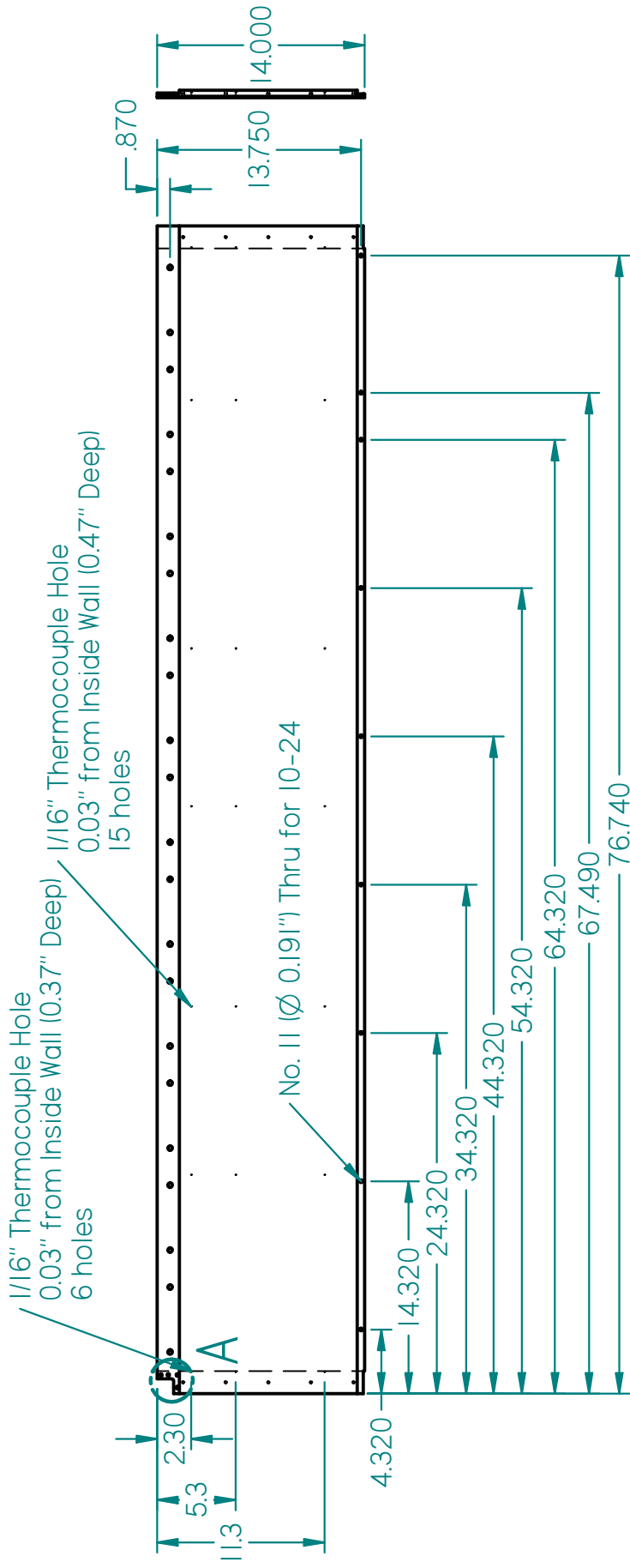
REVISION HISTORY

REV	DESCRIPTION	DATE	APPROVED

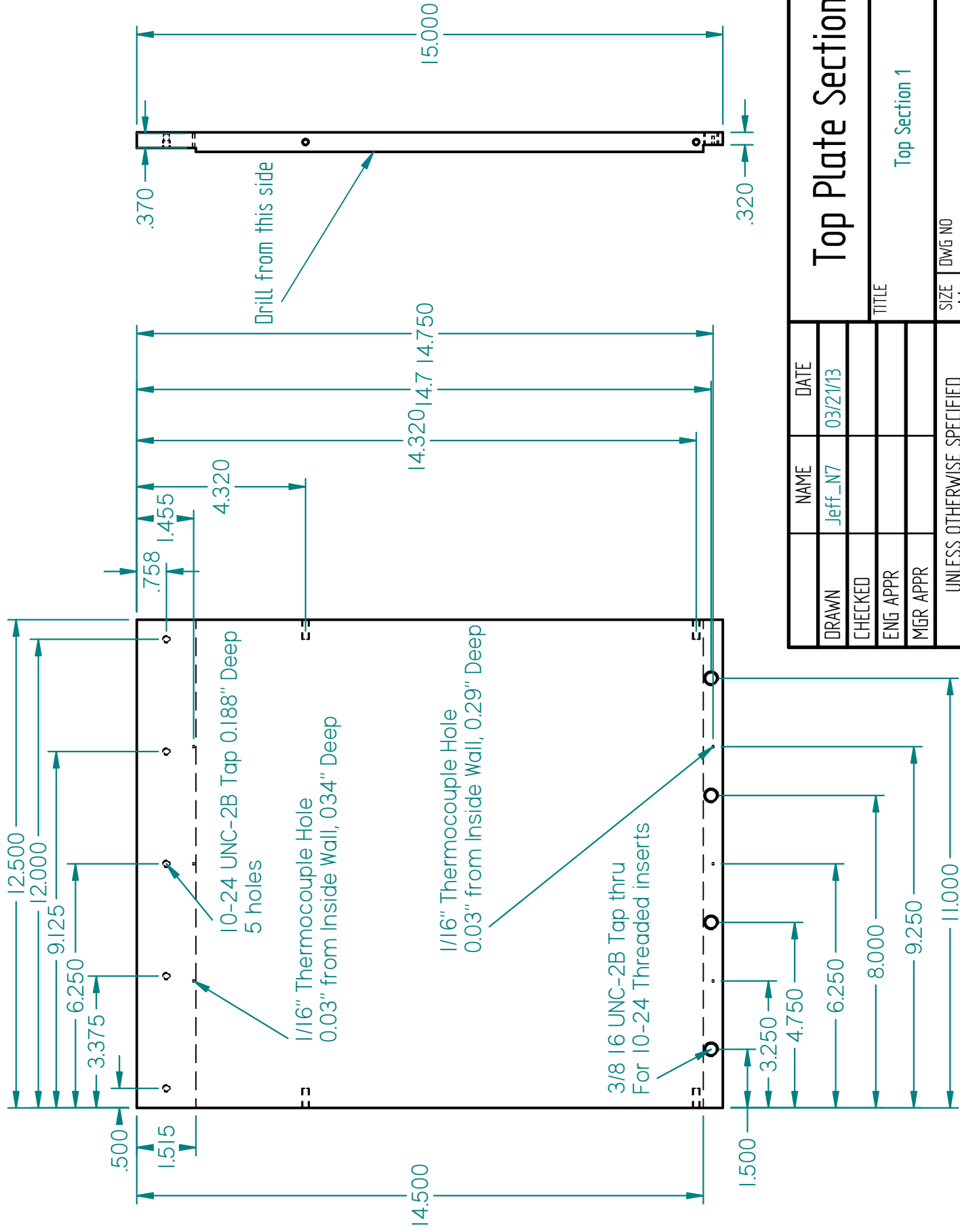


DRAWN	NAME	DATE	Solid Edge	
CHECKED	NAME	DATE		
ENG APPR	NAME	DATE		
MGR APPR	NAME	DATE		
UNLESS OTHERWISE SPECIFIED DIMENSIONS ARE IN MILLIMETERS ANGLES ±XX°			SIZE	KEY
2 PL ±XXX.3 PL ±XXXX			A2	
			FILE NAME	Left Side Mark 2.2.dft
			SCALE	WEIGHT
			SHEET 1 OF 1	

SOLID EDGE ACADEMIC COPY



Right Side Wall		NAME	DATE
TITLE Right Side 2		DRAWN	Jeff_N7 01/20/12
		CHECKED	
		ENG APPR	
		MGR APPR	
UNLESS OTHERWISE SPECIFIED DIMENSIONS ARE IN INCHES ANGLES ±XX° 2 PL ±XXX 3 PL ±X.XXX		SIZE	DWG NO
		A4	
FILE NAME: Right Side Mark 2.2.dft		SCALE:	WEIGHT:
SHEET 1 OF 1		REV	

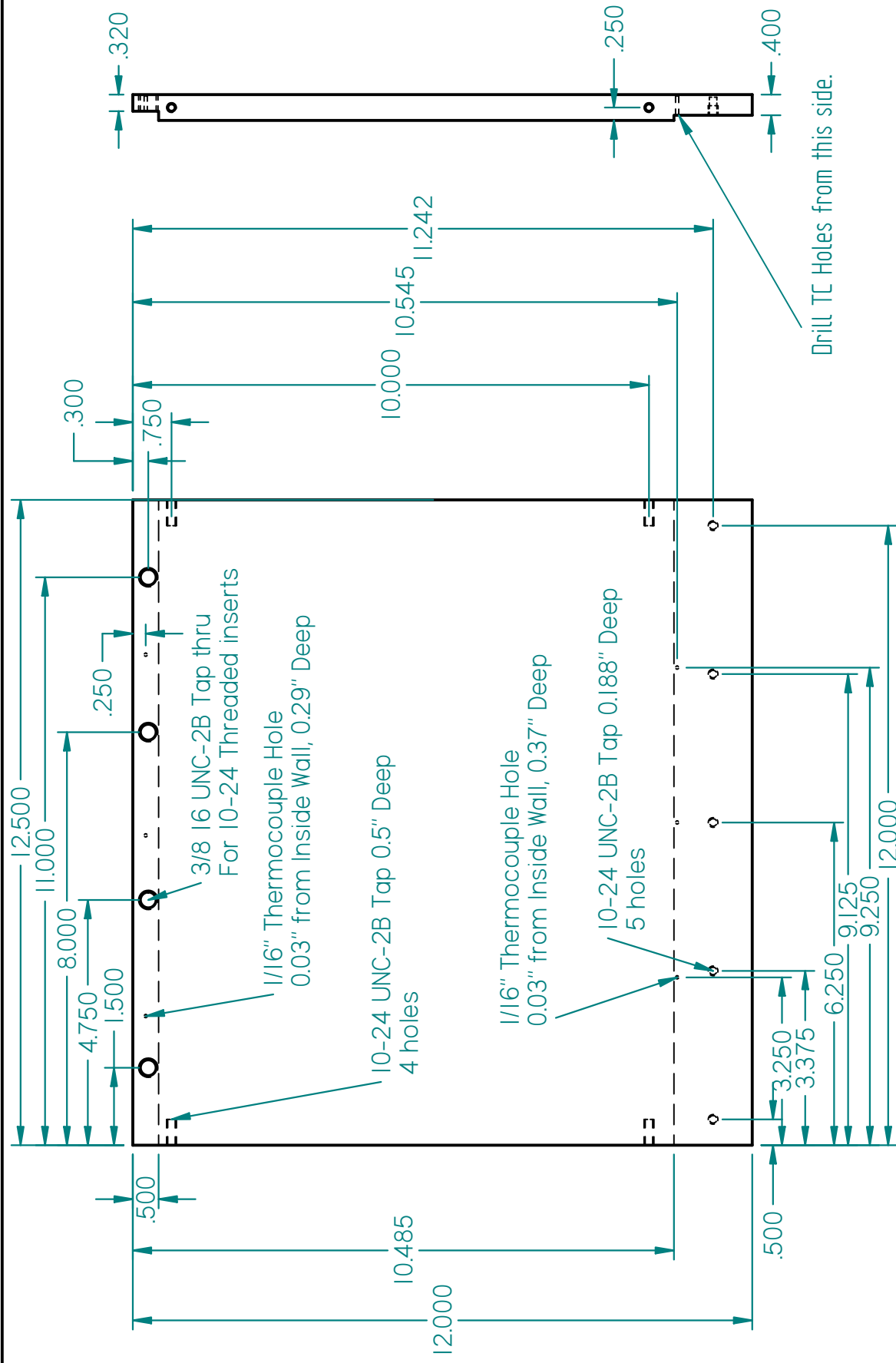


	NAME	DATE
DRAWN	Jeff_N7	03/21/13
CHECKED		
ENG APPR		
MGR APPR		

Top Plate Section 1		
TITLE		
SIZE	DWG NO	REV
A4		

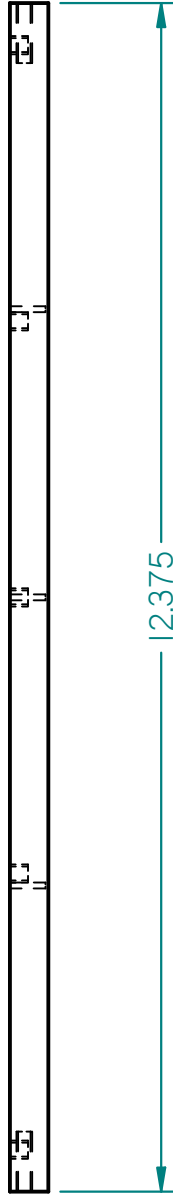
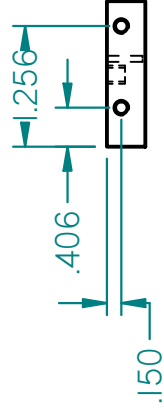
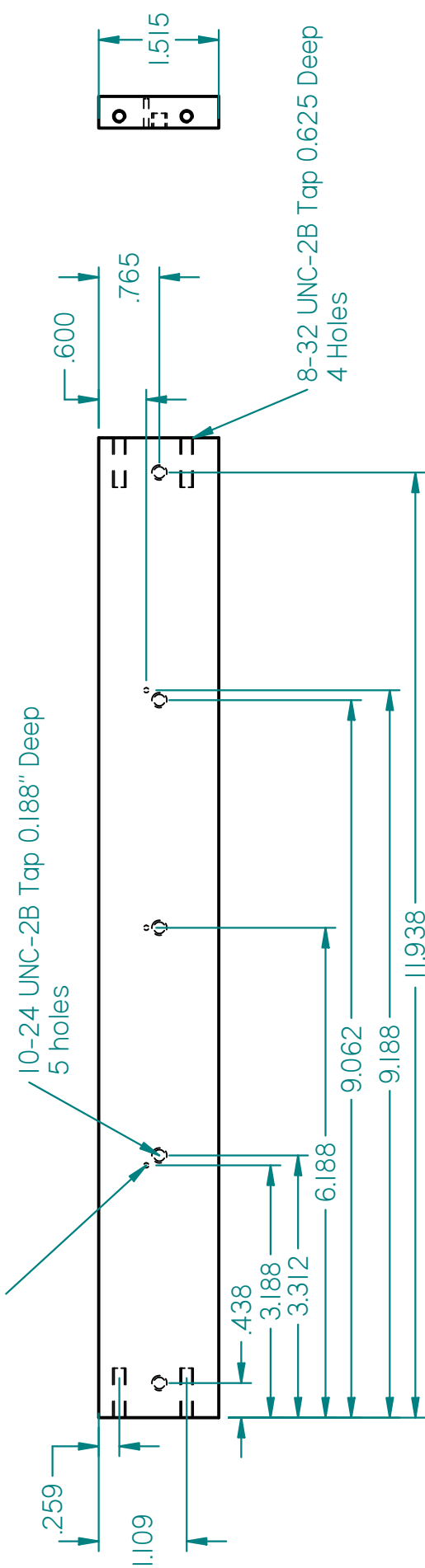
UNLESS OTHERWISE SPECIFIED DIMENSIONS ARE IN INCHES ANGLES ±XX°		
2 PL ±XXX 3 PL ±X.XXX		

FILE NAME: Top Mark 2 section 1b.dft	WEIGHT:	SHEET 1 OF 1
--------------------------------------	---------	--------------



Top Plate Section 3		
TITLE		
Top Section 3		
UNLESS OTHERWISE SPECIFIED DIMENSIONS ARE IN INCHES ANGLES ±XX° 2 PL ±XXX 3 PL ±XXXX	SIZE	DWG NO
	A4	REV
FILE NAME: Top Mark 2 section 3b.dft		
SCALE:		WEIGHT:
SHEET 1 OF 1		

1/16" Thermocouple Hole
0.03" from Inside Wall

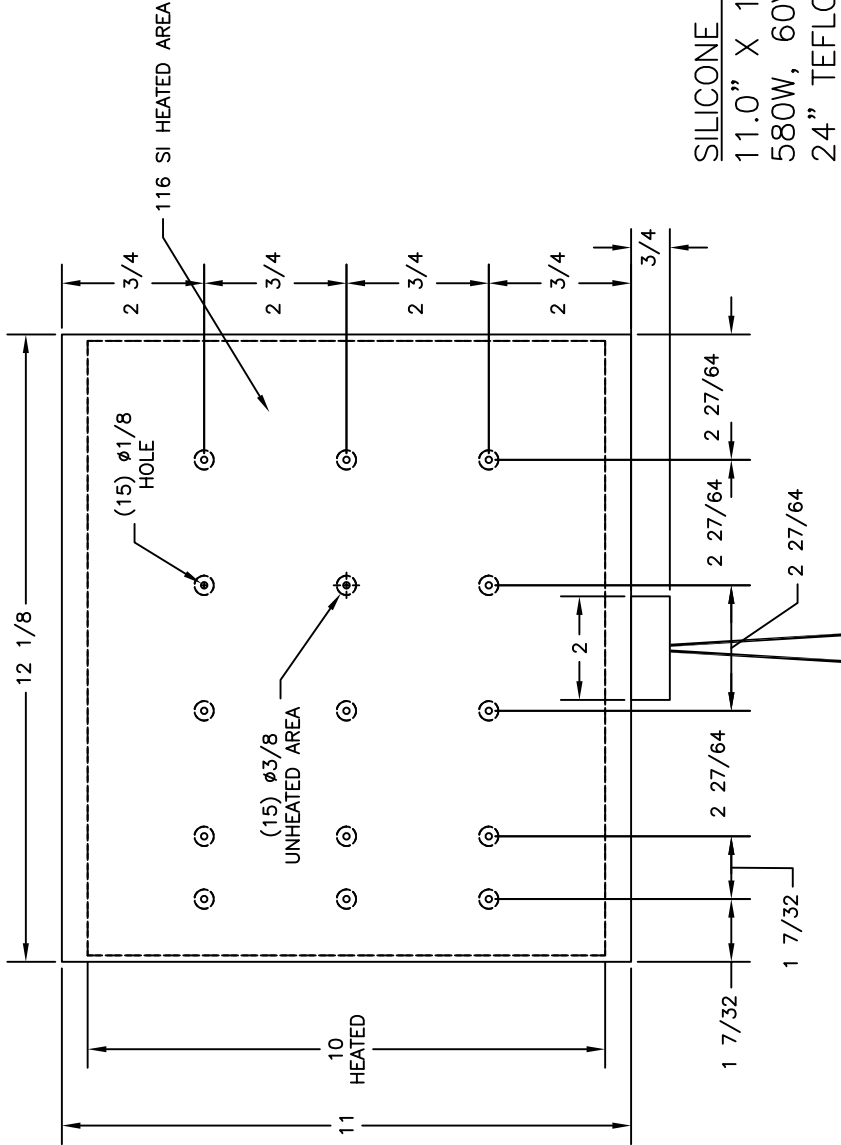


NAME		DATE	Inlet Floor	
DRAWN	Jeff_N7	03/21/13	TITLE	
CHECKED			Inlet Floor	
ENG APPR			SIZE	
MGR APPR			DWG NO	
UNLESS OTHERWISE SPECIFIED DIMENSIONS ARE IN INCHES ANGLES ±XX° 2 PL ±XXX 3 PL ±X.XXX		SCALE:	REV	FILE NAME: Inlet Floor.dft
			WEIGHT:	SHEET 1 OF 1

Appendix D

Custom Silicon Heater


The schematic of the heater from Tempco Electric Heater Corporation. Each heater cost \$158.90 and one time charge of \$60.00 to setup the manufacturing. The heaters have Teflon leads of 24 inches. The heaters have a capacity of 580 Watts and 60 Volts. Failure temperature is above 260°C, but continuous use should stay below 200°C.



THIS DRAWING AND PRINCIPLES OF DESIGN ARE THE EXCLUSIVE PROPERTY OF TEMPACO ELECTRIC HEATER CORP. ANY DUPLICATION OR REPRODUCTION WITHOUT THE CONSENT OF TEMPACO IS PROHIBITED

DRAWING APPROVED
BY:
DATE:

SILICONE RUBBER SURFACE HEATER
11.0" X 12.125"
580W, 60V
24" TEFLON LEADS
(15) HOLES 1/8" DIA
LEAD EXIT TAB 7/8" X 2"
1/2" UNHEATED MARGINS

ITEM	PART NO.	REQD	DESCRIPTION	
<div><div>TOLERANCES UNLESS OTHERWISE SPECIFIED</div><div>FRACTIONS ± 1/64</div><div>DECIMALS .XX ± .010 .XXX ± .005</div><div>ANGLES ± °</div><div>SURFACE FINISH ✓</div></div>		<div></div> <div>Tempco Electric Heater Corporation 607 N. Central Ave. Wood Dale, IL 60191-1452 U.S.A. Phone: (630) 350-2252 Fax: (630) 350-1210 Email: info@tempco.com</div>		
		SCALE: NTS	DATE: 8/13/10	DRAWN BY: BPM
CUSTOMER:		TITLE: SILICONE RUBBER HEATER		DRAWING NUMBER: SHS01814

Appendix E

Inlet Thermocouple Positions

The positions of the inlet thermocouples are shown in Fig. E.1. North is up in the figure and the thermocouples are numbered as in the Master .vi.

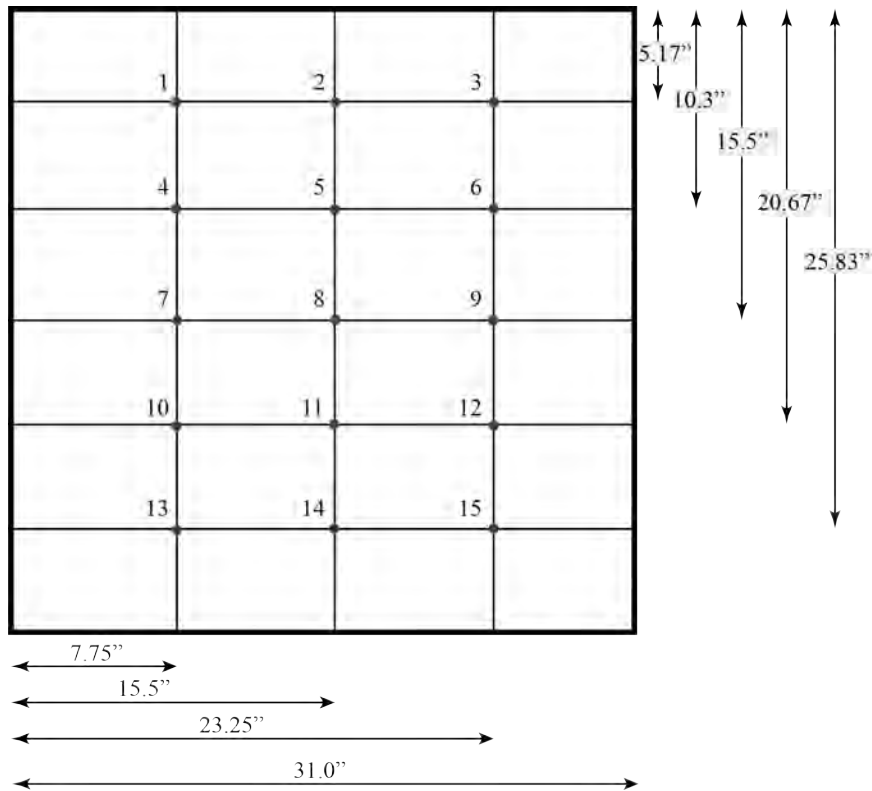


Fig. E.1: A sketch showing the positions of the inlet thermocouples. With the test section in the buoyancy aided orientation (inlet down), up in the image is north.

Appendix F

Boundary Conditions Statistics

```

clear all; close all; clc;format long;
%% Shaun Harris wrote this code Dec. 19, 2013
% email: shaun.r.harris@gmail.com
% feel free to contact if you have many questions

%% User Input
% put a 0 if you have 6 .csv files in one folder for your case or
% put a 1 if you have 5 temperature files in one folder and the heat flux
Filetype=input(['Put a 0 if you have all 6 .csv files in one folder \n'...
    ' Put a 1 if you have 5 temperature files in one spot and the heat'...
    ' flux files in another \n']);
%% if 0... input after running code is a 0
% 5 temperature .csv files under one folder and flux .csv files somewhere else
% Selecting files: This program will ask you to select 2 seperate folders
%
% First folder: Select the folder that is above a series of folders that
% contain the 5 temperature .csv files
% Should be named HeatedWallTemp.csv, InletTemp.csv, RightWallTemp.csv,
% LeftWallTemp.csv and TopWallTemp.csv
%
% Second folder: Select a folder that is above a series of .csv heat flux
% files that you want the stats for. Make sure no other .csv files are in
% there
%
%% if 1... input after running code is a 1
% 6 .csv files in the same folder
% This code will ask you to select one folder. Select the folder that is

```

```

% above a series of folders that contain the 6 .csv files HeatedWallTemp.csv,
% InletTemp.csv, and etc. in each of the folders. Make sure no other folders
% are in the folder.

%% After running code. The variables can be identified
% HW.Mean.Temp is the heated wall average temperatures at each of the
% positions x y and z of multiple laser positions
% HW.SD is the heated wall standard deviation at each of the positions x y
% and z of multiple laser positions
% HW.PU is the heated wall precision uncertainty at each of the positions x
% y and z of multiple laser positions...v is used for the precision
% uncertainty claculation
%% Select files
% This section will bring in the all the temp data into your workspace
tempName={'\HeatedWallTemp.csv';'\InletTemp.csv';'\LeftWallTemp.csv';...
          '\RightWallTemp.csv';'\TopWallTemp.csv'};% Specific Temp file names
sprintf('%s', '          Select the case you want to use')
if Filetype
    folder=uigetdir(' ', ...
        'Select Temperature .csv folder above the series of folders they are in');
    % find folder that contains all different positions
    dirListing=dir(folder); % array of all the names of the files in the folder
    FlxName=uigetdir(folder, 'Select Heat Flux .csv folder for the case');
    %find folder that contains the flux files
    dirListingFlux=dir(fullfile(FlxName, '*csv'));
    % cell array of all names of the flux files in the folder
elseif ~Filetype
    tempName={'\HeatedWallTemp.csv';'\InletTemp.csv';'\LeftWallTemp.csv';...
            '\RightWallTemp.csv';'\TopWallTemp.csv'};% Specific Temp file names
    flxName={'\HeatFlux.csv'};
    folder=uigetdir; % find folder that contains all different positions
    dirListing=dir(folder); %array of all the names of the files in the folder
    dirListingFlux=dirListing;
    FlxName=folder;
else

```

```

        sprintf('%s', ['You need to read the introduction for this '
        'code and input a 1 or 0 for the Filetype'])
    end
    tic
    % initialize a few arrays
    b=0;
    for d=3:length(dirListing)
        if dirListing(d).isdir
            b=b+1;
        end
    end
    c=0;
    if Filetype
        for d=1:length(dirListingFlux)
            if ~dirListingFlux(d).isdir
                c=c+1;
            end
        end
    else
        for d=3:length(dirListingFlux)
            if ~dirListingFlux(d).isdir
                c=c+1;
            end
        end
    end
    fluxName=cell(1,c);
    M_flux=cell(1,c);
    fileName=cell(5,b);
    M_temp=cell(5,b);
    %% loop through files and open and save in workspace as
    if Filetype
        % corresponding fileName and M_temp arrays
        j=1;
        k=1;
        for d=3:b+2

```

```

    if dirListing(d).isdir % if file in selected file is a folder.
        % If it is then run if statement
        for i=1:5
            fileName(i,k)={strcat(fullfile(folder,...
                dirListing(d).name),tempName(i))};
            % full file name for each of the temp/flux files 2 below selected file
            [Num]=csvread(fileName{i,k}{1,1},1,0);
            M_temp{i,k}=Num;
            j=j+1;
        end
        k=k+1;
    else
        k=k+0;
    end
end
How_Many_Folders_Opened=k-1; % show how many folders in the selected file
How_Many_Data_Temp_Sets=j-1; % show how many temperature files you've opened

% loop through for flux files
k=1;
for d=1:c
    if ~dirListingFlux(d).isdir % if file in selected folder is a .csv file
        fluxName(1,k)={fullfile(FlxName,dirListingFlux(d).name)};% for flux
        [Numb]=csvread(fluxName{1,k},0,0);
        M_flux{1,k}=Numb;
        k=k+1;
    end
end
How_Many_Flux_Files_Opened=k-1;
clear j i k d Num ans Numb; % clear extra variables
elseif ~Filetype
    j=1;
    k=1;
    for d=3:b+2
        if dirListing(d).isdir % if file in selected file is a folder.

```

```

%If it is then run if statement
fluxName(1,k)={strcat(fullfile(folder,dirListing(d).name),...
    flxName(1))};% for flux
[Numb]=csvread(fluxName{1,k}{1,1},0,0);
M.flux{1,k}=Numb;
for i=1:5
    fileName(i,k)={strcat(fullfile(folder,...
        dirListing(d).name),tempName(i))};
% full file name for each of the temp/flux files 2 below selected file
[Num]=csvread(fileName{i,k}{1,1},1,0);
M.temp{i,k}=Num;
j=j+1;
end
k=k+1;
else
end
end
How_Many_Folders_Opened=k-1; % show how many folders in the selected file
How_Many_Data_Temp_Sets=j-1; % show how many temperature files you've opened
clear j i d Num ans Numb; % clear extra variables
else
    sprintf('%s','Seriously.... read the introduction')
end
%% Computing Temp Data next 3 sections also
% Mean temperature/Standard Deviation/Precision Uncertainty .csv files
[~,p]=size(M.temp); % size of array of temp files
[~,r]=size(M.flux); % size of array of flux files
% average temperature x y z temperature
[m,~]=size(M.temp{1,1}); % sizes of all walls
[m2,~]=size(M.temp{2,1});
[m3,~]=size(M.temp{3,1});
[m4,~]=size(M.temp{4,1});
[m5,~]=size(M.temp{5,1});
[~,n2]=size(M.flux{1,1}); % size of flux file

```

```

% initialize a few more arrays
HW_temp=zeros(length(1:m),length(1:p));
I_temp=zeros(length(1:m2),length(1:p));
LW_temp=zeros(length(1:m3),length(1:p));
RW_temp=zeros(length(1:m4),length(1:p));
TW_temp=zeros(length(1:m5),length(1:p));
HF=zeros(length(1:r),length(1:n2));

for j=1:p %loop for matrices for each wall temperatures cooresponding to positions
    HW_temp(1:m,j)=M_temp{1,j}(:,4);
    I_temp(1:m2,j)=M_temp{2,j}(:,4);
    LW_temp(1:m3,j)=M_temp{3,j}(:,4);
    RW_temp(1:m4,j)=M_temp{4,j}(:,4);
    TW_temp(1:m5,j)=M_temp{5,j}(:,4);
end
clear j;
for j=1:r
    HF(j,1:n2)=M_flux{1,j}(1,:); %and flux
end

%% average value of each wall and flux
HW_Mean_Temp=mean(HW_temp,2);
I_Mean_Temp=mean(I_temp,2);
LW_Mean_Temp=mean(LW_temp,2);
RW_Mean_Temp=mean(RW_temp,2);
TW_Mean_Temp=mean(TW_temp,2);
HF_MEAN=mean(HF);

% average temperature for each case for plots
HW_Mean_Case=mean(HW_temp);
I_Mean_Case=mean(I_temp);
LW_Mean_Case=mean(LW_temp);
RW_Mean_Case=mean(RW_temp);
TW_Mean_Case=mean(TW_temp);

%% standard deviation
HW_SD=(std(HW_temp,0,2));
I_SD=(std(I_temp,0,2));

```

```

LW_SD=(std(LW_temp,0,2));
RW_SD=(std(RW_temp,0,2));
TW_SD=(std(TW_temp,0,2));
HF_SD=std(HF);

%% precision uncertainty with 95% confidence interval = v*SD/sqrt(N)
mu=p-1; % mu is N-1

% table of mu values
v=[1:20;12.706 4.303 3.182 2.776 2.571 2.447 2.365 2.306 2.262 2.228 2.201...
    2.179 2.160 2.145 2.131 2.12 2.11 2.101 2.093 2.086]';

% precision uncertainty equations for each wall
HW_PU=v(mu,2)*HW_SD/sqrt(p);
I_PU=v(mu,2)*I_SD/sqrt(p);
LW_PU=v(mu,2)*LW_SD/sqrt(p);
RW_PU=v(mu,2)*RW_SD/sqrt(p);
TW_PU=v(mu,2)*TW_SD/sqrt(p);
HF_PU=v(mu,2)*HF_SD/sqrt(r);

clear j l m m2 m3 m4 m5 n n2 m6; % clear extra variables

%% Output
% write headers
% open files to write text headers to
fileIDHW=fopen(fullfile(folder,'Heated_Wall_MEAN_SD_PU.csv'),'w');
fileIDI=fopen(fullfile(folder,'Inlet_MEAN_SD_PU.csv'),'w');
fileIDLW=fopen(fullfile(folder,'Left_Wall_MEAN_SD_PU.csv'),'w');
fileIDRW=fopen(fullfile(folder,'Right_Wall_MEAN_SD_PU.csv'),'w');
fileIDTW=fopen(fullfile(folder,'Top_Wall_MEAN_SD_PU.csv'),'w');
fileIDHF=fopen(fullfile(FlxName,'HF_MEAN_SD_PU.txt'),'w');

% print headers
Head={'X','Y','Z','Tave','SD_T','P_T'};
Head2={'X','Flux','SD_Flux','P_Flux'};
fprintf(fileIDHW,'%s,%s,%s,%s,%s,%s\n',Head{1,:});
fprintf(fileIDI,'%s,%s,%s,%s,%s,%s\n',Head{1,:});
fprintf(fileIDLW,'%s,%s,%s,%s,%s,%s\n',Head{1,:});
fprintf(fileIDRW,'%s,%s,%s,%s,%s,%s\n',Head{1,:});
fprintf(fileIDTW,'%s,%s,%s,%s,%s,%s\n',Head{1,:});

```



```

fprintf(fileIDHF, '%s\t%s\t%s\t%s\n', Head2{1, :});
% close files
fclose('all');

% First get the master arrays
HW_Master_MeanTemp_SD_PU=[M_temp{1,1}(:,1), M_temp{1,1}(:,2), ...
    M_temp{1,1}(:,3), HW_Mean_Temp, HW_SD, HW_PU];
I_Master_MeanTemp_SD_PU=[M_temp{2,1}(:,1), M_temp{2,1}(:,2), ...
    M_temp{2,1}(:,3), I_Mean_Temp, I_SD, I_PU];
LW_Master_MeanTemp_SD_PU=[M_temp{3,1}(:,1), M_temp{3,1}(:,2), ...
    M_temp{3,1}(:,3), LW_Mean_Temp, LW_SD, LW_PU];
RW_Master_MeanTemp_SD_PU=[M_temp{4,1}(:,1), M_temp{4,1}(:,2), ...
    M_temp{4,1}(:,3), RW_Mean_Temp, RW_SD, RW_PU];
TW_Master_MeanTemp_SD_PU=[M_temp{5,1}(:,1), M_temp{5,1}(:,2), ...
    M_temp{5,1}(:,3), TW_Mean_Temp, TW_SD, TW_PU];
HF_Master_MeanTemp_SD_PU=[.1617, .7777, 1.3936; HF_MEAN; HF_SD; HF_PU]';
% includes x coordinates for heat flux sensors
% then write them to files
dlmwrite(fullfile(folder, 'Heated_Wall_MEAN_SD_PU.csv'), HW_Master_MeanTemp_SD_PU, ...
    '-append', 'precision', 7); % for heated Wall
dlmwrite(fullfile(folder, 'Inlet_MEAN_SD_PU.csv'), I_Master_MeanTemp_SD_PU, ...
    '-append', 'precision', 7);
dlmwrite(fullfile(folder, 'Left_Wall_MEAN_SD_PU.csv'), LW_Master_MeanTemp_SD_PU, ...
    '-append', 'precision', 7);
dlmwrite(fullfile(folder, 'Right_Wall_MEAN_SD_PU.csv'), RW_Master_MeanTemp_SD_PU, ...
    '-append', 'precision', 7);
dlmwrite(fullfile(folder, 'Top_Wall_MEAN_SD_PU.csv'), TW_Master_MeanTemp_SD_PU, ...
    '-append', 'precision', 7);
dlmwrite(fullfile(FlxName, 'HF_MEAN_SD_PU.txt'), HF_Master_MeanTemp_SD_PU, ...
    'delimiter', '\t', '-append', 'precision', 7);

%% Plot Average Temperature for each of the cases
% xaxis=case#    yaxis=Temp_average or HFSreading    Used to find outliers of cases
figure('Name', 'Heated Wall Average Temp For Each Case');

```

```

plot(1:p,HW.Mean.Case,'x','MarkerSize',12)
xlabel('Case Name'),ylabel('Average Temperature in Kelvin')
title('Heated Wall Average Temp')
set(gca,'XTick',1:p);set(gca,'XTickLabel',{dirListing(3:p+2).name},'FontSize',8)

figure('Name','Inlet Average Temp For Each Case');
plot(1:p,I.Mean.Case,'x','MarkerSize',12)
xlabel('Case Name'),ylabel('Average Temperature in Kelvin')
title('Inlet Average Temp')
set(gca,'XTick',1:p);set(gca,'XTickLabel',{dirListing(3:p+2).name},'FontSize',8)

figure('Name','Left Wall Average Temp For Each Case');
plot(1:p,LW.Mean.Case,'x','MarkerSize',12)
xlabel('Case Name'),ylabel('Average Temperature in Kelvin')
title('Left Wall Average Temp')
set(gca,'XTick',1:p);set(gca,'XTickLabel',{dirListing(3:p+2).name},'FontSize',8)

figure('Name','Right Wall Average Temp For Each Case');
plot(1:p,RW.Mean.Case,'x','MarkerSize',12)
xlabel('Case Name'),ylabel('Average Temperature in Kelvin')
title('Right Wall Average Temp')
set(gca,'XTick',1:p);set(gca,'XTickLabel',{dirListing(3:p+2).name},'FontSize',8)

figure('Name','Top Wall Average Temp For Each Case');
plot(1:p,TW.Mean.Case,'x','MarkerSize',12)
xlabel('Case Name'),ylabel('Average Temperature in Kelvin')
title('Top Wall Average Temp')
set(gca,'XTick',1:p);set(gca,'XTickLabel',{dirListing(3:p+2).name},'FontSize',8)

% Flux plot
figure('Name','Heat Flux Sensors per case')
plot(1:r,HF(:,1),'o','MarkerSize',12)
hold all
plot(1:r,HF(:,2),'d','MarkerSize',12)
plot(1:r,HF(:,3),'x','MarkerSize',12)

```

```

xlabel('Case Name'),ylabel('HFS reading in W / m^2'),title('Heat Flux Sensors')
legend('HFS 1','HFS 2','HFS 3')
if Filetype
    set(gca,'XTick',1:r);set(gca,'XTickLabel',{dirListingFlux(1:r).name},'FontSize',8)
else
    set(gca,'XTick',1:r);set(gca,'XTickLabel',{dirListingFlux(3:r+2).name},'FontSize',8)
end
%% clear extra variables
clear fileIDHW fileIDI fileIDLW fileIDRW fileIDTW fileIDHF ans Head
clear Head2 p mu r FlxName HF_Mean HF_PU HF_SD HW_Mean_Temp HW_PU HW_SD
clear I_Mean_Temp I_PU I_SD LW_Mean_Temp LW_PU LW_SD RW_Mean_Temp RW_PU
clear RW_SD TW_Mean_Temp TW_PU TW_SD tempName b c k
toc

```

Appendix G

Inlet Analysis Code

```

clear all; close all; clc;

%% User input
proloc =23; % j-index for epsilon profile (increasing from top)
Serial='4.3'; %Name of the sheet to be used for the excel file for the Ustats
z = -0.0762; % Z-coordinate in meters
% 3in=0.0762m, 5in=0.127m, 5.35in=0.13589m, 5.7in=0.14478m
Export = 0; % Export data in *.csv files? (1 for Yes/0 for No)
BL = 65; % The number of data points from each edge to write

TrimTop = 1;
TrimBottom = 1;
TrimLeft = 1;
TrimRight = 1;

sprintf('%c','Select the MatLab Stats file')
[f1,p] = uigetfile('.mat'); % Ask user to choose velocity file
load(strcat(p,f1));
% sprintf('%c','Select the Tecplot file for the RMS (Standard Deviation):')

tic;
x=X'; x=x(:);
y=Y'; y=y(:);
vx1=v_ave'; vx1=vx1(:);vx1(isnan(vx1))=0;
vy1=u_ave'; vy1=vy1(:);vy1(isnan(vy1))=0;
vx2=uut'; vx2=sqrt(vx2(:));vx2(isnan(vx2))=0;
vy2=vvt'; vy2=sqrt(vy2(:));vy2(isnan(vy2))=0;

```

```

nu = 1.632E-5; % kinematic viscosity at 1400 m elevation
[h,w]=size(u_ave);
%w=length(vx1); % width
%h=length(vx2); % height

%% Allocate and initialize
x_2D=zeros(w,h);
y_2D=zeros(w,h);
u=zeros(w,h);
v=zeros(w,h);
Uz=zeros(w,h);
Uxy=zeros(w,h);
SDx=zeros(w,h);
SDy=zeros(w,h);
SDz=zeros(w,h);
SDxy=zeros(w,h);

du_dx = zeros(w,1);
du_dy = zeros(w,1);
dv_dx = zeros(w,1);
dv_dy = zeros(w,1);

%% Run through data and sort
xcount=0;
for i=1:h
    for j=1:w
        xcount = xcount+1;
        x_2D(j,i)=x(xcount);
        y_2D(j,i)=y(xcount);
        u(j,i)=vx1(xcount)% u, v are in the x, y direction according to DaVis
        v(j,i)=vy1(xcount);
        Uz(j,i)=vx1(xcount); % Assume w = v
        Uxy(j,i)=sqrt( vx1(xcount)^2 + vy1(xcount)^2 + vx1(xcount)^2 );
        SDx(j,i)=vx2(xcount);

```

```

        SDy(j,i)=vy2(xcount);
        SDz(j,i)=vx2(xcount);    % Assume SDz=SDy
        SDxy(j,i)=sqrt( vx2(xcount)^2 + vy2(xcount)^2 + vx2(xcount)^2 );
    end
end

%% Adaptive trimming to masked area
[imin,imax,jmin,jmax] = TrimToMask(v');

% iupper is the y index at the upper boundary (lowest index)
ilower = imin - TrimBottom;

% ilower is the y index at the lower boundary (highest index)
iupper = imax + TrimTop;

jlower = jmin + TrimLeft;
jupper = jmax - TrimRight;

xlower = x_2D(jlower,1);
xupper = x_2D(jupper,1);
ylower = y_2D(1,ilower);
yupper = y_2D(1,iupper);

xshift = x_2D(jlower,1);
x_2D = x_2D - xshift;    % Shift x_2D array so y=0 is at the left
xlower = xlower - xshift;
xupper = xupper - xshift;

%% Calculate epsilon based on gradients of fluctuating terms

% dx = abs( x_2D(1,1) - x_2D(2,1) ); %Spacing between vectors in mm given by DaVis
dx = 305./(jupper-jlower+2);    % Spacing between vectors in mm given by geometry

for i=1:w
    du.dy(i) = 1000.*( SDx(i,proloc+1) - SDx(i,proloc-1) )/(2.*dx);

```

```

    dv_dy(i) = 1000.*( SDy(i,proloc+1) - SDy(i,proloc-1) )/(2.*dx);
end
for i=2:w-1
    du_dx(i) = 1000.*( SDx(i+1,proloc) - SDx(i-1,proloc) )/(2.*dx);
    dv_dx(i) = 1000.*( SDy(i+1,proloc) - SDy(i-1,proloc) )/(2.*dx);
end
du_dx(1) = 1000.*( -SDx(3,proloc) + ...
    4.*SDx(2,proloc) - 3.*SDx(1,proloc) )/(2.*dx);
du_dx(w) = 1000.*( 3.*SDx(w,proloc) - ...
    4.*SDx(w-1,proloc) + SDx(w-2,proloc) )/(2.*dx);
dv_dx(1) = 1000.*( -SDy(3,proloc) + ...
    4.*SDy(2,proloc) - 3.*SDy(1,proloc) )/(2.*dx);
dv_dx(w) = 1000.*( 3.*SDy(w,proloc) - ...
    4.*SDy(w-1,proloc) + SDy(w-2,proloc) )/(2.*dx);

% Sharp and Adrian's approximation for the epsilon profile
epsilon = nu*( 2.*du_dx.^2 + 2.*dv_dy.^2 + ...
    3.*du_dy.^2 + 3.*dv_dx.^2 + 2.*du_dy.*dv_dx );

%% Calculate the Turbulence Kinetic Energy
TKE = 0.5*SDxy(:,proloc)'.^2;

%% Transpose
x_2D=x_2D';
y_2D=y_2D';
u=u';
v=v';
Uxy=Uxy';
SDx=SDx';
SDy=SDy';
SDxy=SDxy';
TKE = TKE';

%% Plotting
% Plot contour of velocity magnitude

```

```

figure('Name','Velocity Magnitude'); contourf(x_2D,y_2D,Uxy,50,...
    'edgecolor','none'); hold on;
% quiver(x_2D,y_2D,u,v,3);
plot([x_2D(proloc,1) x_2D(proloc,w)],[y_2D(proloc,1) y_2D(proloc,w)], 'r');
Uxy_max = max(max(Uxy(iupper:ilower,jlower:jupper)));
Uxy_min = min(min(Uxy(iupper:ilower,jlower:jupper)));
h1 = colorbar('EastOutside');
caxis([Uxy_min Uxy_max]); %shading interp
set(get(h1,'ylabel'),'String','Velocity (m/s)')
axis equal; axis([xlower,xupper,ylower,yupper])
xlabel('y (mm)'); ylabel('x (mm)');

% Plot contour of SD
figure('Name','Standard Deviation'); contourf(x_2D,y_2D,SDxy,50,...
    'edgecolor','none'); hold on;
% quiver(x_2D,y_2D,u,v,3);
plot([x_2D(proloc,1) x_2D(proloc,w)],[y_2D(proloc,1) y_2D(proloc,w)], 'r');
SDxy_max = max(max(SDxy(iupper:ilower,jlower:jupper)));
SDxy_min = min(min(SDxy(iupper:ilower,jlower:jupper)));
h1 = colorbar('EastOutside');
caxis([SDxy_min SDxy_max]); %shading interp
set(get(h1,'ylabel'),'String','Standard Deviation (m/s)')
axis equal; axis([xlower,xupper,ylower,yupper])
xlabel('y (mm)'); ylabel('x (mm)');

% plot velocity magnitude across a profile
figure('Name','Velocity Magnitude across a profile');...
    plot(x_2D(proloc,:),Uxy(proloc,:));
axis([xlower,xupper,min(Uxy(proloc,jlower:jupper)),...
    max(Uxy(proloc,jlower:jupper))]);
xlabel('y (mm)'); ylabel('Velocity (m/s)');

% plot SD across a profile
figure('Name','Standard Deviation across a profile');
plot(x_2D(proloc,:),SDxy(proloc,:));

```



```

axis([xlower,xupper,min(SDxy(proloc,jlower:jupper)),...
      max(SDxy(proloc,jlower:jupper))]);
xlabel('y (mm)');   ylabel('Standard Deviation, \sigma (m/s)');

% plot TKE across a profile
figure('Name','TKE across a profile'); plot(x_2D(proloc,:),TKE);
axis([xlower,xupper,min(TKE(jlower:jupper)),max(TKE(jlower:jupper))]);
xlabel('y (mm)');   ylabel('TKE');

% plot epsilon across a profile
figure('Name','Epsilon across a profile'); plot(x_2D(proloc,:),epsilon(:));
axis([xlower,xupper,min(epsilon(jlower:jupper)),max(epsilon(jlower:jupper))]);
xlabel('y (mm)');   ylabel('\epsilon');

%% Write u, v, and w to *.csv file

if Export == 1
%write.xlsx file for variables on separate sheets depending on ...
% what stats file you have chosen
%The Variables of v and u are switched.  DaVis program interprets the
%upward trajectory as v, and in our data we want it to be u.  That is why
%they are switched here.
xlswrite('ProfilesfromUstats.xlsx',{'Position' 'u_ave' 'Uu' 'uut'
    'Uuu_plus' 'v_ave' 'Uv' 'vvt' 'Uvv_plus' 'uvv' 'Uuv_plus' 'Position2'
    'u_ave2' 'Uu2' 'uut2' 'Uuu_plus2' 'v_ave2' 'Uv2' 'vvt2' 'Uvv_plus2'
    'uvv2' 'Uuv_plus2'},Serial,'A1:V1'), warning off MATLAB:xlswrite:AddSheet;

% M_Uxy = zeros(jupper-jlower+1,6);
M_Uxy = zeros(2*BL,6);
% M_Uxy(:,2) = 0.001*x_2D(proloc,jlower+1:jupper+1);
M_Uxy(1:BL,2) = 0.001*(dx:dx:BL*dx); % Spread by geometry
M_Uxy(BL+1:2*BL,2) = 0.001*((jupper-jlower+2-BL)*dx:dx:305.-dx);
M_Uxy(:,3) = z;
M_Uxy(1:BL,4) = v(proloc,jlower:jlower+BL-1);%vfrom DaVis is actually u in Star
M_Uxy(BL+1:2*BL,4) = v(proloc,jupper-(BL-1):jupper);

```

```

M_Uxy(1:BL,5) = u(proloc,jlower:jlower+BL-1);%u from DaVis is actually v in Star
M_Uxy(BL+1:2*BL,5) = u(proloc,jupper-(BL-1):jupper);
M_Uxy(1:BL,6) = u(proloc,jlower:jlower+(BL-1));% we must assume that w=v
M_Uxy(BL+1:2*BL,6) = u(proloc,jupper-(BL-1):jupper);
dlmwrite('Inlet-uvw.csv',M_Uxy,'delimiter',' ','precision',4,'-append')

```

```

%% Write k to *.csv file

```

```

K1 = zeros(2*BL,4);
K1(1:BL,2) = 0.001*(dx:dx:BL*dx); % Spread by geometry
K1(BL+1:2*BL,2) = 0.001*((jupper-jlower+2-BL)*dx:dx:305.-dx);
K1(:,3) = z;
K1(1:BL,4) = TKE(jlower:jlower+(BL-1));
K1(BL+1:2*BL,4) = TKE(jupper-(BL-1):jupper);
dlmwrite('Inlet-k.csv',K1,'delimiter',' ','precision',4,'-append')

```

```

%% Write epsilon to *.csv file

```

```

eps1 = zeros(2*BL,4);
eps1(1:BL,2) = 0.001*(dx:dx:BL*dx); % Spread by geometry
eps1(BL+1:2*BL,2) = 0.001*((jupper-jlower+2-BL)*dx:dx:305.-dx);
eps1(:,3) = z;
eps1(1:BL,4) = epsilon(jlower:jlower+(BL-1));
eps1(BL+1:2*BL,4) = epsilon(jupper-(BL-1):jupper);
dlmwrite('Inlet-epsilon.csv',eps1,'delimiter',' ','precision',4,'-append')

```

```

load(strcat(p,f1));
xlswrite('ProfilesfromUstats.xlsx',{'=OFFSET(A$5,5*(ROW()-2),0)'},...
    Serial,'L5:L5'), warning off MATLAB:xlswrite:AddSheet;

```

```

v_ave(isnan(v_ave))=0;
Uv(isnan(Uv))=0;

```

```

vvt(isnan(vvt))==0;
Uvv_plus(isnan(Uvv_plus))==0;

u_ave(isnan(u_ave))==0;
Uu(isnan(Uu))==0;
uut(isnan(uut))==0;
Uuu_plus(isnan(Uuu_plus))==0;

uv_ave(isnan(uv_ave))==0;
Uuv(isnan(Uuv))==0;
uvt(isnan(uvt))==0;
Uuv_plus(isnan(Uuv_plus))==0;

uvvvt(isnan(uvvvt))==0;
Uuvuv_plus(isnan(Uuvuv_plus))==0;

profile=[X(proloc,:)','v_ave(proloc,:)','Uv(proloc,:)','...
        vvt(proloc,:)','Uvv_plus(proloc,:)'];
profilev=[X(proloc,:)','u_ave(proloc,:)','Uu(proloc,:)','uut(proloc,:)','...
        Uuu_plus(proloc,:)'];
profileuv=[X(proloc,:)','uv_ave(proloc,:)','Uuv(proloc,:)','...
        uvt(proloc,:)','Uuv_plus(proloc,:)'];
profilemag=[X(proloc,:)','uv_ave(proloc,:)','Uuv(proloc,:)','...
        uvvvt(proloc,:)','Uuvuv_plus(proloc,:)'];
profilewhole=[X(proloc,:)','v_ave(proloc,:)','Uv(proloc,:)','...
        vvt(proloc,:)','Uvv_plus(proloc,:)','u_ave(proloc,:)','Uu(proloc,:)','...
        uut(proloc,:)','Uuu_plus(proloc,:)','uvt(proloc,:)','Uuv_plus(proloc,:)'];

xlswrite('ProfilesfromUstats.xlsx',profilewhole,Serial,'A2:K173'), ...
        warning off MATLAB:xlswrite:AddSheet;
end
toc;

```

Appendix H

Interpolator Code for StarCCM+

```

% Code to interpolate the PIV data to a fine grid for input to Star-CCM+

close all; clear all; clc
tic;

%% Read in the files to be interpolated.
% Open the velocity, epsilon, and k files
sprintf('%c','Select the .csv file for the average velocity:')
[f1,p] = uigetfile('.csv'); % Ask user to choose velocity file
[data]=xlsread([p,f1]);
x_o=data(:,1); y_o=data(:,2); z_o=data(:,3);
u_o=data(:,4); v_o=data(:,5); w_o=data(:,6);

sprintf('%c','Select the .csv file for the epsilon:')
[f1,p] = uigetfile('.csv'); % Ask user to choose velocity file
[epsdata]=xlsread([p,f1]);
eps_o=epsdata(:,4);

sprintf('%c','Select the .csv file for the k:')
[f1,p] = uigetfile('.csv'); % Ask user to choose velocity file
[kdata]=xlsread([p,f1]);
k_o=kdata(:,4);

values=1; i=1;
while y_o(i)<y_o(i+1)
    values=values+1;
    i=i+1;
end

```

```

%%
originalsize=size(y_o);
y_1=zeros(values+2,1);
y_1(2:values+1)=y_o(1:values);
y_1(values+2)=0.3048;

z_1=zeros(values+2,1);
z_1(1:values)=z_o(values+1:values*2);
z_1(values+2)=0.1524;
z_1(values+1)=-0.1524;

data_1=zeros(originalsize+(values*4)+8,6);
epsdata2=zeros(originalsize+(values*4)+8,4);
kdata2=zeros(originalsize+(values*4)+8,4);

data_1(1:originalsize,:)=data;
epsdata2(1:originalsize,:)=epsdata;
kdata2(1:originalsize,:)=kdata;

count=0;
for i=originalsize+1:values+2+originalsize
    count=count+1;
    data_1(i,1)=0;
    data_1(i,2)=y_1(count);
    data_1(i,3)=-0.1524;
    data_1(i,4)=0;
    data_1(i,5)=0;
    data_1(i,6)=0;
    %     epsdata2(i,1)=0;
    %     epsdata2(i,2)=y_1(count);
    %     epsdata2(i,3)=-0.1524;
    %     epsdata2(i,4)=0;
    kdata2(i,1)=0;
    kdata2(i,2)=y_1(count);

```

```

        kdata2(i,3)=-0.1524;
        kdata2(i,4)=0;
    end
    count=0;
    for i=originalsize+values+3:(values*2)+4+originalsize
        count=count+1;
        data_1(i,1)=0;
        data_1(i,2)=y_1(count);
        data_1(i,3)=0.1524;
        data_1(i,4)=0;
        data_1(i,5)=0;
        data_1(i,6)=0;
        %     epsdata2(i,1)=0;
        %     epsdata2(i,2)=y_1(count);
        %     epsdata2(i,3)=0.1524;
        %     epsdata2(i,4)=0;
        kdata2(i,1)=0;
        kdata2(i,2)=y_1(count);
        kdata2(i,3)=0.1524;
        kdata2(i,4)=0;
    end
    count=0;
    for i=originalsize+(values*2)+5:(values*3)+6+originalsize
        count=count+1;
        data_1(i,1)=0;
        data_1(i,2)=0;
        data_1(i,3)=z_1(count);
        data_1(i,4)=0;
        data_1(i,5)=0;
        data_1(i,6)=0;
        %     epsdata2(i,1)=0;
        %     epsdata2(i,2)=0;
        %     epsdata2(i,3)=z_1(count);
        %     epsdata2(i,4)=0;
        kdata2(i,1)=0;

```

```

        kdata2(i,2)=0;
        kdata2(i,3)=z_1(count);
        kdata2(i,4)=0;
    end
    count=0;
    for i=originalsize+(values*3)+7:(values*4)+8+originalsize
        count=count+1;
        data_1(i,1)=0;
        data_1(i,2)=0.3048;
        data_1(i,3)=z_1(count);
        data_1(i,4)=0;
        data_1(i,5)=0;
        data_1(i,6)=0;
        %     epsdata2(i,1)=0;
        %     epsdata2(i,2)=0;
        %     epsdata2(i,3)=z_1(count);
        %     epsdata2(i,4)=0;
        kdata2(i,1)=0;
        kdata2(i,2)=0;
        kdata2(i,3)=z_1(count);
        kdata2(i,4)=0;
    end

    %% Define the Fine Grid
    % yp=[0.0018:0.0002:0.3032]';
    y=y_1;%[0.00:0.0002:0.3048]';
    % zp=[-0.1507:0.0002:0.1507]';
    number=size(y,1);
    z=[-0.1524:((0.1524*2)/(number-1)):0.1524]';

    %% Interpolate the data to a fine grid
    Fu = TriScatteredInterp(data_1(:,3),data_1(:,2),data_1(:,4));
    [qx,qy] = meshgrid(z,y);
    u = Fu(qx,qy);

```

```

Fv = TriScatteredInterp(data_1(:,3),data_1(:,2),data_1(:,5));
[qx,qy] = meshgrid(z,y);
v = Fv(qx,qy);
figure
contourf(v)
title('v')

Fw = TriScatteredInterp(data_1(:,3),data_1(:,2),data_1(:,6));
[qx,qy] = meshgrid(z,y);
w = Fw(qx,qy);

Feps = TriScatteredInterp(epsdata2(:,3),epsdata2(:,2),epsdata2(:,4));
[qx,qy] = meshgrid(z(2:131),y_o(1:130));
eps1 = Feps(qx,qy);
eps1(isnan(eps1))=0;
figure
contourf(eps1)
title('epsilon')

Fk = TriScatteredInterp(kdata2(:,3),kdata2(:,2),kdata2(:,4));
[qx,qy] = meshgrid(z,y);
k1 = Fk(qx,qy);
k1(isnan(k1))=0;
figure
contourf(k1)
title('TKE')

%% Now we want to make the left and right side the same as the top side
eps=eps1;
eps(:,1:70)=eps1(:,1:70)+flipdim(eps1(end-69:end,:),2);
eps(:,end-69:end)=eps1(:,end-69:end)+eps1(end-69:end,:);
figure
contourf(eps)
title('epsilon with left and right sides same as top');

```



```

k=k1;

k(:,1:70)=k1(:,1:70)+flipdim(k1(end-69:end,:),2);
k(:,end-69:end)=k1(:,end-69:end)+k1(end-69:end,:);

figure

contourf(k)

title('TKE with left and right sides same as top');

%% Write the files
Vel=zeros(number*number,6);
epsilon=zeros(number*number,4);
turb=zeros(number*number,4);
omega1=zeros(number*number,4);
omega2=zeros(number*number,4);

count=0;
for i=1:number
    for j=1:number
        count=count+1;
        Vel(count,:)= [0,y(i),z(j),u(i,j),v(i,j),w(i,j)];
        %         epsilon(count,:)= [0,y(i),z(j),eps(i,j)];
        turb(count,:)= [0,y(i),z(j),k(i,j)];
    end
end
count=0;
for i=1:number-2
    for j=1:number-2
        count=count+1;
        %         Vel(count,:)= [0,y(i),z(j),u(i,j),v(i,j),w(i,j)];
        epsilon(count,:)= [0,y(i),z(j),eps(i,j)];
        %         turb(count,:)= [0,y(i),z(j),k(i,j)];
    end
end

small=min(Vel);
smalleps=min(epsilon);

```

```

smallk=min(turb);

Vel(isnan(Vel))=small(6);
epsilon(isnan(epsilon))=smalleps(4);
turb(isnan(turb))=smallk(4);

% Create Omega for Transition Model
omega1(:,1:3) = epsilon(:,1:3);
omega2(:,1:3) = epsilon(:,1:3);

B = 0.09; % Cmu parameter found in turbulence solvers
for i = 1:length(epsilon(:,1))
    omega1(i,4) = epsilon(i,4)/turb(i,4);
    omega2(i,4) = epsilon(i,4)/(B*turb(i,4));
end

% Write the velocity inlet file
header=['X,Y,Z,u,v,w,'];
outid = fopen('Inlet-uvw-interp.csv', 'w+');
fprintf(outid, '%s', header);
fprintf(outid, '\n');
fclose(outid);

dlmwrite('Inlet-uvw-interp.csv',Vel,'delimiter',' ','precision',4,'-append')

% Write the epsilon file for the inlet
header=['X,Y,Z,epsilon,'];
outid2 = fopen('Inlet-epsilon-interp.csv', 'w+');
fprintf(outid2, '%s', header);
fprintf(outid2, '\n');
fclose(outid2);

dlmwrite('Inlet-epsilon-interp.csv',epsilon,'delimiter',' ','precision',4,'-append')

% Write the k file for the inlet

```

```

header=['X,Y,Z,k,'];
outid3 = fopen('Inlet-k-interp.csv', 'w+');
fprintf(outid3, '%s', header);
fprintf(outid3, '\n');
fclose(outid3);

dlmwrite('Inlet-k-interp.csv',turb,'delimiter',' ','precision',4,'-append')

% Write the omega files for the inlet
header=['X,Y,Z,w,'];
outid4 = fopen('Inlet-w1-interp.csv', 'w+');      % Omega 1 formulation (w = e/k)
fprintf(outid4, '%s', header);
fprintf(outid4, '\n');
fclose(outid4);

dlmwrite('Inlet-w1-interp.csv',omega1,'delimiter',' ','precision',4,'-append')

outid5 = fopen('Inlet-w2-interp.csv', 'w+');      % Omega 2 formulation (w = e/Bk)
fprintf(outid5, '%s', header);
fprintf(outid5, '\n');
fclose(outid5);

dlmwrite('Inlet-w2-interp.csv',omega2,'delimiter',' ','precision',4,'-append')
toc;

% Code to interpolate the Temperature data to a fine grid for input to Star-CCM+

close all; clear all; clc;
tic;
%% Read in the files to be interpolated.
% Open the velocity, epsilon, and k files
sprintf('%c','Select the .csv file for the inlet temperature:')
[f1,p] = uigetfile('.csv'); % Ask user to choose velocity file
[inlet]=xlsread([p,f1]);

```

```

inletT=inlet(:,4);
inletz=inlet(:,3);
inlety=inlet(:,2);

sprintf('%c','Select the .csv file for the plate temperature:')
[f1,p] = uigetfile('.csv'); % Ask user to choose velocity file
[plate]=xlsread([p,f1]);
plateT=plate(:,4);
platex=plate(:,1);
platez=plate(:,3);

%% Define the Fine Grid for the plate
platex_fine=[0:0.001:1.859]';
platez_fine=[-0.1507:0.001:0.1507]';

% and for the inlet temperature
inlety_fine=[0.076:0.0005:.229]';
inletz_fine=[-0.102:0.0005:0.102]';

%% Interpolate the data to a fine grid
Fu = TriScatteredInterp(inlety,inletz,inletT);
[qx,qy] = meshgrid(inlety_fine,inletz_fine);
InletT = Fu(qx,qy);

Fv = TriScatteredInterp(platex,platez,plateT);
[qx,qy] = meshgrid(platex_fine,platez_fine);
PlateT = Fv(qx,qy);

%% Sort to write out the files

TempI=zeros(size(InletT,1)*size(InletT,2),4);
TempPlate=zeros(size(PlateT,1)*size(PlateT,2),4);

count=0;
for i=1:size(InletT,1)

```

```

    for j=1:size(InletT,2)
        count=count+1;
        TempI(count,:)= [0,inlety_fine(j),inletz_fine(i),InletT(i,j)];
    end
end

count=0;
for i=1:size(PlateT,1)
    for j=1:size(PlateT,2)
        count=count+1;
        TempPlate(count,:)= [platex_fine(j),0,platez_fine(i),PlateT(i,j)];
    end
end

smallTP=min(TempPlate);
TempPlate(isnan(TempPlate))=smallTP(4);

%% Write the inlet temperature file
header=['X,Y,Z,Temp,'];
outid = fopen('Inlet-Temp-interp.csv', 'w+');
fprintf(outid, '%s', header);
fprintf(outid, '\n');
fclose(outid);

dlmwrite('Inlet-Temp-interp.csv',TempI,'delimiter',' ','precision',7,'-append')

header=['X,Y,Z,Temp,'];
outid = fopen('HeatedWall-Temp-interp.csv', 'w+');
fprintf(outid, '%s', header);
fprintf(outid, '\n');
fclose(outid);

dlmwrite('HeatedWall-Temp-interp.csv',TempPlate,'delimiter',' ','precision',7,'-append')
toc;

```

Appendix I

Code to Compute Correlations and Momentum Thickness

```

%% Clear and close everything
clc; close all;

% This program will let you select the plate temperature .csv file, then
% it plots the temperature contour and provides the Forced and Mixed
% correlations, given the inputs below. The last part provides several
% non-dimensional and dimensional parameters for the case.
%%
opposed = 0; % If for an opposed case, opposed = 1
U = 4.489; %m/s free stream 2.62 4.489
rho = 1.0128;
mu = 1.8187*10(-5);
nu = mu/rho;

u_data1 = data1(:,2);
x_data1 = data1(:,1);

u_data2 = data2(:,2);
x_data2 = data2(:,1);

u_data3 = data3(:,2);
x_data3 = data3(:,1);
%% Selecting the csv files
sprintf('%c','Select the Heated Plate Temp file')
[f0,p0] = uigetfile('*.csv','Select the csv file');

Ai=xlsread(strcat(p0,f0));

```

```

xi=Ai(:,1);
yi=Ai(:,3);
ti=Ai(:,4);

%find unique x and y grid points
ai=sort(unique(xi(6:end)));
bi=sort(unique(yi(6:end)));
Ni=length(xi);

%initialize matrices
Ti=zeros(length(bi),length(ai));
Xi=zeros(length(bi),length(ai));
Yi=zeros(length(bi),length(ai));

%generate grid matrix
[Xi,Yi]=meshgrid(ai,bi);

y_dum=[-0.152;yi(1:5);0.152];
X=cat(2,zeros(7,1),Xi);
Y=cat(2,y_dum,Yi);

%generate variable matrices (nans where no data available)
for ni=1:Ni
    Ii=find(bi==yi(ni));
    Ji=find(ai==xi(ni));
    Ti(Ii,Ji) = ti(ni);
end
T = cat(2,[0;ti(1:5);0],Ti);

%%
%Plot Plate Temp
figure('Name','Plate Temp'); contourf(X,Y,T,200);colorbar; shading flat;...
    caxis([290 430]);xlabel('x [m]','FontName','Times New Roman');
ylabel('z [m]','FontName','Times New Roman');title('Plate Temp [K]');
axis image
filename=strcat(p0(end-2:end-1),'.jpg');

```

```

saveas(gcf,filename,'jpg')

%Save figure to be used in the movie later
% [I0,mapI0]=getframe(gcf);
%% Now plot the centerline temperature and correlations for the heat flux
T_center = T(4,:);

% Forced convection correlations
% from Kays and Crawford 12-18, turbulent flow
cp = 1005;
Pr = 0.7;
k = 26.37*10^-3;

Gr_L = (9.81/295).*(T_center-295).*X(4,:).^3./(mu/rho)^2;
Ra_L = Pr*Gr_L;
Re_x = rho*U.*X(4,:)./mu;
St = (0.0287*Re_x.^(-0.2))./(0.169*Re_x.^(-0.1)*(13.2*Pr-9.25)+0.85)';
h = rho*U*cp*St;
Nu_Kays = h.*X(4,:)./k;
Flux_Kays = h.*(T_center'-(21+273));

% Incropera Nusselt number correlation
% Eqn 7.36, Nu for Turbulent flow over isothermal plate
Nu_x = 0.0296.*Re_x.^(4/5)*Pr^(1/3);
h_inc = Nu_x'.*k./X(4,:);
Flux_Incropera = h_inc.*(T_center'-(21+273));

figure
plot(X(4,:),Flux_Kays); hold on;
plot(X(4,:),Flux_Incropera,'r'); hold on;

%% Compute the Mixed Correlations
% Using the popular notion that Nu = Nu_f +- Nu_n

% Compute the natural convection correlation, 9.26 in Incropera
Nu_x_nat = (0.825+(0.387.*Ra_L.^(1/6))./(1+0.492/Pr)^(9/16)).^(8/27)).^2;

```



```

% Compute the mixed convection Nusselt number by either adding (aided) or
% subtracting (opposed) the natural and forced correlations

Nu_x_mixed = (Nu_x.^3 + Nu_x_nat.^3).^(1/3);
if opposed==1
    Nu_x_mixed = (Nu_x.^3 - Nu_x_nat.^3).^(1/3);
end

Nu_x_mixed2 = (Nu_Kays.^3 + Nu_x_nat'.^3).^(1/3);
if opposed==1
    Nu_x_mixed2 = (Nu_Kays.^3 - Nu_x_nat'.^3).^(1/3);
end

% Compute heat flux for mixed
Flux_mixed1 = (Nu_x_mixed'.*k./X(4,:)).*(T_center'-294);
Flux_mixed2 = (Nu_x_mixed2.*k./X(4,:)).*(T_center'-294);

plot(X(4,:),Flux_mixed1,'k'); hold on;
plot(X(4,:),Flux_mixed2,'g');
legend('Kays','Incropera','Incropera Mixed','Kays Mixed')

%% Compute the Case Dimensionless Parameters
[rte,index1]=min(abs(X(4,:)-.1617345));
X1 = X(4,index1);
[rte,index2]=min(abs(X(4,:)-.7776845));
X2 = X(4,index2);
[rte,index3]=min(abs(X(4,:)-1.3936345));
X3 = X(4,index3);

T1 = T_center(index1);
T2 = T_center(index2);
T3 = T_center(index3);

Re_Dh = rho*U*(0.3048)/mu;

```

```

Re_1 = rho*U*0.1617345/mu;
Re_2 = rho*U*0.7776845/mu;
Re_3 = rho*U*1.3936345/mu;

Gr_1 = 9.81/340*(T1-295)*0.1617345^3/nu^2;
Gr_2 = 9.81/340*(T2-295)*0.7776845^3/nu^2;
Gr_3 = 9.81/340*(T3-295)*1.3936345^3/nu^2;

delta2_1 = trapz(x_data1./1000,...
    (u_data1./U).*(1.-(u_data1./U)));
delta2_1b = 0.664*sqrt(nu*X1/U);
Re_delta2_1 = U*delta2_1/nu;

delta2_2 = trapz(x_data2./1000,...
    (u_data2./U).*(1.-(u_data2./U)));
delta2_2b = 0.664*sqrt(nu*X2/U);
Re_delta2_2 = U*delta2_2/nu;

delta2_3 = trapz(x_data3./1000,...
    (u_data3./U).*(1.-(u_data3./U)));
delta2_3b = 0.664*sqrt(nu*X3/U);
Re_delta2_3 = U*delta2_3/nu;

```

Appendix J

Shear Velocity Code to Compute u_τ

```

% Code to fit data to the Spaulding Profile and find u-tau

% Drag data into the workspace - A Ustats file will work best
u=data(:,2);
y=data(:,1); % in mm
opposed = 0; % opposed= 1 if the data is opposed, 0 if aided
if opposed == 1
    u = flipdim(u,1);
    y = flipdim(y,1);
end

rho = 1.0215;
mu = 1.83*10^(-5);
k=0.41;
B=5;
% nu=(1.773E-5);
nu = 1.79E-5;
P = 653.5; %torr
T = 273+23.6; %K
phi=0.34; %Relative Humidity

utau=0.254;
uplus=u/utau;
yplus=0.001*y*utau/nu;
Spaul=uplus+exp(-k*B)*(exp(k*uplus)-1-k*uplus-(k*uplus).^2/2-(k*uplus).^3/6);

%% Compute the Spaulding Profile

```

```

points=80;
LowerPoint=10;

A0 = [0      % y0 in meters
      0.41    % kappa
      5       % B
      .2];    % u_tau

Alb = [-0.1 0.1 3 0]; % lower bound
Aub = [0.1 1 9 1]; % upper bound

for l=1:100 % Repeat least squares curve fit so bad initial guess is overcome
    % Fitting 4 constants ydata is u velocity, function yields y in Kendall
    % paper
    F = @(A,ydata)...
        A(1) + nu/A(4)*(ydata/A(4) + exp(-A(2)*A(3))*(exp(A(2)*ydata/A(4))...
        - 1 - A(2)*ydata/A(4)...
        - 0.5*(A(2)*ydata/A(4)).^2 - (A(2)*ydata/A(4)).^3/6. ));

    [A,resnorm] = lsqcurvefit(F,A0,u(LowerPoint:points),...
        0.001*y(LowerPoint:points),Alb,Aub)

    % % Fitting 2 constants
    % kappa = 0.41;
    % B = 5.0;
    %
    % F = @(A,ydata)...
    %     A(1) + nu/A(4)*(ydata/A(4) + exp(-kappa*B)*(exp(kappa*ydata/A(4))...
    %     - 1 - kappa*ydata/A(4)...
    %     - 0.5*(kappa*ydata/A(4)).^2 - (kappa*ydata/A(4)).^3/6. ));
    %
    % [A,resnorm] = lsqcurvefit(F,A0,u(1:points),...
    %     0.001*y(1:points),Alb,Aub)

    A0 = A;

```

```

end

%% Compute Uncertainty of the Wall Shear
[ShearUncertainty,nu] = ShearVelocityUncertaintyfunc(T,P,phi,y,u,data,opposed);
U_utau = mean(ShearUncertainty(10:end-10));

%% Non-dimensionalize experimental profile
yPlus = ( 0.001*y - A(1) ) * A(4) / nu; % Convert mm to m by *0.001
uPlus = u / A(4);

%% Spalding profile
yPlus_Spal = ( F(A,u) - A(1) ) * A(4) / nu;

%% Law of the wall
uPlus_LofW = log( (0.001*y - A(1) ) * A(4) / nu ) / A(2) + A(3);

% Plot non-dimensional profiles
figure; semilogx(yPlus(LowerPoint:points), uPlus(LowerPoint:points), 'x');
axis([1,max(yPlus),...
      0,max(uPlus)]);
xlabel('y^+'); ylabel('u^+');
hold on; semilogx(yPlus_Spal, uPlus, 'r');
semilogx(yPlus(1:18), yPlus(1:18), 'g');
semilogx(yPlus(10:end), uPlus_LofW(10:end), 'm');
% semilogx(Spaul, uPlus, 'k');
legend('Experiments','Spalding','u^+ = y^+','Law of the Wall','Location','Best');

%% Now we want to confirm the linearity of the total shear stress, from Adrian 07

uv = data(:,10);
dudy = u(2:end);
for i=1:size(u,1)-1;
    dudy(i) = (u(i+1)-u(i)) / (y(i+1)-y(i)) * 1000;
    tau(i) = -rho*uv(i) + mu*dudy(i);
end
% tau=tau';
tau_linefunc=fit(y(2:end),tau(1:end),'poly1');

```

```
tau_line=tau_linefunc(y);

figure
plot(y(2:end),tau'); hold on;
plot(y,-rho*uv,'k')
plot(y(2:end),mu*dudy,'r')
plot(y,tau_line,'g')
xlabel('y');    ylabel('\tau');
```

Appendix K

Copyright Permissions

Copyright permission from Engineering Laboratory Design, Inc. for use of Wind Tunnel Drawings in Appendix B. From email correspondence:

Hello Barton and Jared,

You may use the drawings that we furnished with the wind tunnel in your papers. Indicate that the images are "Used with permission" and credit Engineering Laboratory Design, Inc.

Thanks for requesting permission.

Regards,

Sig Anderson

Sigurd W. Anderson, President

Engineering Laboratory Design, Inc. 2021 South Highway

61 PO Box 278 Lake City, MN 55041 USA

mariner@eldinc.com

651-345-4515

800-795-8536

FAX 651-345-5095

www.eldinc.com

Jeff R. Harris

175 S. 830 E.
Smithfield, UT 84335

Ph.D. Candidate

✉ jeff.harr@aggiemail.usu.edu
☎ 435-232-9976

Education & Training

Utah State University

Logan, UT

Ph.D. Mechanical Engineering

May 2014

- Topic: Experimental Validation for CFD Simulations of Convective Flow
- Thermal/Fluids Experiments and Computational Fluid Dynamics

3.90 GPA

M.S. Mechanical Engineering

May 2012

- Topic: Relative Importance of Some Error Sources in Particle Image Velocimetry
- Thermal/Fluids Experiments and Computational Fluid Dynamics

3.92 GPA

B.S. Mechanical Engineering

May 2010

- Aerospace Emphasis, Math Minor, Passed FE Exam

3.86 GPA

Idaho National Laboratory

Idaho Falls, ID

Modeling, Experimentation, and Validation School

June 2010

- Studied safety analysis, risk assessment, and validation techniques in nuclear science

Relevant Experience

Experimental Fluid Dynamics Laboratory

Utah State University

Graduate Research Assistant

Aug. 2010 – current

- Supervise a team of 4-8 graduate and undergraduate students on validation experiments and measurement techniques on projects funded by the Department of Energy, Nuclear Regulatory Commission and ExxonMobil
- Design the experimental apparatus, budget, plan, and execute validation experiments in and simulations of the Transient/Mixed Convection Wind Tunnel
- Analysis of error sources in particle image velocimetry and uncertainty introduced from non-repeatability of particle image velocimetry and other fluid flow measurements

Idaho National Laboratory

Idaho Falls, ID

Research Intern

Summers 2009, 2010

- Acquired particle image velocimetry data for the setup of the Bypass Flow Experiment and swirl jet validation studies using matched index of refraction
- Designed equipment upgrades for more efficient data acquisition
- Presented research to Nuclear Science group at INL

Apogee Instruments, Inc.

Logan, UT

Mechanical Engineer

May 2008 – June 2009

- Designed and improved instruments for climate and weather measurements
- Communicated designs to multi-disciplinary team to enhance instrument performance

Technical Skills

Experimental Skills

- Experiment budgeting, planning and apparatus design to optimize data acquisition and accuracy, and uncertainty analysis of results
- 2- and 3- component time-averaged and time-resolved particle image velocimetry
- Hot-wire anemometry, thermocouple and various pressure measurements
- Data acquisition timing and control using LabView and DaVis 8

Software and Modeling Skills

- Computational fluid dynamics using StarCCM+ and familiarity with Fluent
- Finite element modeling with FEMAP and solid modeling using SolidWorks and Solid Edge
- Serial and parallel computing with Fortran and Matlab

Publications

Peer-Reviewed Conference Papers and Presentations

1. Harris, J., Lance, B., Smith, B. "Design of Apparatus for Validation Experiments," ANS Annual Meeting, Atlanta, GA, 2013.
2. Lance, B., Harris, J., et. al. "Validation Study on Forced and Mixed Convection in the Rotatable Buoyancy Tunnel." ASME FEDSM, Incline Village, NV, 2013.
3. Smith, B., Lance, B. Harris, J. Iverson, J. Spall, R. "The RoBuT for CFD Validation of Natural, Mixed, and Forced Convection," ASME V&V Symposium, Las Vegas, NV, 2013.
4. Harris, J., Lance, B., Smith, B., Spall, R. "Transient Mixed Convection Validation Facility and Study," NURETH-15, Pisa, Italy, 2013.
5. Harris, J., Lance, B., Iverson, J. "Forced Convection Validation Experiment and Simulation." ANS Student Conference, Boston, MA, 2013 - **awarded "Best Overall Graduate Paper"**
6. Harris, J., Wilson, B., Smith, B. "Investigation of Relative Importance of Some Error Sources in Particle Image Velocimetry," ASME Fluids Engineering Summer Meeting, Puerto Rico, USA, 2012.
7. Harris, J., Nani, D., Jones, K., Khodier, M., Smith, B. "Investigation of the Uncertainty of a Validation Experiment due to Uncertainty in its Boundary Conditions," NURETH-14, 2011.
8. Wilson, B., Smith, B., Spall, R., Harris, J. "Validation of Unsteady CFD in a Confined Row of Cylinders," FEDSM2010-ICNMM2010, Proceedings of the ASME Fluids Engineering Conference, Montreal, Canada, 2010.

Non-Peer-Reviewed Conference Papers and Presentations

1. Harris, J., Lance, B., Smith, B. "Experimental Validation of Simulations for Buoyancy Opposed Convection," APS Division of Fluid Dynamics Meeting, Pittsburgh, PA, 2013
2. Harris, J., Lance, B. "Design and Implementation of Simulation Validation Experiments for Passive Cooling Features in Nuclear Reactors." USU Graduate Research Symposium, Logan, UT, 2013 - **Honorable Mention for Best Oral Presentation**
3. Wilson, B., Harris, J., Smith, B. "Uncertainty in Velocity Fluctuations for Two-Component PIV Measurements," APS Division of Fluid Dynamics, Baltimore, Maryland, 2011.
4. Wilson, B., Harris, J., Smith, B., Spall, R. E. "Unsteady Validation Metrics for CFD in a Cylinder Array," Proceedings of the CFD4NRS, Washington D.C., USA, 2010.

Awards & Societies

- College of Engineering Graduate Researcher of the Year, 2014
- Nuclear Regulatory Commission Fellowship Recipient, 2012
- Founding Vice-President of USU Student Section of the American Nuclear Society, 2012
- Graduate Teaching Assistant of the Year, 2011
- Outstanding Senior, Mechanical and Aerospace Engineering, 2010
- Nuclear Regulatory Commission Scholarship Recipient, 2009
- Tau Beta Pi Scholarship Recipient, 2009
- Academic Excellence Award, Mechanical and Aerospace Engineering, 2008
- USU Presidential Scholarship Recipient, 2008

- Student Host – GLOBAL 2013: International Nuclear Fuel Cycle Conference
- Reviewer – American Society of Mechanical Engineers IMECE Conference, 2013
- Reviewer – American Society of Mechanical Engineers HTFENMM Conference, 2012

EXPERIMENTAL VALIDATION DATA FOR CFD OF STEADY AND TRANSIENT
MIXED CONVECTION ON A VERTICAL FLAT PLATE

by

Blake W. Lance

A dissertation submitted in partial fulfillment
of the requirements for the degree

of

DOCTOR OF PHILOSOPHY

in

Mechanical Engineering

Approved:

Dr. Barton L. Smith
Major Professor

Dr. Robert E. Spall
Committee Member

Dr. Aaron Katz
Committee Member

Dr. Nick A. Roberts
Committee Member

Dr. Eric D. Held
Committee Member

Dr. Mark R. McLellan
Vice President for Research and
Dean of the School of Graduate Studies

UTAH STATE UNIVERSITY
Logan, Utah

2015

Copyright © Blake W. Lance 2015

All Rights Reserved

Abstract

Experimental Validation Data for CFD of Steady and Transient Mixed Convection on a Vertical Flat Plate

by

Blake W. Lance, Doctor of Philosophy

Utah State University, 2015

Major Professor: Dr. Barton L. Smith

Department: Mechanical and Aerospace Engineering

In this computer age, simulations are becoming common in science and engineering. One category of simulation, Computational Fluid Dynamics (CFD), begins with physical equations but adds approximations and calibrations in order to complete solutions. Translating these equations into computer languages may cause unintended errors. If the simulation results are to be used for decision making, their accuracy needs to be assessed. This accuracy assessment is the theory behind the field of Verification & Validation.

Verification involves confirming the translation of physical equations to computer language was performed correctly. It also features methods to detect many types of code errors. Validation is quite different in that it involves the comparison of experimental data with simulation outputs. This way, errors in simulation predictions may be assessed. Validation requires highly-detailed data and description to accompany these data, and uncertainties in these data are very important. Ideally, the validation experiment measures all information required for simulation inputs. Matching inputs ensures that any possible differences in the outputs are only due to the model.

The purpose of this work is to provide highly complete validation data to assess the accuracy of CFD simulations. This aim is fundamentally different from the typical discovery experiments common in research. The measurement of these physics was not necessarily original but performed with modern, high-fidelity methods. The data description was much more complete than found in discovery experiments. Data were tabulated (in table form) through an online database for direct use in simulations. All requisite boundary conditions were measured for use in Reynolds-Averaged Navier-Stokes (RANS) simulations. Detailed instrumentation and documentation were used to make the data more useful for CFD validation. This work fills the validation data gap for steady and transient mixed convection.

The physics in this study included mixed convection on a vertical flat plate. Mixed convection is a condition where both forced and natural convection influence fluid momentum and heat transfer phenomena. Flow was forced over a vertical flat plate in a facility specifically built for validation experiments. Thermal and velocity data were acquired for steady and transient flow conditions. The steady case included both buoyancy-aided and buoyancy-opposed mixed convection while the transient case was for buoyancy-opposed flow. The transient was a ramp-down flow transient, and results were ensemble-averaged for improved statistics. Uncertainty quantification was performed on all results with bias and random sources. Additionally, the transient data were used in a CFD simulation and results compared in a validation study.

An independent method of measuring heat flux was devised to assess the accuracy of commercial heat flux sensors (HFSs) used in the heated wall as they were believed to be in error. It measured the convective heat flux by the temperature gradient in air very near the plate surface. Its accuracy was assessed by error estimations and thorough uncertainty quantification. A further study was conducted to identify the error source of the HFSs.

This work is in multi-paper format with three unique chapters that are independent of each other and could be submitted for publication. Because of this, some sections are repeated for completeness.

(126 pages)

Public Abstract

Experimental Validation Data for CFD of Steady and Transient Mixed Convection on a Vertical Flat Plate

by

Blake W. Lance, Doctor of Philosophy

Utah State University, 2015

Major Professor: Dr. Barton L. Smith

Department: Mechanical and Aerospace Engineering

In this computer age, simulations are becoming common in science and engineering. One category of simulation, Computational Fluid Dynamics (CFD), begins with physical equations but adds approximations and calibrations in order to complete solutions. Translating these equations into computer languages may cause unintended errors. If simulation results are to be used for decision making, their accuracy needs to be assessed. This accuracy assessment is the theory behind the field of Verification & Validation.

Verification involves confirming the translation of physical equations to computer language was performed correctly. It also features methods to detect many types of code errors. Validation is quite different in that it involves the comparison of experimental data with simulation outputs. This way, errors in simulation predictions may be assessed. Validation requires highly-detailed data and description to accompany these data, and uncertainties in these data are very important. Ideally, the validation experiment measures all information required for simulation inputs. Matching inputs ensures that any possible differences in the outputs are only due to the model.

The purpose of this work is to provide highly complete validation data to assess the accuracy of CFD simulations. The physics were mixed convection. Convection is a heat transfer mode where heat is carried by a moving fluid. Mixed convection occurs where natural convection and forced convection forces are similar, such as in low-speed flows. A vertical flat plate is heated and used for a convection boundary condition. A wind tunnel that was built specifically for validation experiments was used. Air is the working fluid whose velocity is measured using a modern optical technique called Particle Image Velocimetry. Many thermocouples were used to measure the temperature of all four walls and the inlet air. Commercial heat flux sensors (HFSs) were used in the heated wall.

The two cases were steady and transient mixed convection. Steady mixed convection was studied in two orientations. First with buoyancy in the same direction of the flow and second with buoyancy in the opposite direction. The transient data were for a ramp-down flow transient. This unsteady flow was repeated many times for ensemble-averaging of the results. In both cases, uncertainty was estimated in all of the results. Additionally, the transient case was simulated with CFD, matching inputs, and a validation study was performed.

An additional study was conducted to assess the accuracy of the commercial HFSs as they were believed to be in error. The air temperature was measured very close to the wall surface. The temperature gradient is proportional to heat flux, the rate of heat energy transfer over an area. Potential errors of this method were estimated and a thorough uncertainty study was performed. Additionally, a study was performed to identify the error source of the HFSs.

Acknowledgments

The assistance, creativity, and trust of Dr. Barton L. Smith are what made this work possible. Also the assistance and example of Jeff Harris was quite inspiring. My colleagues in the Experimental Fluid Dynamics Lab over the years, who are too numerous to name without a high probably of forgetting at least one, are also to thank for the assistance in analysis and in friendship.

My family; especially my wife Rebekah with our children Jacob, Emily, and the little one on the way; was amazingly supportive and patient. The trust and encouragement of my parents inspired me from a young age towards higher education. I also thank my counselors and mentors in my youth for believing in me and giving guidance.

This research was performed using funding received from the U. S. Department of Energy Office of Nuclear Energy's Nuclear Energy University Programs. Also the scholarship and fellowship support of the U. S. Nuclear Regulatory Commission is greatly appreciated.

Blake W. Lance

Contents

	Page
Abstract	iii
Public Abstract	v
Acknowledgments	vii
List of Tables	xi
List of Figures	xii
Notation	xiv
Acronyms	xvii
1 Introduction	1
1.1 The Very High Temperature Reactor	1
1.2 Computational Fluid Dynamics Validation	1
1.3 Mixed Convection	5
1.4 Transient Convection	7
1.5 Wall Heat Flux	8
References	10
2 Experimental Validation Data for CFD of Steady Mixed Convection on a Vertical Flat Plate . .	13
2.1 Introduction	13
2.1.1 Computational Fluid Dynamics Validation	14
2.1.2 Mixed Convection	16
2.2 Experimental Facility	19
2.2.1 Rotatable Buoyancy Tunnel	19
2.2.2 Test Section	20
2.3 Analog Instrumentation and Signal Processing	22
2.3.1 Thermal Instrumentation	23
2.3.2 Particle Image Velocimetry	24
2.3.3 TC Probe	25
2.3.4 Atmospheric Instrumentation	27
2.3.5 Uncertainty Quantification	27
2.4 Boundary Conditions	28
2.4.1 BC Description	28
2.4.2 BC Data	31
2.5 Fluid and Material Properties	32
2.6 Test Conditions	32
2.7 System Response Quantities	32
2.7.1 SRQ Description	33
2.7.2 SRQ Data	38
2.8 Conclusions	39
References	40

3	Experimental Validation Data for CFD of Transient Mixed Convection on a Vertical Flat Plate	42
3.1	Introduction	42
3.1.1	Computational Fluid Dynamics Validation	43
3.1.2	Transient Flows	45
3.1.3	Mixed Convection	47
3.2	Experimental Facility	47
3.2.1	Rotatable Buoyancy Tunnel	48
3.2.2	Test Section	49
3.3	Analog Instrumentation and Signal Processing	52
3.3.1	Thermal Instrumentation	52
3.3.2	Particle Image Velocimetry	53
3.3.3	Atmospheric Instrumentation	55
3.3.4	Uncertainty Quantification	56
3.4	Boundary Conditions	56
3.4.1	BC Description	56
3.4.2	BC Data	58
3.5	Fluid and Material Properties	59
3.6	Test Conditions	59
3.7	System Response Quantities	60
3.7.1	SRQ Description	60
3.7.2	SRQ Data	63
3.8	Conclusions	63
	References	65
4	Wall Heat Flux Measurements in a Convecting Boundary Layer	67
4.1	Introduction	67
4.2	Theory	69
4.3	Method	71
4.4	Results	75
4.5	Conclusions	81
	References	81
5	Conclusions	83
	Appendices	84
A	Unsteady Computational Fluid Dynamics Simulations	85
A.1	Introduction	85
A.2	Methods	85
A.3	Results	86
A.4	Conclusions	89
B	Processing and Post-processing Codes	91
B.1	Introduction	91
B.2	Particle Image Velocity Uncertainty	92
B.3	Inlet Analysis	93
B.4	Boundary Condition Statistics	93
B.5	Interpolation Codes for Boundary Conditions	93
B.6	Virtual Origin	93
B.7	System Response Quantity Analysis	93
B.8	Transient Image Organization	94
B.9	Transient Computational Fluid Dynamics Grid Convergence Index	94
B.10	TC Probe Analysis	94
B.11	Custom Functions	94
C	Mixed Convection Parameters	95

D	Heated Wall Conduction Analysis	98
E	Permission Letter for Steady Mixed Convection Work	101
	References	103
Vita	104

List of Tables

Table	Page
2.1 The tabulated boundary conditions and system response quantities provided in this work . . .	14
2.2 Re_x , Gr_x , and Ri_x at the three locations in x at the spanwise center where SRQ data were acquired. The bulk velocity \bar{u}_{bulk} was 2.44 m/s. These apply for both cases presented.	17
2.3 Heated wall components and thicknesses with names from Fig. 2.4	22
2.4 PIV data parameters. Aided refers to buoyancy-aided case while Opposed refers to buoyancy-opposed case.	25
2.5 Boundary layer analysis results	31
2.6 Links to temperature boundary files for both cases	31
2.7 Links to velocity SRQ files for both cases	39
3.1 The available experimental data presented in this work separated into BC and SRQ types . . .	43
3.2 Gr_x as well as Re_x and Ri_x at the initial condition at the three locations in x at the spanwise center where data were acquired	48
3.3 Heated wall components and thicknesses with names from Fig. 3.4	51
3.4 PIV data parameters	54
4.1 Boundary layer analysis results from velocity data at the inlet	78
4.2 Heat flux results for both cases from the HFSs and the TC Probe results at all three x locations	80

List of Figures

Figure	Page
1.1 Very High Temperature Reactor core, [4]	2
1.2 Difficulty Spectrum of SRQs, after [5]. The variables y and x here are arbitrary.	4
1.3 Validation Hierarchy, after [9]	4
1.4 Wall heat flux comparing measurements with two correlations	9
2.1 The Validation Hierarchy, after [6]	16
2.2 System Response Quantity Difficulty Spectrum, after [3]. The variables y and x are arbitrary.	16
2.3 RoBuT flow components in the buoyancy-aided orientation	20
2.4 Heated wall cross section with component names as in Table 2.3. The relative thicknesses are to scale.	21
2.5 Particle images at x_2	26
2.6 TC probe with its reflection in the heated wall on the right	27
2.7 Measured temperatures on the test section boundaries	29
2.8 Measured streamwise velocity \bar{u} at the inlet for the buoyancy-opposed case	29
2.9 Normalized streamwise mean velocity \bar{u} and Reynolds normal stress $\overline{u'u'}$ at three locations in x for both cases	33
2.10 Measured streamwise mean velocity \bar{u} and streamwise Reynolds normal stress $\overline{u'u'}$ with buoyancy-aided (Aid), buoyancy-opposed (Opp), and their difference (Diff) at three locations in x	34
2.11 Measured temperature profiles for all three x locations for the opposed case	35
2.12 Measured wall heat flux plotted along streamwise direction x with correlations for mixed convection for the bouyancy-aided (Aid), buoyancy-opposed (Opp), and their difference (Aid-Opp). Heat Flux Sensor results are labeled as HFS and correlation results as Corr.	36
2.13 Streamwise mean velocity \bar{u} near the heated wall with linear fit for shear stress measurement of the buoyancy-opposed case	37
2.14 Mean streamwise velocity \bar{u} with several repeats at three locations in x for both cases	38

2.15	Measured mean streamwise Reynolds stress $\overline{u'u'}$ with several repeats at three locations in x for both cases	38
2.16	Scatter of instantaneous u' and v' at the y -location of largest $\overline{u'u'}$ for both cases at x_2	39
3.1	The Validation Hierarchy, after [6]	45
3.2	System Response Quantity Difficulty Spectrum, after [3]. The variables y and x are arbitrary.	45
3.3	RoBuT flow components as configured for transient data acquisition	49
3.4	Heated wall cross section with component names as in Table 3.3. The relative thicknesses are to scale.	50
3.5	Dewarped SRQ particle image at x_2 with mean background removed. Note the image scales are about a factor of nine different.	55
3.6	Measured temperatures on the test section boundaries	57
3.7	Measured streamwise velocity \bar{u} at the inlet and the initial condition	57
3.8	Bulk velocity across the inlet at the spanwise center ($z = 0$) through time	60
3.9	The streamwise velocity \bar{u} and Reynolds normal stress $\overline{u'u'}$ at three locations in x and five phases of the transient	62
3.10	High-resolution PIV data near the heated wall with linear fit	63
3.11	The heated wall heat flux and wall shear stress plotted over time	64
4.1	Important flow components of the Rotatable Buoyancy Tunnel	68
4.2	Heated wall cross section with relative thicknesses to scale. The HFS label is near the top.	69
4.3	Wall heat flux measurements with two correlations	70
4.4	TC Probe with its reflection in the heated wall on the right	72
4.5	Self-alignment process of the TC Probe with the heated wall	72
4.6	Factorial sketch of the DOE study	74
4.7	Measured temperature profiles for both cases and all three x locations	75
4.8	Measured temperature profiles near the heated wall with line fit for both cases for all three x locations. Note the unique wall temperature values T_s as the wall is nearly isothermal. T_s at x_1 is several degrees cooler than at x_2 and x_3	76
4.9	Measured nondimensional temperature profiles with the thermal law of the wall for air for both cases and all three x locations	77
4.10	Measured and predicted heat flux plotted in the streamwise direction	79
4.11	Factorial sketch of the DOE study with errors	80
A.1	The structured rectangular mesh with 1M cells	86
A.2	The streamwise velocity \bar{u} and turbulent kinetic energy \bar{k} for both PIV and CFD results	87
A.3	The heated wall heat flux and wall shear stress plotted over time	89

Notation

Lowercase Roman

dt	Time delay of Particle Image Velocimetry image pairs
$f\#$	Lens aperture f-number
g	Acceleration due to gravity
k	Thermal conductivity
\bar{k}	Time mean turbulent kinetic energy
q''	Heat flux
t	Time or thickness
t_{95}	Confidence level coefficient at the 95% level
\bar{u}	Time mean streamwise velocity
\bar{u}_{bulk}	Time mean streamwise bulk velocity
\bar{u}_{∞}	Time mean streamwise free-stream velocity
u'	Instantaneous fluctuation of u
u_{τ}	Shear velocity
$\overline{u'u'}$	Time mean streamwise Reynolds stress
\bar{v}	Time mean wall-normal velocity
v'	Instantaneous fluctuation of v
$\overline{v'v'}$	Time mean wall-normal Reynolds stress
$\overline{u'v'}$	Time mean Reynolds shear stress
\bar{w}	Time mean transverse velocity
$\overline{w'w'}$	Time mean transverse Reynolds stress
x	Coordinate in streamwise direction
\bar{x}	Arbitrary time mean variable
y	Coordinate normal to the heated wall
y^+	Nondimensional coordinate normal to the heated wall
z	Coordinate in the transverse direction

Uppercase Roman

$B_{\bar{x}}$	Bias uncertainty of variable \bar{x}
---------------	--

D	Experimental data
D_{TC}	Diameter of thermocouple wire in probe
E	Validation error
Gr_x	Local Grashof number
N	Number of samples
Nu_F	Nusselt number of forced convection
Nu_x	Local Nusselt number
Pr	Prandtl number
Re_x	Local Reynolds number
Ri_x	Local Richardson number
S	Simulation result
S_x	Standard deviation of x
$S_{\bar{x}}$	Random uncertainty of \bar{x}
St	Stanton number
T	Temperature
T^+	Nondimensional temperature
T_∞	Temperature of free-stream
T_s	Temperature of surface
U_D	Uncertainty of experimental data
U_ε	Uncertainty of error
U_{input}	Uncertainty of simulation input
U_{num}	Uncertainty of numerics
$U_{q''}$	Uncertainty of heat flux
U_{val}	Uncertainty of validation
$U_{\bar{x}}$	Uncertainty of variable \bar{x}

Lowercase Greek

β	Thermal coefficient of expansion
δ_2	Momentum thickness of boundary layer
ε	Error
μ	Dynamic viscosity of air
ν	Kinematic viscosity of air

ρ	Density of air
τ_s	Shear stress at surface
ξ	Distance to virtual origin upstream of leading edge

Uppercase Greek

ΔT	Change in temperature
Δy	Change in coordinate y

Acronyms

BC	Boundary Condition
CFD	Computational Fluid Dynamics
CJC	Cold Junction Compensation
DAQ	Data Acquisition
DOE	Design of Experiments
FOV	Field of View
HFS	Heat Flux Sensor
IC	Initial Condition
INL	Idaho National Laboratory
LDA	Laser Doppler Anemometry
LOFC	Loss of Forced Convection
M&S	Modeling & Simulation
NI	National Instruments
NRC	U. S. Nuclear Regulatory Commission
PIV	Particle Image Velocimetry
PTU	Programmable Timing Unit
RANS	Reynolds-averaged Navier-Stokes
RoBuT	Rotatable Buoyancy Tunnel
SRQ	System Response Quantity
TC	Thermocouple
TTL	Transistor-Transistor Logic
UQ	Uncertainty Quantification
URANS	Unsteady Reynolds-averaged Navier-Stokes
USU	Utah State University
V&V	Verification & Validation
VHTR	Very High Temperature Reactor

Chapter 1

Introduction

The motivation for studying transient mixed convection in detail came from a possible accident scenario of a new nuclear power plant design. Computational Fluid Dynamics (CFD) is a means to numerically model complex flows with heat transfer and is a major tool for accessing nuclear reactor safety. With the approximations of CFD come the necessity to validate results. This is done by comparing with experimental data to assess whether the model accuracy is sufficient for the intended use. Experiments were conducted to provide detailed measurements of steady and transient mixed convection.

1.1 The Very High Temperature Reactor

The Very High Temperature Reactor (VHTR) concept is a prominent Next Generation Nuclear Plant design under consideration whose reactor core is shown in Fig. 1.1. There are several advantages to this design including improved efficiency from increased temperatures between 900-950°C, passive safety features, potential for process heat or hydrogen production at co-located plants, and an increase from a 40 to 60 year license cycle. The VHTR uses helium gas as the coolant so high temperatures can be realized and efficiency increased. The main core design is either a prismatic core where most of the reactor core is graphite with coolant and fuel passages or a pebble bed core with fuel elements the size of tennis balls. In either design, normal operation has helium forced downward through the core [1, 2]. In the event of a Loss of Forced Convection (LOFC) that may result from a problem with the blower, viscous and buoyant forces initially decrease flow rate. As the blower and helium inertia decreases, buoyancy effects reverse the flow in a chaotic event. Ultimately steady natural convection upward is the final state. Natural convection is the primary mode of heat removal from the core in a Pressured Conduction Cooled event such as this. This phenomenon has been identified as one of high importance and low knowledge by the U.S. Nuclear Regulatory Commission (NRC) [3].

1.2 Computational Fluid Dynamics Validation

Computational methods have been used for many decades to assess reactor design safety in accident scenarios. Modern computational methods began in the 1960s with the programmable computer. Since that

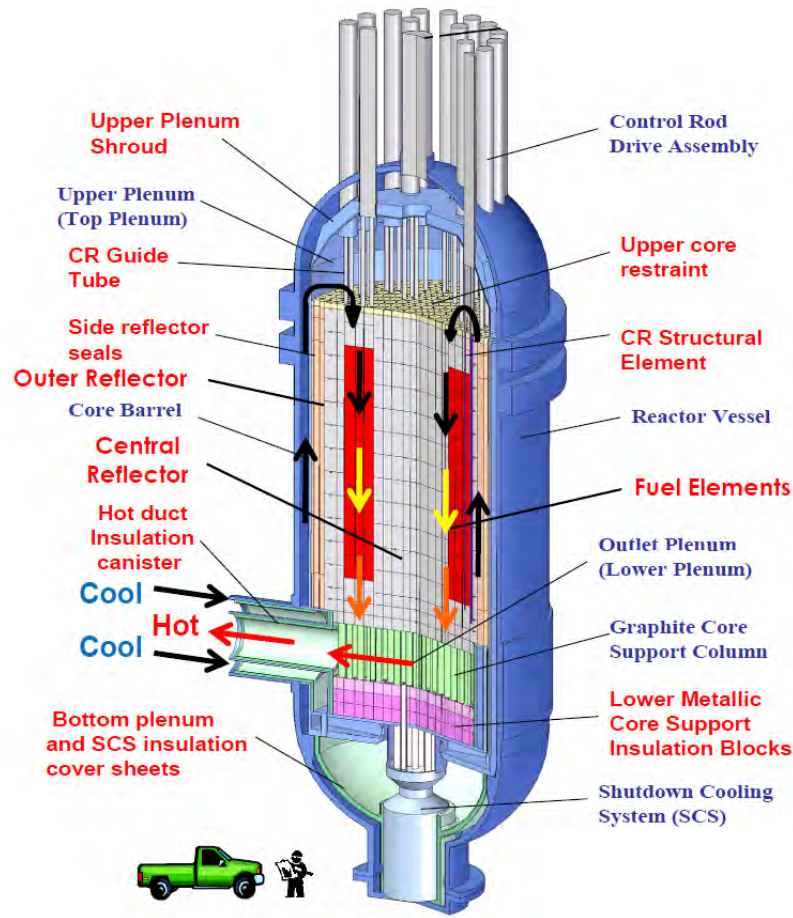


Fig. 1.1: Very High Temperature Reactor core, [4]

time, computational power has increased rapidly. At least over the last twenty years, the speed of the fastest supercomputer has increased by a factor of ten every four years [5]. With computational power increasing rapidly, more researchers and scientists are making use of Modeling & Simulation (M&S). Modeling and Simulation can be used to predict physical phenomena in fields of fluid dynamics, heat transfer, solid mechanics, genetics, finance, and many others where analytic solutions are impractical or impossible. Many M&S results are being used to make decisions, and some of them for high-consequence systems where public safety is of concern. The use of M&S was adopted early in the nuclear power industry for thermal-hydraulics safety codes to predict flow and heat transfer processes in accident scenarios as evidenced by the common use of system codes such as RELAP5.

With the increased use of M&S should also come improved means to assess simulation accuracy, especially for high-consequence systems. From this need, a discipline called Verification & Validation (V&V)

emerged. The first of these, Verification, covers two main methods to determine software correctness, Code Verification and Solution Verification. There are several definitions of these terms that have been identified by different professional organizations to meet their individual needs. One of these is the American Society of Mechanical Engineers that defined these terms as [6]:

Verification: the process of determining that a computational model accurately represents the underlying mathematical model and its solution.

Validation: the process of determining the degree to which a model is an accurate representation of the real world from the perspective of the intended uses of the model.

The purpose of Code Verification is to assure software correctly implements the numerical algorithm and is free of programming errors or “bugs.” Solution Verification is the process of determining the accuracy of the simulation inputs, the accuracy of the solution, and that of the output. Validation is the means to determine how well the simulation predicts real-world behavior by comparing simulation results with experimental data [5]. Stating the definitions another way, verification is checking the math and has nothing to do with physics while validation only has to do with physics. Blottner stated these definitions in memorable terms as “Verification is solving the equations right” and “Validation is solving the right equations” [8]. The attitude in V&V is naturally skeptical and places higher demand on simulations than is common in practice [7].

Verification is solely the responsibility of those that develop models or *modelers*. Validation is a shared responsibility of modelers and experimentalists where the latter provide data that represent physical phenomena. The current work focuses on providing experimental data for validation activities.

The planning and execution of validation studies should include both modelers and experimentalists through all phases. In considering the design of validation systems, it is desirable to measure System Response Quantities (SRQs)—system outputs that are used for validation—from a wide range and high levels of difficulty as shown in Fig. 1.2. Comparing M&S results with experimental data from a wide range on the spectrum increases validation confidence. For example, integral quantities, such as fluid mass flow rate, generally have low experimental noise and random errors. Derivative quantities like fluid shear are more sensitive to non-ideal conditions. If a model and data are in good agreement at a high level, then it is likely that good agreement will be observed in lower levels. But, agreement at lower levels does not imply agreement at higher levels [5].

There are several tiers or levels of validation studies as shown in Fig. 1.3. The levels range from the Complete System to Unit Problems. The Complete System is the highest tier and includes all relevant physics and geometry but for which measurements are coarse. Unit Problems have basic geometry and non-coupled

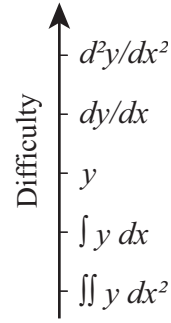


Fig. 1.2: Difficulty Spectrum of SRQs, after [5]. The variables y and x here are arbitrary.

physics with complete measurements but are far removed from the system. Different Complete Systems will appear very different from each other but often share many of the same phenomena of lower tiers, so lower-tiered validation studies may be useful for many systems [5].

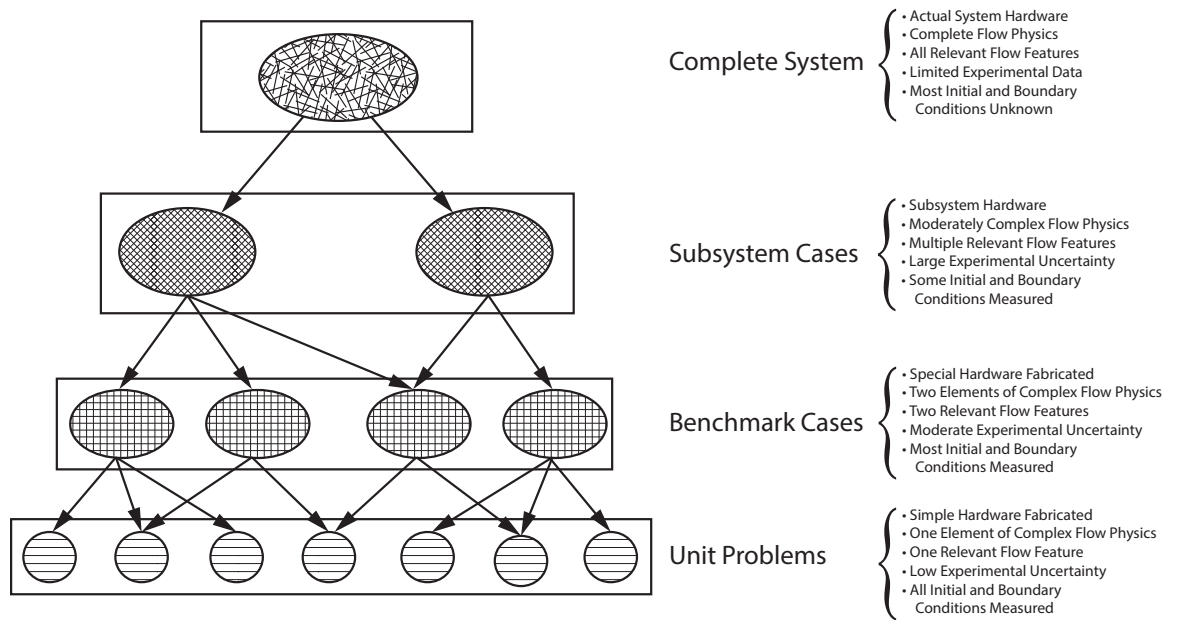


Fig. 1.3: Validation Hierarchy, after [9]

The Benchmark Tier, also called Separate Effects Testing, requires that most model inputs and many model outputs are measured and experimental uncertainty is included. This tier has specialized hardware, simplified geometry, and only some physics coupling [5]. The proposed work has coupled physics in fluid

momentum and heat transfer as well as three-dimensional velocity development that keep it from being a Unit Problem. This Benchmark Case has simplified geometry and high detail of measurements and associated uncertainties make it useful for many systems.

There are several terms in common use that need to be defined in the context of validation. The domain of interest is the region in space and/or time where the physical phenomena being modeled occurs. This domain may have *boundary conditions* (BCs) where the external physical conditions are applied. It may also have *initial conditions* (ICs) which are a form of BC that exists at the initial time, but these conditions also extend into the domain of interest. Generally experimental data are provided to the modeler in the form of BCs and/or ICs. The model output is called the *system response quantity of interest*, herein referred to as *system response quantity* or SRQ, and often there are several. The SRQ is either found within the domain of interest or at a boundary whose conditions are an output. It provides data to be used as a validation metric when assessing the accuracy of a model [5].

Generally older experimental data from discovery experiments are not sufficiently described to be used for validation. Discovery experiments are common in research where new physical phenomena are measured, presented, and discussed. Validation experiments do not necessarily measure unique phenomena but the measurement process and description are more complete [10].

Several databases are available online for the purpose of CFD validation. An updated list of these is found at www.cfd-online.com/Links/refs.html. Data from many other sources are no longer available online as programs and technologies expire. The description associated with these databases is very light and rarely includes a complete set of necessary model inputs. Validation data should be highly described and regularly maintained by organizations that last longer than research programs to ensure the data are useful for as long as possible.

1.3 Mixed Convection

Mixed convection is a coupled fluid momentum and heat transfer phenomenon where both forced and natural convection contribute to the behavior. With forced convection, buoyant forces are negligible and flow is driven by a pressure gradient. Conversely buoyant forces drive natural convection in the direction opposite to gravity as low density fluid rises over higher density fluid [11].

There are generally three types of mixed convection that depend on the relative directions of buoyant and pressure forces. The first is *buoyancy-aided* where buoyant forces and forced flow have the same direction, the second *buoyancy-opposed* where these forces have opposite direction, and the third *transverse* where

these forces are perpendicular [12].

Specifically mixed convection is determined by the local Richardson number as

$$\text{Ri}_x = \text{Gr}_x / \text{Re}_x^2 \quad (1.1)$$

where

$$\text{Re}_x = \bar{u}_{\text{bulk}} x / \nu \quad (1.2)$$

and

$$\text{Gr}_x = g \beta (T_s - T_\infty) x^3 / \nu^2. \quad (1.3)$$

In these, g is acceleration due to gravity, β is fluid thermal coefficient of expansion, T_s and T_∞ are surface and fluid temperatures, respectively, x is local streamwise location, ν is fluid kinematic viscosity, and \bar{u}_{bulk} is time mean bulk velocity. Mixed convection is observed for buoyancy aided flow when $0.3 < \text{Ri}_x < 16$ and for $0.3 < \text{Ri}_x$ for opposed flow [11].

There have been many mixed convection studies on vertical plates and in vertical tubes. Several mixed convection experiments for vertical tubes are cited in a review article by Jackson *et al.* [13]. They surveyed literature and presented results for both laminar and turbulent flows, both theoretical and experimental studies. Results were compared and heat transfer correlations presented. They noted that heat transfer in buoyancy-aided turbulent flow is suppressed for moderate buoyancy levels while, on the other hand, it is augmented in buoyancy-opposed flows. This work provides heat transfer correlations for pipe flow that could be useful for comparison with the current work. They further recommend the use of Low Re models for mixed convection simulations.

Chen *et al.* [14] present correlations for laminar mixed convection on vertical, inclined, and horizontal plates and compare them to experiments performed by Ramachandran *et al.* [15]. Experiments of the latter provided point velocity and temperature measurements via a hot-wire anemometer. The data agreed very well with predictions and were sufficient for comparison to correlations with, but are not reported in sufficient detail for validation.

Kim *et al.* [16] summarize simulations that predict mixed convection in a vertical tube and compare the models to experimental data. The in-house code used published two-equation models and was written to model developing mixed convection flow with variable properties. Consistent with previous works, laminarization of the turbulent flow was reported in the buoyancy-aided case and increased turbulent levels in the opposed case. None of the models investigated showed good agreement over the entire range of flow,

suggesting further model development, or perhaps model calibration, could increase prediction capability for these flows.

Wang *et al.* [17] discuss both an experimental and a numerical study of a vertical plate under turbulent mixed convection. Two-component Laser Doppler Anemometry (LDA) was used to measure boundary layer velocity. Some temperature measurements were also made of the flow using a thermocouple (TC) rake. They reported moderate agreement between experimental data and simulation results, but noted that predictions for the buoyancy-opposed case were less accurate. Although this study provides valuable insight into this flow with plate geometry, the reported information lacks boundary conditions and inflow parameters necessary for validation studies.

Mixed convection literature is abundant. However, all the papers found were performed as discovery experiments, not for the purpose of providing validation data. Most are for pipe flow, boundary and initial conditions are lacking, uncertainties are rarely presented, flow geometry description is simplified, and fluid properties are seldom given. Further, the techniques used were often intrusive, leading to unknown uncertainties, and often provided only point measurements. Modern measurement systems can provide higher fidelity data while disrupting the flow less.

1.4 Transient Convection

Transient convection is of consequence in a LOFC accident of the VHTR as the flow starts with forced convection downward and changes to natural convection upward in a ramp-type flow transient. Some studies of non-periodic transient flow have been performed, but as He & Jackson note, it has only been somewhat recently that technology has allowed for comprehensive measurements of ensemble-averaged transient experiments [18]. Most of the first experiments measured either temperature of tube walls or velocity, not both. A common observation was that accelerating flow suppresses turbulence while decelerating flow augments it.

The first work by Koshkin *et al.* was published in 1970 for turbulent air flow and reported measurements when changing electrical power and different flow transients, measuring and reporting temperature measurements [19]. Two similar studies were published in the 1970s and used electrochemical techniques with probes to measure velocity profiles inside a tube from a step change in flow rate [20,21].

A study performed by Rouai where heat transfer experiments on ramp-up and ramp-down transients as well as periodic pulsating flow with a non-zero time mean were performed. Water was heated by passing an alternating electrical current through a stainless steel tube. Temperature measurements were made by

24 thermocouples welded to this tube. Flow transients were prescribed by using a constant head tank and varying the flow through the test section by a valve. Wall heat flux remained constant and changes in wall temperature were measured. The observed Nusselt number departed more from the psuedo-steady values for faster transients and for decelerating flows, likely from the augmentation of turbulence [22].

Two researchers, He & Jackson, performed experiments in water using two-component LDA measurements in a clear, unheated tube. This non-intrusive velocity measurement was one of the first known for non-periodic flows. Ensemble-averaged results were used for mean and turbulent quantities. The turbulent results were original for this type of flow and were shown to deviate from pseudo-steady results for short transients. Several non-dimensional parameters were recommended for ramp-type transients [18].

In the previous studies, no coupling of velocity and thermal measurements was found for transients and buoyancy effects were negligible. Also, as these were discovery experiments, boundary conditions were not measured and provided as tabulated data, making the results of limited use for validation. The facility description is very basic and flow geometries simplified. The current study contributes high fidelity measurements of a ramp-down transient suitable for validation studies with simultaneous, non-intrusive velocity and thermal measurements to provide validation data on simplified geometry for three-dimensional simulations.

1.5 Wall Heat Flux

As will be discussed later in this work, the experimental facility test section was highly instrumented. Three thin-film heat flux sensors (HFSs) were purchased and potted in the heated wall for heat flux measurements. Being commercial sensors from RdF Corp., they came with factory-calibrated sensitivities. Preliminary experiments have shown that the measured heat flux does not match fundamental trends as shown in Fig. 1.4, specifically decreasing heat flux with boundary layer development with increasing x . Two correlations are shown. The Kays trend is the heat flux from

$$St = \frac{Nu_x}{Re_x Pr} = \frac{0.0287 Re_x^{-0.2}}{0.169 Re_x^{-0.1} (13.2 Pr - 9.25) + 0.85} \quad (1.4)$$

where St is the Stanton number, Nu_x is the local Nusselt number, and Pr is the Prandtl number [11]. The Incropera trend is based on the correlation for convection over an isothermal flat plate [12] and is

$$Nu_x = 0.0296 Re_x^{4/5} Pr^{1/3}. \quad (1.5)$$

Once the Nusselt number is computed, heat flux is calculated as $q'' = Nu_x k (T_s - T_\infty) / x$ where q'' is heat flux

and k is fluid thermal conductivity. Note that the correlation trends are not smooth, a result of the measured center-line plate temperature, which has small gradients.

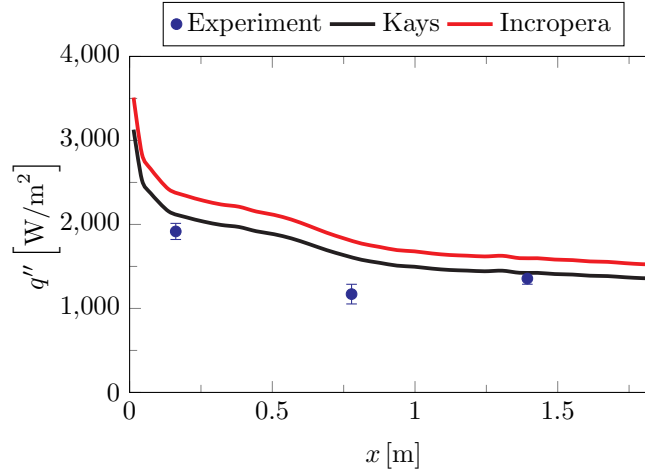


Fig. 1.4: Wall heat flux comparing measurements with two correlations

The difference in these trends was concerning and it was possible that the sensor sensitivities were mixed-up, had an installation error, or other manufacturer-supplied parameters were incorrect. As heat flux was a critical SRQ, developing a means to assess sensor accuracy was desired. Since the sensors were permanently potted, removing them for calibration was not an option. In situ heat flux measurements were made via an independent method. This method should not change heat transfer conditions in the area.

Installation error was possible if heat transfer conditions are different between calibration and use. The RdF sensors were calibrated to a reference sensor that was calibrated at 70°F in radiation using a blackbody source [23]. The heat transfer mode of the sensors in the heated wall was conduction. The different heat transfer modes, the elevated operation temperature, and the possibility of non-uniform thermal resistance in the sensor area have been identified as possible error sources [24].

There are several methods for heat flux calibration. The National Institute of Standards and Technology is an excellent source for heat flux sensor calibration services. They use a variable-temperature blackbody thermal radiation source with symmetric conditions for simultaneous measurements with a reference optical pyrometer and a user-supplied HFS [25]. This method was impractical for the current situation as the sensors could not be removed.

One common HFS design measured the temperature difference across a substrate of known thermal

conductivity using a thermopile (array of thermocouples in series for increased output) [26]. Fourier's Law for conduction was the theory of this measurement and is [12]

$$q'' = -k \frac{dT}{dy} \approx -k \frac{\Delta T}{\Delta y} \quad (1.6)$$

where k is substrate thermal conductivity, T is temperature, and y is the direction of heat flux. This method was used in the purchased RdF thin-film sensors potted in the plate. Adding a reference HFS of this type would disrupt local convection conditions. The calorimeter method uses heat storage over time to measure flux [26], but this would change local conditions for the proposed experiment. The facility geometry and thermal resistance must remain constant in space.

An independent heat flux measurement technique was possible. The potted HFSs measured heat flux near the surface of the heated wall. The convective heat flux from the wall to the air should be equivalent, especially very near the wall and removed from the side walls. Very near the heated wall, within the viscous sublayer, the temperature profile is linear [11]. If the temperature profile can be measured within this region and the thermal conductivity of air k can be estimated by the measured temperature and reference data found in [27], it is possible to measure convective heat flux from a surface.

Others have made near-wall temperature measurements. An early study by Warner and Arpaci described the use of a butt-welded TC probe of 12.7 μm diameter oriented parallel to a vertical flat plate and perpendicular to the flow direction. It was traversed with a motor-driven carriage near the heated wall under turbulent natural convection. The position was accurate to 5.08 μm within the first 25.4 mm and to 15.2 μm farther from the wall. They were able to measure temperature profiles and subsequently heat flux [28]. In another study of a turbulent boundary layer under forced convection, temperature profiles were measured by a TC probe of 76.2 μm diameter and about 12.7 mm long suspended by 22-gauge hypodermic needles oriented parallel to the plate and perpendicular to the flow direction. This probe was also traversed with a traversing mechanism accurate to 25.4 μm . These results, along with velocity measurements, were used to present many heat flux, shear, and turbulent Prandtl number results for this fundamental flow [29].

References

- [1] U. S. Department of Energy, 2010, "Next Generation Nuclear Plant: A Report to Congress," Tech. rep., U. S. Department of Energy Office of Nuclear Energy.
- [2] Oh, C., Kim, E., Schultz, R., Patterson, M., Petti, D., and Kang, H., 2010, "Comprehensive Thermal Hydraulics Research of the Very High Temperature Gas Cooled Reactor," *Nuclear Engineering and*

- Design*, **240**(10), pp. 3361–3371, doi:[10.1016/j.nucengdes.2010.07.007](https://doi.org/10.1016/j.nucengdes.2010.07.007).
- [3] Woods, B. G., Jackson, R. B., and Nelson, B. L., 2009, “Scaling Analysis for the Very High Temperature Reactor Test Facility at Oregon State University,” Tech. rep., Oregon State University.
 - [4] Idaho National Laboratory, *Module 05a Prismatic HTGR Core Design Description*, https://inlportal.inl.gov/portal/server.pt/community/ngnp_public_documents.
 - [5] Oberkampf, W. L., and Roy, C. J., 2010, *Verification and Validation in Scientific Computing*, Cambridge University Press, doi:[10.1017/cbo9780511760396](https://doi.org/10.1017/cbo9780511760396).
 - [6] ASME, 2006, *Guide for Verification and Validation in Computational Solid Mechanics*, ASME Standard V&V 10-2006, New York, NY.
 - [7] Tetlock, P., 2005, *Expert Political Judgment: How Good Is It? How Can We Know?*, Princeton University Press, Princeton, NJ.
 - [8] Blottner, F. G., 1990, “Accurate Navier-Stokes Results for the Hypersonic Flow Over a Spherical Nosedip,” *Journal of Spacecraft and Rockets*, **27**(2), pp. 113–122, doi:[10.2514/3.26115](https://doi.org/10.2514/3.26115).
 - [9] AIAA, 1998, “Guide for the Verification and Validation of Computational Fluid Dynamics Simulations,” Tech. Rep. AIAA G-077-1998, American Institute of Aeronautics and Astronautics, Reston, VA, doi:[10.2514/4.472855](https://doi.org/10.2514/4.472855).
 - [10] Roache, P. J., 2009, *Fundamentals of Verification and Validation*, Hermosa Publ.
 - [11] Kays, W. M., Crawford, M. E., and Weigand, B., 2012, *Convective Heat and Mass Transfer*, 4th ed., McGraw-Hill.
 - [12] Incropera, F. P., Dewitt, D. P., Bergman, T. L., and Lavine, A. S., 2007, *Fundamentals of Heat and Mass Transfer*, 6th ed., John Wiley & Sons.
 - [13] Jackson, J. D., Cotton, M. A., and Axcell, B. P., 1989, “Studies of Mixed Convection in Vertical Tubes,” *International Journal of Heat and Fluid Flow*, **10**(1), pp. 2–15, doi:[10.1016/0142-727x\(89\)90049-0](https://doi.org/10.1016/0142-727x(89)90049-0).
 - [14] Chen, T. S., Armaly, B. F., and Ramachandran, N., 1986, “Correlations for Laminar Mixed Convection Flows on Vertical, Inclined, and Horizontal Flat Plates,” *Journal of Heat Transfer*, **108**(4), p. 835, doi:[10.1115/1.3247020](https://doi.org/10.1115/1.3247020).
 - [15] Ramachandran, N., Armaly, B. F., and Chen, T. S., 1985, “Measurements and Predictions of Laminar Mixed Convection Flow Adjacent to a Vertical Surface,” *Journal of Heat Transfer*, **107**(3), p. 636, doi:[10.1115/1.3247471](https://doi.org/10.1115/1.3247471).
 - [16] Kim, W. S., Jackson, J. D., He, S., and Li, J., 2004, “Performance of a Variety of Low Reynolds Number Turbulence Models Applied to Mixed Convection Heat Transfer to Air Flowing Upwards in a Vertical Tube,” *Proceedings of the Institution of Mechanical Engineers, Part C: Journal of Mechanical Engineering Science*, **218**(11), pp. 1361–1372, doi:[10.1177/095440620421801107](https://doi.org/10.1177/095440620421801107).
 - [17] Wang, J., Li, J., and Jackson, J., 2004, “A Study of the Influence of Buoyancy on Turbulent Flow in a Vertical Plane Passage,” *International Journal of Heat and Fluid Flow*, **25**(3), pp. 420–430, doi:[10.1016/j.ijheatfluidflow.2004.02.008](https://doi.org/10.1016/j.ijheatfluidflow.2004.02.008).
 - [18] He, S., and Jackson, J. D., 2000, “A Study of Turbulence Under Conditions of Transient Flow in a Pipe,” *Journal of Fluid Mechanics*, **408**, pp. 1–38, doi:[10.1017/s0022112099007016](https://doi.org/10.1017/s0022112099007016).
 - [19] Koshkin, V., Kalinin, E., Dreitzer, G., Galitseisky, B., and Izosimov, V., 1970, “Experimental Study of Nonsteady Convective Heat Transfer in Tubes,” *International Journal of Heat and Mass Transfer*, **13**(8), pp. 1271–1281, doi:[10.1016/0017-9310\(70\)90068-2](https://doi.org/10.1016/0017-9310(70)90068-2).

- [20] Kataoka, K., Kawabata, T., and Miki, K., 1975, “The Start-up Response of Pipe Flow to a Step Change in Flow Rate,” *Journal of Chemical Engineering of Japan*, **8**(4), pp. 266–271, doi:[10.1252/jcej.8.266](https://doi.org/10.1252/jcej.8.266).
- [21] Maruyama, T., Kuribayashi, T., and Mizushima, T., 1976, “The Structure of the Turbulence in Transient Pipe Flows,” *Journal of Chemical Engineering of Japan*, **9**(6), pp. 431–439, doi:[10.1252/jcej.9.431](https://doi.org/10.1252/jcej.9.431).
- [22] Rouai, N. M., 1987, “Influence of Buoyancy and Flow Transients on Turbulent Convective Heat Transfer in a Tube,” Ph.D. thesis, University of Manchester, UK.
- [23] RdF, 2014, “Heat Flow Measurement: Calibration, Specifications & Accuracy,” Tech. rep., RdF, corp.
- [24] Holmberg, D. G., and Womeldorf, C. A., 1999, “Performance and Modeling of Heat Flux Sensors in Different Environments,” ASME Heat Transfer Division, pp. 71–77.
- [25] Tsai, B. K., Gibson, C. E., Murthy, A. V., Early, E. A., Dewitt, D. P., and Saunders, R. D., 2004, “NIST Measurement Services: Heat-Flux Sensor Calibration,” Tech. Rep. Special Publication 250-65, National Institute of Standards and Technology.
- [26] Diller, T. E., 1999, *The Measurement, Instrumentation, and Sensors Handbook*, chap. 34, Heat Flux, CRC Press.
- [27] Touloukian, Y. S., Liley, P. E., and Saxena, S. C., 1970, “Thermophysical Properties of Matter-The TPRC Data Series. Volume 3. Thermal Conductivity-Nonmetallic Liquids and Gases,” Tech. rep., DTIC Document.
- [28] Warner, C. Y., and Arpaci, V. S., 1968, “An Experimental Investigation of Turbulent Natural Convection in Air at Low Pressure Along a Vertical Heated Flat Plate,” *International Journal of Heat and Mass Transfer*, **11**(3), pp. 397–406, doi:[10.1016/0017-9310\(68\)90084-7](https://doi.org/10.1016/0017-9310(68)90084-7).
- [29] Blackwell, B. F., Kays, W. M., and Moffat, R. J., 1972, “The Turbulent Boundary Layer on a Porous Plate: an Experimental Study of the Heat Transfer Behavior with Adverse Pressure Gradients,” Tech. Rep. HMT-16, The National Aeronautics and Space Administration.

Chapter 2

Experimental Validation Data for CFD of Steady Mixed Convection on a Vertical Flat Plate

Abstract

Model validation for Computational Fluid Dynamics (CFD), where experimental data and model outputs are compared, is a key tool for assessing model uncertainty. In this work, mixed convection was studied experimentally for the purpose of providing validation data for CFD models with a high level of completeness. Experiments were performed in a facility built specifically for validation with a vertical, flat, heated wall. Data were acquired for both buoyancy-aided and buoyancy-opposed flows. Measured boundary conditions include as-built geometry, inflow mean and fluctuating velocity profiles, and inflow and wall temperatures. Additionally, room air temperature, pressure, and relative humidity were measured to provide fluid properties. Measured system responses inside the flow domain include mean and fluctuating velocity profiles, temperature profiles, wall heat flux, and wall shear stress. All of these data are described in detail and provided in tabulated format.

2.1 Introduction

The purpose of this work is to provide validation data for three-dimensional Computational Fluid Dynamics (CFD) models. Model validation will be discussed as well as the physical phenomenon of steady mixed convection. The following sections describe the experimental facility, the associated instrumentation, the boundary conditions (BCs), the fluid and material properties, the test conditions, and the System Response Quantities (SRQs). This content follows the Validation Experiment Completeness table of Oberkampf and Smith [1] to guide description of validation experiments. This guidance ensures important details are included with a high level of completeness. The work contained herein is a continuation of that by Harris *et al.* [2] which covered forced convection using similar methods and facilities.

This work presents the data in table format for direct use in validating models. The provided data include the BCs and SRQs shown in Table 2.1. The included BCs in this work should provide modelers with

all required information, avoiding assumptions on model inputs and reducing model form uncertainty [3]. The SRQ data are provided to modelers for direct comparison with model outputs. The experimental uncertainties of all provided data from bias and random sources are also provided and quantified at the 95% confidence level. Validation errors can be calculated with the nominal data and validation uncertainty from the uncertainty of the nominal data [4].

Table 2.1: The tabulated boundary conditions and system response quantities provided in this work

BCs	SRQs
As-built geometry	Mean velocity profiles
Wall & inflow temps.	Fluctuating velocity profiles
Inflow mean velocity	Mean temperature profiles ¹
Inflow fluctuating velocity	Wall heat flux
Atmospheric conditions	Wall shear stress

These files are accessible in an online database in the Digital Commons of Utah State University's Library. The page dedicated to the data in this work is found at digitalcommons.usu.edu/all_datasets/8/. Links to specific files are included in this work with descriptive file names with the experimental case (buoyancy-aided or buoyancy-opposed), data type (BC or SRQ), and measured quantity included. All data files may be downloaded in the zipped file [Data](#). Generally data are in table format as csv files.

2.1.1 Computational Fluid Dynamics Validation

To understand the need for experiments expressly aimed at providing validation data, one must first understand the different aims of validation and discovery experiments. Discovery experiments are common in research where new physical phenomena are measured, presented, and discussed. Validation experiments do not necessarily measure unique phenomena, but the measurement process and description are more complete [5]. In general, older experimental data from discovery experiments are not sufficiently described for use in validation. Unobtrusive measurement techniques are important in validation experiments since probes introduce unknown uncertainties to the data. These uncertainties can only be mitigated by including the probe in the CFD model.

The purpose of validation experiments is to provide the information required to quantify the uncertainty of a mathematical model. This uncertainty helps decision makers quantify model credibility. The ASME V&V 20 Standard [4] outlines an approach to estimate the validation comparison error and the validation

¹The SRQ mean temperature profiles are provided for the buoyancy-opposed case only.

uncertainty. The validation error E is the difference between the simulation result S and the validation experiment result D as

$$E = S - D. \quad (2.1)$$

Calculating the validation uncertainty estimates the confidence interval of the error by considering both numerical and experimental uncertainty. Validation uncertainty is calculated as

$$U_{\text{val}} = \sqrt{U_{\text{num}}^2 + U_{\text{input}}^2 + U_D^2}, \quad (2.2)$$

where U_{num} is the numerical uncertainty, U_{input} is the model input uncertainty, and U_D is the experimental data uncertainty. The numerical uncertainty is estimated from solution verification with sources such as iterative and discretization uncertainty. The latter two uncertainties come from the validation data. The uncertainty in the measured BCs that are used for model inputs is U_{input} . The uncertainty of SRQs—experimental data used to compare system outputs—is U_D . If $|E| \gg U_{\text{val}}$, one can conclude model error remains. But if $|E| \leq U_{\text{val}}$ and U_{val} is acceptably small for the intended use of the model, the validation error may be satisfactory. These general equations show validation data and their uncertainties are required to assess model accuracy via model validation.

There are several tiers of detail in validation experiments [6], often four as shown in Fig. 2.1. This work is considered a Benchmark Case that is second in simplicity to Unit Problems. The Benchmark Case, also called Separate Effects Testing, requires that all model inputs and most model outputs are measured and that experimental uncertainty is included. In this tier there is generally some level of multi-physics interaction, such as coupled fluid momentum and heat transfer, that prevents this work from being considered a Unit Problem. On the other hand, the non-prototypical geometry used in this work keeps it from being a Subsystem Case.

The planning and execution of validation studies should include both modelers and experimentalists through all phases. In considering the design of validation systems, SRQs should be measured from a wide range and high difficulty in the difficulty spectrum as shown in Fig. 2.2. Comparing simulation results with experimental data from a wide range on the spectrum increases validation confidence. For example, integral quantities, such as fluid mass flow rate, generally have low experimental noise and random errors. Derivative quantities like fluid shear are more sensitive to non-ideal conditions. If a model and data are in good agreement at a high level, then it is likely that good agreement will be observed in lower levels. But, agreement at lower levels does not imply agreement at higher levels [3].

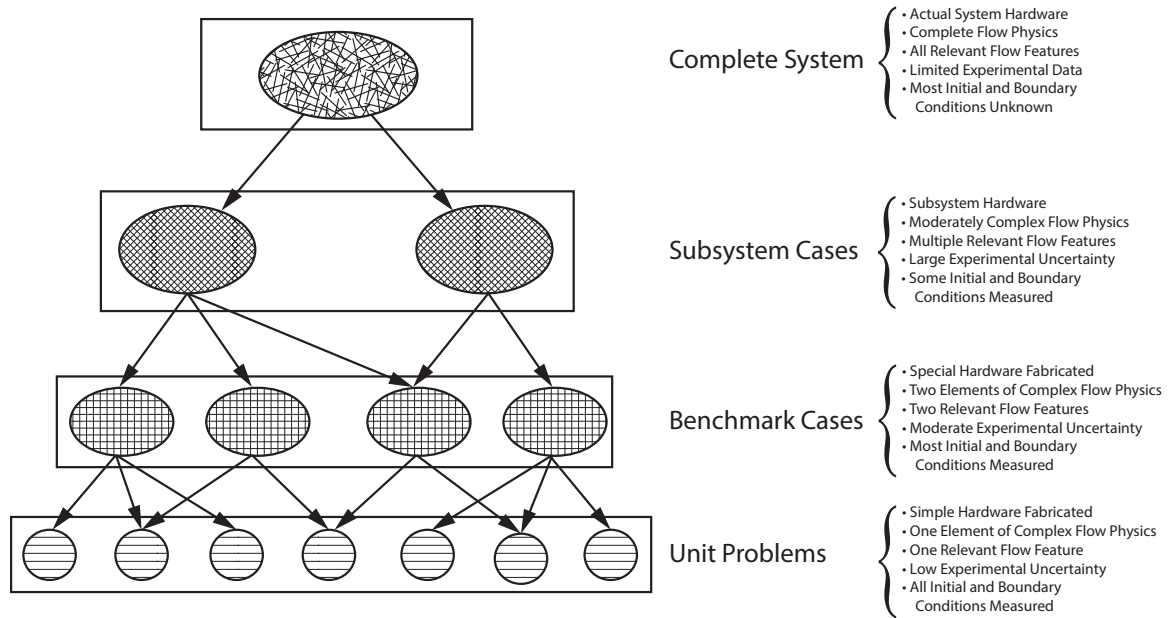
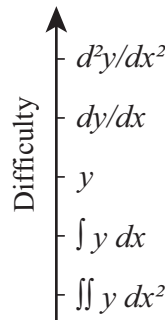


Fig. 2.1: The Validation Hierarchy, after [6]

Fig. 2.2: System Response Quantity Difficulty Spectrum, after [3]. The variables y and x are arbitrary.

2.1.2 Mixed Convection

Mixed convection is a coupled fluid momentum and heat transfer phenomenon where both forced and natural convection contribute to behavior. With forced convection, buoyant forces are negligible and flow is driven by a pressure gradient. Conversely, buoyant forces drive natural convection in the direction opposite to gravity as low density fluid rises over higher density fluid [7].

There are generally three types of mixed convection that depend on the relative direction of buoyant and pressure forces. The first is *buoyancy-aided*, where buoyant forces and forced flow have the same direction.

The second is *buoyancy-opposed*, where these forces have opposite directions. Finally the third is *transverse*, where these forces are perpendicular [8].

The mixed convection regime is defined by the local Richardson number as

$$\text{Ri}_x = \text{Gr}_x / \text{Re}_x^2 \quad (2.3)$$

where

$$\text{Re}_x = \bar{u}_{\text{bulk}} x / \nu \quad (2.4)$$

and

$$\text{Gr}_x = g\beta(T_s - T_\infty)x^3 / \nu^2. \quad (2.5)$$

In these equations, g is acceleration due to gravity, β is fluid thermal coefficient of expansion, T_s and T_∞ are surface and fluid temperatures respectively, x is local streamwise location, ν is fluid kinematic viscosity, and \bar{u}_{bulk} is bulk time mean velocity. Mixed convection is commonly thought to occur for buoyancy-aided flow when $0.3 < \text{Ri}_x < 16$ and for buoyancy-opposed flow when $0.3 < \text{Ri}_x$ [7].

Some flow parameters in this study are given in Table 2.2. Note that external coordinates are used because the flow was not fully developed in the test section as it would be for pipe flow. The flow at x_1 was not in the mixed convection regime; but, as will be shown, buoyancy effects are still observable. The temperature of the heated wall was near the safety limit of the materials, and the air velocity was near the low side of the turbulent regime (large turbulent trips were installed upstream of the test section to enforce boundary layer turbulence at these lower Reynolds numbers).

Table 2.2: Re_x , Gr_x , and Ri_x at the three locations in x at the spanwise center where SRQ data were acquired. The bulk velocity \bar{u}_{bulk} was 2.44 m/s. These apply for both cases presented.

	x [m]	Re_x	Gr_x	Ri_x
x_1	0.16	19,000	3.34×10^7	0.09
x_2	0.78	93,000	3.71×10^9	0.43
x_3	1.39	170,000	2.13×10^{10}	0.77

There have been many mixed convection studies on vertical plates and in vertical tubes. Some will be described now. Several mixed convection experiments for vertical tubes are cited in a review article by Jackson *et al.* [9]. They surveyed literature and presented results for both laminar and turbulent flows, both theoretical and experimental studies. Results were compared and heat transfer correlations presented. They

noted that heat transfer in buoyancy-aided turbulent flow is suppressed for moderate buoyancy levels while, on the other hand, it is augmented in buoyancy-opposed flows. This work provides heat transfer correlations for pipe flow that could be useful for comparison with the current work. They further recommend the use of Low Re models for mixed convection simulations.

Chen *et al.* [10] present correlations for laminar mixed convection on vertical, inclined, and horizontal plates and compare them to experiments performed by Ramachandran *et al.* [11]. Experiments of the latter provided point velocity and temperature measurements via a hot-wire anemometer. The data agreed very well with predictions and were sufficient for comparison to correlations with, but are not reported in sufficient detail for validation.

Kim *et al.* [12] summarize simulations that predict mixed convection in a vertical tube and compare the models to experimental data. The in-house code used published two-equation models and was written to model developing mixed convection flow with variable properties. Consistent with previous works, laminarization of the turbulent flow was reported in the buoyancy-aided case and increased turbulent levels in the opposed case. None of the models investigated showed good agreement over the entire range of flow, suggesting further model development, or perhaps model calibration, could increase prediction capability for these flows.

Wang *et al.* [13] discuss both an experimental and a numerical study of a vertical plate under turbulent mixed convection. Two-component Laser Doppler Anemometry (LDA) was used to measure boundary layer velocity. Some temperature measurements were also made of the flow using a thermocouple (TC) rake. They reported moderate agreement between experimental data and simulation results, but noted that predictions for the buoyancy-opposed case were less accurate. Although this study provides valuable insight into this flow with plate geometry, the reported information lacks boundary conditions and inflow parameters necessary for validation studies.

Mixed convection literature is abundant. However, all the papers found were performed as discovery experiments, not for the purpose of providing validation data. Most are for pipe flow, boundary and initial conditions are lacking, uncertainties are rarely presented, flow geometry description is simplified, and fluid properties are seldom given. Further, the techniques used were often intrusive, leading to unknown uncertainties, and often provided only point measurements. Modern measurement systems can provide higher fidelity data while disrupting the flow less.

2.2 Experimental Facility

All experiments were performed in the Rotatable Buoyancy Tunnel (RoBuT), which will be described in detail. Benchmark-level validation data were acquired with simple geometry and some multi-physics interaction. The square test section allowed easy characterization using optical velocity measurements. The simple geometry is easy to represent numerically and helps isolate model errors.

2.2.1 Rotatable Buoyancy Tunnel

The RoBuT was an open-circuit air tunnel with a large 4.81-m diameter ‘Ferris wheel’ design that allowed rotation, thus changing the relative direction of forced flow and buoyant forces without changing the facility. Many important tunnel components are shown in Fig. 2.3, which is in the buoyancy-aided orientation. Note the coordinate system with the origin on the heated wall at the inlet and the spanwise center. The streamwise distance is x , wall-normal distance is y , and spanwise distance is z with zero along the centerline. The laser and camera were part of a Particle Image Velocimetry (PIV) system that will be described in Sec. 2.3.2.

The test section had a 0.305×0.305 m square cross section and was 2 m long. It had three clear walls for optical access and a heated wall for a thermal BC. More details of the test section are provided in Sec. 2.2.2. The contraction and outlet were made of fiberglass-reinforced plastic with a glass-smooth, black gel-coat.

The contraction had an area ratio of 6.25:1 and was 0.914 m long. The contraction bell at the leading edge had a 102 mm radius. Between the contraction and bell were four modular sections that contained—in order of flow direction—a single row, aluminum fin/copper tube, chilled water heat exchanger (Super Radiator Coils Model 30x30-01R-0.625/048); a settling length section; a precision aluminum honeycomb flow straightener; and two high porosity screens. Square turbulence trips 3.175 mm wide were installed along all four walls and located about 0.12 m upstream of the test section inlet.

The outlet expanded the flow downstream of the test section, had a total included angle of 8.2° , and was 0.686 m long. The blower drew air through the test section and rejected it into the room. It included an inline centrifugal fan assembly, TCF/Aerovent model 14-CBD-3767-5. It was belt driven by a 5 HP, TEFC, 230-460 VAC induction motor, Toshiba model B0052FLF2AMH03. The motor was powered by a Toshiba variable frequency drive, model VFS11-2037PM-WN.

Two Laskin Nozzles [14] were used to atomize olive oil tracer particles. These were measured to have a mean diameter of about $1\mu\text{m}$ with a TSI Aerodynamic Particle Size Spectrometer at the outlet. These particles were mixed with air and injected into a PVC pipe distribution system upstream of the contraction

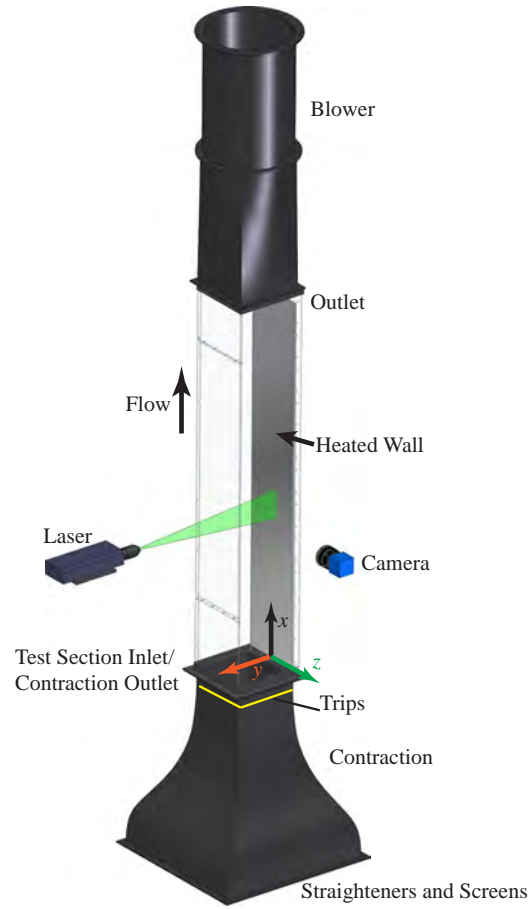


Fig. 2.3: RoBuT flow components in the buoyancy-aided orientation

assembly. A peg board was placed between this system and the beginning of the contraction to help mix particles throughout the flow. It had holes 6.35 mm in diameter and were spaced 25.4 mm apart in a square pattern.

2.2.2 Test Section

The test section had four walls, an inlet, and an outlet that will be described in detail. The heated wall was custom designed with many layers to provide a heated surface for convection and featured embedded instrumentation. Its cross section is shown in Fig. 2.4. This wall was heated to approximately 138°C for this study. It was made of several layers of aluminum, had six silicon rubber heaters arranged in the streamwise direction, and contained thermal insulation to drive most of the heat inward. A list of materials and thicknesses is available in Table 2.3. The surface was nickel plated to reduce thermal radiation which resulted

in a predicted and measured emissivity around 0.03 [2]. Aluminum 2024, though more expensive than the common alloy 6061, was used because its thermal conductivity is well known [15]. The heated portion was 279 mm wide and 1.89 m long. The left and right sides were thermally insulated by 17.5-mm thick Teflon[®] that extended into grooves in the side walls. Two additional 12.7-mm thick Teflon[®] insulators were placed upstream and downstream of the heated wall. There were six heaters, each spanning the width of the heated wall and one sixth of the length. Three HP 6439B power supplies were connected to two heaters each and were used to control the temperature of the wall via a closed-loop PI controller. Three controllers, one for each power supply, allowed the heated wall to be heated in independent sections in the streamwise direction to increase temperature uniformity.

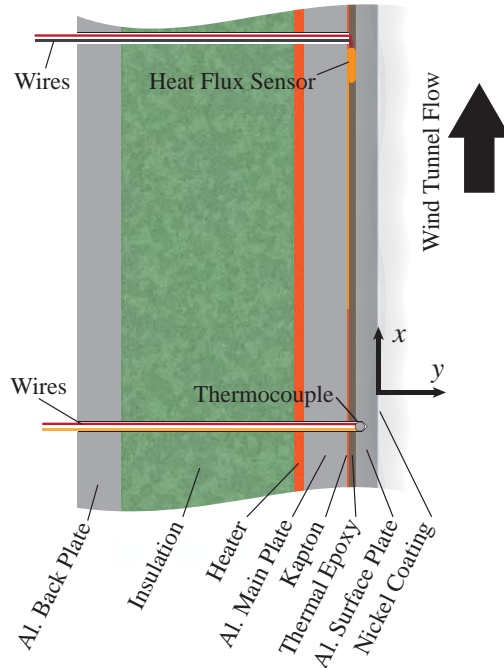


Fig. 2.4: Heated wall cross section with component names as in Table 2.3. The relative thicknesses are to scale.

The other three walls were clear Lexan[®] polycarbonate for optical access and were 12.7 mm thick. From the perspective of standing on the heated wall at the inlet, they are termed left ($z=-152$ mm), top ($y=305$ mm), and right ($z=152$ mm) walls. The top wall had a removable center portion for cleaning and maintenance. This wall also had three 25.4-mm ports for probe insertion that were used for the TC probe described in Sec. 2.3.3.

The as-built geometry was measured to compensate for differences between the as-designed and as-built

Table 2.3: Heated wall components and thicknesses with names from Fig. 2.4

Name	Material	t [mm]
Nickel Coating	Bright Nickel	~0.05
Al. Surface Plate	Al. 2024-T3	3.18
Thermal Epoxy	Dow Corning 3-6751	1.02
Kapton [®]	Kapton [®] HN Film	0.254
Al. Main Plate	Al. 6061-T651	6.35
Heater	Tempco Silicone Rubber	1.59
Insulation	Mineral Wool	25.4
Al. Back Plate	Al. 6061-T651	6.35

test section geometry. The differences were small, but the measurements are presented for completeness. An internal micrometer was used to measure the internal dimensions of the fully assembled test section. Height measurements were performed at the left, center, and right as well as width measurements at the top, middle, and bottom. This was done at seven locations in x and performed three times for a measure of random uncertainty. Modelers may use these dimensions when constructing the simulation domain to ensure greater similarity. A sketch of the measurement locations may be accessed from the online database by the link [All-BC-AsBuiltSketch](#) in the digital version of this work. The nominal values are in [All-BC-AsBuiltMeasurements](#) and uncertainties in [All-BC-AsBuiltMeasurementUncertainties](#). A Parasolid model created from the as-built measurements is available in [All-BC-AsBuiltGeometry](#).

A warm-up procedure was followed each time the RoBuT was used for experiments. Ideally, the HVAC system would be kept active at all times for stable room conditions. The heated wall was first heated to the setpoint temperature. Once this was reached, the blower was set to the desired speed for the experiment and the heater controllers would accordingly increase power. Once the temperature was again stable for at least five minutes, the facility was ready for data acquisition. If the blower setpoint speed was changed, the controller would stabilize temperature and a waiting period was repeated for at least five minutes.

Between data acquisition for the different cases, such as between the aided and opposed cases, the entire test section was cleaned with Ethyl Alcohol and delicate task wipes to ensure optical quality. The cover on the top wall was removed for inside cleaning. High-vacuum grease was used on test section joints to reduce air leakage and was removed and reapplied each time a panel of the test section was adjusted.

2.3 Analog Instrumentation and Signal Processing

Validation experiments require high fidelity instrumentation. Thermocouples were used to measure boundary temperatures, heat flux sensors (HFSs) for heat flux through the heated wall, and PIV for inflow

and boundary layer air velocity. Other sensors measured room air conditions. These systems will now be described in detail.

2.3.1 Thermal Instrumentation

A total of 307 TCs were used to measure boundary temperatures. All test section TCs were 30 gauge Type K from Omega Engineering with Special Limits of Error. They were each welded to length with an Argon-shielded welder. Each TC was calibrated with an Isotherm FASTCAL-M with an accuracy of 0.3°C over a range of $25\text{--}190^{\circ}\text{C}$ with data at every 5°C . Because every TC calibration was very similar and made from the same spool, an average calibration curve was applied. An array of 3×5 TCs, three in y and five in z , was suspended on the downstream side of the honeycomb for inlet air temperature measurements. Each of the three clear walls had 21 TCs with seven rows spaced in x and three across in y for the left and right walls or in z for the top wall. The bulk of the heated wall had 5×32 TCs with five in z and 32 in x . The Teflon[®] edges each had embedded TCs with five across the leading edge in z and 32 along the sides in x . All TCs were embedded to within 3.18 mm of the inside surface using thermal epoxy with enhanced thermal conductivity.

Three HFSs were embedded into the heated wall along the spanwise center at the x -locations found in Table 2.2. They were model 20457-3 from RdF Corporation and were a thin-film type with a thermopile around a Kapton[®] substrate. The manufacturer supplied unique calibration coefficients for each sensor. The manufacturer-specified uncertainty was 5% of reading. An embedded Type T TC was used to measure sensor temperature and correct readings with the supplied multiplication factor curve to compensate for changes in thermal conductivity of the substrate. The HFSs were placed adjacent to the Kapton[®] layer of similar thermal resistance to reduce measurement errors. A thermal resistance network analysis showed only a 2.4% difference in heat flux between HFS and non-HFS conduction paths.

The TC and HFS output voltages were small, so special data acquisition (DAQ) devices were selected. National Instruments (NI) products were used as they interfaced well with the LabVIEW software that was used for system control and thermal data recording. Twenty one NI-9213 TC modules were housed in five NI-cDAQ-9188 chassis. The narrow voltage range of ± 78 mV, 24-bit ADC, and open channel detection made them well suited for these measurements. The built-in CJC was used for TCs. The total uncertainty of the calibrated TCs with these DAQs was 1°C , largely attributable to the CJC uncertainty of 0.8°C . Data from thermal instrumentation was recorded on-demand. Twelve sets of instantaneous measurements were recorded, one to accompany every set of PIV data for each case.

2.3.2 Particle Image Velocimetry

The PIV system allowed for non-intrusive, full-field velocity measurements at several locations. The system consisted of a laser, camera, and timing unit. The laser was a New Wave Research Solo PIV III. It was a dual cavity, frequency-doubled Nd:Yag model with about 22 mJ/pulse and a wavelength of 532 nm. Two LaVision camera designs were used as equipment was upgraded: an Imager Intense CCD camera for buoyancy-aided data and an Imager sCMOS for buoyancy-opposed data. The former had a 12-bit CCD sensor with 1376×1040 pixels and a pixel size of $6.45 \mu\text{m}$. The latter had a 16-bit sCMOS sensor with 2560×2160 pixels and a pixel size of $6.5 \mu\text{m}$. An internal, LaVision standard version PTU 9 timing unit provided accurate timing of the system and had a resolution of 10 ns and jitter of <1 ns. Two Nikon lenses were used: one AF Nikkor 28 mm f/2.8 D for the large field of view inflow and one AF Micro-Nikkor 105 mm f/2.8 D for high resolution SRQ data near the heated wall.

Images were acquired with LaVision DaVis 8.1 software and processed with DaVis 8.2. The optical configuration of the system is shown in Fig. 2.3 with the laser sheet normal to the heated wall and camera viewing angle parallel with it. The equipment was moved manually in the x direction. The inflow was measured in the same configuration with Velmex BiSLide[®] traverses to move the laser and camera consistently in the z direction. In this way, nine planes were measured to map the inflow.

PIV calibration was performed in two ways. The inflow used a conventional two-component ‘ruler’ calibration over a span of about 280 mm since the laser sheet and camera were normal to each other. The SRQ data near the heated wall was calibrated with a single-plane calibration target and the pinhole model as the camera was angled into the wall by $3\text{--}5^\circ$. This angle was required to avoid image diffraction by the large temperature gradient very near the wall. Because this flow had very little through-plane motion, errors in v velocity from through-plane motion appearing as in-plane motion are expected to be small (they are a function of the sine of the angle). The pinhole model was applicable since refraction between the Lexan[®] and air was also small.

Prior to acquisition, the quality of the particle images was checked to ensure proper particle density, diameter, and displacement as well as laser beam overlap and image focus quality. Many of these data parameters and others from the acquired images are found in Table 2.4. The diameter, density, and displacement are spatial averages over the entire image. Both particle diameter and density were determined by methods found in [16] with the local maximum method for density estimation.

The processing of particle images was performed with the window deformation method in DaVis. A mask was carefully defined to remove the influence of walls on the correlation. Round interrogation windows

Table 2.4: PIV data parameters. Aided refers to buoyancy-aided case while Opposed refers to buoyancy-opposed case.

Parameter	Aided-Inlet	Opposed-Inlet
N image pairs	500	1000
sample frequency [Hz]	4	10
dt [μ s]	1000	750
lens	28 mm	28 mm
extension [mm]	–	–
calibration [mm/pixel]	0.223	0.124
$f\#$	5.6	11
diameter [pixels]	1.45	1.39
density [$\#$ / 32×32]	70.8	19.3
displacement [pixels]	11.4	15.7
Parameter	Aided-SRQ	Opposed-SRQ
N image pairs	1000	1000
sample frequency [Hz]	4	10
dt [μ s]	76	62–65
lens	105 mm	105 mm
extension [mm]	39.5	39.5
calibration [mm/pixel]	0.0116	0.0103
$f\#$	5.6	11
diameter [pixels]	3.98–4.89	3.07–3.16
density [$\#$ / 32×32]	6.36–8.99	4.76–8.47
displacement [pixels]	13.8	12.2

were used for reduced noise. The first two passes were at 64×64 pixels and 75% overlap and the final four passes were at 32×32 pixels and 75% overlap. Vector post-processing was performed where vectors were removed if the peak ratio was less than two. Then a two-pass median filter of ‘strongly remove & iteratively replace’ corrected spurious vectors. Vectors were removed if their difference from average was more than one standard deviation of neighbors and subsequently replaced if the difference from average was less than two standard deviations of neighbors.

Particle images had a sliding background removed where the background is the average of nine images symmetrically taken around the image of interest. The pixel range was sometimes narrowed in the flow direction to reduce disk space while keeping at least 512 pixels in this direction. Examples of particle images with background subtracted for both orientations acquired with two cameras are shown in Fig. 2.5. Note that the heated wall is on opposite sides since the tunnel orientation was changed between cases. Also, the buoyancy-aided case used the Imager Intense camera with fewer pixels than the sCMOS used in the buoyancy-opposed case.

2.3.3 TC Probe

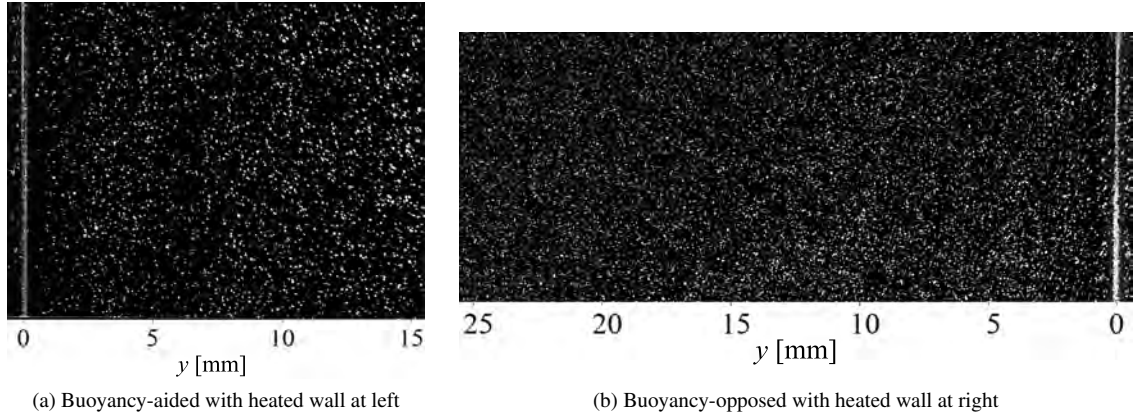


Fig. 2.5: Particle images at x_2

In order to provide an additional SRQ, it was necessary to measure the fluid temperature in the boundary layer. Since the RoBuT is an open-loop air tunnel with a large volume flow rate, optical measurement techniques requiring specialized particles are not practical. Thus, a TC probe was designed similar to that used in [17] with care taken to reduce the size and subsequent disruption of the flow. As this probe was intrusive and changed the flow, it was used after acquiring all other types of data so that its influence is only seen on the measured temperature profiles.

The junction of the probe was formed by type K wires of diameter $D_{TC} = 0.051$ mm from Omega Engineering. The two lead wires are aligned parallel to the wall with a length of 15.3 mm ($\sim 300D_{TC}$) to reduce conduction losses as shown in Fig. 2.6. The junction was formed by spot welding the overlapped wires. After welding, the wire was pulled taut and epoxied in place. The fine wire was welded to thicker 0.511-mm wire that spanned the pivot and was connected to the DAQ. The brace shown in Fig. 2.6 was rigid enough to keep the wire tight. To correct for small misalignments that could cause measurement errors, a pivot was designed into the probe so it could be aligned with the wall before each measurement. This was done by moving the probe into the wall until both ends of the brace were pressed firmly and any angle corrected, then pulling the probe away from the wall. This probe was measured with the same NI-9213 TC modules described in Sec. 2.3.1 and was used in the spanwise center of the tunnel.

The probe may be subject to conduction losses that could lead to measurement error. This error was estimated using a 1-D fin equation. The measured temperature and velocity profiles were used to estimate fluid properties and heat transfer coefficients. Heat conduction was considered from the TC junction to the leads and then convecting to the lower temperature air. The largest error was estimated at 0.03°C at the wall at x_1 .

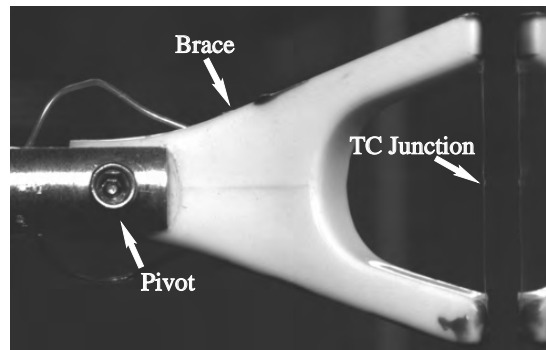


Fig. 2.6: TC probe with its reflection in the heated wall on the right

This TC probe assembly was supported by a stainless steel tube with 3.76-mm outside diameter that spanned the test section. This tube contained the TC wires and was connected to a Velmex Inc. UniSlide® traverse model B4015Q2J. This traverse was used for small, incremental movements. The distance from the wall was estimated by fitting a line to the temperature profile very near the wall to the wall temperature measured by embedded TCs. The largest uncertainty in position resulted from the stepper motor resolution. With 200 steps/rev. and an assumed 1/2 step resolution, the uncertainty was 2.5 μm . The pitch uncertainty was much smaller at 0.04 mm/25.4 cm or 0.0315 μm for a 200 μm step.

2.3.4 Atmospheric Instrumentation

Air temperature, relative humidity, and atmospheric pressure in the RoBuT room were measured to determine air properties. Both temperature and humidity were measured with an Omega HX93A probe. Pressure was measured with an Apogee Instruments BPS 1006 sensor. The output voltage of these sensors was measured by a NI USB-9215A 4-channel ± 10 V analog input DAQ. The uncertainty of temperature was 0.6°C, humidity was 2.5% for readings 20-80% and 3.1% otherwise, and pressure was 3% of reading. These data were sampled at 1 Hz, then averaged and recorded once per minute.

2.3.5 Uncertainty Quantification

Thermal and atmospheric data uncertainty quantification (UQ) is described here following methods of Coleman and Steele [18]. UQ for PIV was considered by other methods and is described later. Bias uncertainty parameters were obtained from sensor documentation at the 95% confidence level. The random

uncertainty of a general mean quantity \bar{x} was calculated by

$$S_{\bar{x}} = t_{95} \frac{S_x}{\sqrt{N}} \quad (2.6)$$

where t_{95} is the confidence level coefficient (taken as 1.96 for 95% confidence and number of samples $N > 30$) and S_x is the sample standard deviation. Bias and random sources are combined as

$$U_{\bar{x}} = \sqrt{B_{\bar{x}}^2 + S_{\bar{x}}^2} \quad (2.7)$$

where $B_{\bar{x}}$ is the expanded bias uncertainty. The data provided with this paper generally specifies the unique bias, random, and total uncertainty numbers with the mean results.

Uncertainty of the PIV results was calculated from the Uncertainty Surface Method that estimates instantaneous bias and random uncertainties due to the effects of particle displacement, particle image density, particle image size, and shear. This method was originally described in [19] and improved on with methods from [16]. The uncertainties of the velocity statistics propagated from the instantaneous uncertainties were calculated by methods of Wilson & Smith [20]. Total uncertainty was calculated as in Eqn. 2.7. The confidence level on all UQ results in this work is 95%.

2.4 Boundary Conditions

This section contains a description of all expected requisite BCs for CFD model inputs. The types of BCs were shown in Table 2.1. The as-built geometry is a BC, but was discussed previously in Sec. 2.2.2.

2.4.1 BC Description

The measured BC temperatures are mapped onto the test section geometry in Fig. 2.7. Note the high measurement resolution on the heated wall and the development of the thermal boundary layer on the right wall as air travels from the inlet to the right of the figure.

As mentioned previously, the inflow was measured in nine planes spaced in z with points concentrated near the side walls. The time-mean streamwise velocity \bar{u} at the inlet is shown in Fig. 2.8 for the buoyancy-opposed case. Gray lines indicate PIV measurement locations that span across y . Data are highly-resolved in y but not in z . Data may be interpolated from the information given. Another approach is to use the high-resolution data near the unheated top wall ($y=305$ mm) boundary layer to the left and right walls which are also unheated.

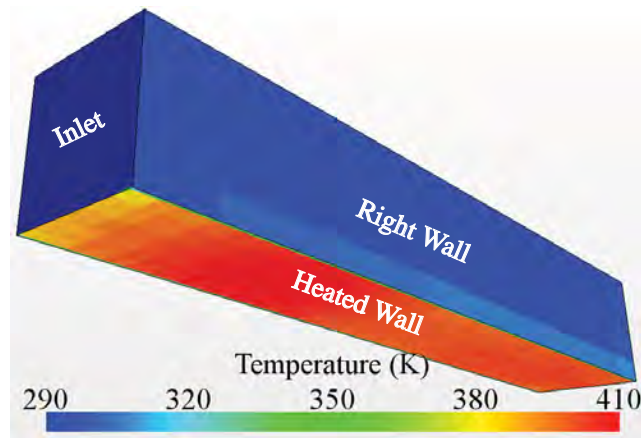


Fig. 2.7: Measured temperatures on the test section boundaries

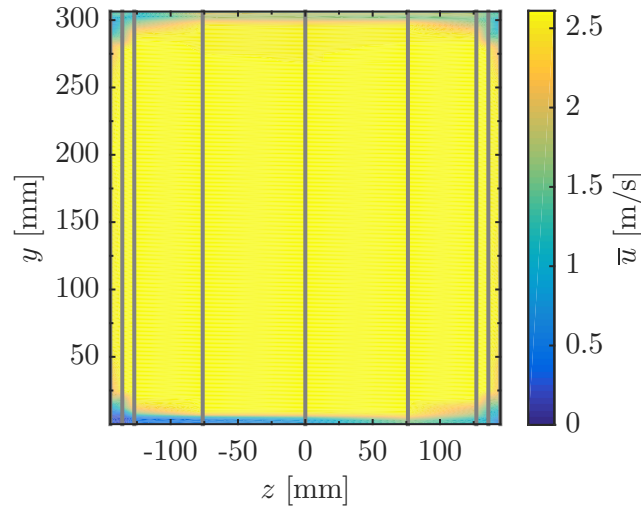


Fig. 2.8: Measured streamwise velocity \bar{u} at the inlet for the buoyancy-opposed case

The atmospheric conditions include atmospheric pressure, relative humidity, and room temperature and were recorded at the time of data acquisition.

Data acquisition procedures were followed to control test conditions. The following list describes the steps followed for acquisition of both BC and SRQ data:

1. Begin heating of the heated wall
2. Upon reaching setpoint temperature, start blower
3. Align traverses, laser, and camera with test section at measurement location

4. Align laser sheets
5. Focus camera on particle images
6. Align calibration plane with laser sheet and calibrate camera
7. Determine optimal dt for particle displacement, proper seeding density, and proper laser intensity
8. Record measurement location and other PIV parameters
9. Confirm stability of wall temperature and room conditions
10. Record PIV data, atmospheric and thermal conditions

This process was repeated for PIV measurement locations for the nine inflow and the three SRQ data sets. Inflow data were acquired in a single day, so only the last three steps were repeated after the first set. Data for PIV were recorded at twelve locations (nine at the inlet and three along the heated wall). Atmospheric conditions and thermal measurements were recorded with each PIV data set.

Since the velocity at the inlet is partially developed, some external flow parameters are included. The momentum thickness was measured from PIV data at the spanwise center ($z = 0$) location using the integral

$$\delta_2 = \int_0^\infty \frac{\bar{u}}{\bar{u}_\infty} \left(1 - \frac{\bar{u}}{\bar{u}_\infty} \right) dy \quad (2.8)$$

where \bar{u}_∞ is the free-stream velocity and constant density has been assumed [7]. The boundary layers on both walls were considered from $y = 0 - 0.305$ m and the result divided by two. Constant density is a good approximation at the inlet but not for downstream locations where the near-wall air was heated.

The concept of a virtual origin may also help predict the equivalent length of a flat plate extending upstream of the inlet. This allows for the impact of the contraction to be assessed. Assuming the flow was always turbulent, others have derived the relationship [7]

$$\frac{\delta_2}{x} = \frac{0.036\nu^{0.2}}{\bar{u}_\infty^{0.2}x^{0.2}} = 0.036\text{Re}_x^{-0.2}. \quad (2.9)$$

The left two portions can be arranged to isolate x as in

$$\xi = \frac{\delta_2^{1.25}\bar{u}_\infty^{0.25}}{0.0157\nu^{0.25}} \quad (2.10)$$

where ξ has been substituted for x and is the distance upstream to a virtual origin given δ_2 defined earlier. The results from these analyses are given in Table 2.5. It is reasonable to add these virtual origin distances to the x values in Table 2.2 when comparing to more canonical flows. Also Re_x and subsequently Ri_x numbers may also be adjusted. As will be presented, it is reasonable that the buoyancy-opposed case had a larger boundary layer at the inlet in this low speed flow as this case showed larger layers downstream.

Table 2.5: Boundary layer analysis results

Parameter	Aided	Opposed
δ_2 [mm]	1.61	1.81
ξ [mm]	417	485

2.4.2 BC Data

These data are available for both the buoyancy-aided and opposed cases on the inflow and all four walls of the test section. There is one file for the measured temperature of each surface that can be found in Table 2.6. The files may be opened by the links in the digital version. The format for all BC files works directly with Star-CCM+ and is easily adaptable to other CFD codes. The columns X, Y, and Z are used throughout this work; adhere to the global coordinates; and are presented in meters. The column ‘T[K]’ is the mean temperature in Kelvin, ‘B-T[K]’ is the bias uncertainty, ‘S-T[K]’ is the random uncertainty, and ‘U-T[K]’ is the total uncertainty.

Table 2.6: Links to temperature boundary files for both cases

Aided	Opposed
Aid-BC-InletTemp	Opp-BC-InletTemp
Aid-BC-HeatedWallTemp	Opp-BC-HeatedWallTemp
Aid-BC-LeftWallTemp	Opp-BC-LeftWallTemp
Aid-BC-TopWallTemp	Opp-BC-TopWallTemp
Aid-BC-RightWallTemp	Opp-BC-RightWallTemp

The data for the inflow mean and fluctuating velocities are found in the files [Aid-BC-Inlet-Vel](#) and [Opp-BC-Inlet-Vel](#). The columns ‘u’, ‘v’, and ‘w’ are mean velocities in the x , y , and z directions respectively. The columns ‘u’u’, ‘v’v’, ‘w’w’, and ‘u’v’ are specific Reynolds stresses. Uncertainties of \bar{u} , \bar{v} , and \bar{w} compose

the remaining columns. Reynolds stresses have unique upper and lower uncertainties with ‘Uuup’ being the plus uncertainty of $\overline{u'u'}$ and so on. The units of velocity and velocity uncertainty are [m/s] while those of Reynolds stresses and their uncertainty are [m²/s²].

Note that inflow out-of-plane velocities \overline{w} and $\overline{w'w'}$ were assumed to be the same as \overline{v} and $\overline{v'v'}$ respectively. This assumption was proved valid in previous work in this facility by measuring the inflow in both directions with two-component PIV and comparing data where measurement planes intersect [2]. Buoyancy-aided inflow data for the plane nearest the right wall was questionable and replaced with data nearest the left wall. As the geometry and thermal conditions are symmetric about $z = 0$, this was considered justified.

The atmospheric measurements, together with their uncertainties, are found in the files [Aid-BC-AtmCond](#) and [Opp-BC-AtmCond](#).

2.5 Fluid and Material Properties

As air is the working fluid, measurements of temperature, pressure, and relative humidity discussed in Sec. 2.4.2 are satisfactory to define all fluid properties. It is important to note that the working pressure is different from that at sea level as the experiment was conducted in Logan, Utah, which is 1460 meters above sea level.

Material properties of the test section can easily be obtained from the information provided in Sec. 2.2.2 about the construction of the test section. It is not necessary to model the heated wall since temperature measurements were made very near the surface, but the information is provided for completeness.

2.6 Test Conditions

The RoBuT room was configured with modern HVAC systems and thermal insulation for stable conditions. Controls were independent of other systems in the building. The refrigerated air conditioning had a $\sim 0.56^\circ\text{C}$ (1°F) deadband. The maximum measured temperature spread for both cases near the inflow location during data acquisition is 0.7°C ($\sim 1.3^\circ\text{F}$). To reduce the rate of temperature change from the on/off behavior of this system, outside air was mixed with refrigerated air before being injected into the room. Heating was performed with a steam heat exchanger with attached fan. The original fan and control system were replaced with a variable speed, tuned, PI-controlled system implemented with the main LabVIEW program, giving the heating system tight control of the room temperature.

2.7 System Response Quantities

The SRQs are the experimental results used to compare with simulation outputs and were listed in

Table 2.1. Since they are similar, the mean velocity profiles and fluctuating velocity profiles in the form of Reynolds stresses are presented together. Temperature profiles from the TC probe are presented for the opposed case. Additionally, scalars of wall heat flux and wall shear stress are also provided.

2.7.1 SRQ Description

Normalized streamwise velocity and Reynolds stress for the buoyancy-aided and buoyancy-opposed cases are shown in Fig. 2.9 for three measurement locations in x . The bulk velocity $\bar{u}_{\text{bulk}} = 2.44$ m/s measured across the inlet is used for normalization. The profile locations correspond to the vertical center of the camera sensor for reduced perspective error. Uncertainty bands are provided on both profiles that are unique for each data point. In other words, the uncertainty of $\bar{u}/\bar{u}_{\text{bulk}}$ and $\overline{u'u'}/(\bar{u}_{\text{bulk}})^2$ varies over y .

The influence of buoyancy is apparent in several regards. The boundary layer velocity and Reynolds stress is nearly constant for all x in the buoyancy-aided case, indicating little growth in the boundary layer thickness. The buoyancy-opposed case, however, shows rapid boundary layer growth. Also apparent is evidence of laminarization in the aided case and the augmentation of Reynolds stresses for the buoyancy-opposed case typical of mixed convection flows as described in previous works [9, 12].

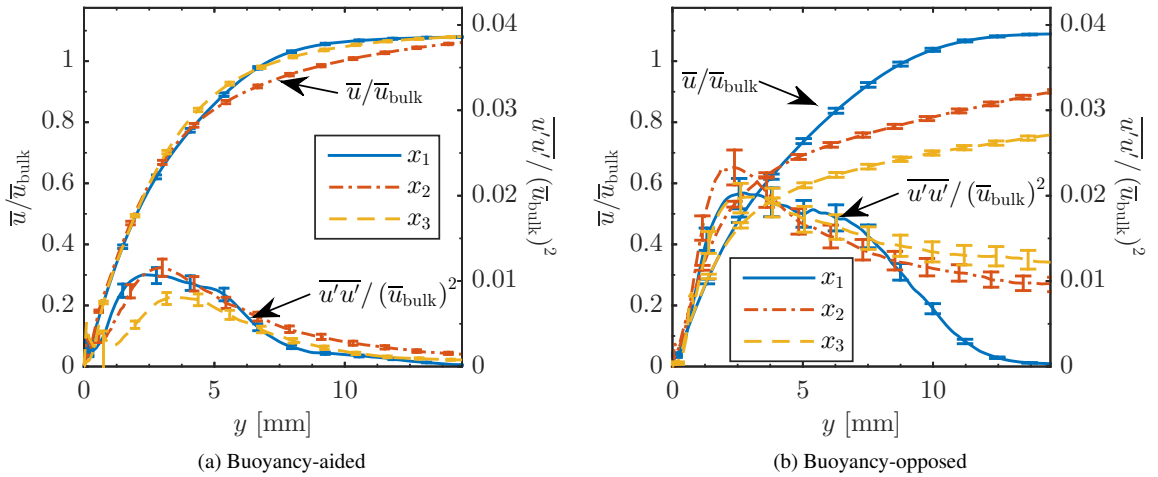


Fig. 2.9: Normalized streamwise mean velocity \bar{u} and Reynolds normal stress $\overline{u'u'}$ at three locations in x for both cases

The difference in the two cases reveals the influence of buoyancy on streamwise velocity and streamwise Reynolds normal stress. This is shown in Fig. 2.10. In these plots, the difference is labeled Diff and is the buoyancy-aided (Aid) minus the buoyancy-opposed (Opp) results. Buoyancy effects accelerate the boundary

layer velocity, but this influence is localized near the heated wall. As in the findings of other researchers in mixed convection, turbulence levels as quantified by $\overline{u'u'}$ are increased for the opposed case. Here the difference is about a factor of two. There is a subtle two-peak nature to $\overline{u'u'}$ that is most apparent in their difference at x_1 . This may be caused by the 3.175-mm-wide turbulence trips that are upstream of the test section, especially considering that this profile feature dies out farther downstream.

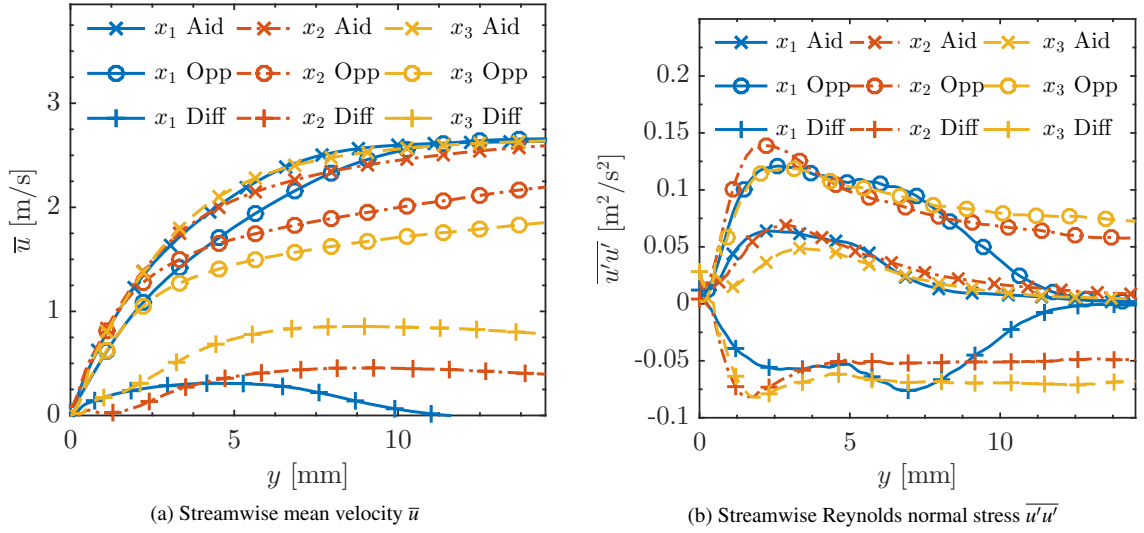


Fig. 2.10: Measured streamwise mean velocity \bar{u} and streamwise Reynolds normal stress $\overline{u'u'}$ with buoyancy-aided (Aid), buoyancy-opposed (Opp), and their difference (Diff) at three locations in x

The measured temperature profile from the TC probe for the buoyancy-opposed case is shown in Fig. 2.11a. The development of the thermal boundary layer is observable in x . The temperature in the near-wall region and line fit are shown in Fig. 2.11b. Errors in distance from the wall are corrected by fitting the line through the measured wall temperature. The first point is not considered as it is likely to have position error. Only data within $y^+ \leq 6.6$ are used in the fit as they should be contained in the inner portion of the viscous or laminar sublayer where linear temperatures are expected. Temperature fluctuations are not included as the mass of the TC wire rendered it insensitive to the higher frequencies in this flow. These frequencies were determined with a 50.8- μm diameter tungsten hot-film probe with much less thermal mass.

The intrusive nature of the probe caused an increase in wall heat flux observable in the HFS data acquired at the time. The largest error of wall heat flux occurred when the probe was touching the heated wall and steadily decreased as the probe was retracted from the wall. Maximum errors of 18.7%, 10.4%, and 7.93% were measured at locations x_1 , x_2 , and x_3 , respectively. This effect will only bias the temperature data

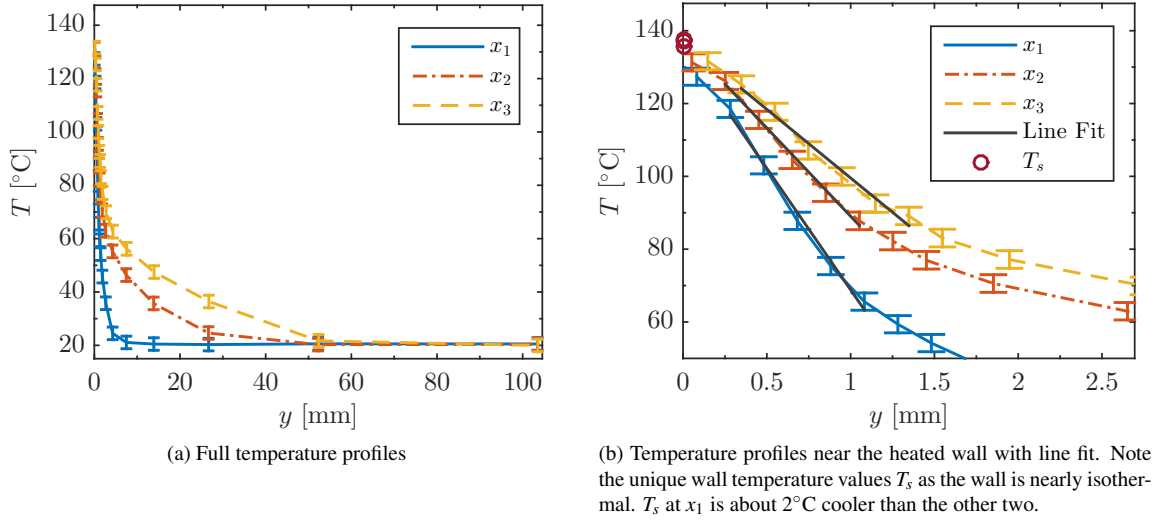


Fig. 2.11: Measured temperature profiles for all three x locations for the opposed case

provided as all other BC and SRQ data were acquired at other times. Intrusive probes should be avoided in validation experiments as the effect of their presence is often difficult to quantify. As such, the use of these temperature data is recommended for qualitative analysis but may not be appropriate for quantitative assessment as an SRQ.

Wall heat flux, as measured by the HFSs, is shown in Fig. 2.12. In laminar flows, buoyancy-aided mixed convection produces higher heat flux values than for buoyancy-opposed [7]. The current experiments show the opposite, suggesting turbulence levels are a major contributor to the flux. These observations are consistent with turbulent mixed convection. As there are no known heat transfer correlations for mixed convection in developing channel flow, the correlation for fully developed flow in vertical tubes was used as Eqn. 6 in the work of Jackson *et al.* [9]. These are consistent with the observed heat flux as the buoyancy opposed case generated higher heat flux. The correlation values have been adjusted to consider an unheated starting length with distances from the virtual origin analysis described earlier. The local Nusselt number was adjusted by

$$\text{Nu}_x = \frac{\text{Nu}_x|_{\xi=0}}{\left[1 - (\xi/x)^{9/10}\right]^{1/9}} \quad (2.11)$$

where the local Nusselt number Nu_x and $\text{Nu}_x|_{\xi=0}$ was measured from the leading edge of the unheated starting length [8].

The measured trends in the streamwise direction x are inconsistent with expected results. The HFS at x_2 gives a smaller reading than that at x_3 for both cases. It is possible that this trend is caused by an installation

error of the potted sensors in the heated wall. Even though the cause is unknown, the likelihood of this error existing is supported by the monotonic decrease in the temperature gradient near the wall with streamwise distance x as observed in Fig. 2.11b. This decrease suggests a decrease in wall heat flux with x , consistent with theory.

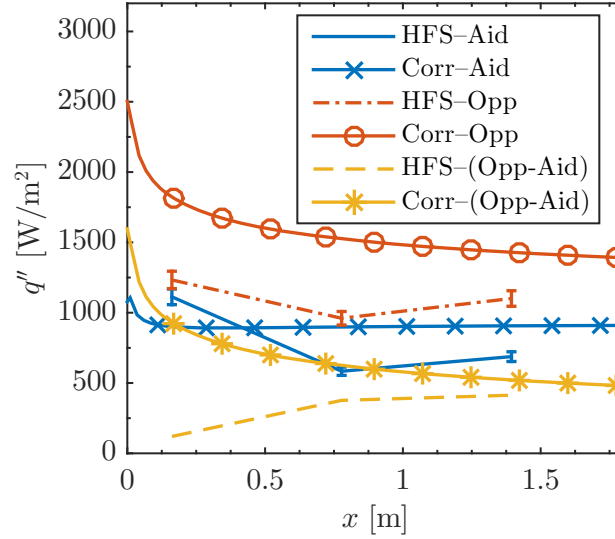


Fig. 2.12: Measured wall heat flux plotted along streamwise direction x with correlations for mixed convection for the buoyancy-aided (Aid), buoyancy-opposed (Opp), and their difference (Aid-Opp). Heat Flux Sensor results are labeled as HFS and correlation results as Corr.

Previous methods to quantify wall shear have fit experimental turbulent velocity data with empirical models such as Spalding or Musker profiles with high accuracy [21]. This method works well for fully turbulent boundary layer data where the models are an accurate representation of velocity, but not for the data in this study due to significant buoyancy effects. Therefore, wall shear stress was estimated directly from PIV data as $\tau_s = \mu \frac{\partial u}{\partial y} \big|_{y=0}$ where τ_s is wall shear stress and μ is dynamic viscosity. High-resolution PIV data were used to fit a line to velocity data where $y^+ = y u_\tau / \nu \leq 3$ to find $\frac{\partial u}{\partial y} \big|_{y=0}$, where $u_\tau = \sqrt{\tau_s / \rho}$ and ρ is the fluid density [7]. Initially 10 points were included in the fit and a stable iterative method was used to calculate τ_s and the number of data points to fit within $y^+ \leq 3$. The wall was located by the particle images with a mask carefully defined. The linear fit was performed using linear regression with more weight given to velocity data with lower uncertainty [22]. The high-resolution PIV data and associated linear fit are shown in Fig. 2.13. The dynamic viscosity was evaluated using Sutherland's Law at the wall temperature. The fit uncertainty was combined with the viscosity uncertainty using the Taylor Series Method [18].

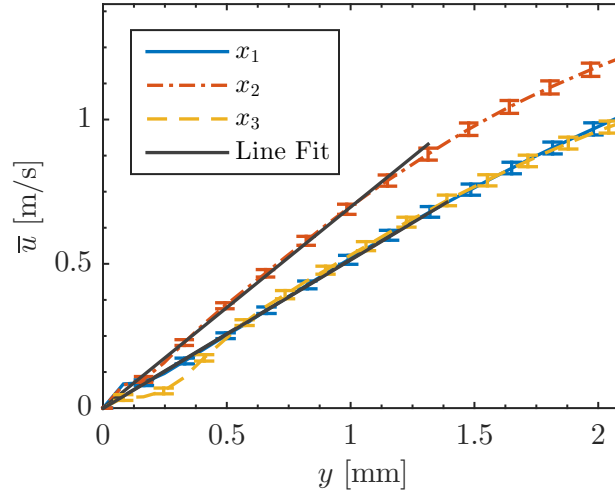


Fig. 2.13: Streamwise mean velocity \bar{u} near the heated wall with linear fit for shear stress measurement of the buoyancy-opposed case

Data acquisition was repeated several times for each case to determine the level of repeatability. There are generally two versions of the same data with the exception of the buoyancy-aided case at x_1 , which has three. Data were acquired between one to ten months apart and, in the buoyancy-opposed case, with a different camera. The acquisitions were also performed by two different users. The test section was disassembled, repaired, and reassembled between the second (R2) and third (R3) series for the buoyancy-aided case. The PIV equipment was removed, replaced, and recalibrated between series. The tabulated data included in this work are from the series R1 in both cases. The results for the mean streamwise velocity are shown in Figs. 2.14a & 2.14b for the buoyancy-aided and opposed cases respectively. They show only small differences that are more apparent in the buoyancy-opposed case.

Repeatability plots for mean streamwise Reynolds stress $\overline{u'u'}$ are shown in Figs. 2.15a & 2.15b for the two cases. The Reynolds stresses are less repeatable than the mean velocity, but only by a moderate amount. The results at x_1 have the largest difference, which may be due to differences in the inflow that become less important with streamwise development.

As mentioned previously, there is a large difference in turbulence levels between the buoyancy-aided and opposed cases. Another method for representing the differences is the scatter plot of $\overline{u'v'}$. There is little scatter in the buoyancy-aided case (Fig. 2.16a) compared to the buoyancy-opposed case (Fig. 2.16b), suggesting laminarization is occurring in the buoyancy-aided case. These results are consistent with the findings of other works in turbulent mixed convection. The results show the typical predominance of events

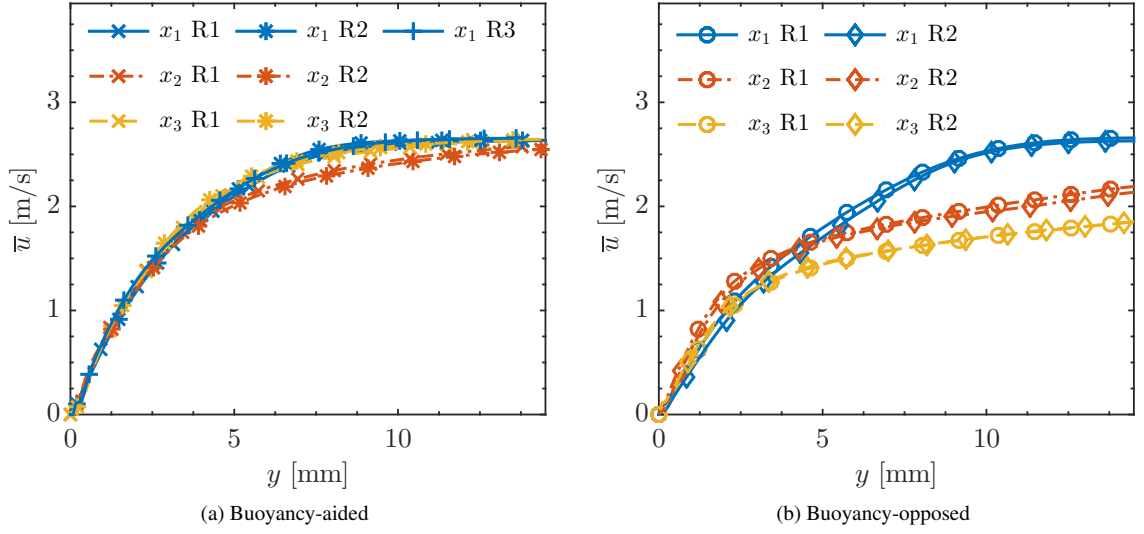


Fig. 2.14: Mean streamwise velocity \bar{u} with several repeats at three locations in x for both cases

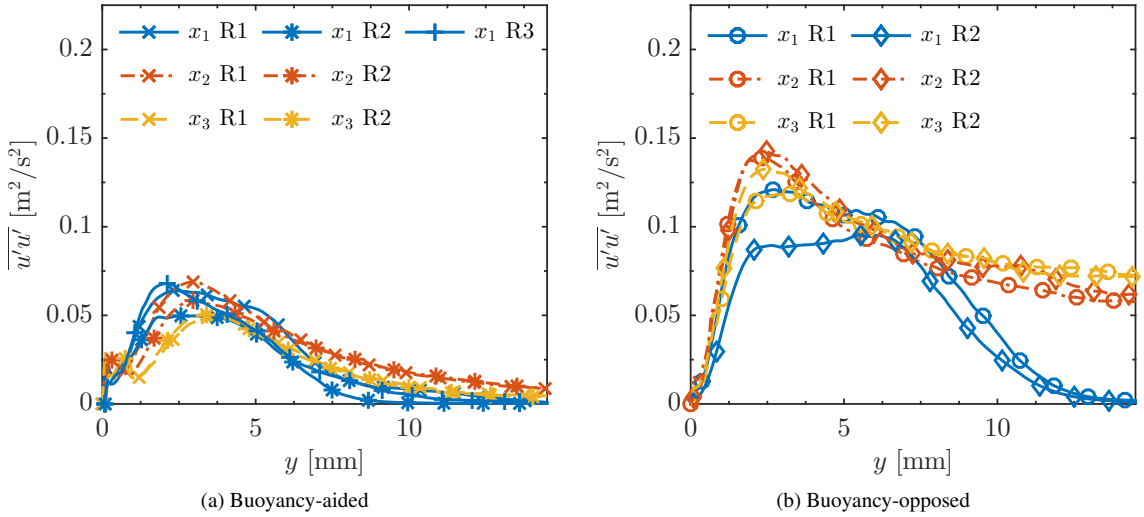


Fig. 2.15: Measured mean streamwise Reynolds stress $\overline{u'u'}$ with several repeats at three locations in x for both cases

in quadrants 2 and 4, which are related to turbulent ejections and sweeps respectively.

2.7.2 SRQ Data

These data are generally found in one file for each x location with unique files for each orientation. For all SRQ files, the same global coordinate system is used and units are included in column headers. Links to

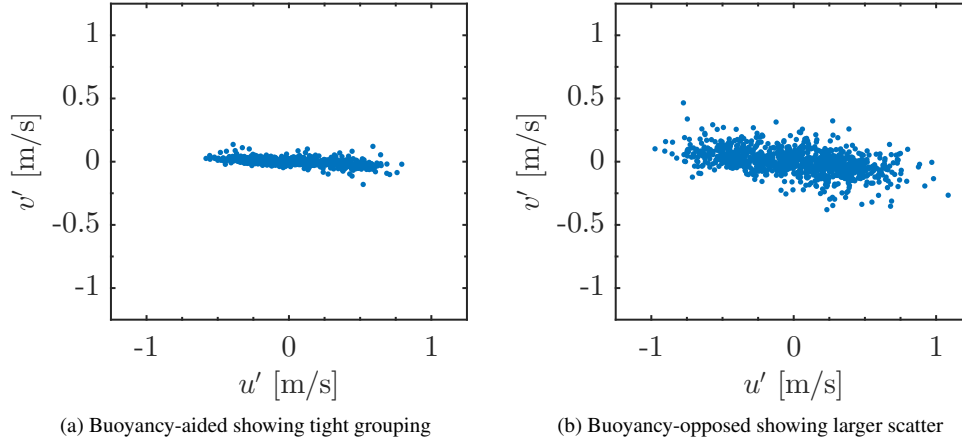


Fig. 2.16: Scatter of instantaneous u' and v' at the y -location of largest $\overline{u'u'}$ for both cases at x_2

the velocity results are found in Table 2.7. Velocities and Reynolds stresses in both measured directions are given as well as Reynolds shear stress. Uncertainties are provided for all provided quantities as before.

Table 2.7: Links to velocity SRQ files for both cases

Aided	Opposed
Aid-SRQ-Vel_x1	Opp-SRQ-Vel_x1
Aid-SRQ-Vel_x2	Opp-SRQ-Vel_x2
Aid-SRQ-Vel_x3	Opp-SRQ-Vel_x3

Temperature profile data are available for the buoyancy-opposed case at all three x locations in files [Opp-SRQ-T_x1](#), [Opp-SRQ-T_x2](#), and [Opp-SRQ-T_x3](#). Tabulated results for the scalar wall heat flux are compiled into the files [Aid-SRQ-HeatFlux](#) and [Opp-SRQ-HeatFlux](#). Shear results are similarly compiled into files [Aid-SRQ-Shear](#) and [Opp-SRQ-Shear](#).

2.8 Conclusions

This work has presented a highly detailed study on turbulent mixed convection along a vertical, flat plate using high fidelity instrumentation. The data and description are believed to be sufficient for a CFD validation study of these physics to determine validation error (Eqn. 2.1) and validation uncertainty (Eqn. 2.2). The effects of buoyancy were investigated in two orientations, buoyancy-aided and buoyancy-opposed. Buoyancy was found to have a laminarizing effect on the boundary layer flow in the buoyancy-aided case that suppressed

heat transfer. The buoyancy-opposed case had increased turbulence levels and higher heat flux. All requisite BCs were measured and provided with their uncertainties. A variety of SRQs were reported for comparison with simulation outputs. Tabulated data were provided by digital links for direct use. This method of data description and dissemination can greatly enhance the ability of modelers to assess simulation accuracy. Furthermore, the inclusion of this information in published works increases their availability.

Acknowledgments

This research was performed using funding received from the DOE Office of Nuclear Energy's Nuclear Energy University Programs, and their support is gratefully acknowledged.

References

- [1] Oberkampf, W. L., and Smith, B. L., 2014, "Assessment Criteria for Computational Fluid Dynamics Validation Benchmark Experiments," 52nd Aerospace Sciences Meeting of AIAA.
- [2] Harris, J. R., Lance, B. W., and Smith, B. L., 2015, "Experimental Validation Data for Computational Fluid Dynamics of Forced Convection on a Vertical Flat Plate," *Journal of Fluids Engineering*, **138**(1), p. 011401, doi:[10.1115/1.4031007](https://doi.org/10.1115/1.4031007).
- [3] Oberkampf, W. L., and Roy, C. J., 2010, *Verification and Validation in Scientific Computing*, Cambridge University Press, doi:[10.1017/cbo9780511760396](https://doi.org/10.1017/cbo9780511760396).
- [4] ASME, 2009, "ASME V&V 20-2009: Standard for Verification and Validation in Computational Fluid Dynamics and Heat Transfer," Standard, American Society of Mechanical Engineers.
- [5] Roache, P. J., 2009, *Fundamentals of Verification and Validation*, Hermosa Publ.
- [6] AIAA, 1998, "Guide for the Verification and Validation of Computational Fluid Dynamics Simulations," Tech. Rep. AIAA G-077-1998, American Institute of Aeronautics and Astronautics, Reston, VA, doi:[10.2514/4.472855](https://doi.org/10.2514/4.472855).
- [7] Kays, W. M., Crawford, M. E., and Weigand, B., 2012, *Convective Heat and Mass Transfer*, 4th ed., McGraw-Hill.
- [8] Incropera, F. P., Dewitt, D. P., Bergman, T. L., and Lavine, A. S., 2007, *Fundamentals of Heat and Mass Transfer*, 6th ed., John Wiley & Sons.
- [9] Jackson, J. D., Cotton, M. A., and Axcell, B. P., 1989, "Studies of Mixed Convection in Vertical Tubes," *International Journal of Heat and Fluid Flow*, **10**(1), pp. 2–15, doi:[10.1016/0142-727x\(89\)90049-0](https://doi.org/10.1016/0142-727x(89)90049-0).
- [10] Chen, T. S., Armaly, B. F., and Ramachandran, N., 1986, "Correlations for Laminar Mixed Convection Flows on Vertical, Inclined, and Horizontal Flat Plates," *Journal of Heat Transfer*, **108**(4), p. 835, doi:[10.1115/1.3247020](https://doi.org/10.1115/1.3247020).
- [11] Ramachandran, N., Armaly, B. F., and Chen, T. S., 1985, "Measurements and Predictions of Laminar Mixed Convection Flow Adjacent to a Vertical Surface," *Journal of Heat Transfer*, **107**(3), p. 636, doi:[10.1115/1.3247471](https://doi.org/10.1115/1.3247471).

- [12] Kim, W. S., Jackson, J. D., He, S., and Li, J., 2004, “Performance of a Variety of Low Reynolds Number Turbulence Models Applied to Mixed Convection Heat Transfer to Air Flowing Upwards in a Vertical Tube,” *Proceedings of the Institution of Mechanical Engineers, Part C: Journal of Mechanical Engineering Science*, **218**(11), pp. 1361–1372, doi:[10.1177/095440620421801107](https://doi.org/10.1177/095440620421801107).
- [13] Wang, J., Li, J., and Jackson, J., 2004, “A Study of the Influence of Buoyancy on Turbulent Flow in a Vertical Plane Passage,” *International Journal of Heat and Fluid Flow*, **25**(3), pp. 420–430, doi:[10.1016/j.ijheatfluidflow.2004.02.008](https://doi.org/10.1016/j.ijheatfluidflow.2004.02.008).
- [14] Kähler, C. J., Sammler, B., and Kompenhans, J., 2002, “Generation and Control of Tracer Particles for Optical Flow Investigations in Air,” *Experiments in Fluids*, **33**, pp. 736–742, doi:[10.1007/s00348-002-0492-x](https://doi.org/10.1007/s00348-002-0492-x).
- [15] Touloukian, Y. S., and Ho, C. Y., 1977, *Thermophysical Properties of Selected Aerospace Materials Part II: Thermophysical Properties of Seven Materials*, Purdue University, West Lafayette.
- [16] Warner, S. O., and Smith, B. L., 2014, “Autocorrelation-based Estimate of Particle Image Density for Diffraction Limited Particle Images,” *Measurement Science and Technology*, **25**(6), p. 065201, doi:[10.1088/0957-0233/25/6/065201](https://doi.org/10.1088/0957-0233/25/6/065201).
- [17] Blackwell, B. F., Kays, W. M., and Moffat, R. J., 1972, “The Turbulent Boundary Layer on a Porous Plate: an Experimental Study of the Heat Transfer Behavior with Adverse Pressure Gradients,” Tech. Rep. HMT-16, The National Aeronautics and Space Administration.
- [18] Coleman, H. W., and Steele, W. G., 2009, *Experimentation, Validation, and Uncertainty Analysis for Engineers*, John Wiley & Sons, doi:[10.1002/9780470485682](https://doi.org/10.1002/9780470485682).
- [19] Timmins, B. H., Wilson, B. W., Smith, B. L., and Vlachos, P. P., 2012, “A Method for Automatic Estimation of Instantaneous Local Uncertainty in Particle Image Velocimetry Measurements,” *Experiments in Fluids*, **53**(4), pp. 1133–1147, doi:[10.1007/s00348-012-1341-1](https://doi.org/10.1007/s00348-012-1341-1).
- [20] Wilson, B. M., and Smith, B. L., 2013, “Taylor-series and Monte-Carlo-method Uncertainty Estimation of the Width of a Probability Distribution Based on Varying Bias and Random Error,” *Meas. Sci. Technol.*, **24**(3), p. 035301, doi:[10.1088/0957-0233/24/3/035301](https://doi.org/10.1088/0957-0233/24/3/035301).
- [21] Kendall, A., and Koochesfahani, M., 2007, “A Method for Estimating Wall Friction in Turbulent Wall-bounded Flows,” *Exp Fluids*, **44**(5), pp. 773–780, doi:[10.1007/s00348-007-0433-9](https://doi.org/10.1007/s00348-007-0433-9).
- [22] Bevington, P. R., and Robinson, D. K., 2003, *Data Reduction and Error Analysis*, McGraw–Hill, New York.

Chapter 3

Experimental Validation Data for CFD of Transient Mixed Convection on a Vertical Flat Plate

Abstract

Transient convection was investigated experimentally for the purpose of providing Computational Fluid Dynamics (CFD) validation data. A specialized facility for validation experiments called the Rotatable Buoyancy Tunnel was used to acquire thermal and velocity measurements of flow over a smooth, vertical heated plate. The initial condition was forced convection downward with subsequent transition to mixed convection, ending with natural convection upward after a flow reversal. Data acquisition through the transient was repeated for ensemble-averaged results. With simple flow geometry, validation data were acquired at the benchmark level. All boundary conditions (BCs) were measured and their uncertainties quantified. Temperature profiles on all four walls and the inlet were measured, as well as as-built test section geometry. Inlet velocity profiles and turbulence levels were quantified using Particle Image Velocimetry. System Response Quantities (SRQs) were measured for comparison with CFD outputs and include velocity profiles, wall heat flux, and wall shear stress. Extra effort was invested in documenting and preserving the validation data. Details about the experimental facility, instrumentation, experimental procedure, materials, BCs, and SRQs are made available through this paper. The latter two are available for download and the other details are included in this work.

3.1 Introduction

The purpose of this work is to provide validation data for three-dimensional Computational Fluid Dynamics (CFD) models. Model validation will be discussed as well as the physical phenomenon of mixed convection. The following sections describe the experimental facility, the associated instrumentation, the boundary conditions (BCs), the fluid and material properties, the test conditions, and the System Response Quantities (SRQs). This content follows the Validation Experiment Completeness table of Oberkampf and Smith [1] to guide description of validation experiments. This guidance ensures important details are in-

cluded with a high level of completeness. The work contained herein is a continuation of that by Harris *et al.* [2] which covered forced convection using similar methods and facilities.

This work presents the data in table format for direct use in validating models. The provided data include the BCs and SRQs shown in Table 3.1. The included BCs in this work should provide modelers with all required information, avoiding assumptions on model inputs and reducing model form uncertainty [3]. The SRQ data are provided to modelers for direct comparison with model outputs. The experimental uncertainties of all provided data from bias and random sources are also provided and quantified at the 95% confidence level. Validation errors can be calculated with the nominal data and validation uncertainty from the uncertainty of the nominal data [4].

Table 3.1: The available experimental data presented in this work separated into BC and SRQ types

BCs	SRQs
As-Built Geometry	Velocity Profiles
Wall Temperatures	Reynolds Stress Profiles
Inlet Temperature	Wall Heat Flux
Inlet Velocity	Wall Shear
Atmospheric Conditions	

These files are accessible in an online database in the Digital Commons of Utah State University's Library. The page dedicated to the data in this work is found at digitalcommons.usu.edu/all_datasets/8/. Links to specific files are included in this work with descriptive file names with the experimental case (Trans), data type (BC or SRQ), and measured quantity. All data files may be downloaded in the zipped file [Data](#). Generally data are in table format as csv files.

3.1.1 Computational Fluid Dynamics Validation

To understand the need for experiments expressly aimed at providing validation data, one must first understand the different aims of validation and discovery experiments. Discovery experiments are common in research where new physical phenomena are measured, presented, and discussed. Validation experiments do not necessarily measure unique phenomena, but the measurement process and description are more complete [5]. In general, older experimental data from discovery experiments are not sufficiently described for use in validation. Unobtrusive measurement techniques are important in validation experiments since probes introduce unknown uncertainties to the data. These uncertainties can only be mitigated by including the probe

in the CFD model.

The purpose of validation experiments is to provide the information required to quantify the uncertainty of a mathematical model. This uncertainty helps decision makers quantify model credibility. The ASME V&V 20 Standard [4] outlines an approach to estimate the validation comparison error and the validation uncertainty. The validation error E is the difference between the simulation result S and the validation experiment result D as

$$E = S - D. \quad (3.1)$$

Calculating the validation uncertainty estimates the confidence interval of the error by considering both numerical and experimental uncertainty. Validation uncertainty is calculated as

$$U_{\text{val}} = \sqrt{U_{\text{num}}^2 + U_{\text{input}}^2 + U_D^2}, \quad (3.2)$$

where U_{num} is the numerical uncertainty, U_{input} is the model input uncertainty, and U_D is the experimental data uncertainty. The numerical uncertainty is estimated from solution verification with sources such as iterative and discretization uncertainty. The latter two uncertainties come from the validation data. The uncertainty in the measured BCs that are used for model inputs is U_{input} . The uncertainty of SRQs—experimental data used to compare system outputs—is U_D . If $|E| \gg U_{\text{val}}$, one can conclude model error remains. But if $|E| \leq U_{\text{val}}$ and U_{val} is acceptably small for the intended use of the model, the validation error may be satisfactory. These general equations show validation data and their uncertainties are required to assess model accuracy via model validation.

There are several tiers of detail in validation experiments [6], often four as shown in Fig. 3.1. This work is considered a Benchmark Case that is second in simplicity to Unit Problems. The Benchmark Case, also called Separate Effects Testing, requires that all model inputs and most model outputs are measured and that experimental uncertainty is included. In this tier there is generally some level of multi-physics interaction, such as coupled fluid momentum and heat transfer, that prevents this work from being considered a Unit Problem. On the other hand, the non-prototypical geometry used in this work keeps it from being a Subsystem Case.

The planning and execution of validation studies should include both modelers and experimentalists through all phases. In considering the design of validation systems, SRQs should be measured from a wide range and high difficulty in the difficulty spectrum as shown in Fig. 3.2. Comparing simulation results with experimental data from a wide range on the spectrum increases validation confidence. For example,

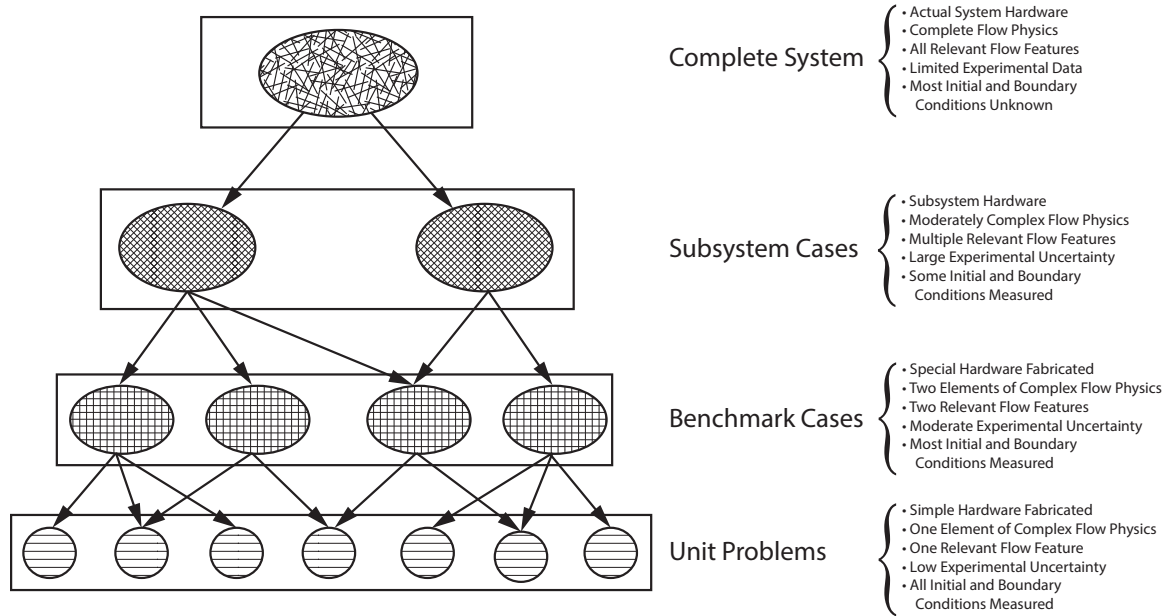


Fig. 3.1: The Validation Hierarchy, after [6]

integral quantities, such as fluid mass flow rate, generally have low experimental noise and random errors. Derivative quantities like fluid shear are more sensitive to non-ideal conditions. If a model and data are in good agreement at a high level, then it is likely that good agreement will be observed in lower levels. But, agreement at lower levels does not imply agreement at higher levels [3].

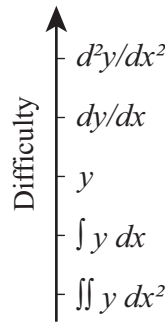


Fig. 3.2: System Response Quantity Difficulty Spectrum, after [3]. The variables y and x are arbitrary.

3.1.2 Transient Flows

Some studies of non-periodic transient flow have been performed, but as He & Jackson note, only

recently has technology allowed for comprehensive measurements of ensemble averaged transient experiments [7]. This review covers adiabatic and convective ramp-type flow transients. Most of the first experiments measured either temperature of tube walls or velocity, but not both. A common observation was that accelerating flow suppresses turbulence while decelerating flow augments it.

The first known work by Koshkin *et al.* was published in 1970 for turbulent air flow. This study reported measurements during a change in electrical power and different flow transients, measuring and reporting temperature [8]. Two similar studies were published in the 1970s and used electrochemical techniques with probes to measure velocity profiles inside a tube from a step change in flow rate [9, 10].

Rouai [11] performed heat transfer experiments on ramp-up and ramp-down transients as well as periodic pulsating flow with a non-zero time mean. Water was heated by passing an alternating electrical current through a stainless steel tube. Temperature measurements were made by 24 thermocouples (TCs) welded to this tube. Flow transients were prescribed by using a constant head tank and varying the flow through the test section by a valve. Wall heat flux remained constant and changes in wall temperature were measured. The observed Nusselt number departed more from the psuedo-steady values for faster transients and for decelerating flows, likely from the augmentation of turbulence.

Jackson *et al.* performed a study on non-periodic ramping transients in a water tube [12]. It was similar to that by Rouai but measured local fluid temperature with a TC probe and improved computer control and data logging for greater repeatability and ensemble averaging. The TC probe was small enough to capture turbulent fluctuations. They also found a suppression of turbulence and consequently wall heat transfer for accelerating ramps and augmentation during decelerating ramps. They also observed a peak in temperature fluctuations soon after the start of the ramps.

He & Jackson performed experiments in water using two-component LDA measurements in a clear, unheated tube. This non-intrusive velocity measurement was one of the first known to the authors for non-periodic flows. Ensemble averaged results were used for mean and turbulent quantities. The turbulent results were shown to deviate from psuedo-steady results for short transients. Several nondimensional parameters were recommended for ramp-type transients [7].

Barker and Williams [13] reported high speed measurements of an unsteady flow with heat transfer in air. They used a hot wire anemometer, a cold wire temperature probe, and a surface heat flux sensor to measure heat transfer coefficients for fully-developed turbulent pipe flow. Most results were for periodic flows, but some were presented for ramp-type transients with negligible buoyancy effects. The measurements were basic and provided data for conceptual model development.

In the previous studies, little coupling of velocity and thermal measurements was found for flow transients and buoyancy effects were negligible. Also, as these were discovery experiments, boundary conditions were not measured and provided as tabulated data, making the results of limited use for validation. The facility description is very basic and flow geometries simplified. The current study contributes high fidelity measurements of a ramp-down transient suitable for validation studies with simultaneous, non-intrusive velocity and thermal measurements to provide validation data on simplified geometry for three-dimensional simulations.

3.1.3 Mixed Convection

The physics in this study include a flow transient with buoyancy effects, phenomena that have not been studied together in the known literature. Convective flows with notable buoyancy effects are considered mixed or combined convection [14]. The Richardson number Ri is a measure of the relative magnitudes of buoyant and inertial forces and is defined by

$$Ri_x = Gr_x / Re_x^2 \quad (3.3)$$

where

$$Gr_x = g\beta(T_s - T_\infty)x^3/\nu^2 \quad (3.4)$$

and

$$Re_x = \bar{u}_{bulk}x/\nu. \quad (3.5)$$

In these, g is acceleration due to gravity, β is fluid thermal coefficient of expansion, $T_s = 130^\circ$ and $T_\infty = 20$ are surface and fluid temperatures, respectively, x is local streamwise location, ν is fluid kinematic viscosity, and \bar{u}_{bulk} is bulk mean velocity. Mixed convection is observed for buoyancy-aided flow when $0.3 < Ri_x < 16$ and for $0.3 < Ri_x$ for opposed flow [14].

Table 3.2 shows the streamwise locations x where data were acquired at the spanwise center with the associated Gr_x , as well as Re_x and Ri_x at the initial condition. External coordinates were used as the boundary layers generally do not meet as in fully-developed pipe flow. Fluid properties were evaluated at the film temperature. Initially buoyancy effects were small but became dominant at later phases of the transient.

3.2 Experimental Facility

All experiments were performed in the Rotatable Buoyancy Tunnel (RoBuT), which will be described

Table 3.2: Gr_x as well as Re_x and Ri_x at the initial condition at the three locations in x at the spanwise center where data were acquired

	x [m]	Gr_x	$Re_x (t=0)$	$Ri_x (t=0)$
x_1	0.16	3.13×10^7	34,200	0.027
x_2	0.78	3.48×10^9	164,000	0.129
x_3	1.39	2.00×10^{10}	294,000	0.231

in detail. Benchmark-level validation data were acquired with simple geometry and some multi-physics interaction. The square test section allowed easy characterization using optical velocity measurements. The simple geometry is easy to represent numerically and helps isolate model errors.

3.2.1 Rotatable Buoyancy Tunnel

The RoBuT was an open-circuit air tunnel with a large 4.81-m diameter ‘Ferris wheel’ design that allowed rotation, thus changing the relative direction of forced flow and buoyant forces without changing the facility. Many important tunnel components are shown in Fig. 3.3, which is in the buoyancy-opposed orientation. Note the coordinate system with the origin on the heated wall at the inlet and the spanwise center. The streamwise distance is x , wall-normal distance is y , and spanwise distance is z with zero along the centerline. The laser and cameras were part of a Particle Image Velocimetry (PIV) system that will be described in Sec. 3.3.2.

The test section had a 0.305×0.305 m square cross section and was 2 m long. It had three clear walls for optical access and a heated wall for a thermal BC. More details of the test section are provided in Sec. 3.2.2. The contraction and outlet were made of fiberglass-reinforced plastic with a glass-smooth, black gel-coat.

The contraction had an area ratio of 6.25:1 and was 0.914 m long. The contraction bell at the leading edge had a 102 mm radius. Between the contraction and bell were four modular sections that contained—in order of flow direction—a single row, aluminum fin/copper tube, chilled water heat exchanger (Super Radiator Coils Model 30x30-01R-0.625/048); a settling length section; a precision aluminum honeycomb flow straightener; and two high porosity screens. Square turbulence trips 3.175 mm wide were installed along all four walls and located about 0.12 m upstream of the test section inlet.

The outlet expanded the flow downstream of the test section, had a total included angle of 8.2° , and was 0.686 m long. The blower drew air through the test section and rejected it into the room. It included an inline centrifugal fan assembly, TCF/Aerovent model 14-CBD-3767-5. It was belt driven by a 5 HP, TEFC, 230-460 VAC induction motor, Toshiba model B0052FLF2AMH03. The motor was powered by a Toshiba

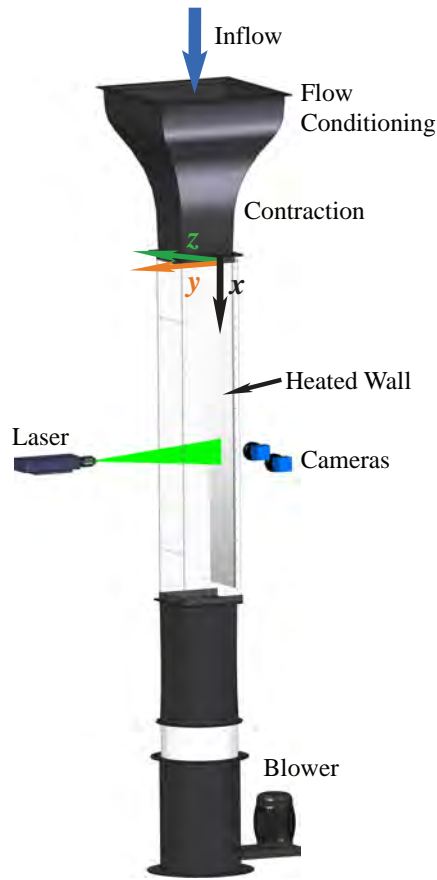


Fig. 3.3: RoBuT flow components as configured for transient data acquisition

variable frequency drive, model VFS11-2037PM-WN.

Two Laskin Nozzles [15] were used to atomize olive oil tracer particles. These were measured to have a mean diameter of about $1\mu\text{m}$ with a TSI Aerodynamic Particle Size Spectrometer at the outlet. These particles were mixed with air and injected into a PVC pipe distribution system upstream of the contraction assembly. A peg board was placed between this system and the beginning of the contraction to help mix particles throughout the flow. It had holes 6.35 mm in diameter and were spaced 25.4 mm apart in a square pattern.

3.2.2 Test Section

The test section had four walls, an inlet, and an outlet that will be described in detail. The heated wall was custom designed with many layers to provide a heated surface for convection and featured embedded instrumentation. Its cross section is shown in Fig. 3.4. This wall was heated to approximately 130°C for this

study. It was made of several layers of aluminum, had six silicon rubber heaters arranged in the streamwise direction, and contained thermal insulation to drive most of the heat inward. A list of materials and thicknesses is available in Table 3.3. The surface was nickel plated to reduce thermal radiation which resulted in a predicted and measured emissivity around 0.03 [2]. Aluminum 2024, though more expensive than the common alloy 6061, was used because its thermal conductivity is well known [16]. The heated portion was 279 mm wide and 1.89 m long. The left and right sides were thermally insulated by 17.5-mm thick Teflon[®] that extended into grooves in the side walls. Two additional 12.7-mm thick Teflon[®] insulators were placed upstream and downstream of the heated wall. There were six heaters, each spanning the width of the heated wall and one sixth of the length. Three HP 6439B power supplies were connected to two heaters each and were used to control the temperature of the wall via a closed-loop PI controller. Three controllers, one for each power supply, allowed the heated wall to be heated in independent sections in the streamwise direction to increase temperature uniformity.

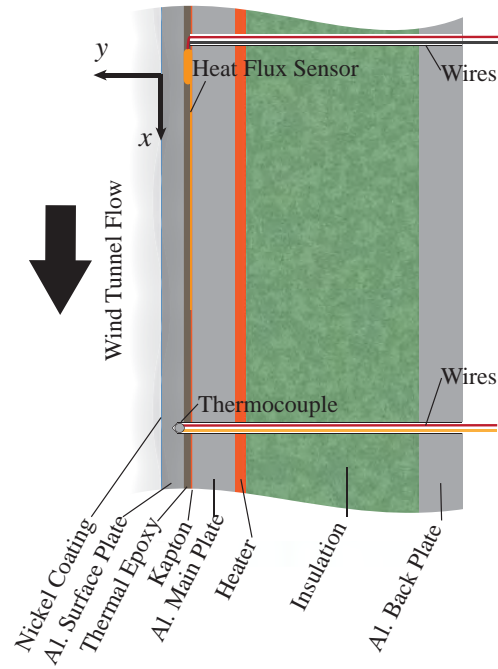


Fig. 3.4: Heated wall cross section with component names as in Table 3.3. The relative thicknesses are to scale.

The other three walls were clear Lexan[®] polycarbonate for optical access and were 12.7 mm thick. From the perspective of standing on the heated wall at the inlet, they are termed left ($z=-152$ mm), top ($y=305$ mm),

Table 3.3: Heated wall components and thicknesses with names from Fig. 3.4

Name	Material	t [mm]
Nickel Coating	Bright Nickel	~0.05
Al. Surface Plate	Al. 2024-T3	3.18
Thermal Epoxy	Dow Corning 3-6751	1.02
Kapton [®]	Kapton [®] HN	0.254
Al. Main Plate	Al. 6061-T651	6.35
Heater	Tempco Silicone Rubber	1.59
Insulation	Mineral Wool	25.4
Al. Back Plate	Al. 6061-T651	6.35

and right ($z=152$ mm) walls. The top wall had a removable center portion for cleaning and maintenance. This wall also had three 25.4-mm ports for probe insertion.

The as-built geometry was measured to compensate for differences between the as-designed and as-built test section geometry. The differences were small, but the measurements are presented for completeness. An internal micrometer was used to measure the internal dimensions of the fully assembled test section. Height measurements were performed at the left, center, and right as well as width measurements at the top, middle, and bottom. This was done at seven locations in x and performed three times for a measure of random uncertainty. Modelers may use these dimensions when constructing the simulation domain to ensure greater similarity. A sketch of the measurement locations may be accessed from the online database by the link [All-BC-AsBuiltSketch](#) in the digital version of this work. The nominal values are in [All-BC-AsBuiltMeasurements](#) and uncertainties in [All-BC-AsBuiltMeasurementUncertainties](#). A Parasolid model created from the as-built measurements is available in [All-BC-AsBuiltGeometry](#).

A warm-up procedure was followed each time the RoBuT was used for experiments. Ideally, the HVAC system would be kept active at all times for stable room conditions. The heated wall was first heated to the setpoint temperature. Once this was reached, the blower was set to the desired speed for the experiment and the heater controllers would accordingly increase power. Once the temperature was again stable for at least five minutes, the facility was ready for data acquisition. If the blower setpoint speed was changed, the controller would stabilize temperature and a waiting period was repeated for at least five minutes.

Between acquiring different series of data, the entire test section was cleaned with Ethyl Alcohol and delicate task wipes to ensure optical quality. The cover on the top wall was removed for inside cleaning. High-vacuum grease was used on test section joints to eliminate air leakage and was removed and reapplied each time a panel of the test section was adjusted.

3.3 Analog Instrumentation and Signal Processing

Validation experiments require high fidelity instrumentation. Thermocouples were used to measure boundary temperatures, heat flux sensors (HFSs) for heat flux through the heated wall, and PIV for inflow and boundary layer air velocity. Other sensors measured room air conditions. These systems will now be described in detail.

3.3.1 Thermal Instrumentation

A total of 307 TCs were used to measure boundary temperatures. All test section TCs were 30 gauge Type K from Omega Engineering with Special Limits of Error. They were each welded to length with an Argon-shielded welder. Each TC was calibrated with an Isotherm FASTCAL-M with an accuracy of 0.3°C over a range of $25\text{--}190^{\circ}\text{C}$ with data at every 5°C . Because every TC calibration was very similar and made from the same spool, an average calibration curve was applied. An array of 3×5 TCs, three in y and five in z , was suspended on the downstream side of the honeycomb for inlet air temperature measurements. Each of the three clear walls had 21 TCs with seven rows spaced in x and three across in y for the left and right walls or in z for the top wall. The bulk of the heated wall had 5×32 TCs with five in z and 32 in x . The Teflon[®] edges each had embedded TCs with five across the leading edge in z and 32 along the sides in x . All TCs were embedded to within 3.18 mm of the inside surface using thermal epoxy with enhanced thermal conductivity.

Three HFSs were embedded into the heated wall along the spanwise center at the x -locations found in Table 3.2. They were model 20457-3 from RdF Corporation and were a thin-film type with a thermopile around a Kapton[®] substrate. The manufacturer supplied unique calibration coefficients for each sensor. The manufacturer-specified uncertainty was 5% of reading. An embedded Type T TC was used to measure sensor temperature and correct readings with the supplied multiplication factor curve to compensate for changes in thermal conductivity of the substrate. The HFSs were placed adjacent to the Kapton[®] layer of similar thermal resistance to reduce measurement errors. A thermal resistance network analysis showed only a 2.4% difference in heat flux between HFS and non-HFS conduction paths.

The TC and HFS output voltages were small, so special data acquisition (DAQ) devices were selected. National Instruments (NI) products were used as they interfaced well with the LabVIEW software that was used for system control and thermal data recording. Twenty one NI-9213 TC modules were housed in five NI-cDAQ-9188 chassis. The narrow voltage range of ± 78 mV, 24-bit ADC, and open channel detection made them well suited for these measurements. The built-in CJC was used for TCs. The total uncertainty of the calibrated TCs with these DAQs was 1°C , largely attributable to the CJC uncertainty of 0.8°C . Data from

thermal instrumentation were recorded throughout each transient run.

Data from thermal instrumentation was recorded through 2400 runs of the transient. These data were ensemble-averaged and the bias, random, and total uncertainty were quantified.

3.3.2 Particle Image Velocimetry

The PIV system allowed for non-intrusive, full-field velocity measurements at several locations. The system consisted of a laser, camera, and timing unit. The laser was a New Wave Research Solo PIV III. It was a dual cavity, frequency-doubled Nd:Yag model with about 22 mJ/pulse and a wavelength of 532 nm. The cameras were model Imager sCMOS that featured a 16-bit sCMOS sensor with 2560×2160 pixels with a pixel size of 6.5 μm . An internal, standard version timing unit was used for the stringent timing requirements of PIV and had a resolution of 10 ns and jitter of <1 ns. Two Nikon lenses were used. The first was an AF Nikkor 28 mm f/2.8 D used for the large field of view (FOV) inflow and the large FOV SRQ data that spanned the 0.305-m test section. The second was an AF Micro-Nikkor 105 mm f/2.8 D for high resolution (small FOV) SRQ data near the heated wall.

DaVis 8.2 software was used to acquire and process images. The optical configuration of Fig. 3.3 was used with the laser sheet normal to the heated wall and cameras viewing angles nearly parallel with it. The equipment was moved manually in the x direction. The inflow was measured in the same orientation but Velmex BiSlide[®] traverses were used to move the laser and camera consistently in the z direction. In this way five planes were measured to map the inflow.

PIV calibration was performed in two ways. The inflow used a conventional two-component ‘ruler’ calibration over a span of about 280 mm since the laser sheet and camera were normal to each other. The SRQ data were acquired with two independent two-component cameras, one that spans the entire test section and one that provides high resolution data near the heated wall. The SRQ data that spanned the test section used a custom two-plane calibration target that filled the image. The SRQ data near the heated wall was calibrated with a single-plane calibration target. Both SRQ sets used the pinhole model as the cameras were angled generally less than 5° . The pinhole model was applicable as refraction between the Lexan[®] and air was small. The near-wall SRQ camera angle was required to avoid image diffraction by the large temperature gradient very near the wall. Because this flow had very little through-plane motion, errors in v velocity from through-plane motion appearing as in-plane motion are expected to be small (they are a function of the sine of the angle).

Prior to acquisition, the quality of the particle images was checked to ensure proper particle density,

diameter, and displacement as well as laser beam overlap and image focus quality. Many of these data parameters and others from the acquired images are found in Table 3.4. The diameter, density, and displacement are spatial averages over the entire image. The maximum displacement was set between 8–32 pixels for all phases of the transient. To optimize dynamic range, two values of dt were used for each PIV data set. These are represented with a i/j in the table with the former being used for early phases and the latter for later phases. Since the reported values are spatially averaged, some may appear different from ideal simply due to their non-uniformity in space and in time. These data were taken from a phase near the middle of the transient. Both particle diameter and density were determined by methods found in [17] with the local maximum method for density estimation.

Table 3.4: PIV data parameters

Parameter	Inlet	SRQ-Large FOV	SRQ-Small FOV
N image pairs	100/200	100	100
Sample frequency [Hz]	5	5	5
dt [μ s]	860/3150	385/1541	96/385
lens	28 mm	28 mm	105 mm
extension [mm]	–	–	39.5
Calibration [mm/pixel]	0.123	0.121	0.0137
$f\#$	4	4	8
diameter [pixels]	1.98	1.98–2.55	2.68–3.00
density [$\#$ /32 \times 32]	86.7	57.3–88.1	8.04–11.8
displacement [pixels]	5.35–31.9	1.34–30.3	2.71–29.8

A MATLAB code was written to reorganize images. During acquisition, a set was recorded over all phases of the transient. The code would copy images from all runs for a given phase and create a new set. This process was repeated for all runs so data within each phase could be ensemble-averaged and fluctuations quantified.

The processing of particle images was performed using the window deformation method in DaVis. A mask was carefully defined to remove the influence of walls on the correlation. Round interrogation windows were used for reduced noise. The first two passes were at 128 \times 128 pixels, the next two at 64 \times 64 pixels, and the final four passes were at 32 \times 32 pixels. The overlap on every pass was 75%. Vector post-processing was performed where vectors were removed if the peak ratio was less than two. Then a two-pass median filter of ‘strongly remove & iteratively replace’ corrected spurious vectors. Vectors were removed if their difference

from average was more than one standard deviation of neighbors and subsequently replaced if the difference from average was less than two standard deviations of neighbors.

Particle images have a sliding background removed where the background is the average of the set. The pixel range was narrowed in the flow direction to reduce disk space and processing time and was 340 pixels for the inflow images and 512 pixels for the SRQ images. Examples of dewarped particle images with background subtracted are shown in Fig. 3.5. The heated wall is on right of both images.

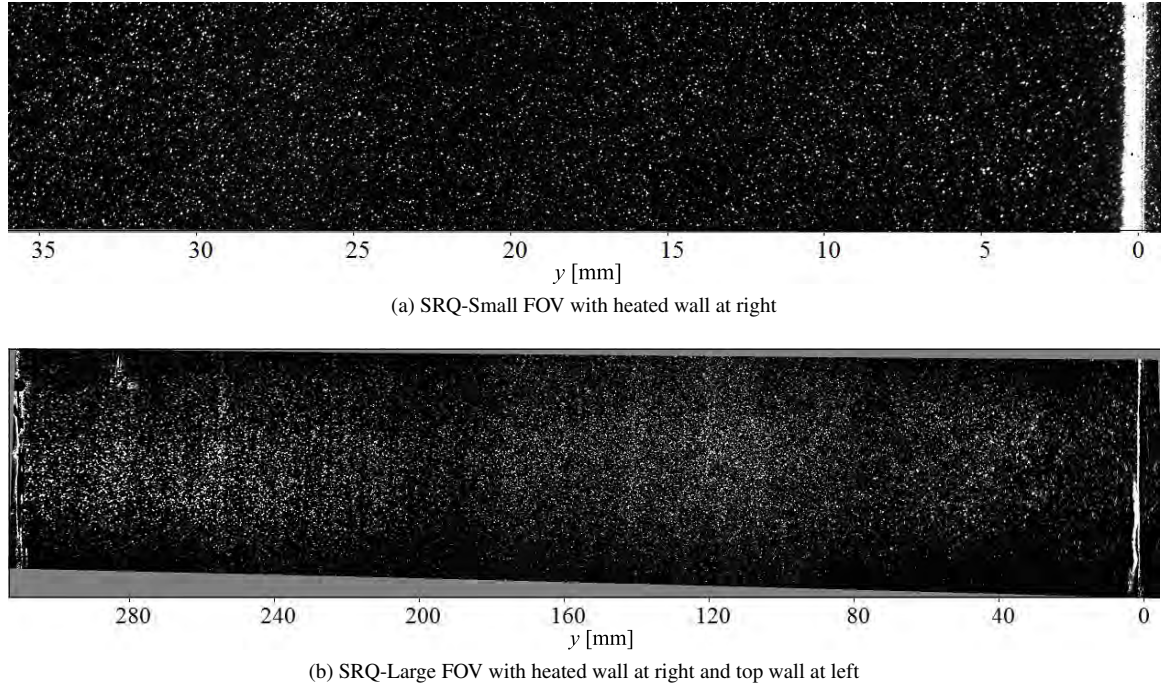


Fig. 3.5: Dewarped SRQ particle image at x_2 with mean background removed. Note the image scales are about a factor of nine different.

3.3.3 Atmospheric Instrumentation

Air temperature, relative humidity, and atmospheric pressure in the RoBuT room were measured to determine air properties. Both temperature and humidity were measured with an Omega HX93A probe. Pressure was measured with an Apogee Instruments BPS 1006 sensor. The output voltage of these sensors was measured by a NI USB-9215A 4-channel ± 10 V analog input DAQ. The uncertainty of temperature was 0.6°C , humidity was 2.5% for readings 20-80% and 3.1% otherwise, and pressure was 3% of reading. These data were sampled at 1 Hz, then averaged and recorded once per minute.

3.3.4 Uncertainty Quantification

Thermal and atmospheric data uncertainty quantification (UQ) is described here following methods of Coleman and Steele [18]. UQ for PIV was considered by other methods and is described later. Bias uncertainty parameters were obtained from sensor documentation at the 95% confidence level. The random uncertainty of a general mean quantity \bar{x} was calculated by

$$S_{\bar{x}} = t_{95} \frac{S_x}{\sqrt{N}} \quad (3.6)$$

where t_{95} is the confidence level coefficient (taken as 1.96 for 95% confidence and number of samples $N > 30$) and S_x is the sample standard deviation. Bias and random sources are combined as

$$U_{\bar{x}} = \sqrt{B_{\bar{x}}^2 + S_{\bar{x}}^2} \quad (3.7)$$

where $B_{\bar{x}}$ is the expanded bias uncertainty. The data provided with this paper generally specifies the unique bias, random, and total uncertainty numbers with the mean results.

Uncertainty of the PIV results was calculated from the Uncertainty Surface Method that estimates instantaneous bias and random uncertainties due to the effects of particle displacement, particle image density, particle image size, and shear. This method was originally described in [19] and improved on with methods from [17]. The uncertainties of the velocity statistics propagated from the instantaneous uncertainties were calculated by methods of Wilson & Smith [20]. Total uncertainty was calculated as in Eqn. 3.7. The confidence level on all UQ results in this work is 95%.

3.4 Boundary Conditions

This section contains a description of all expected requisite BCs for CFD model inputs. The types of BCs are shown in Table 3.1. The as-built geometry is a BC, but was discussed previously in Sec. 3.2.2.

3.4.1 BC Description

The measured BC temperatures are mapped onto the test section geometry in Fig. 3.6. Note the high measurement resolution on the heated wall and the development of the thermal boundary layer on the right wall as air travels from the inlet to the right of the figure.

As mentioned previously, the inflow was measured in five planes spaced in z with locations concentrated near the side walls. The time mean streamwise velocity \bar{u} at the inlet is shown in Fig. 3.7 at the initial

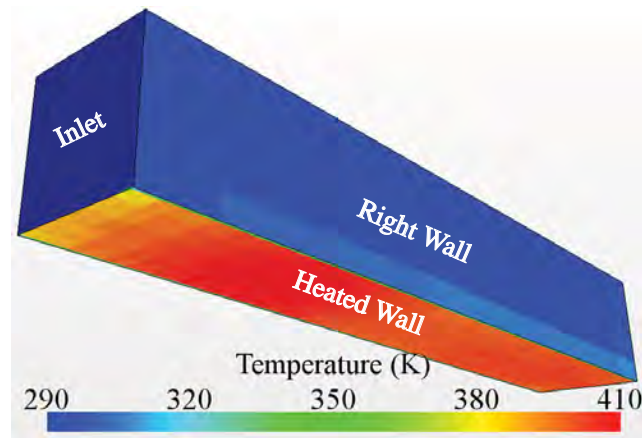


Fig. 3.6: Measured temperatures on the test section boundaries

condition. Gray lines indicate PIV measurement locations that span across y (two are at the left and right edges). Data are highly-resolved in y but not in z . Data may be interpolated from the information given. Another approach is to use the high-resolution data near the unheated top wall ($y=305$ mm) boundary layer to the left and right walls which are also unheated.

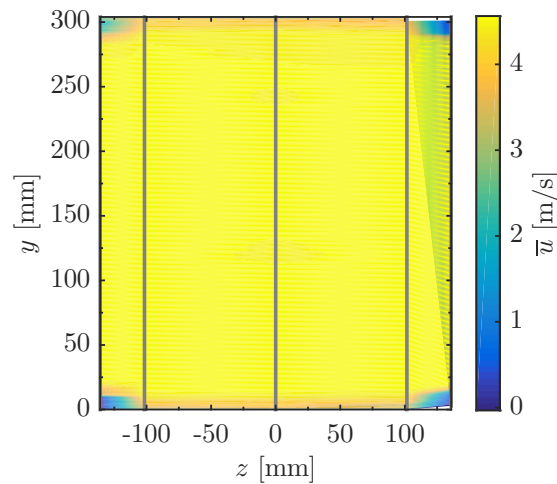


Fig. 3.7: Measured streamwise velocity \bar{u} at the inlet and the initial condition

The atmospheric conditions include atmospheric pressure, relative humidity, and room temperature and were recorded at the time of data acquisition.

Data acquisition procedures were followed to control test conditions. The following list describes the steps followed for acquisition of both BC and SRQ data:

1. Begin heating of the heated wall
2. Upon reaching setpoint temperature, start blower
3. Align traverses, laser, and camera with test section at measurement location
4. Align laser sheets
5. Focus camera on particle images
6. Align calibration plane with laser sheet and calibrate camera(s)
7. Determine optimal dt for particle displacement, proper seeding density, and proper laser intensity
8. Record measurement location and other PIV parameters
9. Confirm stability of wall temperature and room conditions
10. Record PIV data, atmospheric and thermal conditions

This process was repeated for PIV measurement locations for the five inflow and the three SRQ data sets. The acquisitions were automated by a LabVIEW program which controlled the conditions, determined when they were stable, initiated the transient and data acquisition (both thermal and PIV), and repeated.

3.4.2 BC Data

These data are available for all phases of the transient on the inflow and all four walls of the test section. There is one file for each surface that can be found through the following links: [Trans-BC-InletTemp](#), [Trans-BC-HeatedWallTemp](#), [Trans-BC-LeftWallTemp](#), [Trans-BC-RightWallTemp](#), and [Trans-BC-TopWallTemp](#). The format for all BC files works directly with Star-CCM+ and is easily adaptable to other CFD codes. The columns X, Y, and Z are used throughout this work; adhere to the global coordinates; and are presented in meters. The column 'T(K)' is the mean temperature in Kelvin, 'B_T(K)' is the bias uncertainty, 'S_T(K)' is the random uncertainty, and 'U_T(K)' is the total uncertainty. Additionally the time stamps are included for each column header as in 'T(K)[t=0s]', 'T(K)[t=0.2s]' and so forth.

The data file for the inflow mean and fluctuating velocities is found in [Trans-BC-Inlet-Vel](#). Here X, Y, and Z are again used as before and are presented in meters. The columns 'u', 'v', and 'w' are mean velocities in the x, y, and z directions, respectively. The columns 'u'u'', 'v'v'', 'w'w'', and 'u'v'' are specific Reynolds stresses. Uncertainties compose the remaining columns with the uncertainty of \bar{u} , \bar{v} , and \bar{w} . Reynolds stresses have unique plus and minus uncertainties with 'Uuup' being the plus uncertainty of $\overline{u'u'}$ and so on. The

units of velocity and velocity uncertainty are [m/s] while those of Reynolds stresses and their uncertainty are [m²/s²]. Again, time stamps are included in column headers.

Note that inflow out-of-plane velocities \bar{w} and $\overline{w'w'}$ were assumed to be the same as \bar{v} and $\overline{v'v'}$ respectively. This assumption was proved valid in previous work in this facility by measuring the inflow in both directions with two-component PIV and comparing data where measurement planes intersect [2]. The atmospheric measurements, together with their uncertainties, are found in the file [Trans-BC-AtmCond](#).

3.5 Fluid and Material Properties

As air is the working fluid, measurements of temperature, pressure, and relative humidity discussed in Sec. 3.4.2 are satisfactory to define all fluid properties. It is important to note that the working pressure is different from that at sea level as the experiment was conducted in Logan, Utah, which is 1460 meters above sea level.

Material properties of the test section can easily be obtained from the information provided in Sec. 3.2.2 about the construction of the test section. It is not necessary to model the heated wall since temperature measurements were made very near the surface, but the information is provided for completeness.

3.6 Test Conditions

For improved statistics, the data were ensemble-averaged over repeated runs. A total of 2400 runs were used, with 100-200 for each PIV acquisition location and dt . Steady thermal conditions triggered data acquisitions and simultaneously cut power to the blower, initiating transient conditions. Heater power was fixed through each run.

LabView was used to control the conditions and to acquire thermal data via a National Instruments data acquisition system. This system created the master TTL clock and also triggered the PIV system for synchronized thermal and velocity data acquisition. Data were acquired at 5 Hz for a period of 20.2 s. The initial condition was forced convection downward with the heated wall at 130°C. Blower power was removed and the drum-type blower was allowed to coast to a stop, which took about 10 s. This resulted in ramp-down bulk velocity and subsequent flow reversal by natural convection. The bulk velocity at the test section inlet at the centerline plane is shown in Fig. 3.8. The bulk velocity approaches zero at the end since there is both natural convection upward near the heated wall and recirculating flow downward far from the wall. There was measurable delay in the blower drive system, so $t = 0$ was prescribed as the last phase where the bulk velocity matched the initial condition. Thus, the useful transient time spans $0 \leq t \leq 18.2$ s and data are presented in this range.

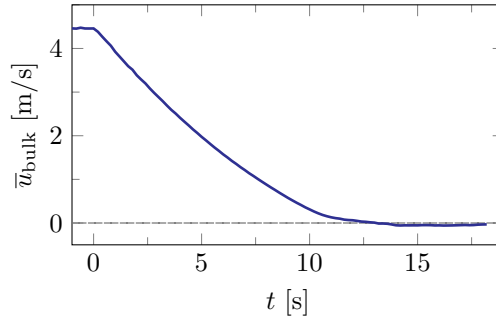


Fig. 3.8: Bulk velocity across the inlet at the spanwise center ($z = 0$) through time

The RoBuT room was configured with modern HVAC systems and thermal insulation for stable conditions. Controls were independent of other systems in the building. The refrigerated air conditioning had a $\sim 0.56^\circ\text{C}$ (1°F) deadband. The maximum measured temperature spread during data acquisition was 0.9°C ($\sim 1.6^\circ\text{F}$). To reduce the rate of temperature change from the on/off behavior of this system, outside air was mixed with refrigerated air before being injected into the room. Heating was performed with a steam heat exchanger with attached fan. The original fan and control system were replaced with a variable speed, tuned, PI-controlled system implemented with the main LabVIEW program, giving the heating system tight control of the room temperature.

3.7 System Response Quantities

The SRQs are the experimental results used to compare with simulation outputs and were listed in Table 3.1. They are included for all phases of the transient and include uncertainty on all results. Since they are similar, the ensemble-average and fluctuating velocity profiles in the form of Reynolds stresses are presented together. Additionally scalars of wall heat flux and wall shear stress are also included.

3.7.1 SRQ Description

Profiles of streamwise velocity \bar{u} and Reynolds normal stress $\overline{u'u'}$ are shown in Fig. 3.9 at three locations in x for the top (x_1), middle (x_2), and bottom (x_3). The boundary layer thickness increases in the streamwise direction x as evidenced in both the \bar{u} and $\overline{u'u'}$ profiles at the initial condition as expected. The velocity profile shape generally remains similar but is reduced in magnitude during the first four seconds. At $t = 8$ s, the contribution from natural convection begins affecting the profiles near the heated wall ($y = 0$). At $t = 12$ s the profiles show a strong influence from natural convection. The changes from $t = 12 - 16$ s are subtle as

steady natural convection is asymptotically reached. The results for Reynolds normal stress $\overline{u'u'}$ show larger uncertainty, but this is expected as fluctuations are more challenging to quantify than averages. Initially $\overline{u'u'}$ is elevated near both walls as expected. The influence of natural convection increases $\overline{u'u'}$ near the heated wall initially. The area of elevated $\overline{u'u'}$ moves away from the wall over time. The phase of $t = 12$ s has the highest levels, likely from a chaotic flow reversal. The final measured state has reduced stresses and may still be decreasing.

Uncertainty of the PIV results was calculated from the Uncertainty Surface Method which estimates instantaneous bias and random uncertainties due to the effects of particle displacement, particle image density, particle image size, and shear originally described in [19] and improved upon with methods from [17]. The uncertainties of the velocity statistics propagated from the instantaneous uncertainties were calculated by methods of Wilson & Smith [20]. Total uncertainty was calculated as in Eqn. 3.7. The confidence level on all UQ results in this work is 95%.

Previous methods to quantify wall shear have fit experimental velocity data with empirical correlations such as Spalding or Musker profiles with high accuracy [21]. This method works well for steady boundary layer data where the profiles are an accurate representation of velocity, but not for the transient conditions in the current study. Therefore wall shear stress was estimated directly from PIV data as $\tau_s = \mu \frac{\partial \bar{u}}{\partial y} \big|_{y=0}$ where τ_s is wall shear stress and μ is dynamic viscosity. High-resolution PIV data were used to fit a line to velocity data where $y^+ = y u_\tau / \nu \leq 5$ for $\frac{\partial \bar{u}}{\partial y} \big|_{y=0}$, where $u_\tau = \sqrt{\tau_s / \rho}$ and ρ is the fluid density [14]. Initially 10 points were included in the fit and a stable iterative method was used to calculate τ_s and the number of data points to fit within $y^+ \leq 5$. The wall was located by the particle images with a mask carefully defined. The linear fit was performed using linear regression with more weight given to velocity data with lower uncertainty [22]. The high-resolution PIV data at x_2 and associated linear fit are shown in Fig. 3.10 for five phases of the transient. The fit was not forced to the wall as wall location errors would be compounded and not easily quantifiable in the uncertainty estimation. The dynamic viscosity was evaluated using Sutherland's Law at the wall temperature. The fit uncertainty was combined with the viscosity uncertainty using the Taylor Series Method [18].

Results for the scalars of wall heat flux and wall shear stress are shown in Fig. 3.11 at the same three x locations through time with their associated uncertainty bands. The experimental heat flux came from the Heat Flux Sensors (HFSs) using the manufacturer-calibrated sensitivity. The uncertainty included 5% bias while the random values were measured. The experimental results from the HFSs show a low sensitivity to convection due to the thermal capacitance of the heated wall in which they were embedded. The wall shear

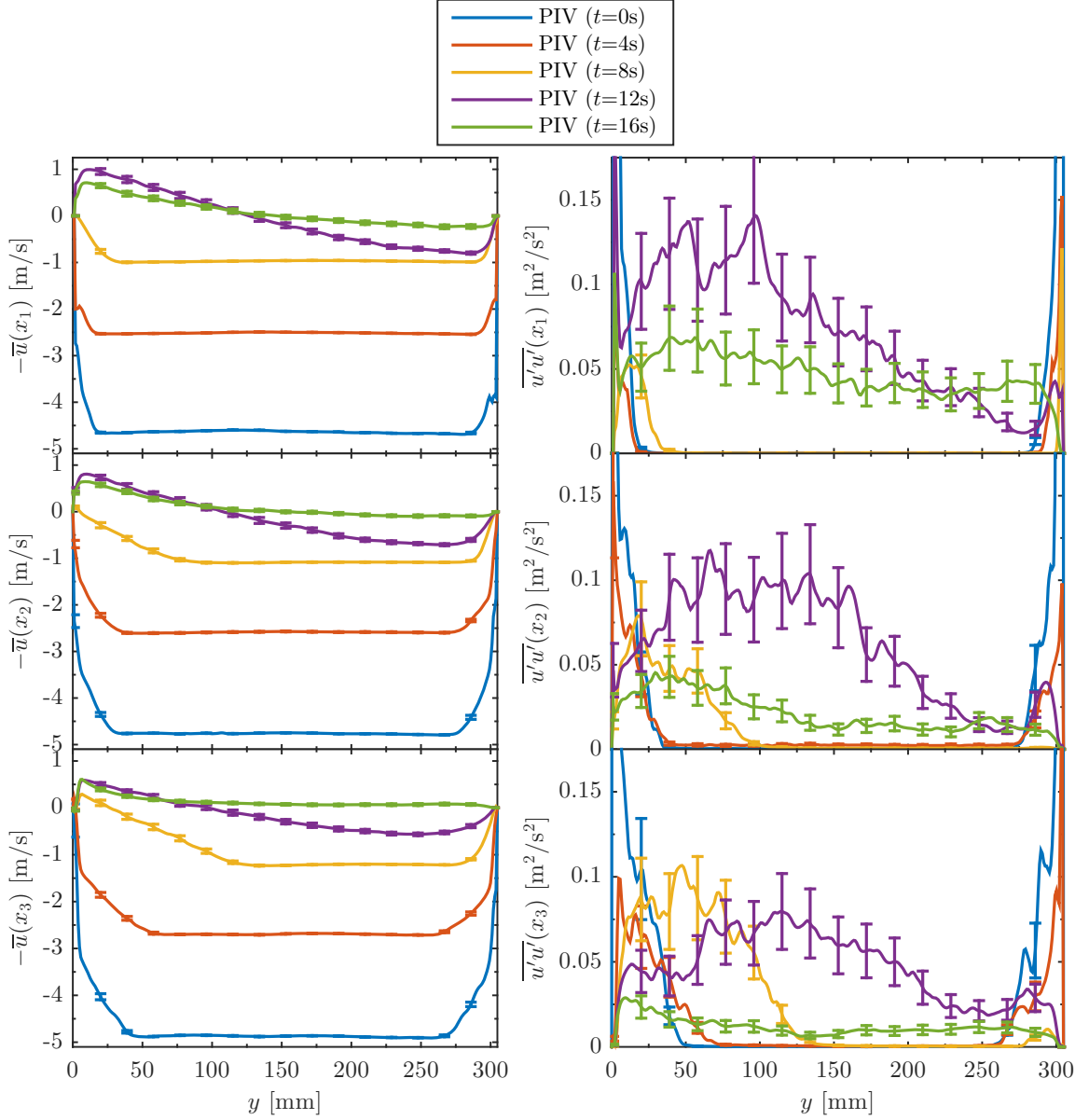


Fig. 3.9: The streamwise velocity \bar{u} and Reynolds normal stress $\overline{u'u'}$ at three locations in x and five phases of the transient

results are somewhat noisy at high levels of shear, likely from the decreased accuracy of PIV data near walls with large velocity gradients and the relatively lower number of points in the fit. When the shear decreases, more points can be used in the fit for smoother results with decreased uncertainty. The shear smoothly changes sign as the near-wall flow reverses.

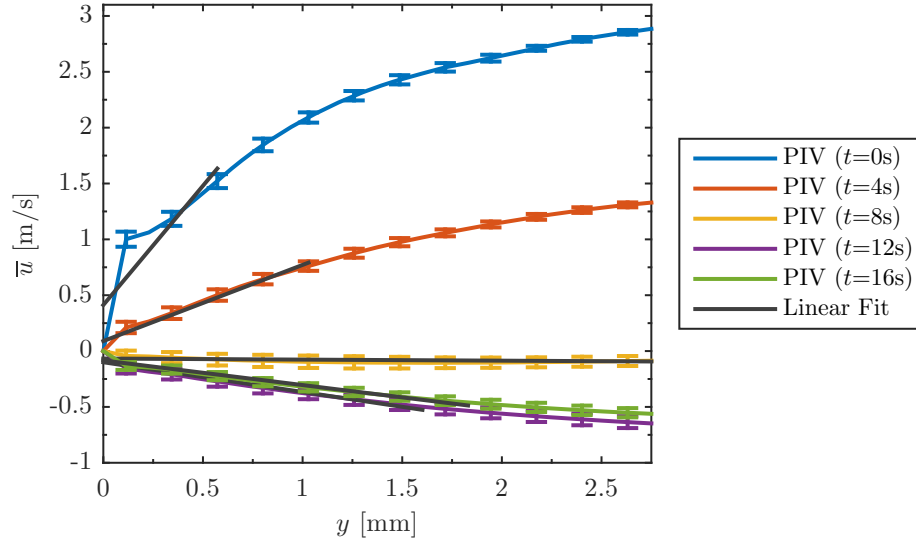


Fig. 3.10: High-resolution PIV data near the heated wall with linear fit

3.7.2 SRQ Data

Like the BC data, the SRQ data and their uncertainties are tabulated for use in validation studies. They are contained in comma separated files with the *.csv extension and can be opened in a spreadsheet program or a simple text editor. All resulting PIV data are made available from both cameras with headers similar to the BC PIV data presented earlier. They contain data at all three x locations as specified in the files. As with the BC data, the full uncertainties at 95% confidence are provided with unique positive and negative uncertainties for Reynolds stresses. The small FOV data are found in the file [Trans-SRQ-Vel-SmallFOV](#) and the large FOV in [Trans-SRQ-Vel-LargeFOV](#).

Wall heat flux results are given for all three sensors along x with specified bias, random, and total uncertainty and found in the file [Trans-SRQ-HeatFlux](#). Wall shear is similarly formatted, has the total uncertainty, and is found in the file [Trans-SRQ-Shear](#).

3.8 Conclusions

This paper presented the study of a ramp-down flow transient with heat transfer and buoyancy effects in simplified geometry to provide CFD validation data. Repeated runs provide high resolution data for ensemble-averaging and turbulent statistics of high resolution data. The provided BCs and SRQs, listed in Table 3.1 for the conditions in Table 3.2, are tabulated and available for download. Uncertainty is also included for all presented data. The data contain rich and comprehensive coverage of this flow. They enable

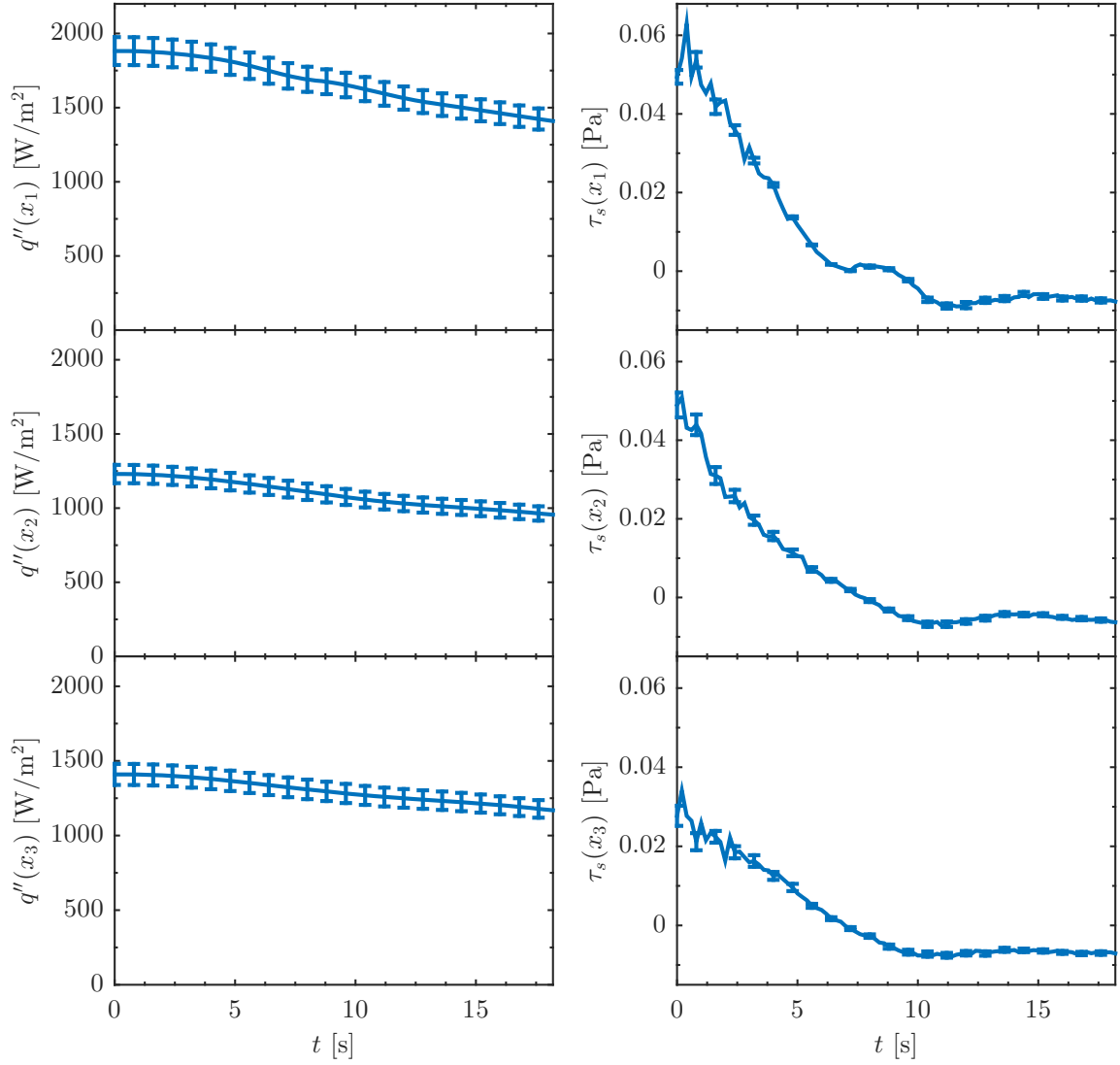


Fig. 3.11: The heated wall heat flux and wall shear stress plotted over time

validation studies to assess model accuracy and are necessary to calculate simulation uncertainty.

Acknowledgments

This research was performed using funding received from the DOE Office of Nuclear Energy's Nuclear Energy University Programs, and their support is gratefully acknowledged. Also, the authors appreciate Dr. Nam Dinh who originally suggested transient convection for CFD validation.

References

- [1] Oberkampf, W. L., and Smith, B. L., 2014, “Assessment Criteria for Computational Fluid Dynamics Validation Benchmark Experiments,” 52nd Aerospace Sciences Meeting of AIAA.
- [2] Harris, J. R., Lance, B. W., and Smith, B. L., 2015, “Experimental Validation Data for Computational Fluid Dynamics of Forced Convection on a Vertical Flat Plate,” *Journal of Fluids Engineering*, **138**(1), p. 011401, doi:[10.1115/1.4031007](https://doi.org/10.1115/1.4031007).
- [3] Oberkampf, W. L., and Roy, C. J., 2010, *Verification and Validation in Scientific Computing*, Cambridge University Press, doi:[10.1017/cbo9780511760396](https://doi.org/10.1017/cbo9780511760396).
- [4] ASME, 2009, “ASME V&V 20-2009: Standard for Verification and Validation in Computational Fluid Dynamics and Heat Transfer,” Standard, American Society of Mechanical Engineers.
- [5] Roache, P. J., 2009, *Fundamentals of Verification and Validation*, Hermosa Publ.
- [6] AIAA, 1998, “Guide for the Verification and Validation of Computational Fluid Dynamics Simulations,” Tech. Rep. AIAA G-077-1998, American Institute of Aeronautics and Astronautics, Reston, VA, doi:[10.2514/4.472855](https://doi.org/10.2514/4.472855).
- [7] He, S., and Jackson, J. D., 2000, “A Study of Turbulence Under Conditions of Transient Flow in a Pipe,” *Journal of Fluid Mechanics*, **408**, pp. 1–38, doi:[10.1017/s0022112099007016](https://doi.org/10.1017/s0022112099007016).
- [8] Koshkin, V., Kalinin, E., Dreitser, G., Galitseisky, B., and Izosimov, V., 1970, “Experimental Study of Nonsteady Convective Heat Transfer in Tubes,” *International Journal of Heat and Mass Transfer*, **13**(8), pp. 1271–1281, doi:[10.1016/0017-9310\(70\)90068-2](https://doi.org/10.1016/0017-9310(70)90068-2).
- [9] Kataoka, K., Kawabata, T., and Miki, K., 1975, “The Start-up Response of Pipe Flow to a Step Change in Flow Rate,” *Journal of Chemical Engineering of Japan*, **8**(4), pp. 266–271, doi:[10.1252/jcej.8.266](https://doi.org/10.1252/jcej.8.266).
- [10] Maruyama, T., Kuribayashi, T., and Mizushima, T., 1976, “The Structure of the Turbulence in Transient Pipe Flows,” *Journal of Chemical Engineering of Japan*, **9**(6), pp. 431–439, doi:[10.1252/jcej.9.431](https://doi.org/10.1252/jcej.9.431).
- [11] Rouai, N. M., 1987, “Influence of Buoyancy and Flow Transients on Turbulent Convective Heat Transfer in a Tube,” Ph.D. thesis, University of Manchester, UK.
- [12] Jackson, J. D., Büyükalaca, O., and He, S., 1999, “Heat Transfer in a Pipe Under Conditions of Transient Turbulent Flow,” *International Journal of Heat and Fluid Flow*, **20**(2), pp. 115–127, doi:[10.1016/s0142-727x\(98\)10056-5](https://doi.org/10.1016/s0142-727x(98)10056-5).
- [13] Barker, A. R., and Williams, J. E. F., 2000, “Transient Measurements of the Heat Transfer Coefficient in Unsteady, Turbulent Pipe Flow,” *International Journal of Heat and Mass Transfer*, **43**(17), pp. 3197–3207, doi:[10.1016/s0017-9310\(99\)00305-1](https://doi.org/10.1016/s0017-9310(99)00305-1).
- [14] Kays, W. M., Crawford, M. E., and Weigand, B., 2012, *Convective Heat and Mass Transfer*, 4th ed., McGraw-Hill.
- [15] Kähler, C. J., Sammler, B., and Kompenhans, J., 2002, “Generation and Control of Tracer Particles for Optical Flow Investigations in Air,” *Experiments in Fluids*, **33**, pp. 736–742, doi:[10.1007/s00348-002-0492-x](https://doi.org/10.1007/s00348-002-0492-x).
- [16] Touloukian, Y. S., and Ho, C. Y., 1977, *Thermophysical Properties of Selected Aerospace Materials Part II: Thermophysical Properties of Seven Materials*, Purdue University, West Lafayette.
- [17] Warner, S. O., and Smith, B. L., 2014, “Autocorrelation-based Estimate of Particle Image Density for Diffraction Limited Particle Images,” *Measurement Science and Technology*, **25**(6), p. 065201, doi:[10.1088/0957-0233/25/6/065201](https://doi.org/10.1088/0957-0233/25/6/065201).

- [18] Coleman, H. W., and Steele, W. G., 2009, *Experimentation, Validation, and Uncertainty Analysis for Engineers*, John Wiley & Sons, doi:[10.1002/9780470485682](https://doi.org/10.1002/9780470485682).
- [19] Timmins, B. H., Wilson, B. W., Smith, B. L., and Vlachos, P. P., 2012, “A Method for Automatic Estimation of Instantaneous Local Uncertainty in Particle Image Velocimetry Measurements,” *Experiments in Fluids*, **53**(4), pp. 1133–1147, doi:[10.1007/s00348-012-1341-1](https://doi.org/10.1007/s00348-012-1341-1).
- [20] Wilson, B. M., and Smith, B. L., 2013, “Taylor-series and Monte-Carlo-method Uncertainty Estimation of the Width of a Probability Distribution Based on Varying Bias and Random Error,” *Meas. Sci. Technol.*, **24**(3), p. 035301, doi:[10.1088/0957-0233/24/3/035301](https://doi.org/10.1088/0957-0233/24/3/035301).
- [21] Kendall, A., and Koochesfahani, M., 2007, “A Method for Estimating Wall Friction in Turbulent Wall-bounded Flows,” *Exp Fluids*, **44**(5), pp. 773–780, doi:[10.1007/s00348-007-0433-9](https://doi.org/10.1007/s00348-007-0433-9).
- [22] Bevington, P. R., and Robinson, D. K., 2003, *Data Reduction and Error Analysis*, McGraw–Hill, New York.

Chapter 4

Wall Heat Flux Measurements in a Convecting Boundary Layer

Abstract

Wall heat flux measurements were made by measuring the temperature gradient in air very near a heated plate under convection conditions. Air thermal conductivity was predicted using the locally-measured temperature and reference data. A fine-wire thermocouple probe was designed, built, and used for these measurements and has the ability to self-align to the surface. Commercial sensors that were potted inside the plate were compared with this first-principles method for accuracy assessment.

4.1 Introduction

Heat flux is one desirable measurement for computational fluid dynamics (CFD) validation experiments performed with the Rotatable Buoyancy Tunnel (RoBuT) at Utah State University. Model Validation is done by matching inputs and comparing outputs of experiments and simulations. Simulation accuracy can be assessed by this comparison. Validation is more rigorous with derivative quantities such as heat flux as they are more susceptible to experimental noise and numerical errors compared to integral quantities [1].

Validation experiments are the main purpose of the RoBuT, whose major flow components are shown in Fig. 4.1. The components shown were mounted in a rotating ‘Ferris wheel’ structure to change the relative direction of natural convection and forced convection. The test section had three clear walls for optical access and one heated wall for a convection boundary condition. The cross section was 0.305 m square and the test section 2 m long. Three thin-film heat flux sensors (HFSSs) from RdF Corporation were potted inside the heated wall in the streamwise (x) direction at the spanwise center. These sensors were based on the spatial temperature gradient method and are shown, along with the many layers of the heated wall, in Fig. 4.2.

The sensors were model 20457-3 and had a thermopile around a Kapton[®] substrate. The manufacturer supplied unique calibration coefficients for each sensor. The manufacturer-specified uncertainty was 5% of reading. An embedded Type T thermocouple (TC) was used to measure sensor temperature. This temperature was used to correct readings for changes in thermal conductivity of the substrate with a multiplication factor

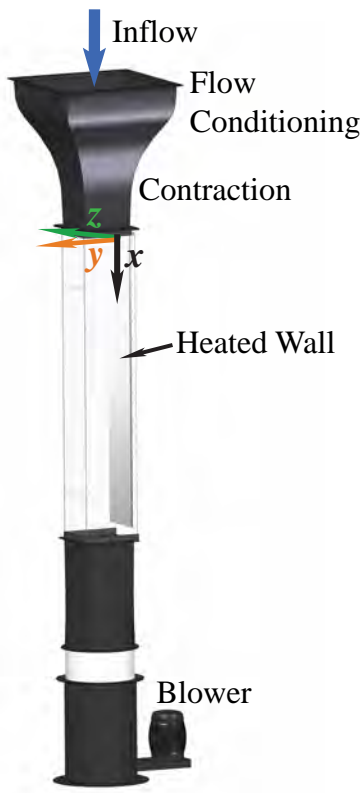


Fig. 4.1: Important flow components of the Rotatable Buoyancy Tunnel

curve. The HFSs were placed adjacent to the Kapton[®] layer of similar thermal resistance to reduce measurement errors by non-uniform conduction paths. An initial thermal resistance network analysis between HFS and non-HFS conduction paths showed only a 2.4% difference in heat flux.

Preliminary experiments have shown that the measured heat flux does not match fundamental trends as shown in Fig. 4.3, specifically decreasing heat flux with boundary layer development with increasing x . Two correlations are shown with the experimental results [2, 3]. The correlation trends are not smooth, a result of the measured center-line wall temperature, which has small gradients. The trend was concerning and it was possible that the sensor sensitivities were mixed-up, the sensors had an installation error, or other manufacturer-supplied parameters were incorrect. As heat flux was important to this experiment, developing a means to assess sensor accuracy and possibly quantify errors was desired. Since they were potted inside the heated wall, only in-situ methods were possible without damaging the heated wall.

Installation error is possible if heat transfer conditions were different between calibration and use. The

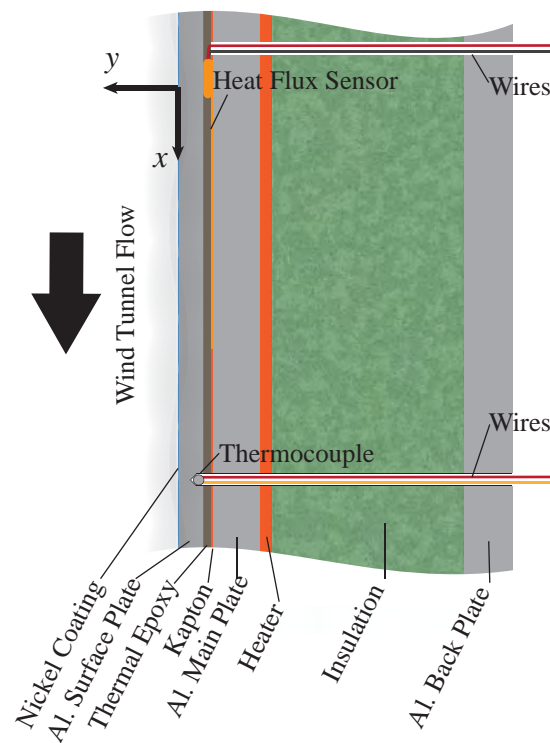


Fig. 4.2: Heated wall cross section with relative thicknesses to scale. The HFS label is near the top.

RdF sensors were calibrated to a reference sensor that was calibrated at 70°F in radiation using a blackbody source [4]. Since the sensors were potted in the heated wall, the heat transfer mode was conduction. The different heat transfer modes, the elevated operation temperature, and the possibility of non-uniform thermal resistance in the sensor area have been identified as possible error sources [5].

4.2 Theory

Heat flux measurements can be challenging due to the complex thermal environments involved and multi-mode heat transfer which is often present. All known sensors are intrusive and are likely to disrupt thermal conditions where they are placed. Several commercial sensor options are available, but care must be taken to maintain uniform thermal resistance around the sensors [6].

The three main methods for measuring heat flux are based on: 1) spatial temperature gradients, 2) temperature change with time, and 3) surface heating [6]. The spatial temperature gradient method is used in the purchased RdF thin-film sensors. Adding a reference HFS of this type to the surface would disrupt local convection conditions. The calorimeter method uses heat storage over time to measure flux, but this

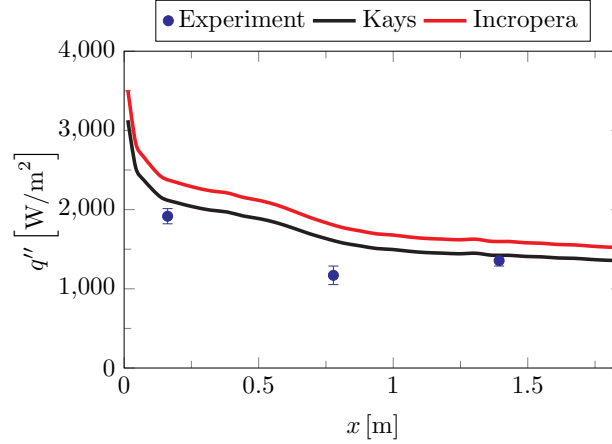


Fig. 4.3: Wall heat flux measurements with two correlations

assumes the temperature throughout the body is uniform. The heated wall was likely to have temperature gradients through the thickness, especially in the epoxy where the thermal conductivity was about 1/100 of that of the adjacent aluminum. Temperature gradients were also likely in both spanwise directions. Surface heating methods were not well developed nor described and were not a good option.

Sensors based on spatial temperature gradients are common and will be described in greater detail. Fourier's law is essential to their operation and is

$$q'' = -k \frac{dT}{dy} \approx -k \frac{\Delta T}{\Delta y} \quad (4.1)$$

where q'' is heat flux, k is the substrate thermal conductivity, T is temperature, and y is the direction of heat flux [3]. The temperature gradient is often estimated by a differential temperature measurement (ΔT) across a thermopile (array of differential TCs) across a substrate, such as in the RdF sensors. Generally the substrate thickness (Δy) and thermal conductivity are not known accurately enough for the overall desired accuracy, so sensor calibration is commonly performed.

An independent heat flux measurement technique was desirable to assess the accuracy of the potted HFSs. The HFSs measured heat flux near the surface of the heated wall. The convective heat flux from the wall to the air should be equivalent, especially very near the wall and departed from the side walls. Radiation heat transfer was minimized by the nickel plating on the heated wall meant to reduce thermal radiation. The predicted and measured emissivity was around 0.03 [7]. Very near the wall, within the inner portion of the viscous sublayer, the temperature profile should be linear [2]. If the temperature profile can be measured

within this region and the thermal conductivity of air k can be estimated by the measured temperature and reference data [8], convective heat flux measurements from a surface are possible.

Others have made near-wall temperature measurements. An early study by Warner and Arpaci used a butt-welded TC probe of 12.7 μm diameter oriented parallel to a vertical flat plate and perpendicular to the flow direction. It was traversed with a motor-driven carriage near the heated wall under turbulent natural convection. The position was accurate to 5.08 μm within the first 25.4 mm and to 15.2 μm farther from the wall. They were able to measure temperature profiles and subsequently heat flux [9]. In another study of a turbulent boundary layer under forced convection, temperature profiles were measured by a TC probe of 76.2 μm diameter and about 12.7 mm long suspended by 22-gauge hypodermic needles oriented parallel to the plate and perpendicular to the flow direction. This probe was also traversed with a mechanism that was accurate to 25.4 μm . These results, along with velocity measurements, were used to present many heat flux, shear, and turbulent Prandtl number results for this canonical flow [10].

4.3 Method

An independent heat flux measurement was conceived to assess the accuracy of the HFSs inside the heated wall. After several iterations of design and testing, the final sensor was able to measure heat flux with an uncertainty of less than 10% while disrupting the actual heat flux only moderately. The design was based on the spatial temperature gradient like the thin-film sensors, but measured heat flux in air very near the heated wall. The heat transfer inside the wall was by conduction. At the surface, heat transfer was mainly due to convection. As mentioned previously, thermal radiation from the heated wall was minimized by a nickel coating.

The sensor design was similar to that used by Blackwell *et al.* [10] and was a TC oriented parallel to the wall and perpendicular to the flow direction. The new design is shown in Fig. 4.4 with the pivot, brace, and TC junction identified. The junction of the probe was formed by type K wires of diameter $D_{\text{TC}} = 0.051$ mm from Omega Engineering. The two lead wires were aligned parallel to the wall with a length of 15.3 mm ($\sim 300D_{\text{TC}}$) to reduce conduction losses. The junction was formed by spot welding overlapping wires. After welding, the wire was pulled tight and epoxied in place. The fine wire was welded to thicker 0.511-mm wire that spanned the pivot and was connected to the data acquisition system (DAQ). The brace was rigid enough to keep the wire tight and made of plastic for small conduction losses.

The pivot allowed the probe to self-align to the wall prior to each acquisition, reducing measurement errors. Alignment was done by moving the probe into the wall until both ends of the brace were pressed

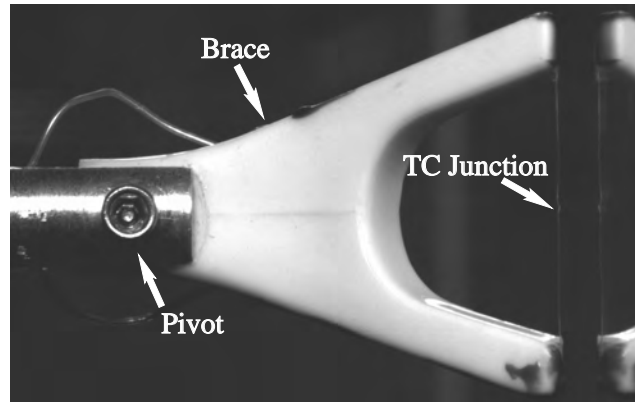


Fig. 4.4: TC Probe with its reflection in the heated wall on the right

firmly and any angle corrected, then pulling the probe away from the wall. The alignment process is shown in Fig. 4.5 and involves three steps.

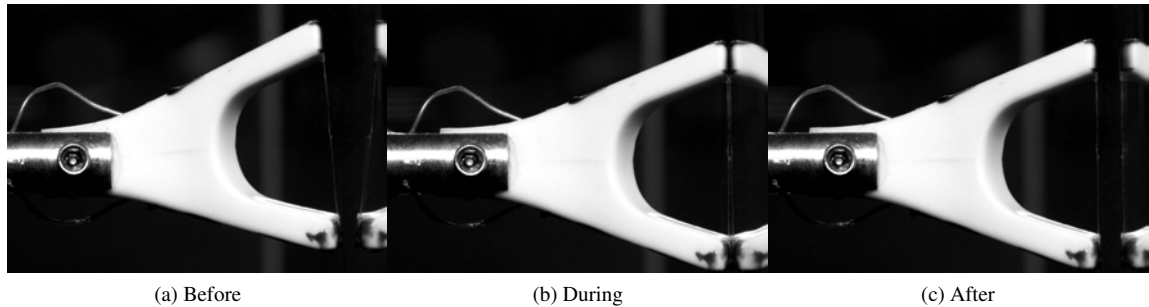


Fig. 4.5: Self-alignment process of the TC Probe with the heated wall

The pictured head of the TC probe was supported by a stainless steel tube with 3.76-mm outside diameter that spanned the test section and exited the wall opposite the heated wall. This tube contained the TC wires and was connected to a Velmex Inc. UniSlide[®] traverse model B4015Q2J. This traverse was used for small, incremental movements such as 200 μm . The distance from the wall was estimated by fitting a line to the measured temperature profile very near the wall to the temperature of the wall measured by embedded TCs. The largest uncertainty in position resulted from the stepper motor resolution. With 200 steps/rev. and assuming 1/2 step resolution, the uncertainty was 2.5 μm . The pitch uncertainty was much smaller at 0.04 mm/25.4 cm or 0.0315 μm for a 200 μm step. Traverse backlash should not be a problem since traversing was done in one direction only and the first point was ignored.

The probe was used in the spanwise center of the test section, directly over the three potted HFSs. Three

25.4 mm access ports were drilled into the wall opposite the heated wall at the x locations of the HFSs. Once inserted, a collar was used to support the probe tube and fill the port gap. The x locations of the HFSs and the ports were $x_1 = 16.2$ cm, $x_2 = 77.8$ cm, and $x_3 = 139$ cm from the inlet to the test section. These three positions were used for analysis throughout this work.

The output voltages of the TCs and HFSs were small, so specialized DAQ devices were selected. National Instruments (NI) products were used as they interfaced well with the LabVIEW software that was used for system control and thermal data recording. All TCs and HFSs were measured with NI-9213 TC modules. The narrow voltage range of ± 78 mV, 24-bit ADC, and open channel detection capability made them well suited for these measurements. The built-in CJC was used for TCs.

The TC probe was not calibrated, so the standard bias uncertainty of 2.2°C for type K TCs was used. The bias uncertainty of the DAQ was 0.8°C , resulting in overall bias uncertainty as

$$B_T = \sqrt{B_{TC}^2 + B_{DAQ}^2} = 2.34^\circ\text{C}. \quad (4.2)$$

The random uncertainty was calculated from the data as

$$S_T = t_{95} \frac{S_T}{\sqrt{N}} \quad (4.3)$$

where t_{95} is the confidence level coefficient (taken as 1.96 for 95% confidence and number of samples $N > 30$) and S_T is the sample standard deviation. Bias and random sources were combined as

$$U_T = \sqrt{B_T^2 + S_T^2}. \quad (4.4)$$

The probe may be subject to conduction losses that could lead to measurement error. Accordingly, this error was estimated using a 1-D fin equation with non-uniform ambient temperature. Velocity profiles were measured at the three x locations by Particle Image Velocimetry (PIV) under the same conditions but with the probe removed. The measured temperature and velocity profiles were used to estimate fluid properties and heat transfer coefficients. Heat conduction was considered from the TC junction through the wires that were parallel with the heated wall. Then combined conduction and convection were considered in the wires departing from the wall to the lower temperature air. The epoxy in this area would have an insulating effect on the potted wires, reducing errors, but this effect was conservatively neglected. The largest predicted error from losses was estimated at 0.03°C at the wall at x_1 .

Two convection conditions were measured, forced and mixed. In forced convection, buoyancy forces were small compared to pressure forces and the effects of natural convection were practically negligible. Mixed convection, however, had natural convection forces similar in magnitude to pressure forces. The forced flow was downward, creating buoyancy-opposed mixed convection where forces of natural and forced convection are in opposite directions [3]. The wall temperature was about 140°C for both cases. The bulk velocities were 4.31 and 2.44 m/s for forced and mixed convection respectively. The flow was only partially-developed in the test section, so the physics were more like external than internal flow.

In addition to forced and mixed convection tests at the three x locations, tests were performed to isolate the error source of the HFS readings. Factorial experiments from Design of Experiments (DOE) were implemented [11]. Data were acquired and errors quantified at the farthest downstream location at x_3 with the TC probe. Three parameters were changed during the tests: air velocity, axial conduction in the heated wall, and temperature magnitude of the heated wall. Axial conduction was prescribed by independently controlling the temperature in three heating zones in the streamwise direction. The variation of these parameters is depicted in Fig. 4.6 with two levels of temperature and velocity and three for axial conduction. The two velocity levels correspond to forced and mixed convection. The cases numbered 1–10 represent unique combinations of the three parameters with relative magnitudes properly shown on the three axes. The order of these tests was randomized for measurement independence and repeated three times to determine the level of repeatability.

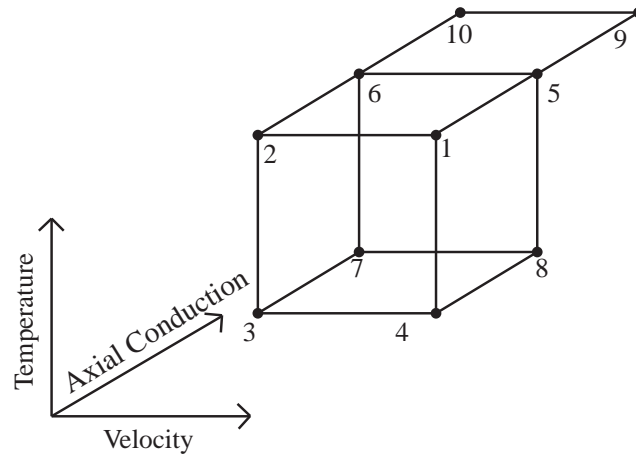


Fig. 4.6: Factorial sketch of the DOE study

4.4 Results

The measured temperature profiles from the TC probe for both forced and mixed convection are shown in Fig. 4.7. The spatial resolution of the first eight points was $200\mu\text{m}$. Subsequent spacing increases with increasing distance from the heated wall and the last several points measured the free-stream temperature. The development of the thermal boundary layer is observable in x in both cases and the larger boundary layer is seen for the mixed case (lower velocity) as expected. Each location is the time mean of 250 points acquired at 15 hz. The traverse started the probe head at the heated wall and pulled it away, allowing several seconds for each move and for the probe to come into thermal equilibrium.

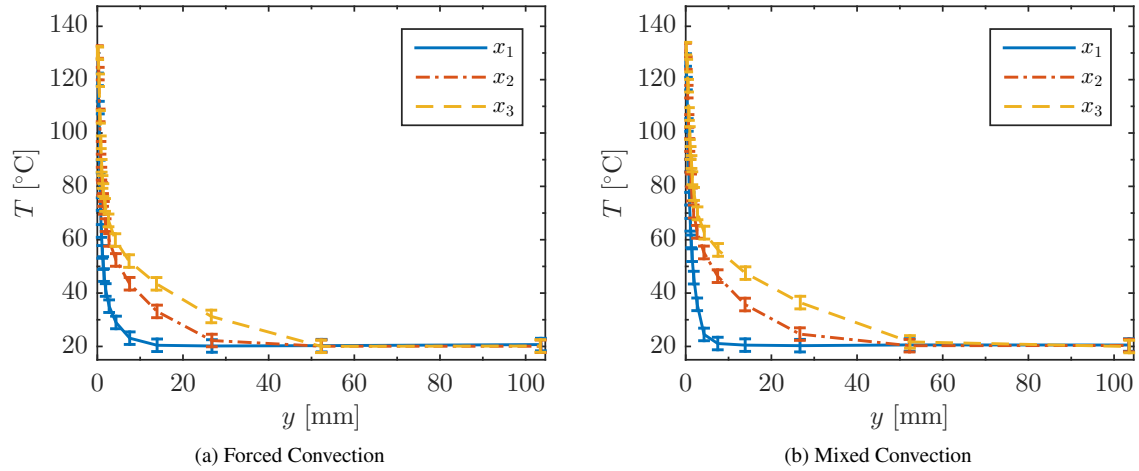


Fig. 4.7: Measured temperature profiles for both cases and all three x locations

The same temperature data in the near-wall region and line fit are shown in Fig. 4.8. For the line fit, initially eight points were included in the fit and a stable iterative method was used to calculate the temperature gradient and the number of data points to fit within $y^+ \leq 6.6$, half the critical y^+ value for air. This ensured the fitted data were within the inner portion of the viscous sublayer where linear temperatures were expected. The first point was not considered as it is likely to have position error. Errors in wall position were corrected by taking the temperature gradient to the measured wall temperature. The linear fit was performed using linear regression with more weight given to data with lower uncertainty [12]. This method also provided a measure of the fit uncertainty.

Nondimensional profiles are shown and compared with the thermal law of the wall [2] in Fig. 4.9. The agreement is excellent for $y^+ \leq \sim 6$. The results in the buffer layer and fully turbulent region are about five

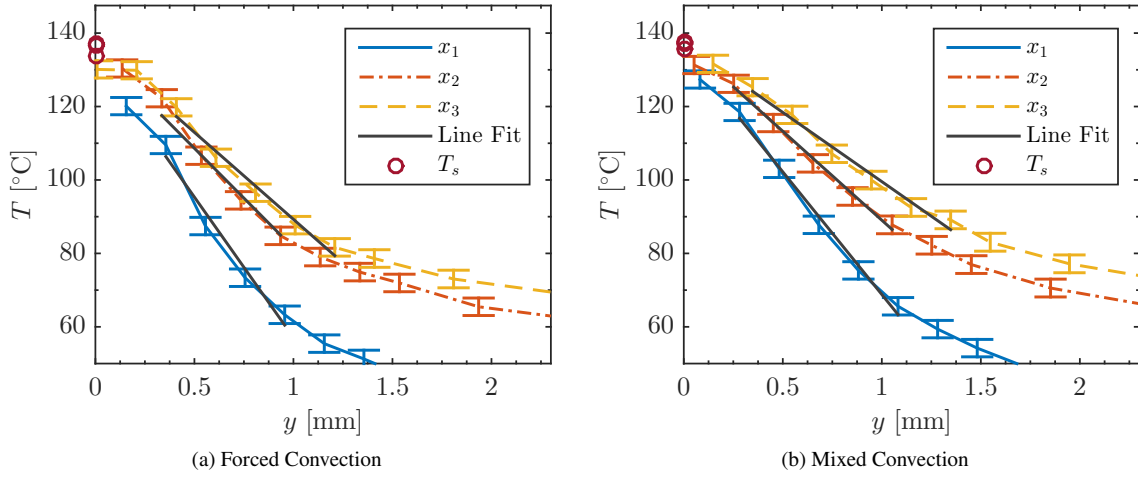


Fig. 4.8: Measured temperature profiles near the heated wall with line fit for both cases for all three x locations. Note the unique wall temperature values T_s as the wall is nearly isothermal. T_s at x_1 is several degrees cooler than at x_2 and x_3 .

below the expected values, likely due to the partially-developed nature of the measurement region. Temperature fluctuations are not presented as the mass of the TC wire rendered it insensitive to the higher frequencies in this flow. These frequencies were determined to be about 300–600 Hz with a 50.8- μm diameter tungsten hot-film probe with much less thermal mass.

The intrusive nature of the probe caused an increase in wall heat flux observable in the HFS data acquired at the time. The largest error of wall heat flux occurred when the probe was touching the heated wall and steadily decreased as the probe was retracted from the wall. Maximum errors of 9.84%, 9.90%, and 8.61% for the forced case and of 18.7%, 10.4%, and 7.93% for the mixed case were measured at locations x_1 , x_2 , and x_3 respectively. The likely cause of the heat flux increase is an increase in local turbulence levels caused by the probe. The forced convection case had very consistent errors and was fully turbulent as measured with PIV at a separate time in these conditions. The mixed convection case had a large range of error levels and was likely intermittently turbulent. In this case, the presence of the probe likely increased turbulence levels such as by a turbulence trip.

Published correlations for heat transfer can be used for comparison with both the HFS and TC probe results. First is turbulent forced convection over a flat plate. The local Stanton number correlation is

$$\text{St} = \frac{\text{Nu}_x}{\text{Re}_x \text{Pr}} = \frac{0.0287 \text{Re}_x^{-0.2}}{0.169 \text{Re}_x^{-0.1} (13.2 \text{Pr} - 9.25) + 0.85} \quad (4.5)$$

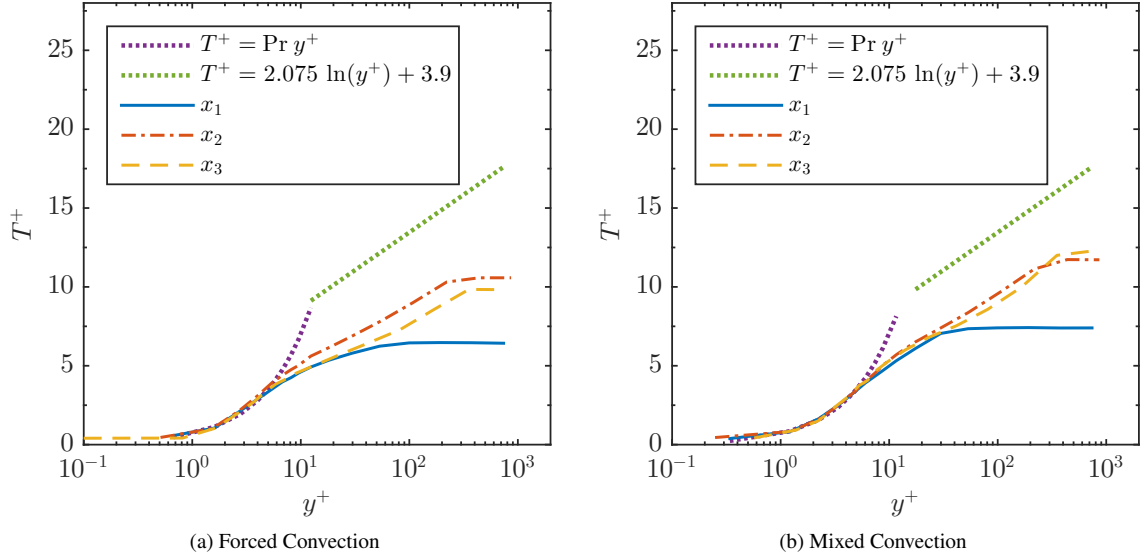


Fig. 4.9: Measured nondimensional temperature profiles with the thermal law of the wall for air for both cases and all three x locations

where Nu_x is the local Nusselt number, Re_x is the local Reynolds number, and Pr is the Prandtl number [2]. Once the Nusselt number is solved from this correlation, heat flux was calculated as $q'' = Nu_x k (T_s - T_\infty) / x$ where q'' is heat flux, k is fluid thermal conductivity, T_s and T_∞ are surface and free-stream temperatures respectively, and x is the streamwise distance from the leading edge.

As there are no known heat transfer correlations for mixed convection in developing channel flow, the correlation for fully developed turbulent flow in vertical tubes was used from the work of Jackson *et al.* [13] as in

$$\frac{Nu}{Nu_F} = \left| 1 \pm \frac{10^4 Gr}{Re^{2.7} Pr^{0.5}} \right|^{0.46} \quad (4.6)$$

where Nu_F is the forced convection Nusselt number as calculated by Eqn. 4.5 and Gr is the Grashof number. The plus sign is used for buoyancy-opposed flows such as that investigated in this work while a minus sign applies to buoyancy-aided flows. Local values for Nu_x , $Nu_{F,x}$, Gr_x , and Re_x were used in place of the fully-developed variables.

As the boundary layers are partially developed at the inlet where $x = 0$, considering an unheated starting length was thought to improve agreement between measured values and correlations. This process required three calculations: 1) the momentum thickness at the inlet, 2) the distance upstream to a virtual origin, and 3) adjusting heat transfer correlations using the virtual origin as an unheated starting length. First the momentum thickness was calculated from PIV data at the spanwise center ($z = 0$) location at the inlet ($x = 0$) using the

integral

$$\delta_2 = \int_0^\infty \frac{\bar{u}}{\bar{u}_\infty} \left(1 - \frac{\bar{u}}{\bar{u}_\infty}\right) dy \quad (4.7)$$

where δ_2 is the momentum thickness, \bar{u} is the time mean velocity across y , and \bar{u}_∞ is the time mean free-stream velocity [2]. Constant density has been assumed. This is a good approximation at the inlet which is upstream of the heated wall but would be inappropriate downstream where the near-wall air was heated. The boundary layers on both walls were considered and the result divided by two.

The calculation of a virtual origin was the second step and predicts the equivalent length of a flat plate extending upstream of the inlet. This allows for the impact of the contraction to be assessed simply, even though the geometry is very complex. Assuming the flow was always turbulent, the relationship has been derived as

$$\frac{\delta_2}{x} = \frac{0.036\nu^{0.2}}{\bar{u}_\infty^{0.2}x^{0.2}} = 0.036\text{Re}_x^{-0.2} \quad (4.8)$$

where ν is kinematic viscosity [2]. The left two portions can be arranged to isolate x as in

$$\xi = \frac{\delta_2^{1.25}\bar{u}_\infty^{0.25}}{0.0157\nu^{0.25}} \quad (4.9)$$

where ξ has been substituted for x and is the distance upstream to a virtual origin given δ_2 defined earlier. The results from the first two analyses are given in Table 4.1 for both cases. As expected, the momentum thickness is larger for mixed convection. It is reasonable to add these virtual origin distances to the x values in this work when comparing to more canonical flows. Also Re_x may be adjusted.

Table 4.1: Boundary layer analysis results from velocity data at the inlet

Parameter	Forced	Mixed
δ_2 [mm]	1.18	1.73
ξ [mm]	327	458

The third calculation was to adjust the correlation results for an unheated starting length with distances from the virtual origin analysis. The local Nusselt number was augmented by

$$\text{Nu}_x = \frac{\text{Nu}_x|_{\xi=0}}{\left[1 - (\xi/x)^{9/10}\right]^{1/9}} \quad (4.10)$$

where the local Nusselt number Nu_x and $Nu_x|_{\xi=0}$ was measured from the leading edge of the unheated starting length [3]. The adjusted flux values were slightly higher than the original, also an expected result.

Wall heat flux as measured by the HFSs and TC probe is shown in Fig. 4.10 with published correlations. The measured HFS trends in the streamwise direction x are inconsistent with expected results. The HFS at x_2 gives a smaller reading than that at x_3 for both cases. The likelihood that this error is real is supported by the monotonic decrease in the temperature gradient near the wall with streamwise distance x as observed in the TC probe results of Fig. 4.8. This decrease suggests a decrease in wall heat flux with x , consistent with theory. The TC probe results follow an expected trend and measured higher fluxes in both cases. The correlation prediction of heat flux uses the equations presented previously and the measured temperatures along the heated wall centerline. The first point very near $x = 0$ is low, attributable to the relatively cooler, insulated leading edge. The bump near $x = 0.5$ m in both cases is due to a temperature peak in the heated wall.

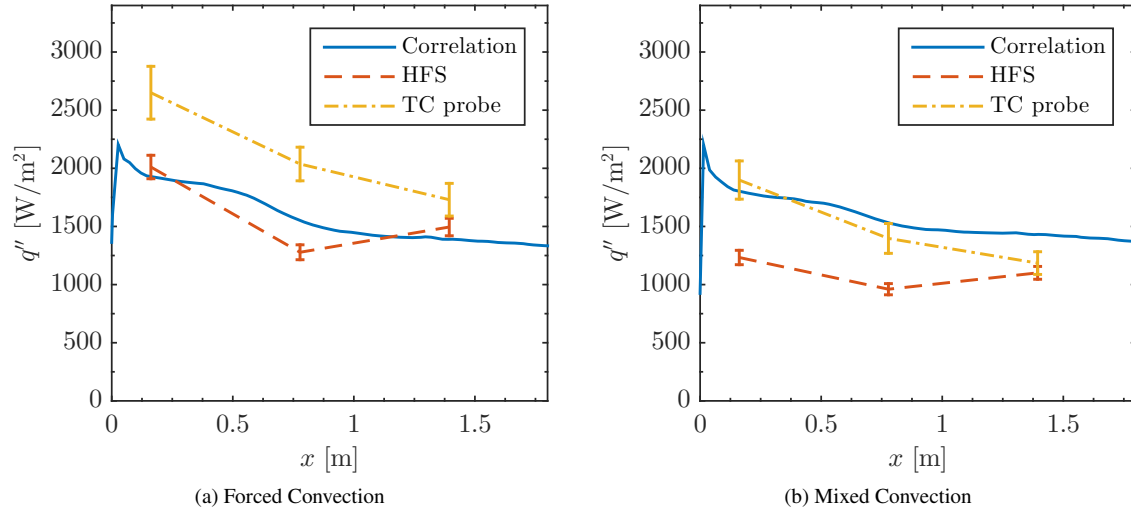


Fig. 4.10: Measured and predicted heat flux plotted in the streamwise direction

Heat flux results from the HFSs and TC probe are presented in numeric format in Table 4.2 for both cases and at all three x locations investigated. Taking the TC probe as the reference, HFS errors were quantified. Uncertainty at the 95% confidence level was calculated for all quantities, including the error. The errors are all negative as the HFS results are consistently low. The errors are moderately high, with the best agreement at x_3 . These results are consistent with the notion that measurements of derivative quantities are challenging and moderate errors can be expected.

Table 4.2: Heat flux results for both cases from the HFSs and the TC Probe results at all three x locations

		x [cm]	16.2	77.8	139
Forced	HFS	q'' [W/m ²]	2010	1280	1500
		$U_{q''}$ [%]	5.02	5.01	5.02
	TC Probe	q'' [W/m ²]	2650	2037	1730
		$U_{q''}$ [%]	8.56	7.09	8.12
	Error	ε [%]	-24.1	-37.2	-13.6
		U_ε [%]	7.53	5.45	8.25
Mixed	HFS	q'' [W/m ²]	1230	960	1101
		$U_{q''}$ [%]	5.01	5.01	5.01
	TC Probe	q'' [W/m ²]	1900	1400	1180
		$U_{q''}$ [%]	8.65	9.18	8.24
	Error	ε [%]	-35.1	-31.3	-7.06
		U_ε [%]	6.49	7.19	8.96

The results of the DOE study were the flux errors of the HFSs relative to the TC probe. This study was performed at x_3 , where the errors were the smallest and the boundary layer the largest. The resulting errors are shown on the factorial sketch for cases 1–10 as shown in Fig. 4.11. The resulting errors show surprising consistency around 20%. There is no apparent trend, suggesting that the error is relatively insensitive to the three parameters tested.

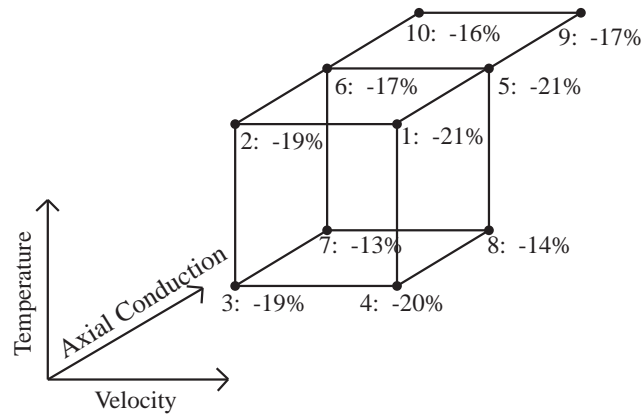


Fig. 4.11: Factorial sketch of the DOE study with errors

The consistency of these results suggests a constant bias to the error. Further investigation revealed that there may be non-uniform thermal resistance in the heated wall. After checking the thermal conductivity

of Kapton[®] used adjacent to the HFSs, an error was found. The most likely thermal conductivity was 42% higher than the design value. Using a 1-D thermal circuit, the predicted error of the heat flux measurement due to spatial non-uniformity was -17.5% instead of 2.4% originally predicted. The results presented previously were not corrected from this information as there was a lack of confidence in either thermal conductivity specification.

4.5 Conclusions

The purpose of this work was to assess the accuracy of the commercial HFSs used in a validation experiment. These sensors were believed to be in error from an unknown source. An independent method of measuring heat flux in air near a heated wall under convection was developed and tested. The intrusive nature of the probe caused moderate errors in heat flux. The TC probe results, while possessing moderate uncertainties and flow disruptions, provide expected trends. A HFS error from non-uniform thermal resistance in the heated wall was identified. The probe results have known uncertainties and errors, while the HFSs have at least one unknown error remaining as evidenced by the illogical trends in the streamwise direction. The measured flux from the probe should be used for validation data while considering the limitations mentioned.

References

- [1] Oberkampf, W. L., and Roy, C. J., 2010, *Verification and Validation in Scientific Computing*, Cambridge University Press, doi:[10.1017/cbo9780511760396](https://doi.org/10.1017/cbo9780511760396).
- [2] Kays, W. M., Crawford, M. E., and Weigand, B., 2012, *Convective Heat and Mass Transfer*, 4th ed., McGraw-Hill.
- [3] Incropera, F. P., Dewitt, D. P., Bergman, T. L., and Lavine, A. S., 2007, *Fundamentals of Heat and Mass Transfer*, 6th ed., John Wiley & Sons.
- [4] RdF, 2014, "Heat Flow Measurement: Calibration, Specifications & Accuracy," Tech. rep., RdF, corp.
- [5] Holmberg, D. G., and Womeldorf, C. A., 1999, "Performance and Modeling of Heat Flux Sensors in Different Environments," ASME Heat Transfer Division, pp. 71–77.
- [6] Diller, T. E., 1999, *The Measurement, Instrumentation, and Sensors Handbook*, chap. 34, Heat Flux, CRC Press.
- [7] Harris, J. R., Lance, B. W., and Smith, B. L., 2015, "Experimental Validation Data for Computational Fluid Dynamics of Forced Convection on a Vertical Flat Plate," *Journal of Fluids Engineering*, **138**(1), p. 011401, doi:[10.1115/1.4031007](https://doi.org/10.1115/1.4031007).
- [8] Touloukian, Y. S., Liley, P. E., and Saxena, S. C., 1970, "Thermophysical Properties of Matter-The TPRC Data Series. Volume 3. Thermal Conductivity-Nonmetallic Liquids and Gases," Tech. rep., DTIC Document.

- [9] Warner, C. Y., and Arpaci, V. S., 1968, “An Experimental Investigation of Turbulent Natural Convection in Air at Low Pressure Along a Vertical Heated Flat Plate,” *International Journal of Heat and Mass Transfer*, **11**(3), pp. 397–406, doi:[10.1016/0017-9310\(68\)90084-7](https://doi.org/10.1016/0017-9310(68)90084-7).
- [10] Blackwell, B. F., Kays, W. M., and Moffat, R. J., 1972, “The Turbulent Boundary Layer on a Porous Plate: an Experimental Study of the Heat Transfer Behavior with Adverse Pressure Gradients,” Tech. Rep. HMT-16, The National Aeronautics and Space Administration.
- [11] Montgomery, D., 2012, *Design and Analysis of Experiments, 8th Edition*, John Wiley & Sons, Inc.
- [12] Bevington, P. R., and Robinson, D. K., 2003, *Data Reduction and Error Analysis*, McGraw–Hill, New York.
- [13] Jackson, J. D., Cotton, M. A., and Axcell, B. P., 1989, “Studies of Mixed Convection in Vertical Tubes,” *International Journal of Heat and Fluid Flow*, **10**(1), pp. 2–15, doi:[10.1016/0142-727x\(89\)90049-0](https://doi.org/10.1016/0142-727x(89)90049-0).

Chapter 5

Conclusions

This work has described the theory behind model validation, provided an example of a validation experiment, and provided links to a validation database. Steady and transient mixed convection have been studied experimentally with high-fidelity instrumentation. Steady mixed convection has been presented in previous works, but never in a validation experiment. This is the first presentation of transient mixed convection in known publications. The coupled fluid momentum and heat transfer, together with measurements of dependent variables and their spatial derivatives, make this a robust benchmark for thorough CFD validation studies. The data were provided in tabular format with adequate significant figures to make approximations unnecessary. Boundary conditions may be implemented directly in CFD models ensuring consistent inputs between experiment and simulations. System response quantities were in table format for direct comparison with model outputs and can be plotted in any program. Additionally, uncertainties of all results were provided to aid in quantifying simulation uncertainty through validation studies.

Model development and application are certain to continue as an integral part of science and engineering. The procedures and reporting in this validation experiment were good examples for others to follow for future works, though the physics and geometry will be different in each case. There is danger in performing simulations alone because the natural tendency is to trust a prediction when there is nothing with which to compare. Every research program that develops models or seeks to apply existing models to new problems needs to allot time and resources to validation. And if the physics have not been measured, the large expense of conducting experiments should be put forth. The attitude of validation is skeptical, but an appropriate level of skepticism will avoid at least some costly setbacks that often accompany incorrect predictions in science and engineering.

Appendices

Appendix A

Unsteady Computational Fluid Dynamics Simulations

A.1 Introduction

Since the purpose of this work was to provide validation data for computational fluid dynamics (CFD), simulations were always being performed in parallel with experiments. Initially a senior engineer at the Idaho National Laboratory (INL) performed blind studies, meaning that the knowledge was limited to the information provided in reports and the data associated with them. This approach was meant to decrease the level of bias of the modeler towards the experimental results. Modelers and experimentalists at Utah State University (USU) also ran simulations to guide the experiments as to what information was needed for model inputs, where output data should be measured, and what System Response Quantities (SRQs) would be useful for comparison. Many steady cases were run, such as for the steady mixed convection case described in this work. Furthermore, Unsteady Reynolds-Averaged Navier-Stokes (URANS) simulations were performed by the experimentalist as the previous modelers at the INL and USU were not available. This section describes the modeling approach and compares results with experimental data for the transient mixed convection case.

A.2 Methods

The URANS simulations were performed using Star-CCM+ 9.06 [1] with the experimental boundary conditions (BCs). The BCs were the as-built geometry, the temperature on all four walls and the inflow, the inflow ensemble-averaged velocity profiles, the inflow turbulence kinetic energy k profiles, and the air properties. The inflow turbulence dissipation rate profiles were determined by an empirical correlation using k [2]. The implicit unsteady model was used in combination with the Low-Re $\overline{v^2} - f, k - \epsilon$ model [3]. This model was found to perform well with buoyant flows in vertical channels [4]. Air was modeled as an ideal gas with properties as functions of temperature. Thus, buoyancy is modeled directly. Coupled momentum and coupled energy were also used to capture natural convection. Solvers were second-order accurate in space and in time. The as-built geometry was used for the fluid domain.

All normalized residuals were driven to below 1×10^{-6} at every time step. The time step was chosen for a particle to displace no more than one cell length in the streamwise direction. Converged solutions were

obtained for three meshes of 15.625k, 125k, and 1M cells with equivalent cell counts in each direction of 25, 50, and 100, respectively. Cells were concentrated near the walls. The configuration for the finest mesh is shown in Fig. A.1 with the global coordinates specified. The cell size in each direction and the time step were reduced by a factor of two with each refinement. The maximum wall y^+ values were 1.5, 0.76, and 0.36, respectively. Three meshes allowed for the Grid Convergence Index method first proposed by Roache and improved upon by others to quantify numerical uncertainty [5,6]. The safety factor was allowed to increase to compensate for results with less consistency. These results are at the 95% confidence level and are used as uncertainty bands for CFD outputs in Figs. A.2 and A.3.

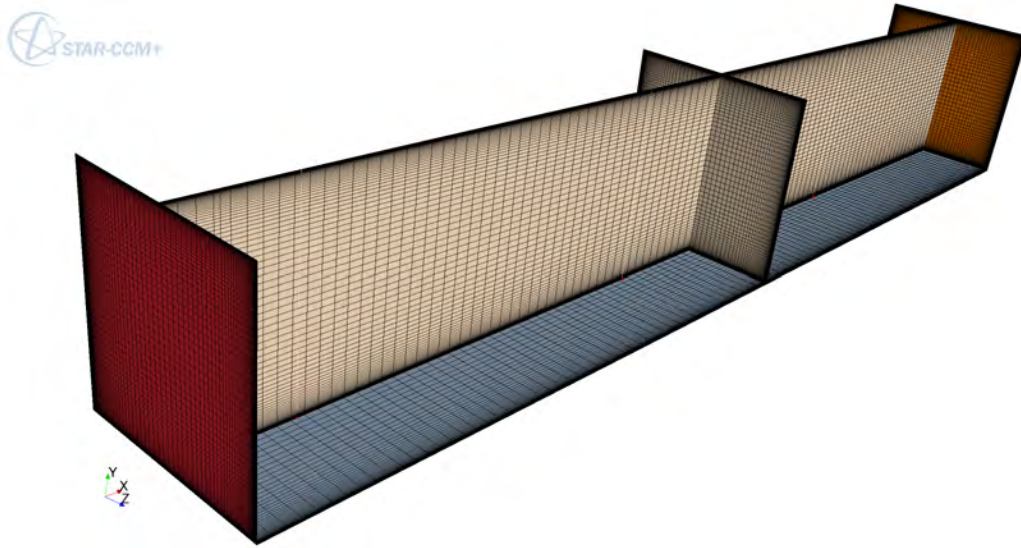


Fig. A.1: The structured rectangular mesh with 1M cells

The unsteady nature of the simulations and strict requirements placed on iterative convergence motivated the use of a computing cluster. The Division of Research Computing cluster Navier at USU was used for the medium and fine meshes while the coarsest mesh was solved on a local workstation. Simulations were setup on a local workstation and submitted as a batch job to the cluster. The workstation had 16 cores. Each node of Navier had 64 cores between four CPUs. The medium-mesh simulation used one node for 22 hours while the fine-mesh simulation used three nodes for 89 hours.

A.3 Results

Both experimental and CFD predicted profiles of ensemble-averaged streamwise velocity \bar{u} and turbulent

kinetic energy \bar{k} are shown in Fig. A.2 at three locations in x for the top (x_1), middle (x_2), and bottom (x_3). The definition $\bar{k} = \frac{1}{2} (\overline{u'u'} + \overline{v'v'} + \overline{w'w'})$ was used, assuming $\overline{w'w'} = \overline{v'v'}$ since the third component of velocity was not measured. Since the CFD model used modified two-equation RANS, the Reynolds stresses are not available and \bar{k} was the logical choice for an SRQ.

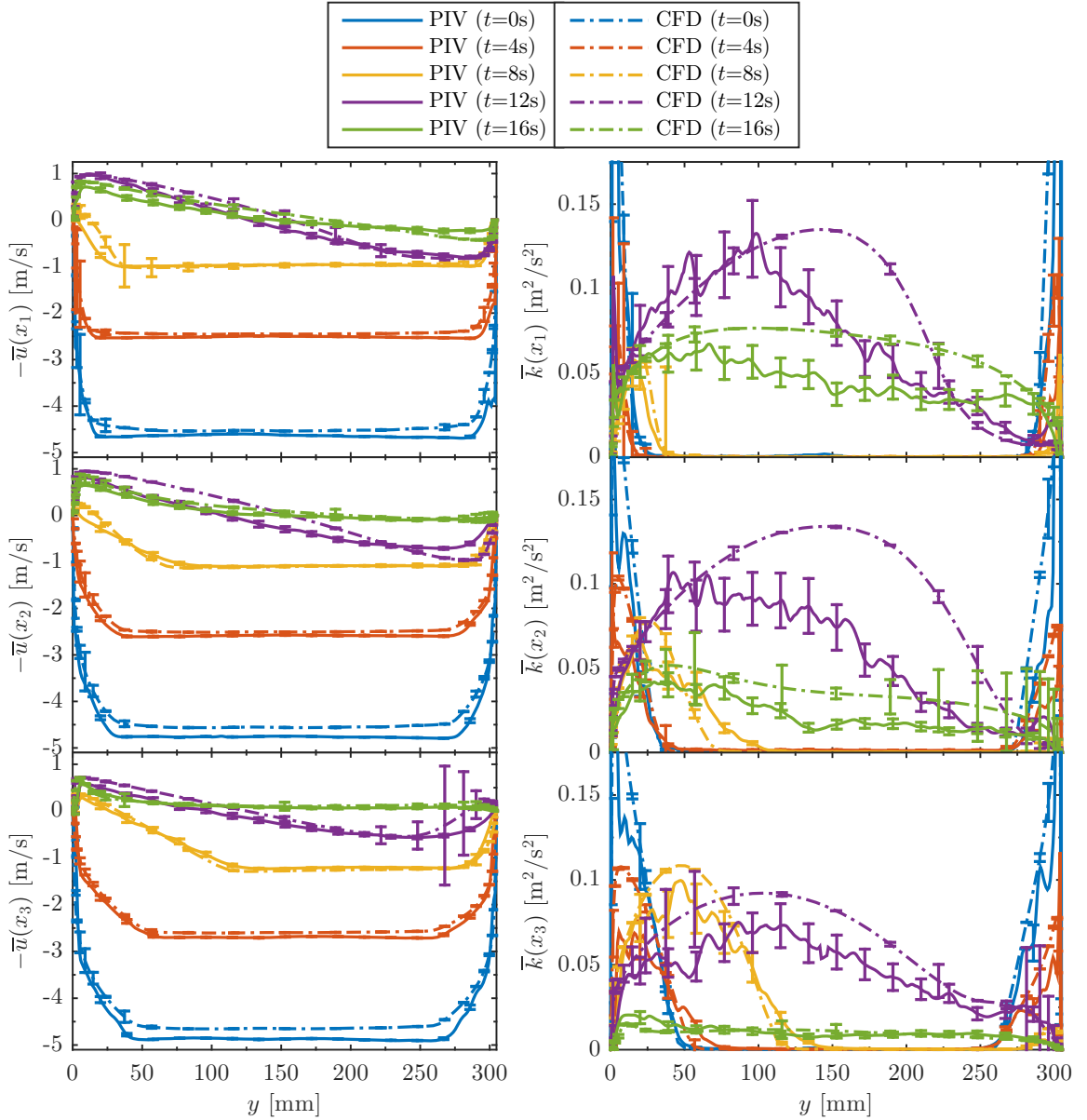


Fig. A.2: The streamwise velocity \bar{u} and turbulent kinetic energy \bar{k} for both PIV and CFD results

The streamwise velocity \bar{u} profiles from PIV and CFD show acceptable consistency through the transient.

The boundary layer thickness increases in the streamwise direction x at the initial condition as expected. There is a small difference in the bulk velocity in PIV and CFD results at this initial condition, perhaps due to a discrepancy in the inflow velocity mapping in the direction not measured. Any errors here are not inherent in the experimental BCs as inflow mapping is left to the modeler. The velocity profile shape generally remains similar but is reduced in magnitude during the first four seconds. At $t = 8$ s, the contribution from natural convection begins affecting the profiles near the heated wall ($y = 0$). At $t = 12$ s the profiles show a strong influence from natural convection. The large uncertainty bands for x_3 and large y are from the flow reversal phenomena not being mesh converged locally in the CFD. The changes from $t = 12 - 16$ s are subtle as steady natural convection is reached. The uncertainty bands are generally small on both PIV and CFD results and do not overlap, suggesting remaining model form uncertainty which is not represented nor easily quantified.

The results for turbulent kinetic energy \bar{k} are similar but have greater spatial variability and uncertainty. Initially \bar{k} is elevated near both walls as expected. The influence of natural convection increases \bar{k} near the heated wall initially. The area of elevated \bar{k} moves away from this wall over time. The phase of $t = 12$ s has the highest levels, likely from the chaotic flow reversal. The final measured state has reduced kinetic energy and may still be decreasing. Similar to streamwise velocity, the uncertainty bands generally do not overlap suggesting remaining model form uncertainty.

The uncertainty bands on CFD data are from the grid convergence study and are presented at the 95% confidence level. Particle Image Velocimetry (PIV) uncertainties are from the Uncertainty Surface Method and consider bias uncertainty from particle displacement, particle image density, particle image size, and shear originally described in [7] and improved upon with methods from [8]. Precision uncertainty was calculated by methods of Wilson & Smith [9]. Total uncertainty was calculated by the root-sum-square of the bias and precision uncertainties at the 95% confidence level.

Results for the scalars of wall heat flux and wall shear stress are shown in Fig. A.3 at the same three x locations, through time, with their associated uncertainty bands. The experimental heat flux came from the Heat Flux Sensors (HFSs) using the manufacturer-calibrated sensitivity. The uncertainty included 5% bias while the random values were measured. The heat flux results of the experiment and CFD are not in good agreement. The experimental results from the HFSs show a low sensitivity to convection due to the thermal capacitance of the heated wall, but the CFD had no capacitance modeled. Also, the CFD mesh was not well refined when considering heat flux as noted by large uncertainty bands during some phases of the transient and some physical locations. Further efforts should be made in CFD to model capacitance and refine the mesh. Wall shear has better agreement between PIV and CFD results. The experimental measurements are

somewhat noisy at high levels of shear, likely from the decreased accuracy of PIV data near walls and the relatively fewer points included in the fit. When the shear decreases, more points can be used in the fit for smoother results. The uncertainty bands on the CFD results suggest that the mesh was well resolved for shear, but again not as well in regions in space and time of flow reversal near the heated wall.

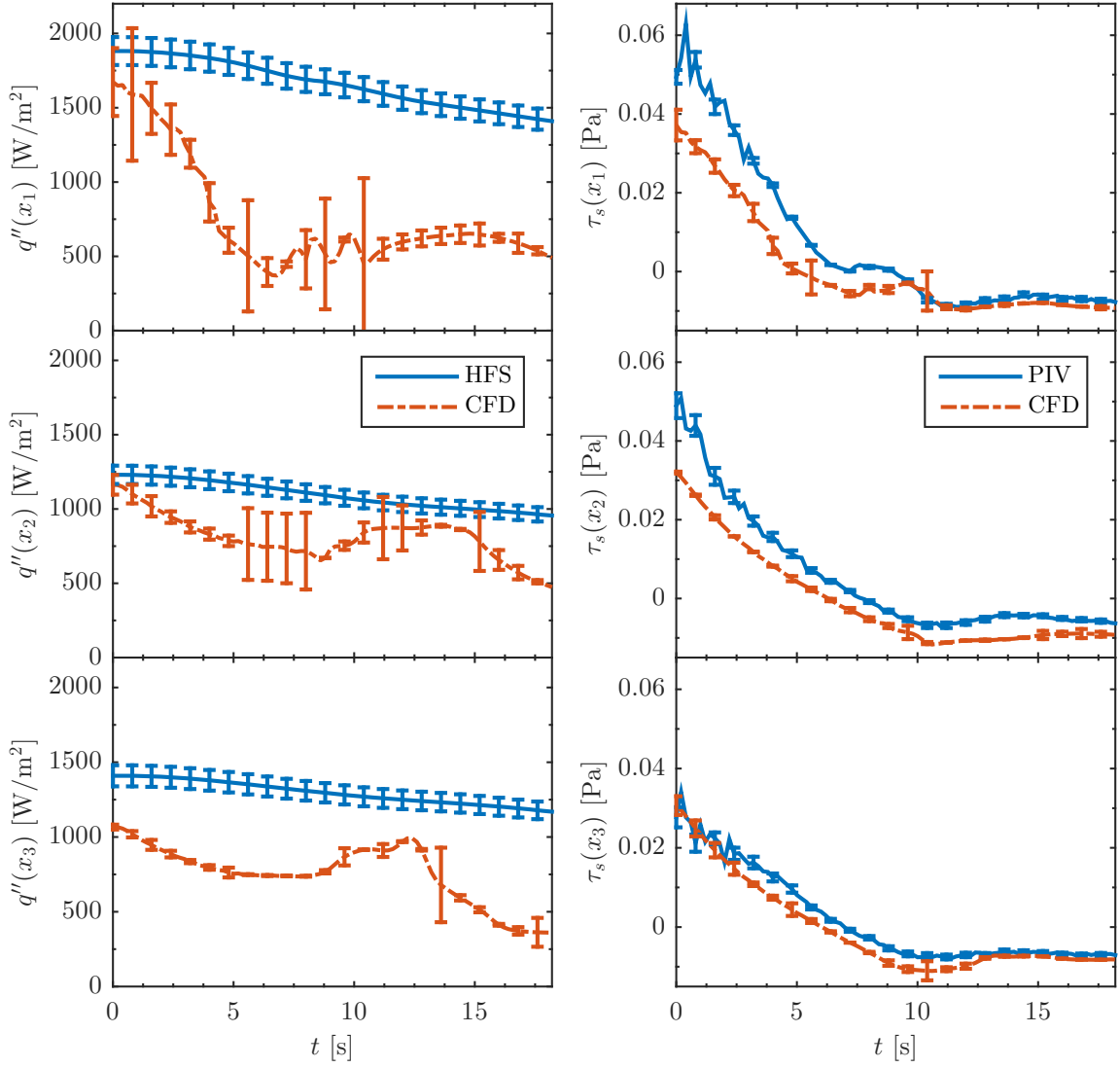


Fig. A.3: The heated wall heat flux and wall shear stress plotted over time

A.4 Conclusions

Simulations were run by the experimenter using the measured BCs. These activities confirmed the BCs

were complete and formatted properly. The simulation used commercial software Star-CCM+ that ran the URANS simulations in three-dimensions. Convergence criteria were strict. A grid convergence study was performed to estimate numerical uncertainty. Experimental results and simulation outputs were plotted on the same axes with uncertainty bands on each. This comparison can help identify simulation errors. With further work, simulation uncertainty could be quantified with the data in this study. On the other hand, the complicated nature of the data make this process challenging as the data cover two dimensions in space and one in time.

Appendix B

Processing and Post-processing Codes

B.1 Introduction

The purpose of this work was to provide validation data for computational fluid dynamics simulations. Therefore, meaningful data, their correct treatment, and proper reduction were crucial. Some have said that all raw data should be available for validation studies. In some instances this is the best approach. But there is danger in presenting raw data acquired with modern experimental techniques as the data become 1) overwhelmingly large and 2) very complicated quickly.

To address the first issue, overwhelmingly large data, it is easy to understand with examples from this work. The main measurement technique was Particle Image Velocimetry (PIV) which measured velocity fields in planes. Each plane often has at least 10,000 vectors, each with two components in the case of two-component PIV as used in this work. The uncertainty of each vector component was also quantified, doubling the data stored. A single acquisition is insufficient for averaging in time, so often 1000 acquisitions were performed for each data set. Each case included about ten sets, and there were several repeats of the data. Furthermore, the transient case had 101 phases measured. So it's easy to see how the number of data points can easily reach into the billions. These, with the many PIV images acquired, comprise several TB of space. Backing up and sharing these data becomes difficult very quickly.

With modern techniques, misinterpreting the meaning of the data is a real possibility that could have significant consequences. For instance, in nuclear reactor thermal-hydraulics, simulations are often used to assess the safety of designs in transient accident scenarios. If, in the validation of these codes, experimental data were misinterpreted, code predictions may be trusted when they shouldn't. The PIV data in this study were saved in a proprietary format that was difficult to analyze without commercial software. If a researcher were to attempt to fill the knowledge gaps, mistakes are very plausible. Data post-processing techniques are another form of complexity that may make the data misinterpreted.

In conclusion, the sharing of data is crucial to CFD validation. The data should be carefully reduced to a meaningful form and be presented in a concise way. This reduces the burden of both large data and

the complexities associated with modern measurement techniques. Data averages, fluctuations, and the uncertainty in both (with confidence level used) should be included whenever possible. A global coordinate system should be defined and included with all BC and SRQ data. Units should always be included. Any codes and/or procedures for data processing and post-processing should always be included for future reference. As such, the MATLAB codes used in this work are described and available for download through digitalcommons.usu.edu/all_datasets/8/. All of the codes may be downloaded in a single zipped file [Codes](#). If any of these codes are used for future works, a proper citation is required.

B.2 Particle Image Velocity Uncertainty

The methods and code to calculate PIV uncertainty used throughout this work were developed by others [7–9]. They were customized only slightly to plot data parameters such as particle image diameter, density, and shear relative to the range in the look-up table in the Uncertainty Surface Method. The process of quantifying the uncertainty began with creating synthetic images with known image parameters with [SIG_parallel_New_4x32x32_75%_Round_2.m](#) that contains the parameters used in this work. These images were processed in DaVis with the same steps as the data of interest. Then an uncertainty surface generator was used to read the synthetic image parameters, the velocity results from DaVis, and create an uncertainty surface with [DaVisSurfaceGeneratorFo.m](#). The uncertainty surface used in this work was [Uncertainty_4x32x32_75%_Round_PostProc_2_Used.mat](#) associated with the DaVis PIV processing settings in [Uncertainty_4x32x32_75%_Round_PostProc_2.xml](#). The code [surfaceViewer.m](#) was written to view the uncertainty surface. The uncertainty code was [PIVuncertaintyCode.m](#) with associated [PIVuncertaintyGUI.m](#) and [PIVuncertaintyGUI.fig](#). Some dependent functions of these codes were [DiaDen2.m](#) and [PIV_Stats.m](#), the latter of which had plotting capabilities added. In the steady work, the GUI was used to configure uncertainty calculation jobs and call the appropriate functions. Because the transient data had very many sets to be analyzed, this manual setup was impractical. The code [PIVuncertainty_TransientDriver2.m](#) was written to call the uncertainty code in a batch mode with much less time required by the user, at least when the file paths follow the pattern within this work. One [*Stats.m](#) file for each data set would be created that included data for the ensemble-average, Reynolds stresses, and the associated uncertainties of each. One code that will plot the nominal data and uncertainties of a given [*Stats.m](#) file was called [Plot_Uncertainties.m](#).

Since the time of this work, commercial PIV codes have included uncertainty calculations that are much easier to use and are often more accurate [10–12]. Another set of codes independent from the first was written by others to calculate only the particle image diameter and density. This set remains useful for these

parameters as they are not available in known commercial software. They are in [DiaDen2.m](#), [PIVdiaden.m](#) with the associated [PIVdiadenGUI.m](#) and [PIVdiadenGUI.fig](#).

B.3 Inlet Analysis

As mentioned in this work, the inflow was measured with PIV in several planes. Several codes were written to map these velocities in space appropriately by taking single rows of data and matching them with global coordinates. The formatting is compatible as an input to commercial CFD code Star-CCM+. The code for the steady work was [InletAnalysisAndProfilesFromStats6_1.m](#) and for the transient work was [InletAnalysisAndProfilesFromStats_Transient_6_4.m](#). Another code was written to visualize the output of this code as a filled contour plot with superimposed lines to depict where data were acquired in [PlotVelocityInletContour_2.m](#).

B.4 Boundary Condition Statistics

In addition to the inflow BC data, boundary temperatures were included in several sets of files. These sets of files could be analyzed for time means and uncertainties with [BC_Stats2_2.m](#) for the steady work and ensemble-averaging and uncertainties with [BC_Stats_Transient.L.m](#) for the transient work. These codes also performed these calculations on the HFS heat flux results as they were recorded at the same time. Outlier detection and rejection was performed with the transient version.

B.5 Interpolation Codes for Boundary Conditions

The inflow velocity data could be interpolated or ‘mapped’ onto a fine grid for use in CFD by [ToStarInterpolator4_4.m](#) and [ToStarInterpolator_Transient_5_3.m](#). Also the heated wall temperatures could be interpolated by [TemptoStar.m](#).

B.6 Virtual Origin

The virtual origin analysis was performed for the steady case using velocity data at the inlet in [InletVirtualOrigin.m](#).

B.7 System Response Quantity Analysis

The averaged SRQs were analyzed with [SteadySRQ_Plots_2_8.m](#) and [TransientSRQ_Plots_2_8.m](#) as well as [SteadySRQ_Plots_HeatFlux_2_3.m](#). These codes called the functions [PIV_dudy.m](#) and [LineFitFunc.m](#) to

estimate wall shear from velocity data. The code [InstantVelAnalysis.m](#) made histograms and scatter plots from instantaneous PIV data.

B.8 Transient Image Organization

The transient PIV data had a series of image pairs recorded for each run. For a given set of parameters, 101 image pairs were recorded and this was repeated for 100 or 200 runs. For proper ensemble-averaging, these data needed to be organized in 101 folders with 100 or 200 image pairs in each. The code [TransientImageOrganization_2.3.m](#) was used for this purpose. Acquisition of PIV data had inconsistent start times caused by variable delay in the PIV timing system. This delay was recorded by the master LabVIEW program and used in the organization code to properly align the data in phase. Also, outlier detection was performed on spatial averaged streamwise velocities to compensate for timing jitter with the code [Transient_OutlierDetetion.m](#) and data for subsequent runs were removed from further analysis.

B.9 Transient Computational Fluid Dynamics Grid Convergence Index

Unsteady RANS models were performed to accompany the transient work. These simulations were performed on three grids for a grid convergence study using Roache's modified method [5,6]. The four SRQ outputs from the CFD were exported at each time step associated with data acquisition in the experiment. The code [TransientCFD_GCI.m](#) read the data from the CFD simulations on all three meshes, performed the analysis, and saved the CFD SRQ data in an output file with uncertainties at the 95% confidence level.

B.10 TC Probe Analysis

The work involving the TC probe had unique codes used to analyze these results. The analysis used to estimate measurement errors from conduction losses within the probe was performed in [ConductionAnalysis2.m](#). The measured temperature profiles were analyzed and line fitted in [TempProfileAnalysis_y0_yPlusMax_loop_2.3.m](#). The heat flux results from HFSs and the TC probe, with predicted flux from correlations, were in [SteadySRQ_Plots_HeatFlux_TC_Probe.m](#).

B.11 Custom Functions

Several custom functions were used with many being written by others. Occasionally these were modified for more desired results. These included [columnlegend2.m](#), [csvwrite_with_headers.m](#), [line_fewer_markers.m](#), [sort_nat.m](#), [subtightplot.m](#), [tightfig.m](#), [tightfig2_1.m](#), [TrimToMask.m](#), and [uigetfile_n_dir.m](#).

Appendix C

Mixed Convection Parameters

Several nondimensional numbers for mixed convection are included in the following MathCAD document. Also heat transfer correlations were used for estimates. All parameters are local for the given value of x defined near the top.

Properties

$$T_{\text{inf}} := (20 + 273.15)\text{K} \quad T_{\text{plate}} := (138.6 + 273.15)\text{K} \quad T_f := \frac{T_{\text{plate}} + T_{\text{inf}}}{2} = 352.45\text{K}$$

$$L_{\text{ww}} := 74.25\text{in} \quad w_{\text{plate}} := 11\text{in} \quad A_{\text{plate}} := L \cdot w_{\text{plate}} = 0.527\text{m}^2$$

Fluid Properties at 75 deg C from Fluid Mechanics, Cengel and Cimbala

$$\beta := \frac{1}{T_f} = 2.837 \times 10^{-3} \frac{1}{\text{K}} \quad \nu := 2.046 \cdot 10^{-5} \frac{\text{m}^2}{\text{s}} \quad \text{Pr} := 0.7166 \quad k := 0.02917 \frac{\text{W}}{\text{m} \cdot \text{K}}$$

Choose the appropriate x

$$x_{\text{xx}} := 6.3675\text{in} \quad x := 30.6175\text{in} \quad x_{\text{xx}} := 54.8675\text{in} \quad x_{\text{xx}} := 74.25\text{in}$$

Free Convection

$$\text{Gr}_x := \frac{g \cdot \beta \cdot (T_{\text{plate}} - T_{\text{inf}}) \cdot x^3}{\nu^2} = 3.335 \times 10^7$$

$$\text{Ra}_x := \text{Pr} \cdot \text{Gr}_x = 2.39 \times 10^7$$

$$\text{Nu}_N := \left[0.825 + \frac{0.387 \cdot \text{Ra}_x^{\frac{1}{6}}}{\left[1 + \left(\frac{0.492}{\text{Pr}} \right)^{\frac{9}{16}} \right]^{\frac{8}{27}}} \right]^2 = 40.13$$

$$h_{\text{nat}} := \frac{k \cdot \text{Nu}_N}{L} = 0.621 \cdot \frac{\text{W}}{\text{m}^2 \cdot \text{K}}$$

Forced Convection

Bulk velocity u taken mean of u column in Inlet-uvw-interp.csv

$$u_{\text{ww}} := 2.44 \frac{\text{m}}{\text{s}} \quad u := 4.32 \frac{\text{m}}{\text{s}}$$

$$\text{Re}_x := \frac{u \cdot x}{\nu} = 1.929 \times 10^4$$

$$Nu_F := 0.664 \cdot Re_x^{\frac{1}{2}} \cdot Pr^{\frac{1}{3}} = 82.522$$

$$Ar_x := \frac{Gr_x}{Re_x^2} = 0.09$$

$$h_{forced} := \frac{k \cdot Nu_F}{L} = 1.276 \cdot \frac{W}{m^2 K}$$

Mixed Convection

$$Nu_{mixed} := \left(Nu_F^3 + Nu_N^3 \right)^{\frac{1}{3}} = 85.571$$

$$h_{mixed} := \frac{k \cdot Nu_{mixed}}{L} = 1.324 \cdot \frac{W}{m^2 K}$$

$$q_{mixed} := A_{plate} \cdot h_{mixed} \cdot (T_{plate} - T_{inf}) = 82.713 \text{ W}$$

$$q''_{mixed} := \frac{q_{mixed}}{A_{plate}} = 156.971 \cdot \frac{W}{m^2}$$

Another Correlation from the Handbook of Single-phase Convective Heat Transfer by Kakac, Shah, and Aung; Eqn 14.43:

$$c := 0.36 \quad \text{for vertical plates}$$

$$n := 3$$

$$F(Pr) := 0.0287 \cdot Pr^{0.6}$$

$$G(Pr) := 0.15 \cdot Pr^{\frac{1}{3}} \left[1 + \left(\frac{0.492}{Pr} \right)^{\frac{9}{16}} \right]^{\frac{-16}{27}}$$

$$Nu_x := F(Pr) \cdot Re_x^{\frac{4}{5}} \left[1 + c \cdot \left[\frac{G(Pr)}{F(Pr)} \left(\frac{Gr_x}{Re_x^{\frac{12}{5}}} \right)^{\frac{1}{3}} \right]^n \right]^{\frac{1}{n}} = 63.83$$

Appendix D

Heated Wall Conduction Analysis

The one-dimensional conduction analysis by thermal resistance network is provided in the following MathCAD document. It was used to determine the thermal resistance by conduction path going through HFSs and non-HFSs paths. The error by non-uniform resistance was estimated. The error was originally 2.4%, but with an updated thermal conductivity of Cirlex[®] (laminated Kapton[®]), was estimated to be -17.5%.

Thermal Circuit to determine heat flux difference inside Heated Plate from different conduction paths

Assume Base temperature of $T_{\text{base}} := 413.15\text{K}$ (140 C)

and Surface temperature of $T_s := 410.15\text{K}$ (137 C)

Define Thicknesses and Thermal Conductivities

Surface plate, Aluminum 2024 $t_{\text{surface}} := 0.125\text{in}$ $k_{\text{surface}} := 141 \frac{\text{W}}{\text{m}\cdot\text{K}}$

Total thickness of adhesive in combination with HFS or Cirlex $t_{\text{total}} := 0.05\text{in}$

Heat Flux Sensor $t_{\text{HFS}} := 0.013\text{in}$ $k_{\text{HFS}} := 0.156 \frac{\text{W}}{\text{m}\cdot\text{K}}$

Cirlex $t_{\text{Cirlex}} := 0.010\text{in}$ $k_{\text{Cirlex}} := 0.12 \frac{\text{W}}{\text{m}\cdot\text{K}}$

updated k for Cirlex from Fralock and Katco $k_{\text{Cirlex}} := 0.17 \frac{\text{W}}{\text{m}\cdot\text{K}}$

Adhesive layer over HFS $t_{\text{ad_HFS}} := t_{\text{total}} - t_{\text{HFS}} = 0.037\text{in}$

Adhesive layer over Cirlex $t_{\text{ad_Cirlex}} := t_{\text{total}} - t_{\text{Cirlex}} = 0.04\text{in}$

$k_{\text{ad}} := 1.0 \frac{\text{W}}{\text{m}\cdot\text{K}}$

Base Metal, Aluminum 6061 $t_{\text{base}} := 0.25\text{in}$ $k_{\text{base}} := 167 \frac{\text{W}}{\text{m}\cdot\text{K}}$

Thermal Circuit Analysis

$$V = I \cdot R \quad T_1 - T_2 = q'' \cdot R'' \quad q'' = \frac{T_1 - T_2}{R''}$$

Consider two parallel paths and compare thermal resistance and heat flux

$$R''_{\text{HFS}} := \frac{t_{\text{base}}}{k_{\text{base}}} + \frac{t_{\text{HFS}}}{k_{\text{HFS}}} + \frac{t_{\text{ad_HFS}}}{k_{\text{ad}}} + \frac{t_{\text{surface}}}{k_{\text{surface}}} = 3.117 \times 10^{-3} \cdot \frac{\text{m}^2\text{K}}{\text{W}}$$

$$R''_{\text{Cirlex}} := \frac{t_{\text{base}}}{k_{\text{base}}} + \frac{t_{\text{Cirlex}}}{k_{\text{Cirlex}}} + \frac{t_{\text{ad_Cirlex}}}{k_{\text{ad}}} + \frac{t_{\text{surface}}}{k_{\text{surface}}} = 2.571 \times 10^{-3} \cdot \frac{\text{m}^2\text{K}}{\text{W}}$$

$$q''_{\text{HFS}} := \frac{T_{\text{base}} - T_s}{R''_{\text{HFS}}} = 962.461 \cdot \frac{\text{W}}{\text{m}^2}$$

$$q''_{\text{Cirlex}} := \frac{T_{\text{base}} - T_s}{R''_{\text{Cirlex}}} = 1.167 \times 10^3 \cdot \frac{\text{W}}{\text{m}^2}$$

$$\frac{q''_{\text{HFS}}}{q''_{\text{Cirlex}}} = 0.825$$

Error on k_{Cirlex} with a Measured Error From the Design of Experiments Analysis

$$\frac{q''_{\text{Cirlex}}}{q''_{\text{HFS}}} = \frac{T_1 - T_2}{R''_{\text{Cirlex}}} \cdot \frac{R''_{\text{HFS}}}{T_1 - T_2} = \frac{R''_{\text{HFS}}}{R''_{\text{Cirlex}}} = \frac{\frac{t_{\text{base}}}{k_{\text{base}}} + \frac{t_{\text{HFS}}}{k_{\text{HFS}}} + \frac{t_{\text{ad_HFS}}}{k_{\text{ad}}} + \frac{t_{\text{surface}}}{k_{\text{surface}}}}{\frac{t_{\text{base}}}{k_{\text{base}}} + \frac{t_{\text{Cirlex}}}{k_{\text{Cirlex}}} + \frac{t_{\text{ad_Cirlex}}}{k_{\text{ad}}} + \frac{t_{\text{surface}}}{k_{\text{surface}}}} = E$$

Solving for k_{Cirlex}

$$k_{\text{Cirlex_Corrected}} := t_{\text{Cirlex}} \cdot \left[\left(\frac{t_{\text{base}}}{k_{\text{base}}} + \frac{t_{\text{HFS}}}{k_{\text{HFS}}} + \frac{t_{\text{ad_HFS}}}{k_{\text{ad}}} + \frac{t_{\text{surface}}}{k_{\text{surface}}} \right) \cdot \frac{1}{E} \dots \right]^{-1} + \left(\frac{t_{\text{base}}}{k_{\text{base}}} + \frac{t_{\text{ad_Cirlex}}}{k_{\text{ad}}} + \frac{t_{\text{surface}}}{k_{\text{surface}}} \right)$$

$$k_{\text{Cirlex_Corrected}} = 0.162 \cdot \frac{\text{W}}{\text{m} \cdot \text{K}} \quad \frac{k_{\text{Cirlex_Corrected}}}{k_{\text{Cirlex}}} = 0.955$$

The thermal conductivity k of the original Cirlex would have to be off by 35% to have an 18% error. This seems unlikely.

The updated k_{Cirlex} could be off by 4.5%, which suggests that its value is pretty close.

Appendix E

Permission Letter for Steady Mixed Convection Work

Jeff Harris

PO Box 30
State College, PA 16801
Phone: 814-863-3025

► **Utah State University**

Old Main Hill
Logan, UT 84322
Phone: 435-797-1000

To whom it may concern:

The paper *Experimental Validation Data for CFD of Mixed Convection on a Vertical Flat Plate* written by Blake Lance, Barton Smith, and myself may be used to fulfil the dissertation and graduation requirements of the first author.

Respectfully,
Jeff Harris
Research Associate
The Pennsylvania State University
8/6/2015

References

- [1] CD-Adapco, Melville, NY, *Star-CCM+ User Guide*, 9.06 ed.
- [2] Versteeg, H. K., and Malalasekera, W., 2007, *An Introduction to Computational Fluid Dynamics*, Prentice Hall.
- [3] Davidson, L., Nielsen, P., and Sveningsson, A., October 12-17, 2003, “Modifications of the $\overline{v^2} - f$ Model for Computing the Flow in a 3D Wall Jet,” Proceedings of the International Symposium on Turbulence, Antalya, Turkey.
- [4] Moutaouakil, L. E., Zrikem, Z., and Abdelbaki, A., 2014, “Performance of Various RANS Eddy-viscosity Models for Turbulent Natural Convection in Tall Vertical Cavities,” *Heat Mass Transfer*, **50**(8), pp. 1103–1113, doi:[10.1007/s00231-014-1322-4](https://doi.org/10.1007/s00231-014-1322-4).
- [5] Roache, P. J., 1997, “Quantification of Uncertainty in Computational Fluid Dynamics,” *Annual Review of Fluid Mechanics*, **29**(1), pp. 123–160, doi:[10.1146/annurev.fluid.29.1.123](https://doi.org/10.1146/annurev.fluid.29.1.123).
- [6] Oberkampf, W. L., and Roy, C. J., 2010, *Verification and Validation in Scientific Computing*, Cambridge University Press, doi:[10.1017/cbo9780511760396](https://doi.org/10.1017/cbo9780511760396).
- [7] Timmins, B. H., Wilson, B. W., Smith, B. L., and Vlachos, P. P., 2012, “A Method for Automatic Estimation of Instantaneous Local Uncertainty in Particle Image Velocimetry Measurements,” *Experiments in Fluids*, **53**(4), pp. 1133–1147, doi:[10.1007/s00348-012-1341-1](https://doi.org/10.1007/s00348-012-1341-1).
- [8] Warner, S. O., and Smith, B. L., 2014, “Autocorrelation-based Estimate of Particle Image Density for Diffraction Limited Particle Images,” *Measurement Science and Technology*, **25**(6), p. 065201, doi:[10.1088/0957-0233/25/6/065201](https://doi.org/10.1088/0957-0233/25/6/065201).
- [9] Wilson, B. M., and Smith, B. L., 2013, “Taylor-series and Monte-Carlo-method Uncertainty Estimation of the Width of a Probability Distribution Based on Varying Bias and Random Error,” *Meas. Sci. Technol.*, **24**(3), p. 035301, doi:[10.1088/0957-0233/24/3/035301](https://doi.org/10.1088/0957-0233/24/3/035301).
- [10] LaVision, 2015, “DaVis,” Version 8.2.
- [11] Wieneke, B., 2015, “PIV Uncertainty Quantification from Correlation Statistics,” *Measurement Science and Technology*, **26**(7), doi:[10.1088/0957-0233/26/7/074002](https://doi.org/10.1088/0957-0233/26/7/074002).
- [12] Sciacchitano, A., Neal, D. R., Smith, B. L., Warner, S. O., Vlachos, P. P., Wieneke, B., and Scarano, F., 2015, “Collaborative Framework for PIV Uncertainty Quantification: Comparative Assessment of Methods,” *Measurement Science and Technology*, **26**(7), doi:[10.1088/0957-0233/26/7/074004](https://doi.org/10.1088/0957-0233/26/7/074004).

Vita

Blake W. Lance**Curriculum vitae****CONTACT
INFORMATION**

Blake Lance
29 Aggie Vlg Apt G
Logan UT 84341

Work: 435-797-8147
Cell: 435-512-7968
E-mail:
b.lance@aggiemail.usu.edu
LinkedIn.com/in/BlakeLance

**EDUCATION &
TRAINING****Utah State University**, Logan UT

Ph.D., Mechanical & Aerospace Engineering, Sept. 2015 GPA: 4.0

- Dissertation Topic: "Steady and Transient Mixed Convection on a Vertical Flat Plate for CFD Validation"
- Adviser: Professor Barton L. Smith

M.S., Mechanical & Aerospace Engineering, 19 Sept. 2012 GPA: 3.91

- Thesis Topic: "Using Stereo Particle Image Velocimetry to Quantify and Optimize Mixing in an Algae Raceway Using Delta Wings"
- Advisers: Department Head Byard Wood & Professor Barton L. Smith
- Magna cum Laude

B.S., Mechanical & Aerospace Engineering, 15 Dec. 2012 (Concurrent w/M.S.)
GPA: 3.90

- Magna cum Laude
- Minor in Mathematics

Advanced Studies Institute, Los Alamos National Lab, Los Alamos, NM, April-May 2015

- Developed practical research planning and proposal writing skills
- Learned from technology experts in many fields on advanced scientific topics
- Worked on a multi-disciplinary team to plan research and write a proposal

Modeling, Experimentation, and Validation (MeV) Summer School, Idaho National Lab, Idaho Falls, ID, July 2014

- Learned from experts in the field of Nuclear Reactor Safety over the 10-day course
- Contributed greatly to group paper and presentation
- Earned Best Group Presentation Award

ASME Verification, Validation, and Uncertainty Quantification in Fluid Dynamics and Heat Transfer Workshop, Bill Oberkampf & Christopher Roy, Las Vegas, NV, May 2014

- Learned theory and best practices from two leading experts in the VVUQ field

AWARDS**Fellowship**

- Nuclear Regulatory Commission Fellowship, 2012–2016

Scholarships

- Nuclear Regulatory Commission Scholarship, 2009–2011
- Presidential Scholarship, USU, 2004
- Community Scholarship, Sam Walton Corporation, 2004

Recognitions

- Outstanding Ph.D. Researcher, Mechanical & Aerospace Engineering (MAE), 2015

- Outstanding Undergraduate Researcher, MAE, 2011
- Tau Beta Pi Engineering Honor Society Membership, 2009
- Academic Excellence Award, MAE, 2009–2011
- A-Pin Awarded for Academic Excellence, MAE, 2008
- Lundberg Excellence Award, MAE, 2007–2009
- Dean's List, Utah State University (USU), 2004–2008

RESEARCH EXPERIENCE

Utah State University, Logan UT

Graduate Research Assistant

August 2012 to Present

- Ph.D. Dissertation: "Transient Convection from Forced to Natural with Flow Reversal for CFD Validation"
- Funding: DOE Office of Nuclear Energy's Nuclear Energy University Programs
- Major Professor: Dr. Barton L. Smith
- Activities:
 - Performed validation experiments using specialized Rotatable Buoyancy Tunnel at USU
 - Acquired velocity data using Particle Image Velocimetry (PIV) and best practices
 - Developed detailed instrumentation and control hardware and software
 - Developed data post-processing codes for organizing, reduction, and plotting data
 - Developed validation database for Computational Fluid Dynamics (CFD) models
 - Ran CFD simulations in commercial package using best practices
 - Performed grid convergence and sensitivity studies and validated with experimental data
 - Advised undergraduate research assistants on experimental setup and execution, code development, and database management

Graduate Research Assistant

August 2011 to August 2012

- Masters Thesis: "Using Stereo Particle Image Velocimetry to Quantify and Optimize Mixing in an Algae Raceway Using Delta Wings"
- Funding: US Department of Energy (Grant Number DE-EE0003114)
- Co-Major Professors: Dr. Byard Wood & Dr. Barton L. Smith
- Activities:
 - Quantified fluid mixing enhancement in scaled raceway with PIV by use of delta wings
 - Performed optimization study on wing configuration and raceway fluid speed to potentially increase algae productivity and reduce operation costs
 - Developed Stereo PIV expertise in water
 - Performed power measurement on three-phase, pulsed power
 - Advised undergraduate research assistants on experimental setup and execution

Utah State University, Logan UT

Undergraduate Researcher

May 2009 to May 2011

- Designed, built, and tested heated and instrumented plate for CFD validation experiments on Rotatable Buoyancy Tunnel (RoBuT)
- Assisted in the design and implementation of the RoBuT facility at USU
- Designed, built, and tested reference heat flux generator for sensor calibration
- Assisted others in the execution, troubleshooting, and data analysis of experiments
- Completed coding project modifying commercial code

TEACHING EXPERIENCE **Utah State University**, Logan UT
 Graduate Teaching Assistant **August 2011 to December 2011**

- Assisted 100 students in learning the concepts of Thermodynamics II
- Tutored during weekly recitation and office hours
- Consistently graded homework every week

PROFESSIONAL EXPERIENCE **Sandia National Laboratories**, Albuquerque NM
 Graduate Student Intern **May 2013 to November 2014**

- Configured unsteady experiment for phase locked data acquisition in oscillatory water tunnel
- Performed first known statistical analysis for coherent turbulent structures in oscillating flow
- Acquired experimental data independently and on schedule
- Demonstrated best practices for data acquisition and processing

Apogee Instruments, Logan UT
 Mechanical Engineering Intern **May 2011 to August 2011**

- Improved design of Aspirated Radiation Shield through heat transfer analyses
- Contributed to several R&D projects in multi-disciplinary groups for new products
- Developed new products and manufacturing facilities, including solid model development

PEER-REVIEWED PAPERS & PRESENTATIONS –Lance, B., Harris, J., and Smith, B. “Experimental Validation Data for CFD of Mixed Convection on a Vertical Flat Plate,” *Journal of Fluids Engineering*, submitted September 2015.

–Lance, B. and Smith, B. “Transient Convection from Forced to Natural with Flow Reversal for CFD Validation,” 16th International Topical Meeting on Nuclear Reactor Thermal Hydraulics, August 30–September 4, 2015, Chicago, IL.

–Lance, B. and Smith, B. “Transient Convection from Forced to Natural with Flow Reversal for CFD Validation,” 2015 American Nuclear Society Annual Meeting, June 7-11, 2015, San Antonio, TX.

–Harris, J., Lance, B., and Smith, B. “Experimental Validation Data for Computational Fluid Dynamics of Forced Convection on a Vertical Flat Plate,” **138(1)**, *Journal of Fluids Engineering*, 2015, doi:10.1115/1.4031007.

–Lance, B. and Harris, J. “Mixed Convection Validation and Simulation,” American Nuclear Society 2014 Student Conference, April 3–5, 2014, State College, PA.

–Lance, B., Harris, J., Iverson, J., Spall, R., Johnson, R., and Smith, B., “Validation Study on Forced and Mixed Convection in the Rotatable Buoyancy Tunnel,” ASME 2013 Fluids Engineering Division Summer Meeting, July 7-11, 2013, Incline Village, NV, Paper Number 16214.

–Harris, J., Lance, B., and Smith, B., “Design of Apparatus for Validation Experiments,” American Nuclear Society Annual Meeting, June 16-20, 2013, Atlanta, GA.

–Harris, J., Lance, B., Spall, R., and Smith, B., “Transient Mixed Convection Validation Facility and Study,” The 15th International Topical Meeting on Nuclear Reactor Thermal Hydraulics (NURETH), May 12–16, 2013, Pisa, Italy, Paper Number 15-356.

–Harris, J., Lance, B., and Iverson, J., “Single Phase Forced Convection Validation and Simulation,” American Nuclear Society 2013 Student Conference, April 4–6, 2013, Boston, MA. ◦ **Awarded Best Overall Graduate Paper.**

INVITED
PRESENTATIONS

–Lance, B., “Transient Convection from Forced to Natural with Flow Reversal on a Vertical Flat Plate for CFD Validation,” VVUQ Colloquium at Sandia National Labs, Aug. 25, 2015, Albuquerque, NM.

–Lance, B. and Smith, B. “Particle Image Velocimetry and the Nuclear Field,” American Nuclear Society Chapter Lecture, Nov. 19, 2014, Logan, UT.

NON-REVIEWED
CONFERENCE
PRESENTATIONS

–Lance, B. and Smith, B. “Experimental Transient Convection from Forced to Natural with Flow Reversal for CFD Validation,” ASME 2015 Verification and Validation Symposium, May 11-15, 2015, Las Vegas, NV.

–Lance, B., Roberts, J., Kearney, S., and Smith, B. “Wall Shear Stress in Oscillating Channel Flow Using Particle Image Velocimetry,” 66th Annual Division of Fluid Dynamics Meeting of the American Physical Society, Nov. 24-26, 2013, Pittsburgh, PA.

–Harris, J., Lance, B., and Smith, B. “Experimental Validation Dataset for CFD Simulations of Buoyancy Opposed Convection,” 66th Annual Division of Fluid Dynamics Meeting of the American Physical Society, Nov. 24-26, 2013, Pittsburgh, PA.

–Smith, B., Lance, B., Harris, J., Iverson, J., and Spall, R. “The RoBuT Wind Tunnel for CFD Validation of Natural, Mixed, and Forced Convection,” ASME 2013 Verification and Validation Symposium, May 22-24, 2013, Las Vegas, NV.

–Harris, J., and Lance, B. “The Design and Implementation of Simulation Validation Experiments for Passive Cooling Features in Nuclear Reactors,” Utah State University Graduate Research Symposium, April 12, 2013, Logan UT. ◦ **Honorable Mention Award**

–Lance, B., Wood, B., and Smith, B., “Optimizing Open Raceway Design,” USTAR BioEnergy Summit, August 7, 2012, Logan, UT.

POSTER
PRESENTATIONS

–Lance, B., Wood, B., and Smith, B., “Optimizing Vertical Mixing in Algal Raceways Using Delta Wings,” Synthetic Biomanufacturing Institute Winter Meeting, January 29, 2013, Logan, UT.

–Lance, B., Wood, B., and Smith, B., “Optimizing Vertical Mixing in Algal Raceways Using Delta Wings,” Algae Biomass Summit, September 23-27, 2012, Denver, CO.

–Lance, B., and Smith, B., “Design of Heated and Instrumented Plate for Vertical Wind Tunnel,” Engineering Undergraduate Research Poster Symposium, October 2010, Logan, UT.

SPECIALIZED SKILLS

Experimental Experience:

- Calibration, data filtering, amplification, fourier transforms, cross-correlations, and uncertainty analysis
- Steady and unsteady 2-component and 3-component PIV in water and air
- Phase-locked data acquisition and analysis of transient and periodic experiments
- Data acquisition and systems control using LabVIEW
- Significant temperature measurement theory and practice
- Electrical circuit theory and design
- Laser alignment and safety practices

Numerical Experience:

- Significant data post-processing and plotting in FORTRAN and MATLAB on large data sets
- CFD modeling with FLUENT, Star-CCM+, and personal codes using RANS and URANS models
- High performance computing experience with personal and commercial codes using Linux clusters
- Finite element modeling with FEMAP and ALGOR
- Desktop computer assembly and repair

Computing Languages:

- FORTRAN, MATLAB, LabVIEW

Software Packages:

- Office, \LaTeX , SolidEdge, SolidWorks, MathCAD, FLUENT, STAR-CCM+, DaVis

SERVICE

Treasurer of USU Nuclear Club (Interim ANS Chapter)

- Was elected to the first executive council of interim ANS Chapter at USU
- Prepared activities and official petition to gain official chapter recognition
- Performed public outreach at Engineering Week Community Night

Clerk in local church organization

- Recorded minutes of meetings and submitted performance reports
- Kept member and financial records
- Trained and supervised other clerks
- Coordinated schedules and prepared meeting agendas

Volunteer Amateur Radio Operator

- Provided volunteer communications for church organization and athletic events
- Built radio equipment systems for emergency operations
- Initiated and organized class for public to acquire licenses and learn operating practices

Boy Scouts of America Eagle Scout Award

- Prepared 80 personal chalkboards for humanitarian education kits
- Managed several groups of volunteers and raised funds for materials
- Learned life skills and personal management

Jeff R. Harris

Department of Mechanical and
Aerospace Engineering,
Utah State University,
Logan, UT 84322
e-mail: jeff.harr@aggiemail.usu.edu

Blake W. Lance

Department of Mechanical and
Aerospace Engineering,
Utah State University,
Logan, UT 84322
e-mail: b.lance@aggiemail.usu.edu

Barton L. Smith

Professor
Fellow ASME
Department of Mechanical and
Aerospace Engineering,
Utah State University,
Logan, UT 84322
e-mail: barton.smith@usu.edu

Experimental Validation Data for Computational Fluid Dynamics of Forced Convection on a Vertical Flat Plate

A computational fluid dynamics (CFD) validation dataset for turbulent forced convection on a vertical plate is presented. The design of the apparatus is based on recent validation literature and provides a means to simultaneously measure boundary conditions (BCs) and system response quantities (SRQs). All important inflow quantities for Reynolds-Averaged Navier-Stokes (RANS) CFD are also measured. Data are acquired at two heating conditions and cover the range $40,000 < Re_x < 300,000$, $357 < Re_{\delta_2} < 813$, and $0.02 < Gr/Re^2 < 0.232$. [DOI: 10.1115/1.4031007]

1 Introduction

The primary purpose of this work is to generate and disseminate experimental data for CFD validation for forced convection on a vertical plate. In addition, some features and differences of buoyancy aided and opposed forced convection will be discussed.

This facility, instrumentation, and measurements are described in detail. The SRQs include the heat flux from the plate at three locations and the velocity field over the heated plate (including wall shear stress) at the same three locations. All inputs required for the numerical model, including BCs, inflow velocity, and temperature and material properties are measured. All SRQs, BCs, and inflow data may be accessed using data in the supplemental results which are available under “Supplemental Data” tab for this paper on the [ASME Digital Collection](#). The data and descriptions required to satisfy the completeness level (as outlined in Ref. [1]) for the validation data are also provided along with some description included in this document and in the Supplemental results which are available under “Supplemental Data” tab for this paper on the [ASME Digital Collection](#).

Obtaining validation data from journal articles is inconvenient. Online databases are better suited for dissemination of validation data and documentation of the experiment. Though some validation datasets are available from online databases, these typically lack the detail necessary to fully describe the measurements and uncertainties [1]. Many such sources are listed at the CFD-Online website [2], including the National Aeronautics and Space Administration (NASA) NPARC Alliance Verification and Validation Archive [3] and the European Research Community on Flow, Turbulence and Combustion database [4]. As part of the present effort, a database was developed to enable users to download the BCs, SRQ data, and other relevant information to conduct their own validation studies, using the same BCs to which the SRQ data correspond [5]. This database is included in the Supplemental results which are available under “Supplemental Data” tab for this paper on the [ASME Digital Collection](#).

1.1 Model Validation. Validation is “the process of determining the degree to which a model is an accurate representation of the real world from the perspective of the intended uses of the model” [6,7]. To perform a CFD validation study, one must have measurements of both the model inputs and outputs.

The model outputs, or SRQs, are the quantities to be compared between the experiment and the simulation. No specific application motivates the present work, and we seek to produce the most broadly useful dataset possible. To this end, we consider the recommendations of Oberkampf and Roy [6], who described the difficulty spectrum of measurements and computed quantities, as shown in Fig. 1. Using SRQs from a wide range of the spectrum will ensure a more robust validation study. For instance, the model that best predicts boundary layer velocity for this particular experiment (dependent variable) may not predict the heat flux (derivative of a dependent variable) as accurately. Using SRQs from a wide range on the spectrum will better determine which model is the best predictor of the physical phenomena. In the present study, SRQs are chosen based on project budget and time constraints while covering as much of the spectrum as possible.

Many have recommended (e.g., Ref. [6]) that model validation be performed in a hierarchy, as shown in Fig. 2, with the lower tiers involving simpler physics and higher resolution measurement and the top tier covering the complete system of interest with more coarse measurements. Since the heat transfer and the fluid flow are coupled, this problem cannot be considered as a unit problem. To meet the requirements of the benchmark tier in the

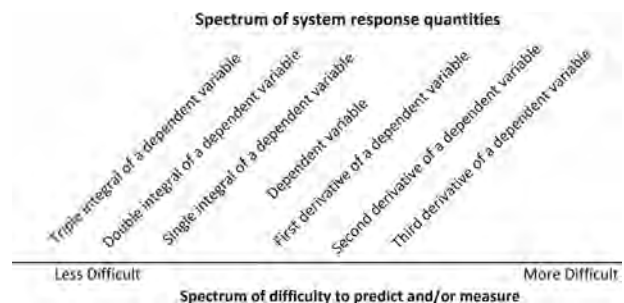


Fig. 1 The difficulty spectrum of SRQs, after Ref. [6]

Contributed by the Fluids Engineering Division of ASME for publication in the JOURNAL OF FLUIDS ENGINEERING. Manuscript received April 15, 2014; final manuscript received July 4, 2015; published online August 10, 2015. Editor: Malcolm J. Andrews.

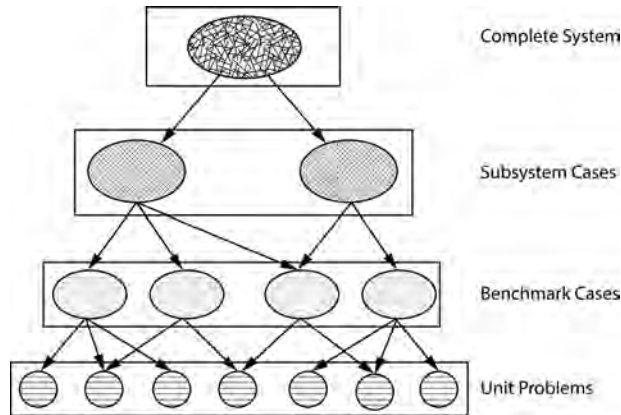


Fig. 2 The validation hierarchy with cross-hatch showing the amount of detail in each level, after Ref. [6]

validation hierarchy, the hardware used in this wind tunnel was specially fabricated to validate specific aspects of flow over a heated flat plate. The experiments were carried out in a new facility made specifically for benchmark tier validation experiments. The wind tunnel and plate are the simplified hardware meant to improve predictive capability of complicated flow physics for real-world scenarios for many applications. The inputs required to perform a CFD simulation (wall locations and temperatures, as well as inlet temperature and velocity) were measured and their uncertainties were estimated.

Figure 3 is used to illustrate the importance of using measured inflow conditions in a simulation. It is a common practice in CFD simulations to assume an idealized inlet profile, such as a parabolic or uniform profile. For our wind tunnel, a uniform inlet velocity assumption is valid for most of the inlet area, but not in the boundary layer. It is also a common practice to assume that the Reynolds normal stress at the inlet is a fixed percentage of the time-mean velocity (10% of the free stream velocity in this example), while the measured turbulence level is found to be large only in the thin boundary layers near the walls.

It is necessary to know the uncertainty of the experimental data as well as the simulation uncertainty to obtain the model uncertainty [6,8]. Therefore, the SRQ data must have quantified uncertainty. Since the simulation uses experimentally determined

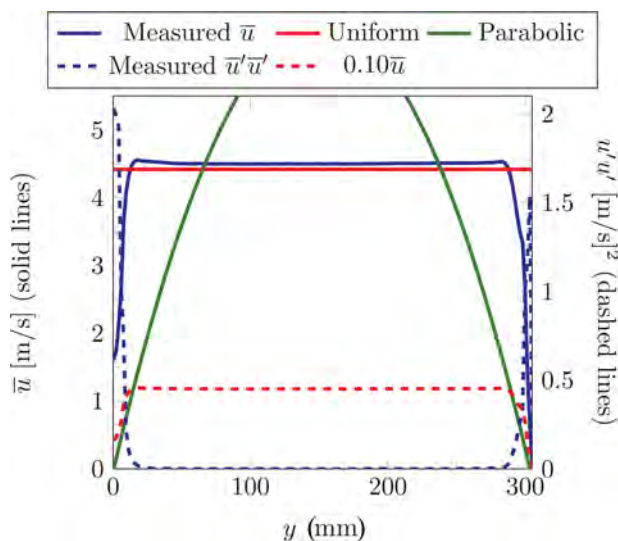


Fig. 3 A velocity profile for the inlet of the test section is shown, along with uniform and parabolic profiles. The Reynolds stress is also plotted along with a line of 10% of the time-mean streamwise velocity.

BCs, uncertainty is introduced into the simulation from uncertainty in the measurements. This also necessitates the uncertainty quantification of measured BCs.

Both inflow and SRQs for the present study are velocity data measured with particle image velocimetry (PIV). The uncertainty of the velocity measurements is quantified using the methods described by Timmins et al. [9], Warner et al. [10], and Wilson and Smith [11,12]. Other measured BCs include the wall geometry and temperature and inlet air temperature. The uncertainties of these quantities are determined using methods discussed by Coleman and Steele [13]. The manufacturer provided the uncertainty of the heat flux sensors used in this study. The uncertainty of wall locations, wall shear stress, and other quantities is discussed below.

1.2 Forced Convection. The forced convection regime theoretically has little effect from gravity (buoyancy) and is defined as $Gr_x/Re_x^2 < 0.3$ [14], where the local Grashof number is $g\beta(T_s - T_\infty)x^3/\nu^2$ and the local Reynolds number is $\bar{u}_\infty x/\nu$, with the inlet velocity $\bar{u}_\infty = 4.48$ m/s. For the purpose of this study, the kinematic viscosity ν is determined from the measured atmospheric air properties. Lloyd and Sparrow [15] conducted a theoretical analysis of forced convection over an isothermal vertical surface and cited experimental data for the same flow scenario. A later experimental study of convection from a vertical heated plate was presented by Gryzagoridis [16], who used hot-wire anemometry to measure the flow velocity. Temperature profiles were used to find heat transfer rates. These measurements, though state-of-the-art at the time, were obtrusive and therefore less useful for CFD validation.

Wang et al. [17] presented an experimental study of a heated vertical plate similar to the one considered in this work. The velocity was measured using a two-component laser Doppler anemometry system, which is unobtrusive, but provides a point velocity rather than a velocity field. Temperature measurements were acquired using a thermocouple rake and a correlation was presented for $Nu_x = hx/k$, which can be used to understand the effects of buoyancy on heat transfer. While the study provided much useful insight, it was not intended for CFD validation. The necessary BCs were not reported nor were the measurement uncertainties.

Finally, a study that used PIV to study the velocity field along a heated plate was described by Hattori et al. [18]. The measurements were also acquired using hot-wire anemometry. The study focused on the laminarization of the flow and provided valuable information using PIV measurements for convection flow from a vertical plate. Again, the measurements obtained were not intended for CFD validation and are incomplete for that purpose.

This is a small sample of published studies on forced convection. A large number of studies show that forced convection is a mature field. However, each of these studies was a discovery experiment rather than a validation data experiment. The present study represents the first validation data study for forced convection known to the authors.

In what follows, we will describe our facility and measurements followed by a description of the data acquisition procedures. This will be followed by the BCs and SRQ results of two nominally isothermal cases: (1) buoyancy-aided forced convection and (2) buoyancy-opposed forced convection. Several comparisons will be presented showing the small but detectable effects on the flow due to the gravitational direction.

2 Facility and Measurements

2.1 Rotatable Buoyancy Tunnel. The experimental apparatus used for this project is called the rotatable buoyancy wind tunnel (RoBuT). The $12 \times 12 \times 78$ in. ($305 \times 305 \times 1981$ mm) test section is fixed to a Ferris wheel-like frame that allows the direction of gravity relative to the flow to be changed without

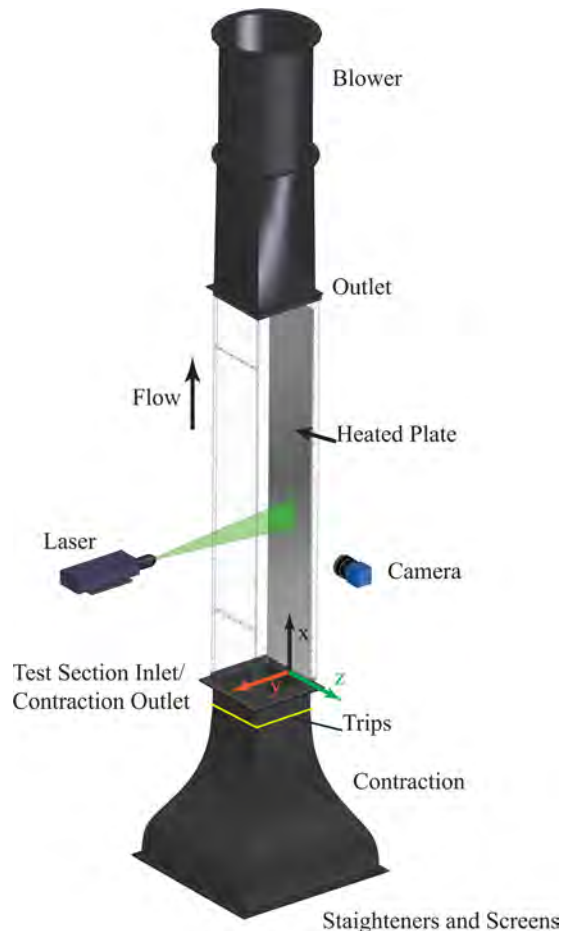


Fig. 4 A schematic of the wind tunnel showing the inlet contraction, test section, and the coordinate system

modifying the wind tunnel inlet or test section. Figure 4 shows a schematic of the RoBuT without its rotating frame.

This facility is intended for benchmark level validation where two or more different physical phenomena (such as momentum and heat transfer) are analyzed [6]. A benchmark tier validation experiment uses special hardware meant to represent main features of subsystems. The square test section allows for easy characterization of the inflow using planar PIV. Simultaneous measurements of BCs (wall temperature, inlet temperature, and atmospheric properties) and SRQs (boundary layer velocity and heat flux) can be acquired. PIV is used to measure all of the velocity data (both at the inlet and for SRQs). For additional details on the facility, see Supplemental results which are available under “Supplemental Data 26” tab for this paper on the [ASME Digital Collection](#).

2.1.1 Test Section. The test section is made of three optically clear Lexan® walls that are 12.7 mm (0.5 in.) thick. The walls are referenced using the coordinate system in Fig. 4, where the heated plate is at $y = 0$ with $x = 12.7$ mm (0.5 in.) being the leading edge of the heated plate, and the left and right walls are at $z = -152.4$ mm (−6 in.) and $z = 152.4$ mm (6 in.), respectively. The wall opposite the heated plate is at $y = 304.8$ mm (12 in.) and is also referred to as the top wall.

The fourth wall is formed by the heated plate and its mounting components. A cross section of the plate near one of the heat flux sensors is shown in Fig. 5. The exterior wall of the tunnel is formed by an aluminum back plate. A layer of insulation lies between the back plate and an electric heater, which is pressed against a second aluminum plate on its other side. The heat flux sensor is potted between two aluminum plates with thermal epoxy

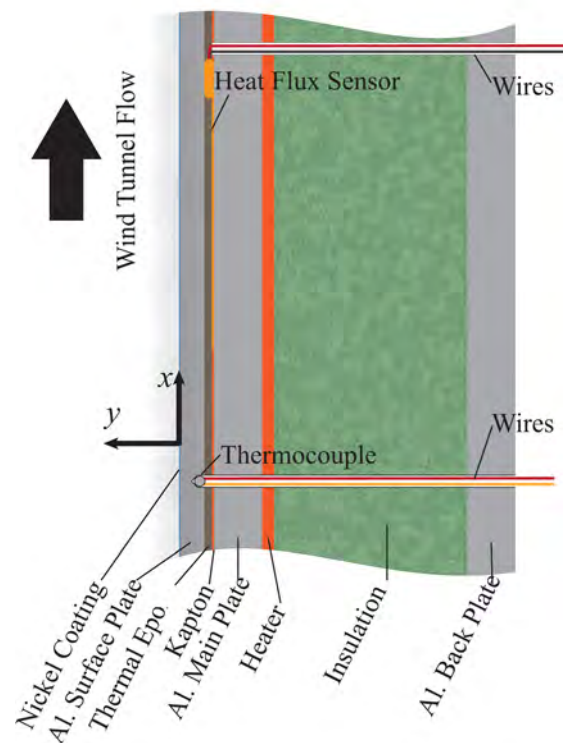


Fig. 5 Cross section of the heated wall

and surrounded with Kapton, which has a similar thermal resistance. The aluminum surface plate is nickel coated on the air side to suppress radiation. For additional information about the heated plate, see Supplemental results which are available under “Supplemental Data 28” tab for this paper on the [ASME Digital Collection](#).

Two methods are used to estimate the emissivity of the nickel-coated plate. First, from Howell et al. [19], the normal emissivity is

$$\varepsilon_n = \frac{4n}{(n+1)^2 + k_r^2} \quad (1)$$

where $n = 5.76$ and $k_r = 27.34$ are material constants for nickel-plated aluminum at 413 K ($\lambda = 7.0 \mu\text{m}$ to find the optical properties n and k in Ref. [19]). Equation (1) gives a normal emissivity of 0.029.

Second, the plate emissivity can be estimated by performing an energy balance on the surface of the nickel plate

$$q'' = h(T_s - T_\infty) + \varepsilon_n \sigma T_s^4 - \varepsilon_L \sigma T_L^4 \quad (2)$$

The emissivity of the Lexan ε_L is assumed to be 0.9. Using measured data from a natural convection state, the emissivity of the heated plate is estimated to be 0.034, which is in good agreement with Eq. (1). A Taylor series method uncertainty propagation [13] is used to compute the uncertainty of the plate emissivity using the energy balance method and is found to be on the order of the computed emissivity itself.

The heated plate is surrounded on the leading, trailing, and spanwise edges with blocks of Teflon® to allow for thermal expansion and to increase the thermal resistance between the heated plate and the Lexan side walls. Springs and a silicone rubber gasket at the outlet of the test section push the plate assembly toward the inlet, minimizing gaps. A layer of insulation on the outer side of the heaters (the right of Fig. 5) increases heat flux

from the plate into the test section. The insulation only serves to increase the efficiency of the heaters, ensuring that most of the power from the heaters goes into the flow. For analysis of the heat flow through the layers of the plate, see Supplemental results which are available under “Supplemental Data 1” tab for this paper on the [ASME Digital Collection](#). Note that the heat flux was measured using sensors, not heater power. All the other materials are described in the Supplemental results which are available under “Supplemental Data” tab for this paper on the [ASME Digital Collection](#).

2.1.2 Inflow. The inlet to the wind tunnel includes a contraction with a 6.25:1 area reduction. The inlet to the contraction includes honeycomb flow straighteners and screens (see Fig. 4). A 3.175 mm (1/8 in.) square trip is fixed to each of the four walls at a position 11.6 cm (4.58 in.) upstream of the heated plate leading edge. These trips make the transition location consistent between datasets.

The test section inlet velocity time-mean, kinetic energy, and dissipation are derived from the experimental inlet measurements acquired at $x=0$. The turbulent kinetic energy k (per unit mass) is [14]

$$k = \frac{1}{2} (\overline{u'u'} + \overline{v'v'} + \overline{w'w'}) \quad (3)$$

where $\overline{u'u'}$, $\overline{v'v'}$, and $\overline{w'w'}$ are the specific Reynolds normal stresses in the x , y , and z directions, respectively.

Velocity data were acquired with the measurement system in both its nominal position and rotated 90 deg, as shown in Fig. 6, to show that $\bar{w} = \bar{v}$ and $\overline{w'w'} = \overline{v'v'}$ at the inlet and that these values are much smaller than \bar{u} and $\overline{u'u'}$. The measurements show that $\overline{v'v'} \approx \overline{w'w'} \neq \overline{u'u'}$, as shown in Fig. 7. The majority of the inlet plane has negligible fluctuations, but near the wall $\overline{u'u'} > \overline{v'v'} = \overline{w'w'}$ and $\overline{v'v'} = \overline{w'w'} < 0.1 \text{ m}^2/\text{s}^2$. At this location, $\overline{u'u'} = 1.8 \pm 0.17 \text{ m}^2/\text{s}^2$ justifying an approximation that $\overline{v'v'} = \overline{w'w'} \approx 0$. We note that this assumption does not hold true for the SRQ data farther downstream.

The turbulence dissipation rate ε is a function of the spatial derivatives of the fluctuating components of velocity and in tensor notation is

$$\varepsilon = \nu \frac{\partial u'_i}{\partial x_k} \frac{\partial u'_i}{\partial x_k} \quad (4)$$

where repeated indices are summed. Not all of the components of the dissipation can be measured with the available diagnostics, but the largest of these components, $(\partial u'/\partial y)^2$ can be computed from the instantaneous velocity field using the methods described in Ref. [20] to compute the derivatives. Using this conservative value for all of the derivative terms in the definition of ε and the measured kinematic viscosity, the inlet turbulence dissipation rate was found to be less than 10^{-4} . It is shown in the Appendix that RANS CFD models are insensitive to the inlet value of ε until several orders of magnitude larger than this value.

The inlet velocity is shown in the contour plot of Fig. 8. The inflow is mostly uniform except near the walls of the test section. Note that PIV measurements do not extend all the way to the wall in the z direction, as that measurement is impossible in orientation A. The plot shows the nine measured PIV planes mapped across the inlet. These data are provided to the numerical analyst as inflow data for the simulation. Any interpolation or wall treatments to make the inflow conditions closer to reality (such as applying a no-slip condition on all walls and defining the boundary layer near the $z = -150 \text{ mm}$ and 150 mm walls) are left to the analyst. One suggested method is to copy the unheated wall boundary layer to the other unheated walls and leave the heated wall as measured.

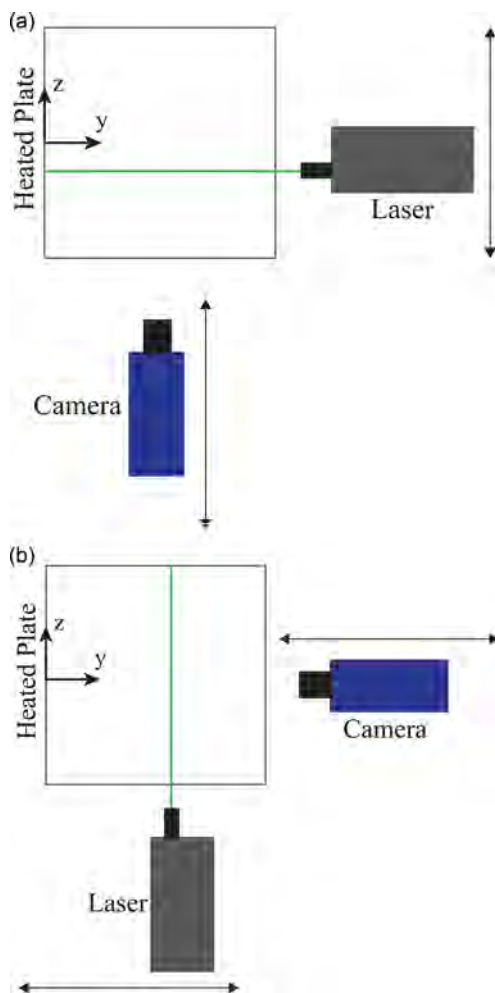


Fig. 6 The orientation of the camera and laser for PIV inflow data acquisition ($x=0$). The laser and camera are traversed across the test section to obtain nine planes of velocity data. The flow direction is out of the page. (a) shows the nominal setup that is also used to obtain the velocity over the heat flux sensors and is referred to as orientation A. (b) shows the inlet profile specific orientation to obtain the w component of velocity and is orientation B.

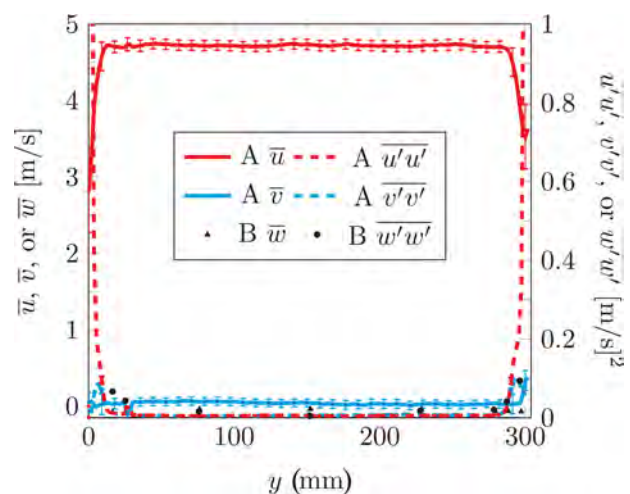


Fig. 7 The centerline inlet profiles for A and B orientations. The A orientation profiles are at $z=0$. The points for the B orientation are data at the $z=0$ intersections of profiles in the x - z plane. The uncertainty of the B orientation data is within the size of the symbols.

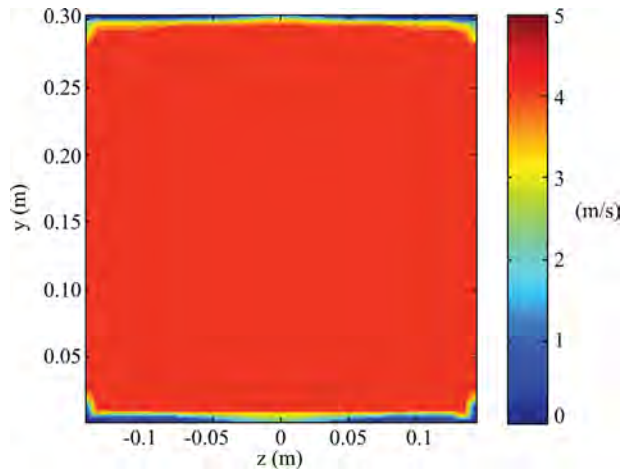


Fig. 8 A time-averaged streamwise velocity contour plot of the PIV measurements at the inlet of the test section, $x = 0$. This velocity field was formed by plotting nine vertical (constant z) profiles of velocity.

2.2 Instrumentation and Controls. A LABVIEW code was used to drive the acquisition of the temperature, heat flux, and room conditions and to control the room temperature, the plate temperature, the seeding for the PIV, and the blower speed. The National Instruments hardware included 5 NI-cDAQ-9188 chassis, which hold 20 NI-9213 16-channel thermocouple modules. All type K thermocouples were calibrated to a 0.3°C source before installation. Another module and chassis controlled the larger voltage equipment, including the three power supplies for the six plate heaters and the room temperature control system. Figure 9 shows the test section assembly and the layout of the heaters and heat flux sensors. The room conditions were monitored and logged continuously, including temperature, pressure, and relative humidity. These were used to determine the air properties for each dataset.

Three heat flux sensors were embedded under the surface of the heated plate at positions $P1 = 6.37$ in. (162 mm), $P2 = 30.62$ in. (778 mm), and $P3 = 54.87$ in. (1394 mm) from the leading edge

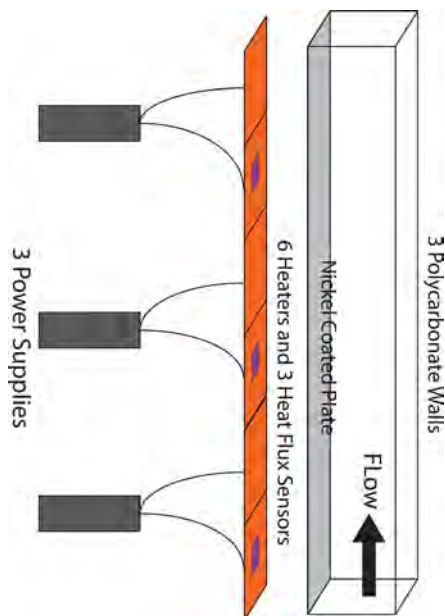


Fig. 9 A schematic showing the locations of heaters and heat flux sensors. Each of the three power supplies powers two heaters.

(see Fig. 9). These sensors were centered in the z direction. R&F Corporation heat flux sensors, model 20457-3, were used, with the first and third sensors having manufacturer-specified properties and an uncertainty of 5%. The second heat flux sensor had a larger uncertainty due to installation errors estimated to be 10% [21]. For additional details about the temperature, pressure, and velocity measurement sensors and systems, see Supplemental results which are available under “Supplemental Data 2” tab for this paper on the [ASME Digital Collection](#).

To control the temperature of the heated plate, the thermocouples in the heat flux sensors were used as the inputs to a proportional-integral-derivative (PID) control system. A desired plate temperature was input, and the controller (with optimized gain and integral time of 0.5 and 2.5 mins, respectively) adjusted the voltage to the heaters. A nominally isothermal steady-state case was easily maintained to within the thermocouple accuracy of less than 1°C over time. That is, the temperature control system maintained a steady state, even though the plate temperature was not perfectly isothermal.

To acquire the wall temperature BCs, all four walls were instrumented with thermocouples. The thermocouples in the heated plate were spaced at intervals of 2 in. (50.8 mm). The thermocouples in the two clear side walls were at $x = 0.0$, 33.66, 62.55, 96.84, 123.8, 166.4, and 192.4 cm and $y = 19.05$, 95.25, and 247.7 mm. On the top clear wall, the thermocouples were placed at $z = -76.2$, 0.0, and 76.2 mm and $x = 0.0$, 33.66, 76.2, 103.2, 137.5, 166.4, and 192.4 cm. The depth of the holes for placement of the thermocouples into the heated plate is included in the Supplemental results which are available under “Supplemental Data 2” tab for this paper on the [ASME Digital Collection](#).

Pressure measurements were also acquired using a MKS 270D Baratron 1-Torr pressure sensor with a MKS 270D signal conditioner. Four pressure taps were installed in the wind tunnel at the contraction inlet, the contraction outlet, near the test section inlet, and the test section outlet.

Included with the BCs are the ambient air properties (atmospheric pressure, temperature, and relative humidity). The barometric pressure was acquired using an Apogee Instruments, Inc. SB-100. The temperature and humidity were acquired using a temperature/humidity probe (Omega HX93A).

The PIV camera was an Imager Intense 12-bit digital camera from LaVision [22]. The charge-coupled device sensor was 1376×1040 pixels with a pixel size of $6.45 \mu\text{m}$ (0.000254 in.) square. The laser pair was a New Wave Research Solo PIV III 15. Two lasers at 50 mJ/pulse and 532 nm could fire up to 15 Hz. Due to limitations of the camera, data could be acquired at 4 Hz in double-pulse mode.

The PIV data were acquired and processed using DaVis 8.1.6. A ruler was used to calibrate the camera for the inlet data, and a single plane calibration plate was used to scale and dewarp the images for the SRQ data using a pinhole model. The calibration plate used laser-etched circles on an anodized aluminum plate. The dots were 0.980 mm (0.039 in.) in diameter and spaced 3.175 mm (0.125 in.) apart.

The particle displacements were generally around 12 pixels in the free stream, with the particle diameters usually between 1 and 2 pixels. The small particle image diameters were unavoidable due to illumination issues for the large field of view at the inlet. The uncertainty method accounts for the variation in particle diameter and displacements, addressing any pixel locking errors. The images for the SRQ data used the entire imaging chip (1376×1040 pixels). The inlet data region of interest was generally 1376×256 pixels, capturing the inlet of the test section. The images were processed using the following steps after acquisition:

- (1) The images were corrected for small vibrations and rotation based on the wall image. In particular, the wall image was forced to be vertical and in the same position for every image.
- (2) The average image of the dataset was subtracted from the instantaneous images to decrease the background noise.

- (3) Vectors were computed using 64×64 windows with one pass, then decreased to a 32×32 windows with 75% overlap for two passes. In addition, the SRQ images were processed with image correction, which is possible due to the two-dimensional, plate-based calibration.
- (4) The PIV data were postprocessed with an allowable vector range of 0–10 m/s in \bar{u} and -1 to 1 m/s in \bar{v} . The vectors were deleted if the correlation peak ratio was less than two. A median filter was used to remove vectors for which the difference to the average was greater than $1.75 \times$ root mean square (RMS) of its neighbors and inserted (or reinserted) if the difference to the average was less than $2.5 \times$ RMS of its neighbors. Also, groups with less than five vectors were removed and the allowable vector range was computed again.
- (5) The time-average velocity and Reynolds stresses were also computed.

Two different lenses were used on the camera. A Nikon 105-mm lens and extension tube were used when acquiring images for the SRQ measurements over the heat flux sensors. A Nikon 28-mm lens was used when acquiring images for the inflow. In all cases, a 532 nm notch filter was placed over the lens to remove room light and decrease reflections (rhodamine paint was used on the highly reflective Teflon to shift reflected light outside the filter pass band).

The camera and laser were both mounted to Velmex [23] traverse stages that allow for synchronized motion in the y and z directions. The traverses were each independently controlled with LABVIEW. To move the equipment in the x direction, the hardware was designed to mount easily at increments of 5 in. (127 mm), with mounts for the laser and camera providing more accurate placement.

PIV measurements require seed particles distributed in the flow. Two Laskin nozzles were used to generate olive oil droplets that are approximately $0.8 \mu\text{m}$ in diameter. These devices are similar to those described by Kähler [24]. The droplets were then blown into a system of polyvinyl chloride pipe that is fixed to the inlet of the contraction of the wind tunnel (bottom of Fig. 4). The system was laid out in a grid pattern allowing for even dispersion of the seed particles. These pipes are upstream of the flow straighteners and screens and have no detectable impact on the test section inflow.

2.3 Measurement Uncertainties. The PIV uncertainty is determined using the methods described in Refs. [9,11,12]. The uncertainty of length dimensions comes from the resolution of the measurement devices and statistics of repeated measurements. These values are all included in the data in the Supplemental results which are available under “Supplemental Data” tab for this paper on the ASME Digital Collection. The remainder of this section will describe our estimate of uncertainties that are not as straight forward as those previously described.

2.3.1 Uncertainty of Friction Velocity. The friction velocity is found using two methods described below. The first directly calculates the wall shear using a linear fit to the data near the wall. The uncertainty of the wall shear velocity u_τ based on the velocity gradient at the wall is found using the Taylor series method [13] and the data reduction equation $u_\tau = \sqrt{\nu(du/dy)_w}$. The uncertainty of the shear velocity is

$$U_{u_\tau} = \sqrt{\left(U_{du/dy} \frac{\sqrt{\nu}}{2\sqrt{du/dy}} \right)^2 + \left(U_\nu \frac{\sqrt{du/dy}}{2\sqrt{\nu}} \right)^2} \quad (5)$$

where U_ν is the uncertainty of the kinematic viscosity

$$U_\nu = \sqrt{\left(U_\mu \frac{1}{\rho} \right)^2 + \left(U_\rho \frac{-\mu}{\rho^2} \right)^2} \quad (6)$$

and $U_{du/dy}$ is the uncertainty of the velocity gradient

$$U_{du/dy} = \sqrt{\left(\frac{U_{u1}}{dy} \right)^2 + \left(\frac{U_{u2}}{dy} \right)^2 + \left(U_{dy} \frac{u1 - u2}{dy^2} \right)^2} \quad (7)$$

where the velocity uncertainties are computed using the methods described in Refs. [9–12] and the velocities are data points in the velocity profile. The dy term is the vector spacing of the data and the uncertainty of dy is explained below.

The dynamic viscosity μ is found from a polynomial fit to data contained in Ref. [25]. As a function of the temperature in Celsius, the viscosity is

$$\mu(T) = 1.714 \times 10^{-5} + 4.879 \times 10^{-8}T - 4.5675 \times 10^{-11}T^2 + 7.3469 \times 10^{-14}T^3 \quad (8)$$

The uncertainty of the viscosity is dominated by the uncertainty of the data in Ref. [25]. The density is found from the ideal gas law and the air density uncertainty is

$$U_\rho^2 = \left(\frac{U_P}{TR_{\text{air}}} \right)^2 + \left(U_T \frac{-PR_{\text{air}}}{(TR_{\text{air}})^2} \right)^2 + \left(U_{R_{\text{air}}} \frac{-PT}{(TR_{\text{air}})^2} \right)^2 \quad (9)$$

where the air gas constant is found from $R_{\text{air}} = 8.31434/M_{\text{mix}}$ and

$$M_{\text{mix}} = (1 + \omega) / \left(\frac{\omega}{18.02} + \frac{1}{28.97} \right) \quad (10)$$

The humidity ratio ω is a function of the measured relative humidity, pressure, and temperature and is defined as

$$\omega = \frac{0.622}{\frac{P}{\phi P_{\text{sat}}} - 1} \quad (11)$$

with $P_{\text{sat}} = 0.57574 + 0.0554T + 4.1195 \times 10^{-4}T^2 + 6.0733 \times 10^{-5}T^3$. The uncertainty of the air gas constant is negligible. The uncertainty of this temperature is $U_T = 0.6^\circ\text{C}$ (note that this is not a thermocouple, but a thermistor-based probe) and the uncertainty of the atmospheric pressure is $U_P = 1.5\%$ of reading.

2.3.2 Uncertainty of Wall Position. The most obvious method for setting the spatial origin in the velocity data is to locate an unmoving object (such as a wall) in the raw PIV images. However, the laser source commonly generates a wide flare in the camera image at the wall making it difficult to pinpoint its location. An example is shown in Fig. 10, which shows a small part of the image. The wall is the white band near the left side of the image.

This estimate can be improved upon using information from the turbulent flow along a wall. The error in the wall location was first



Fig. 10 An image of the wall, with the image width being 2.25 mm

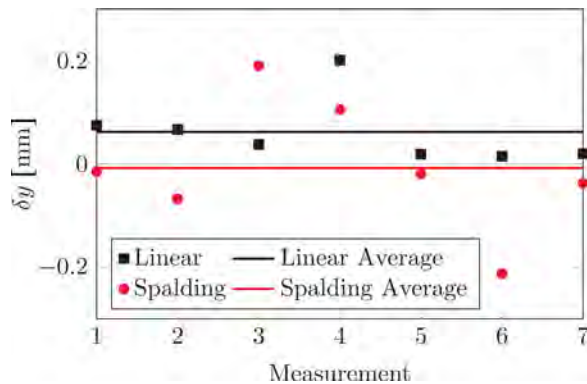


Fig. 11 The error of the wall location relative to the wall image using two methods. The scale factor is approximately 84 pixels/mm.

found by fitting theoretical (Spalding [26]) velocity profiles to the hundreds of streamwise time-averaged velocity data points (some of which are located in the viscous sublayer, and most of which are in the log-layer), and using the wall location as a parameter of the fit. The log-layer data have low uncertainty, but this procedure relies on the applicability of the Spalding model. Alternately, the wall location can be found by fitting a line through the three velocity values closest to the wall. These should behave linearly and go to zero at the wall. It was found that replications of this process, with the measurement system setup from scratch each time, resulted in large variations in the wall location error.

Seven replications are shown in Fig. 11. The error δy of each method relative to the wall location based on inspection of the raw images is shown. For both methods, the variations in the wall position error were on the order of 16 pixels. The average of these samples could be viewed as the bias of each method relative to the wall location by inspection. Unfortunately, we have no evidence that any one of these methods is clearly superior to any other, but these data are sufficient to provide a reasonable uncertainty estimate of the wall location. Based on the results, the Spalding fit method has very little bias and a 1-sigma random uncertainty of 0.13 mm.

3 Data Acquisition Procedures

For the inflow data, nine planes of two-component PIV data were acquired in orientation A shown in Fig. 6. The procedure for acquiring the inlet data is described as:

- (1) Setup laser, camera, and traverse stages and align with the test section in space (the calibration target is fixed to the test section).
- (2) Calibrate camera and match laser plane to calibration plane.
- (3) Set acquisition timing for sufficient particle displacements, set seed flow rate, laser intensity, and f-stop (impacting particle image intensity and size).
- (4) Stabilize room, wall, and flow conditions.
- (5) Record PIV data, temperatures, heat flux, equipment position, blower speed, heater and seeding settings, camera and laser settings, and room conditions.
- (6) Move to next plane and repeat the previous step.

The process for acquiring SRQ data is the same, except there is only one plane at which to acquire data ($z=0$). The boundary layer flow images are acquired with the camera at a slight angle with respect to the plate to decrease the length of the light path through air, consisting of a density gradient that would otherwise distort the images. Because the angle is small, a planar scaling of the images was sufficient. The inlet data use 500 image pairs and the SRQ data use 1000 image pairs.

Table 1 The available data from the experiments described in this article. Corresponding uncertainties are included for each.

Buoyancy aided and opposed	
BCs	SRQs
Geometry	Heat flux (three locations)
Wall temperatures	Boundary layer velocity
Inlet temperature	Shear velocity
Inlet velocity	
Atmospheric conditions	

4 Validation Data Results

The following Secs. 4.2 and 4.3 describe measurements for isothermal forced convection for buoyancy-aided and buoyancy-opposed flow. The Reynolds number based on the test section hydraulic diameter and free stream velocity is 77,000. The data that are acquired and available to the reader are outlined in Table 1.

4.1 BCs. The geometry of the wind tunnel test section was measured prior to all experiments to provide the as-built (as opposed to as-designed) test section and is included in the Supplemental results which are available under “Supplemental Data 3” tab for this paper on the [ASME Digital Collection](#) with the measurement uncertainties outlined in the Supplemental results which are available under “Supplemental Data 4” tab for this paper on the [ASME Digital Collection](#). The height and width of the test section were measured using a micrometer at the transparent-wall thermocouple locations, as described in the Supplemental results which are available under “Supplemental Data 2” tab for this paper on the [ASME Digital Collection](#). The inflow velocity, inflow temperature, and wall temperature on all four walls were also recorded to provide the necessary BCs.

The average of all relevant cases is used as the BC. For example, there are 12 datasets for the forced convection isothermal case. The wall and inlet temperatures used for the BCs are the average of these 12 sets. The atmospheric conditions for the buoyancy-aided flow case including the measured barometric pressure, ambient temperature, and relative humidity are included in the Supplemental results which are available under “Supplemental Data 5” tab for this paper on the [ASME Digital Collection](#). The atmospheric conditions for the buoyancy-opposed case are included in the Supplemental results which are available under “Supplemental Data 6” tab for this paper on the [ASME Digital Collection](#).

4.2 Buoyancy-Aided Case. The first case presented is buoyancy-aided forced convection over a plate that was nominally isothermal and set to about 140 °C. The controller seeks isothermal heating, but the BC thermocouples are much more resolved spatially than the PID controller (which uses only three temperature readings as shown in Fig. 9), limiting the ability to actually reach isothermal heating. For example, the corner of the leading edge is 30 °C cooler than the maximum plate temperature.

The temperature BCs are included in the Supplemental results which are available under “Supplemental Data” tab for this paper on the [ASME Digital Collection](#) and there are five temperature files; four for walls and one for the inflow. Supplemental results which are available under “Supplemental Data 7” tab for this paper on the [ASME Digital Collection](#) contain the temperature of the heated wall ($y=0$), Supplemental results which are available under “Supplemental Data 8” tab for this paper on the [ASME Digital Collection](#) contain the temperature of the top wall ($y=12$ in.), Supplemental results which are available under “Supplemental Data 9” tab for this paper on the [ASME Digital Collection](#) contain the temperature of the left wall ($z=-6$ in.), Supplemental results which are available under “Supplemental Data 10” tab for this

Table 2 The “isothermal” heat flux results along with the Graetz to Reynolds number ratio (showing the cases are forced convection) and the momentum thickness Reynolds number

x position (mm)	Heat flux (W/m^2)	Re_x	$\text{Gr}_x/\text{Re}_x^2$	δ_2 (mm)	Re_{δ_2}
P1 = 162	1917	40,300	0.026	1.4	357
P2 = 778	1170	194,000	0.131	2.2	554
P3 = 1394	1356	347,000	0.232	2.3	564

paper on the [ASME Digital Collection](#) contain the temperature of the right wall ($z = 6$ in.), and Supplemental results which are available under “[Supplemental Data 11](#)” tab for this paper on the [ASME Digital Collection](#) contain the temperature of the inlet ($x = 0$ in.). The values are measured by the 312 thermocouples used in the experiment at the time the SRQ data were acquired. As there are 12 instances of SRQ and BC acquisitions for each case, these 12 BCs are averaged and the statistics are also reported in the csv files. The x , y , and z columns specify the position of each measurement in meters. The Temp column is temperature in Kelvin. The bias, precision, and total uncertainty of the temperature with 95% confidence are also presented.

The inlet velocity and inlet Reynolds stresses are included in the Supplemental results which are available under “[Supplemental Data 12](#)” tab for this paper on the [ASME Digital Collection](#). The columns in data file are as follows: X , Y , and Z are positions of the vectors in meters. Columns u , v , and w are the velocities (m/s) in the x , y , and z directions, respectively. Columns $u'u'$, $v'v'$, $w'w'$, and $u'v'$ are the specific Reynolds stresses with the justified assumption that $\overline{v'v'} = \overline{w'w'}$. The uncertainty of the velocities is also included within the spreadsheet. Uu is the uncertainty of the \bar{u} velocity, similarly with Uv and Uw for their respective velocity components. $Uuup$ is the upper uncertainty of $u'u'$, and $Uuul$ is the lower uncertainty of $u'u'$. The uncertainties of $v'v'$, $u'v'$, and $w'w'$ are similarly notated.

The heat flux, Reynolds number, Richardson number, and momentum thickness Reynolds number are shown in Table 2 for three x locations. The flow at the location of the third heat flux sensor is near the boundary of the mixed convection ratio using the ratio specified in Ref. [14]. The momentum thickness Reynolds number was found at each heat flux sensor position. Kays and Crawford show that the critical momentum thickness Reynolds number is 162 [14].

Figure 12 shows the measured heat flux compared with two correlations. The measured heat flux is the heat flux reading from the sensors shown in Fig. 9 and is an ensemble average of the 12 acquisition cases for the buoyancy-aided forced isothermal condition. The trend labeled Kays is the heat flux predicted by the correlation [14]

$$\text{St} = \frac{\text{Nu}_x}{\text{Re}_x \text{Pr}} = \frac{0.0287 \text{Re}_x^{-0.2}}{0.169 \text{Re}_x^{-0.1} (13.2 \text{Pr} - 9.25) + 0.85} \quad (12)$$

The Incropera trend is based on the correlation for convection over an isothermal flat plate [27] and is

$$\text{Nu}_x = 0.0296 \text{Re}_x^{4/5} \text{Pr}^{1/3} \quad (13)$$

The Stanton number is the Nusselt number divided by the product of the Reynolds and Prandtl numbers. Once the Nusselt number is computed, the heat flux can be found as $q'' = \text{Nu}_x k (T_x - T_\infty) / x$. Note that the correlation trends are not smooth, a result of the measured centerline plate temperature, which has small gradients.

The boundary layer streamwise velocity profiles in the wall-normal direction are shown in Fig. 13. Note that only the near wall region is shown, and the larger velocities at P1 do not correspond to a larger total flow rate compared to P2 and P3. The higher velocity at the first heat flux sensor is a repeatable trend

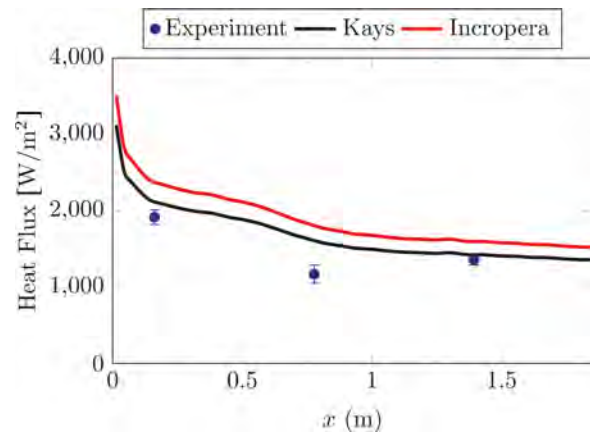


Fig. 12 The measured heat flux and two correlations with the Kays trend found from Eq. (12) and the Incropera from Eq. (13) for the buoyancy-aided case

and results from the thickening of the boundary layer between P1 and P2. These data are shown nondimensionally while dimensional plots are provided in the validation database included with this document.

In addition to the time-mean velocity, the specific Reynolds normal stress $u'u'$ may also be used as a SRQ. The uncertainty bands on velocity and specific Reynolds stresses are at the 95% confidence level.

The cross-stream time-mean velocity \bar{v} , Reynolds normal stress $v'v'$, and Reynolds shear stress $u'v'$ cross-stream profiles are not shown here but are available in the Supplemental results which are available under “[Supplemental Data](#)” tab for this paper on the [ASME Digital Collection](#). The magnitudes of these quantities are small compared to the velocity resolution of the PIV, and this is reflected in the uncertainty bands.

The wall coordinate quantities u_τ , κ , y_0 , and B can be found using the method described by Kendall and Koochesfahani [26]. A curve fit to the Spalding profile yields shear velocities shown in Table 3, where the Spalding profile is

$$y^+ = u^+ + \exp(-\kappa B) \left[\exp(\kappa u^+) - 1 - \kappa u^+ - \frac{(\kappa u^+)^2}{2} - \frac{(\kappa u^+)^3}{6} \right] \quad (14)$$

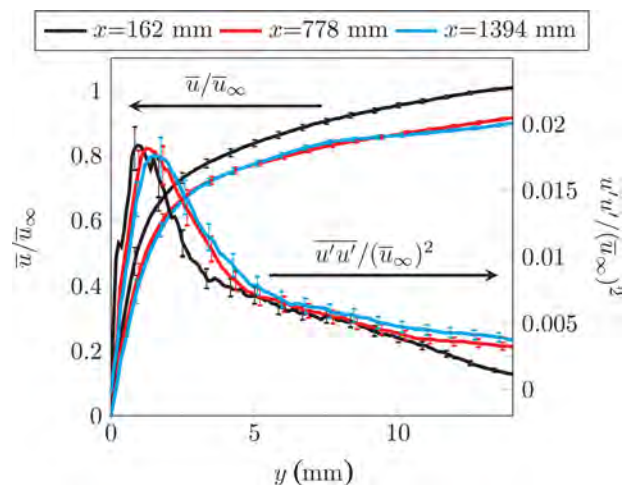


Fig. 13 The nondimensional boundary layer time-mean streamwise velocity and Reynolds normal stress for the flow over the three heat flux sensor positions with $\bar{u}_\infty = 4.49$ m/s for the buoyancy-aided case

Table 3 The von Kármán constant, y-intercept, shear velocity from the Spalding fit, and the shear velocity from a linear fit near the wall at the heat flux sensor positions for the buoyancy-aided case are tabulated

Position	κ	B	u_{τ} Spalding	u_{τ} linear
P1	0.41	5.00	0.248	0.233 ± 0.004
P1	0.36	5.49	0.228	
P2	0.41	5.00	0.233	0.216 ± 0.004
P2	0.405	5.61	0.223	
P3	0.41	5.00	0.235	0.216 ± 0.004
P3	0.354	4.85	0.219	

Units of u_{τ} are m/s.

and $y^+ = (y - y_0)u_{\tau}/\nu$ and $u^+ = \bar{u}_{\infty}/u_{\tau}$. Two results are shown for each profile: one with the traditional $\kappa = 0.41$ and $B = 5.0$ and a second where κ and B are found in the fitting process. Care was taken to exclude wake region data for the curve fit. Using the shear velocities shown in Table 3, the wall coordinate profiles for velocity at the heat flux sensor positions are shown in Fig. 14.

The data are acquired at the streamwise (x) location of the three heat flux sensors. Note that the v velocities are very small and near the velocity resolution of the PIV measurements (thus, the large uncertainty bands). The velocity profiles at the first, second, and third heat flux sensor positions are included in the Supplemental results which are available under “Supplemental Data 13” tab for this paper on the ASME Digital Collection containing the velocity data over the first heat flux sensor position, Supplemental results which are available under “Supplemental Data 14” tab for this paper on the ASME Digital Collection over the second, and Supplemental results which are available under “Supplemental Data 15” tab for this paper on the ASME Digital Collection over the third heat flux sensor position. The files contain columns of data as follows: Position x , y , z in meters, the time-average velocities in the streamwise and wall-normal directions in m/s, u and v respectively. The specific Reynolds stresses $\overline{u'u'}$, $\overline{v'v'}$, and $\overline{u'v'}$ are also included. The uncertainty of these values are given along with the upper (such as $Uuup$) and lower (such as $Uuum$) uncertainty components of the Reynolds stresses.

The shear velocity is also an SRQ and is presented in Table 3. The heat flux SRQ is contained in the Supplemental results which are available under “Supplemental Data 16” tab for this paper on the ASME Digital Collection. The columns in this file are the position, the heat flux, the bias uncertainty of the heat flux measurements, the precision uncertainty of the heat flux measurement, and the total uncertainty of the heat flux.

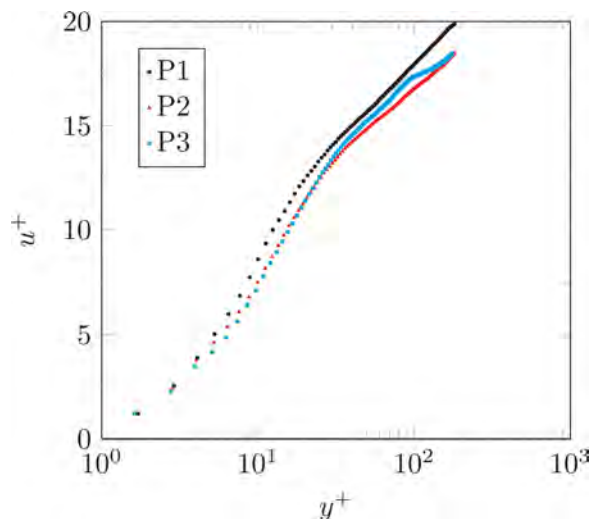


Fig. 14 The wall coordinate profiles at each heat flux sensor position using the variable κ and B for the buoyancy-aided case

Table 4 The buoyancy-opposed isothermal forced convection heat flux results along with the Grashof to Reynolds number ratio and the momentum thickness Reynolds number

x position (mm)	Heat flux (W/m^2)	Re_x	Gr_x/Re_x^2	δ_2 (mm)	Re_{δ_2}
P1 = 162	1947	41,400	0.02	1.8	466
P2 = 778	1241	199,000	0.12	2.8	713
P3 = 1394	1442	357,000	0.22	3.2	813

4.3 Buoyancy-Opposed Case. The same heating conditions and flow rate are considered with the wind tunnel rotated in such a way that the forced flow is downward, opposing the effects of buoyancy. The heated wall temperature BCs for the buoyancy-opposed case are included in the Supplemental results which are available under “Supplemental Data 17” tab for this paper on the ASME Digital Collection. The top wall ($y = 12$ in.) temperatures are in the Supplemental results which are available under “Supplemental Data 18” tab for this paper on the ASME Digital Collection. The left ($z = -6$ in.) wall temperatures are in the Supplemental results which are available under “Supplemental Data 19” tab for this paper on the ASME Digital Collection. The right ($z = 6$ in.) wall temperatures are in the Supplemental results which are available under “Supplemental Data 20” tab for this paper on the ASME Digital Collection. The inlet temperature is provided in the Supplemental results which are available under “Supplemental Data 21” tab for this paper on the ASME Digital Collection. The inlet flow field is provided in the Supplemental results which are available under “Supplemental Data 27” tab for this paper on the ASME Digital Collection. The file structure for the buoyancy-opposed case BCs is identical to the buoyancy-aided case in Sec. 4.2.

The heat flux, local Reynolds number, the ratio of the Grashof to Reynolds number squared, the momentum thickness, and momentum thickness Reynolds number are all tabulated in Table 4. It is noted that the values for the convection ratio are very similar to the buoyancy-aided case. The momentum thickness and momentum thickness Reynolds number show a different trend as a function of x position than the buoyancy-aided case. The buoyancy-aided case had very similar values at the second and third positions, whereas the buoyancy-opposed case shows an increase. This suggests that the two flows will show a different boundary layer development based solely on the influence of gravity.

The heat flux is plotted in Fig. 15 and compared with the two correlations presented previously. The subtle differences between these results and the SRQs presented in Fig. 12 are discussed further in Sec. 5.2.

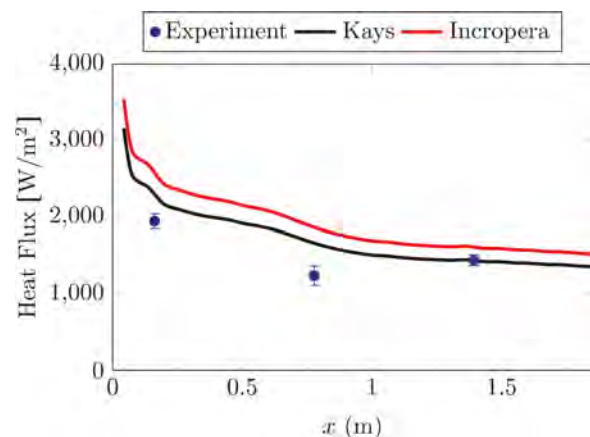


Fig. 15 The measured heat flux and two correlations with the Kays trend found from Eq. (12) and the Incropera trend from Eq. (13) for the buoyancy-opposed case

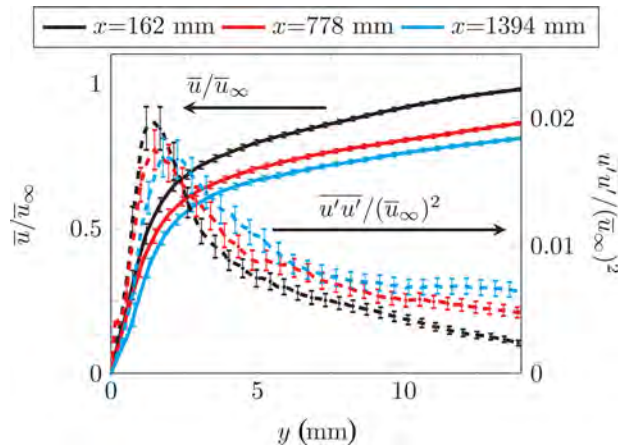


Fig. 16 The nondimensional boundary layer time-mean streamwise velocity and Reynolds normal stress for the flow over the three heat flux sensor positions with $\bar{u}_\infty = 4.56$ m/s for the buoyancy-opposed case

The boundary layer velocity profiles for the buoyancy-opposed isothermal forced convection case are plotted in Fig. 16. Note that the velocity profiles for the second and third positions are not as similar as they are in the buoyancy-aided case. This demonstrates that this forced convection flow has buoyancy effects and will be discussed more in Sec. 5.2.

The wall shear velocities computed using the two methods described above are tabulated in Table 5. Comparing the values in Table 5 to those in Table 3, the values at the first position are similar, but the second and third positions are not. The linear method shows a larger difference between the two cases than the Spalding fit method.

The SRQ data are included in the Supplemental results which are available under “Supplemental Data” tab for this paper on the ASME Digital Collection and the file structure is the same as the aided case, so the description is not replicated. The velocity profile over the first heat flux sensor is provided in the Supplemental results which are available under “Supplemental Data 22” tab for this paper on the ASME Digital Collection. The velocity over the second and third heat flux sensors is contained in the Supplemental results which are available under “Supplemental Data 23 and 24” tab for this paper on the ASME Digital Collection, respectively. The shear velocity is also an SRQ and is presented in Table 5. The heat flux SRQ is presented in the Supplemental results which are available under “Supplemental Data 25” tab for this paper on the ASME Digital Collection.

5 Discussion

5.1 Repeatability. In this section, the repeatability of the velocity measurement is considered, as suggested by Oberkamp

Table 5 The von Kármán constant, intercept, shear velocity from the Spalding fit, and the shear velocity from a linear fit near the wall at the heat flux sensor positions for the buoyancy-opposed isothermal forced convection case

Position	κ	B	u_τ Spalding	u_τ linear
P1	0.41	5.00	0.244	0.184±0.016
P1	0.39	5.17	0.237	
P2	0.41	5.00	0.220	0.176±0.015
P2	0.448	4.40	0.240	
P3	0.41	5.00	0.210	0.137±0.017
P3	0.499	6.16	0.221	

Note that $\kappa = 0.41$ and $B = 5.0$ are classical values not optimized in the fit.

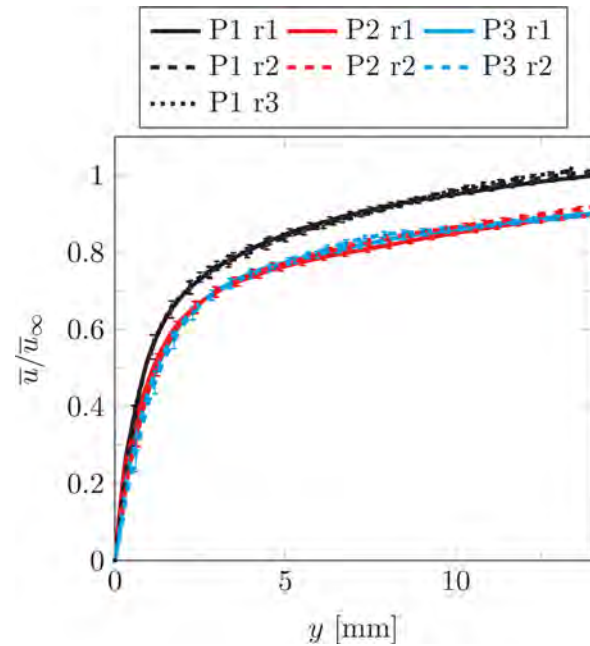


Fig. 17 The boundary layer streamwise velocity profiles for the flow over the three positions for three repeats of the isothermal measurement

and Trucano [28]. Figure 17 shows the boundary layer velocity for the several repeats of data at each position. Excellent repeatability is found in all cases. We note that these measurements were recorded several months apart, with a disassembly, reassembly, and recalibration of the PIV equipment between the second (r2) and third (r3) cases. A recalibration was performed between the first (r1) and second cases (r2). Note that a third measurement was not done for P2 and P3. Both the inlet and the boundary layer at the first position were found to be repeatable during the acquisition of the third measurement.

Figure 18 shows these profiles as a difference from the mean of the data of all replications at each of the locations P1, P2, and P3.

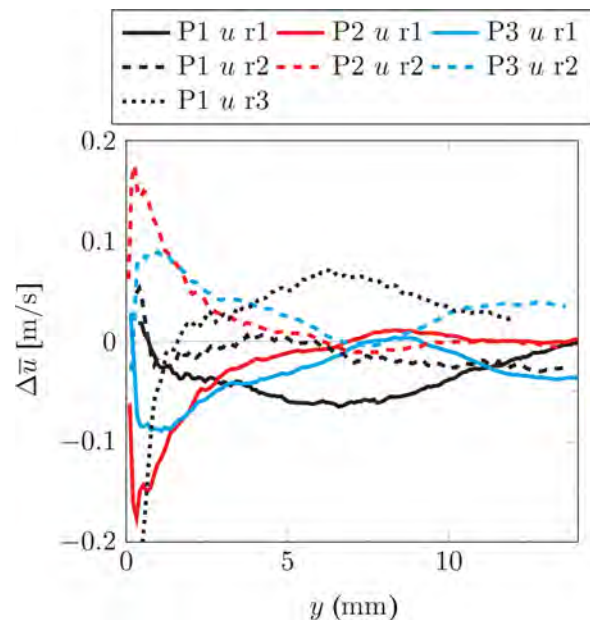


Fig. 18 The boundary layer streamwise velocity residuals for the flow over the three positions for three repeats of the isothermal measurement

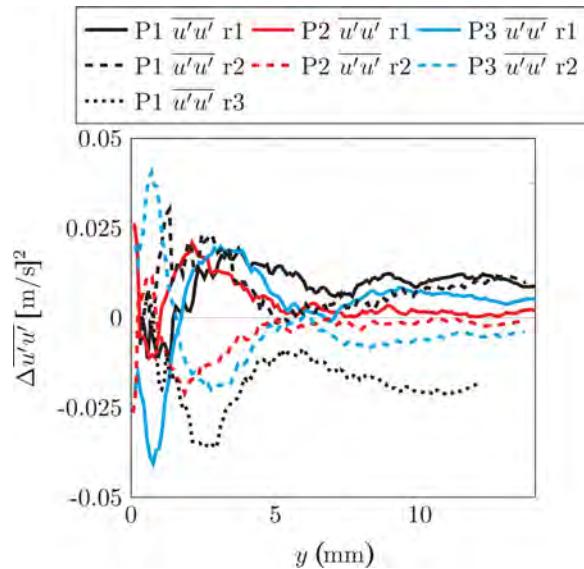


Fig. 19 The boundary layer streamwise velocity Reynolds normal stress residuals for the flow over the three positions for three repeats of the isothermal measurement

It is shown that three replications of the streamwise velocity over the first heat flux sensor have an average residual level of 0.05 with larger values near the wall. The PIV data near the wall have larger uncertainty. The large residual here could also result from an error in the y position in the presence of the large velocity gradient. The fact that the P2 and P3 trends are equal and opposite in Fig. 18 is because there are only two replications used to compute the average. The residuals for $u'u'$, included in Fig. 19, are small.

5.2 Gravity Effects. Figure 20 shows the boundary layer velocity profiles for buoyancy aided and opposed isothermal forced convection. Gravity is seen to have an effect at P2 and P3. The relative difference (the difference between the buoyancy aided and opposed velocity divided by the buoyancy-opposed velocity, denoted $\delta\bar{u}_{F,G}$ where F means forced and G means

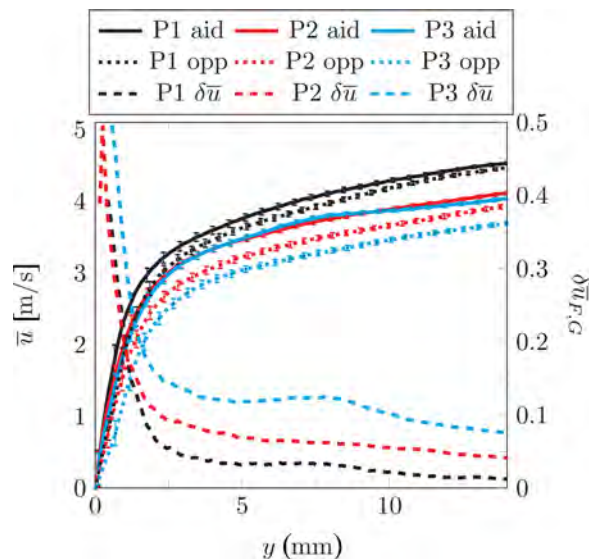


Fig. 20 The boundary layer velocity comparison for the isothermal forced convection buoyancy aided and opposed cases. The relative difference between the cases is also plotted as $\delta\bar{u}_{F,G}$.

gravity) for the isothermal forced convection is also shown in Fig. 20. The difference between the aided and opposed cases increases with streamwise length, suggesting that gravity affects the development of the boundary layer in these cases.

5.3 Buoyancy Influence on Heat Flux. Now we consider the buoyancy influence on heat flux from the plate. Wang et al. showed data comparing the effects of buoyancy on heat transfer for buoyancy aided and opposed flow [17]. The Nusselt number is divided by a forced convection Nusselt number and plotted as a function of the special buoyancy parameter

$$Bo^* = \frac{Gr^*}{Re^{3.425} Pr^{0.8}} \quad (15)$$

This is shown in Fig. 21 and is compared with the data presented in Ref. [17].

In this analysis, the characteristic length of the Nusselt number Nu is the hydraulic diameter of the test section (12 in.). The developing, variable property forced convection Nusselt number Nu_f is

$$Nu_f = C \times 0.0228 Re^{0.79} Pr^{0.4} \left(\frac{T_s}{T_\infty} \right)^{-0.34} \quad (16)$$

with

$$C = 1.0 + \left(\frac{x}{D_h} \right)^{-0.29} \exp \left(-0.07 \frac{x}{D_h} \right) \left[0.69 + \frac{5520}{Re} \left(\frac{x}{D_h} \right)^{-0.7} \right] \quad (17)$$

as described in Ref. [17].

It is shown in the Wang et al. data and study [17] that the buoyancy-aided flow experiences a suppression of heat transfer followed by a recovery of the heat flux for an increase in buoyancy effects. The data obtained in the present study show a similar trend. For example, the buoyancy-aided case shows a decrease in the Nusselt number ratio from position 1 to 2 and an increase again from 2 to 3 (right to left in Fig. 21). The buoyancy-opposed case shows a suppression of heat flux similar to the buoyancy-aided case. The difference from unity at each position

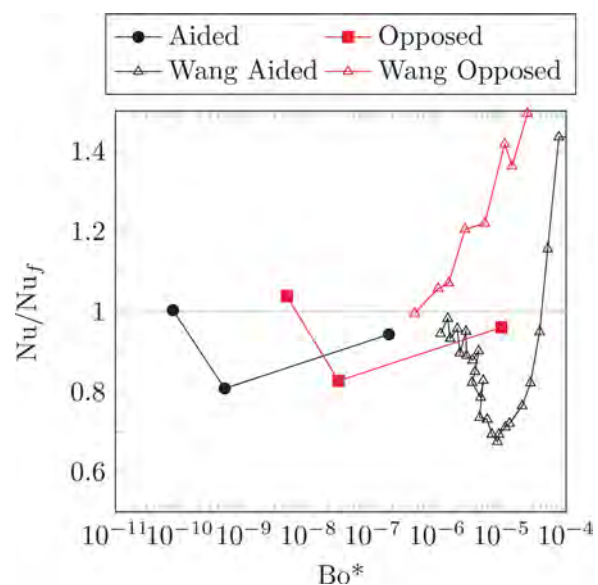


Fig. 21 A plot of the Nusselt number ratio versus the special buoyancy parameter for the data in this study and the data presented in Ref. [17]

is nearly the same for the two cases. The difference from unity at the third position for the buoyancy-aided case is negligible. However, for the buoyancy-opposed case, there is an improvement of heat transfer. This is due to the change in the direction of gravity.

5.4 Comparison of Classical Boundary Layer Shape Factors. The shape factor H , which is the ratio of the displacement thickness and the momentum thickness, is plotted in Fig. 22. The shape factor is plotted as a function of a second shape factor, η , which is defined as [29]

$$\eta = 1 - \left(\frac{\bar{u}(H)}{\bar{u}_\infty} \right)^2 \quad (18)$$

The $\bar{u}(H)$ term in Eq. (18) is the measured velocity at a distance H from the wall. The expected trend for η as a function of H is [29]

$$\eta_{\text{expected}} = 1 - \left[\frac{H-1}{H(H+1)} \right]^{H-1} \quad (19)$$

It is noted that for $\eta > 0.46$, a pressure rise exists in the flow [29]. From Fig. 22, we see that all of the buoyancy-aided cases are in the adverse pressure range. The experimental measurements also match trends shown in the data presented by Schlichting (see Fig. 22.6 in Ref. [29]). The text also states that separation occurs near $\eta \approx 0.8$. However, the data show no signs of separation.

To help understand if one should expect heating to impact the shape factor analysis, an unheated case is compared to a heated case. An additional two datasets that are not part of the validation dataset are now considered. They include an unheated and heated flow at a Reynolds number (based on hydraulic diameter) of 13,400. This flow is much slower than the cases considered previously, having a free stream velocity of 0.7 m/s. The buoyancy effects on the flow are significant for this flow rate. The velocity profiles for these additional cases are shown in Fig. 23. It is obvious that the heating accelerates the boundary layer when compared with the unheated case. In both cases, the Reynolds normal stress is small.

The corresponding shape factor correlation is included in Fig. 22 labeled as heated, unheated, and heated max velocity. Notice that when the free stream velocity is used to compute η in the heated case (solid square), the resultant point is far different

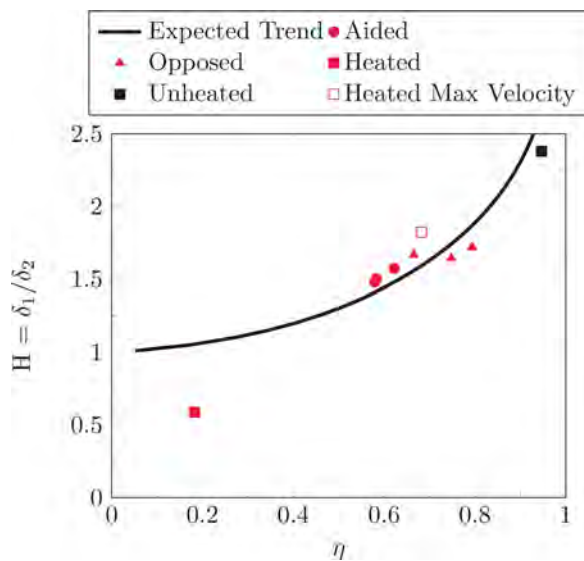


Fig. 22 A comparison of the classic shape factor with the expected trend as a function of the second shape factor η (see Eq. (18))

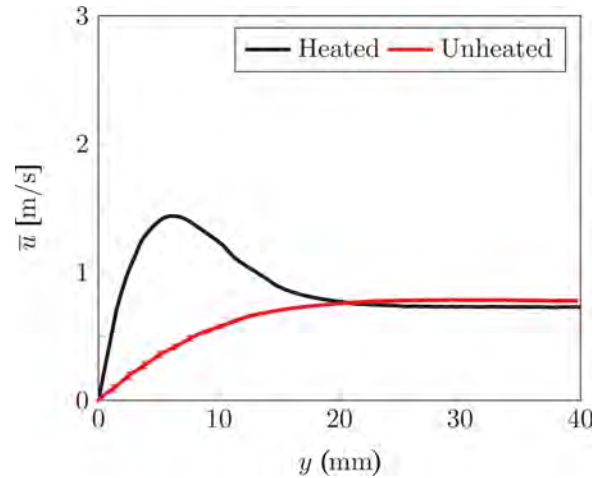


Fig. 23 The boundary layer velocity profiles for an unheated and heated low Reynolds number flow

from an expected trend. The free stream velocity is used in the literature and the other cases previously presented. However, if the maximum velocity is used (heated max velocity, hollow square), the point is closer to expected values. The unheated case is near the expected trend as well (solid square). This suggests that the boundary layers considered in this flow behave similarly to unheated boundary layers considered in the classical literature. Also, when discussing this shape factor trend, the maximum velocity should be used, particularly when significant accelerations are in the flow. The maximum velocity is higher than the free stream velocity for the low Reynolds number case shown by Fig. 23.

6 Conclusions

This work describes a CFD validation experiment for turbulent forced convection using guidelines described by Oberkampf and Roy [6] and Oberkampf and Smith [1]. It represents a departure from typical journal articles in that the aim of the study is not discovery, but rather to carefully measure all inputs and outputs of a CFD RANS simulation for the purpose of validation. A database in the Supplemental results which are available under "Supplemental Data" tab for this paper on the [ASME Digital Collection](#) is used to make the data (boundary and inflow conditions as well as system response) available digitally. This is the first in a series of convection validation data experiments that will be made available for CFD validation.

Acknowledgment

This research was funded by the DOE Office of Nuclear Energy's Nuclear Energy University Programs. The support of the Nuclear Regulatory Commission was also gratefully acknowledged. The authors also thank Professor Nam Dinh and Dr. William Oberkampf for their helpful discussions and insight.

Nomenclature

- B = coefficient for wall coordinate profiles
- dy = PIV data vector spacing
- g = standard gravity constant
- Gr_x = Grashof number
- h = convection coefficient
- H = boundary layer shape factor, δ_1/δ_2
- k = turbulent kinetic energy
- k_r = material property for radiation emission
- n = index of refraction
- Nu_x = Nusselt number

P = pressure
 Pr = Prandtl number
 Re_x = Reynolds number
 Re_{δ_2} = momentum thickness Reynolds number
 St_x = Stanton number
 T = temperature
 T_L = clear Lexan wall temperature
 T_s = surface temperature
 T_∞ = free stream temperature
 \bar{u} = mean streamwise velocity
 \bar{u}_∞ = free stream velocity
 u_τ = shear velocity
 $u'u'$ = variance of u
 $u1$ = velocity at a point in the profile
 $u2$ = velocity at a second point in the profile
 U_P = uncertainty of pressure
 U_T = uncertainty of temperature
 U_μ = uncertainty of dynamic viscosity
 U_ν = uncertainty of kinematic viscosity
 U_ρ = uncertainty of density
 $U_{du/dy}$ = uncertainty of the velocity gradient
 U_{u1} = uncertainty of velocity at a point
 U_{u2} = uncertainty of velocity at a second point
 U_{u_τ} = uncertainty of shear velocity
 u' = instantaneous velocity fluctuation
 \bar{v} = mean velocity normal to wall
 $v'v'$ = variance of v
 \bar{w} = mean velocity normal to \bar{u} and \bar{v}
 $w'w'$ = variance of w
 x = direction parallel with flow
 y = direction normal to plate
 y_0 = correction for the wall location
 z = direction normal to x and y plane (right-handed system)
 β = the volumetric thermal expansion coefficient of air
 δ_2 = the momentum thickness of the boundary layer
 ε = turbulence dissipation rate
 ε_L = emissivity of Lexan wall
 ε_n = emissivity of nickel-coated plate
 η = a secondary boundary layer shape factor
 κ = von Kármán constant
 μ = dynamic viscosity
 ν = kinematic viscosity
 ρ = fluid density
 σ = Stefan–Boltzmann constant

Appendix: CFD Sensitivity to Inlet ε

The turbulence dissipation rate ε is a function of the spatial derivatives of the fluctuating components of velocity (cf. Eq. (4)). Since ε cannot be directly measured in this study, the sensitivity of a RANS model to inlet ε was investigated. Four simulations were run using several uniform distributions of ε at the inlet of the test section; $\varepsilon=0$, 10^{-6} , 10^{-3} , and 10^1 . For more information regarding the simulation parameters, see Ref. [21]. Additionally, a distribution of ε was found using the measured k and the common expression

$$\varepsilon = 0.09^{3/4} \frac{k^{3/2}}{l} \quad (20)$$

where l is 0.07 times the equivalent pipe diameter [30,31]. The equivalent pipe diameter can be computed from Heubscher's equation as [32]

$$d_{eq} = 1.3 \frac{(ab)^{0.625}}{(a+b)^{0.25}} \quad (21)$$

There is some controversy about this equation and there are several other suggestions for computing the equivalent pipe diameter. However, the differences result in similar values of ε .

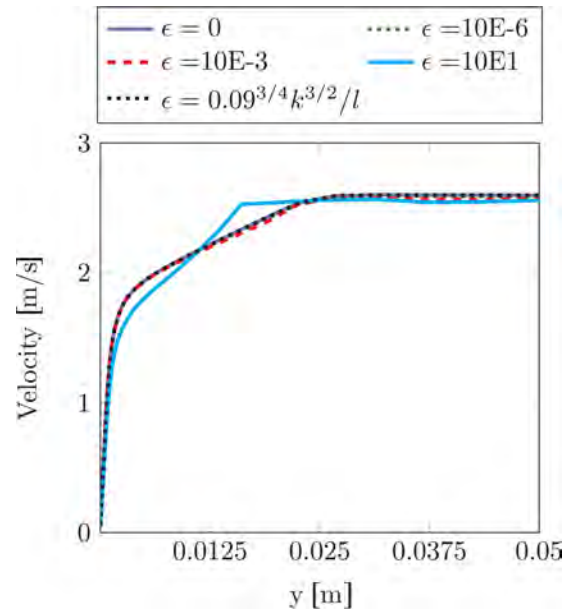


Fig. 24 The streamwise velocity at the first heat flux sensor position for several inlet ε treatments

Using these five profiles of ε , the effects on a velocity profile are shown in Fig. 24. Only the largest values of ε affect the simulation results. Using Eq. (20) at the inlet yields an inlet turbulence dissipation rate below 0.01. Profiles of other SRQs at the three heat flux sensor locations show the same trend as Fig. 24, with $\varepsilon = 10^1$ being the only case having significant influence on the SRQ. This insensitivity of CFD to ε was noted by Wilcox [31, p. 148] who states that investing resources into accurately finding ε is unwise.

References

- [1] Oberkampf, W., and Smith, B., 2014, "Assessment Criteria for Computational Fluid Dynamics Validation Benchmark Experiments," AIAA SciTech Conference, AIAA, <http://arc.aiaa.org/doi/abs/10.2514/6.2014-0205>
- [2] CFD-Online, 2013, "Validation Cases Links References," <http://www.cfd-online.com/Links/refs.html>
- [3] NPARC Alliance, 2013, "Turbulent Flat Plate," <http://www.grc.nasa.gov/WWW/wind/valid/fturb/fturb.html>
- [4] ERCofTC, 2013, "Classic Collection Database," <http://cfd.mace.manchester.ac.uk/ercofac/classif.html>
- [5] Experimental Fluid Dynamics Laboratory, 2014, "Buoyancy Aided Forced Convection Database," http://efdl.neng.usu.edu/ValidationPages/FC_VValidation/Main.html
- [6] Oberkampf, W. L., and Roy, C. J., 2010, *Verification and Validation in Scientific Computing*, Cambridge University Press, New York.
- [7] Oberkampf, W. L., Sindir, M., and Conlisk, A., 1998, *Guide for the Verification and Validation of Computational Fluid Dynamics Simulations*, American Institute of Aeronautics and Astronautics, Reston, VA.
- [8] ASME, 2009, "Standard for Verification and Validation in Computational Fluid Dynamics and Heat Transfer," ASME Standard V&V 20-2009, New York.
- [9] Timmins, B. H., Wilson, B. W., Smith, B. L., and Vlachos, P. P., 2012, "A Method for Automatic Estimation of Instantaneous Local Uncertainty in Particle Image Velocimetry Measurements," *Exp. Fluids*, **53**(4), pp. 1133–1147.
- [10] Warner, S. O., and Smith, B. L., 2014, "Autocorrelation-Based Estimate of Particle Image Density for Diffraction Limited Particle Images," *Meas. Sci. Technol.*, **25**(6).
- [11] Wilson, B. M., and Smith, B. L., 2013, "Uncertainty on PIV Mean and Fluctuating Velocity Due to Bias and Random Errors," *Meas. Sci. Technol.*, **24**(3), p. 035302.
- [12] Wilson, B. M., and Smith, B. L., 2013, "Taylor-Series and Monte-Carlo-Method Uncertainty Estimation of the Width of a Probability Distribution Based on Varying Bias and Random Error," *Meas. Sci. Technol.*, **24**(3), p. 035301.
- [13] Coleman, H. W., and Steele, W. G., 2009, *Experimentation, Validation, and Uncertainty Analysis for Engineers*, 3rd ed., Wiley, Hoboken, NJ.
- [14] Kays, W. M., Crawford, M. E., and Weigand, B., 2004, *Convective Heat and Mass Transfer*, 4th ed., McGraw-Hill, New York.

- [15] Lloyd, J., and Sparrow, E., 1970, "Combined Forced and Free Convection Flow on Vertical Surfaces," *Int. J. Heat Mass Transfer*, **13**(2), pp. 434–438.
- [16] Gryzagoridis, J., 1975, "Combined Free and Forced Convection From an Isothermal Vertical Plate," *Int. J. Heat Mass Transfer*, **18**(7), pp. 911–916.
- [17] Wang, J., Li, J., and Jackson, J., 2004, "A Study of the Influence of Buoyancy on Turbulent Flow in a Vertical Plane Passage," *Int. J. Heat Fluid Flow*, **25**(3), pp. 420–430.
- [18] Hattori, Y., Tsuji, T., Nagano, Y., and Tanaka, N., 2001, "Effects of Freestream on Turbulent Combined-Convection Boundary Layer Along a Vertical Heated Plate," *Int. J. Heat Fluid Flow*, **22**(3), pp. 315–322.
- [19] Howell, J. R., Siegel, R., and Mengüç, M. P., 2011, *Thermal Radiation Heat Transfer*, CRC Press, Boca Raton.
- [20] Karri, S., Charonko, J. J., and Vlachos, P. P., 2009, "Robust Wall Gradient Estimation Using Radial Basis Functions and Proper Orthogonal Decomposition (POD) for Particle Image Velocimetry (PIV) Measured Fields," *Meas. Sci. Technol.*, **20**(4), p. 045401.
- [21] Harris, J., 2014, "A CFD Validation Experiment for Forced and Mixed Convection on a Vertical Heated Plate," Ph.D. thesis, Utah State University, Logan, UT.
- [22] LaVision, "DaVis[®] Version 8.1," Goettingen, Germany, <http://www.lavision.de/en/techniques/piv.php>
- [23] Velmex, Inc., "Linear Motor-Driven Bi- and UniSlide Assemblies," <http://www.velmex.com/index.asp>
- [24] Kähler, C., 2003, "General Design and Operating Rules for Seeding Atomisers," 5th International Symposium on Particle Image Velocimetry.
- [25] Weast, R. C., Astle, M. J., and Beyer, W. H., 1988, *CRC Handbook of Chemistry and Physics*, Vol. 69, CRC Press, Boca Raton.
- [26] Kendall, A., and Koochesfahani, M., 2008, "A Method for Estimating Wall Friction in Turbulent Wall-Bounded Flows," *Exp. Fluids*, **44**(5), pp. 773–780.
- [27] Incropera, F. P., and DeWitt, D. P., 2002, *Introduction to Heat and Mass Transfer*, 5th ed., Wiley, New York.
- [28] Oberkampf, W. L., and Trucano, T. G., 2002, "Verification and Validation in Computational Fluid Dynamics," *Prog. Aerosp. Sci.*, **38**(3), pp. 209–272.
- [29] Schlichting, H., 1968, *Boundary-Layer Theory*, McGraw-Hill, New York.
- [30] Versteeg, H. K., and Malalasekera, W., 2007, *An Introduction to Computational Fluid Dynamics: The Finite Volume Method*, Prentice Hall, New York.
- [31] Wilcox, D., 2010, *Turbulence Modeling for CFD*, 3rd ed., Vol. 93, DCW Industries, La Cañada, CA.
- [32] Huebscher, R. G., 1948, "Friction Equivalents for Round, Square and Rectangular Ducts," *ASHVE Trans. (ASHRAE Trans.)*, **54**, pp. 101–144.